



**University of
Nottingham**
UK | CHINA | MALAYSIA

**Experimental and Numerical Investigations into the
Behaviour of a 7175-T7351 Aluminium Alloy for Aerospace
Gearbox Housing Applications at Elevated Temperatures**

Marc F. Lam Wing Cheong, MEng (Hons)

Supervisors:

Dr. Christopher J. Hyde

Dr. Andrew R. Kennedy

Dr. James P. Rouse

Thesis submitted to The University of Nottingham for
the degree of Doctor of Philosophy

August 2017

Abstract

The 7175-T7351 aluminium alloy was studied to determine its suitability for the step-aside gearbox housing on the Rolls Royce Trent 1000 engine. The industrial motivation of this work was to reduce the weight of the gearbox housing using this lightweight material to ultimately improve the specific fuel consumption of the aircraft. This involved obtaining the mechanical properties of the aluminium alloy via a series of uniaxial mechanical tests with parameters based on the operating conditions of the gearbox housing during a typical flight cycle. Furthermore, a constitutive viscoplasticity model, with the inclusion of material ageing parameters, was developed to predict the material's cyclic response under strain-controlled isothermal fatigue conditions at the gearbox housing's operating temperatures. With this capability, a prediction for when the strength of the gearbox housing falls below the required design strength for safe use could be made.

The room temperature hardness tests demonstrated the effect of time spent at elevated temperatures on the material's hardness. It was found that the higher the soak temperature, the greater the initial rate of decrease in room temperature hardness and the lower the asymptotic value of hardness that was reached. For example, up to 24 hours of soaking at 200°C, the hardness decreased by 33%, and up to 1000 hours the hardness had decreased by 55%. For the same durations at 180°C, the hardness decrease was 17% and 47% respectively. Soaking at 120°C had an insignificant effect on the hardness of the material, indicating that the microstructure was thermally stable. Hardness testing could be used as a method to assess the strength of the gearbox housing for service monitoring during certification.

Similar to the hardness tests, the elevated temperature tensile test results also revealed degradation in the mechanical strength of the alloy after prior soaking at elevated temperatures. The tests at 200°C on the as-received material decreased the yield stress by 31% and after soaking at test temperature for 20 hours prior to testing, the yield strength dropped by 52%. After a 2 hour temperature, the yield stress decreased from 220MPa to 165MPa which is alarming since the gearbox housing spends about 18 minutes at 200°C and 190MPa during climb. This suggests that in less than 6 flight cycles, the material's strength will fall below the maximum operating stress of the gearbox housing and will be unsafe for continued use.

Samples were soaked for up to 400 hours at 200°C and prepared for microstructural analysis. EBSD images showed that the grains were not

significantly affected by the temperature exposure and showed no signs of coarsening. TEM and EDX analysis revealed that the majority of the particles within the grains were zinc-magnesium rich particles and were assumed to be MgZn_2 precipitates based on the TEM particle identification. The precipitate size and inter-particle spacing were found to increase with soak time. The change in monotonic yield strength was therefore attributed to the coarsening of these precipitates. The material characterisation suggested that, although the 7175-T7351 aluminium alloy initially appeared to have desirable mechanical properties, it is unsuitable for this or similar applications due to the rapid decrease in strength and thermally unstable microstructure. Furthermore, if an aluminium alloy is considered for this application, then it may be vital to account for material ageing behaviour.

The unified, uniaxial viscoplasticity Chaboche model was implemented to predict the material response strain-controlled isothermal fatigue tests at 160°C and 200°C. A material ageing term was added to the model to account for the material ageing that decreased the yield strength with time. With this addition, two assumptions were made: 1) material ageing only affects isotropic hardening and 2) isotropic hardening can be de-coupled into material ageing (as a function of time at elevated temperature) and mechanical softening (a function of accumulated plastic strain). The tests at 160°C and 200°C showed that numerical and experimental results were in good agreement, providing accurate isothermal cyclic stress behaviour of the 7175-T7351 aluminium alloy. Furthermore, it was shown that the mechanical softening and material ageing components could be de-coupled. However, when the model was used to predict stress-controlled isothermal fatigue data and a cyclic stress relaxation tests, a number of deficiencies arose. The predicted ratcheting and ageing rate was greater than expected. The material ageing term may require an additional function to change the ageing rate depending on whether the material is elastically or plastically loaded. Norton's creep power law could not predict term long stress relaxation behaviour but it was sufficient enough to describe to short-term viscous effects under the strain-controlled fatigue conditions. Despite these deficiencies, the model provided an initial point for a unified, viscoplasticity model for the 7175-T7351 alloy. Due to the rapid ageing of the material, the model could be used to predict if or when a material's strength is unsuitable for safe operating use.

Acknowledgements

I would like to thank my supervisors, Dr. Chris Hyde, Dr. Andrew Kennedy and Dr. James Rouse for their support, encouragement and extensive knowledge on material behaviour and analytical modelling. I would also like to thank Rolls-Royce plc. for funding my research and the Gas Turbine and Transmission Research Centre (G2TRC) for welcoming me to their research division.

For technical support, I would like to thank Tom Buss, Shane Maskill, Jason Greaves, Graham Malkinson and Max Mason, for assisting me with experimental testing and for their guidance. Additional thanks to Dr. Nigel Neate and Dr. Chris Parmenter from the Nanoscale and Microscale Research Centre (NMRC) for their assistance and knowledge in electron microscopy and analysis.

Lastly, I would like to thank my family for their love and support throughout my time at the University of Nottingham.

Nomenclature

Roman Symbols

A	Norton creep law constant
C_i	Kinematic hardening parameter that determines the rate to reach the saturation value a_i
E	Young's modulus
M	Total number of back stresses
N_f	Number of cycles to failure
Q	Drag stress saturation value for isotropic hardening
R	Total isotropic drag stress
T	Temperature
T_m	Melting temperature
Z	Viscous parameter in the Chaboche model
a_i	Kinematic hardening parameter that determines a saturation value for χ_i
b	Isotropic hardening parameter that determines the rate at which the saturation value Q is reached
f	yield function in the Chaboche model
k	Initial cyclic yield strength
n	Norton power law constant
p	Accumulated plastic strain
t	Time
t_f^0	Time to failure for the virgin creep sample
t_f^p	Time to failure for the prestrained creep sample

Greek Letters

$\dot{\epsilon}_{min}^c$	Minimum creep strain rate
γ	Shear strain
χ	Total back stress
ω	Damage factor

α	Triaxiality material constant
ϕ	The ratio of the minimum secondary creep rate
ψ	Total back stress
σ_1	Principal stress 1
σ_2	Principal stress 2
σ_3	Principal stress 3
τ_{Orowan}	Orowan bowing stress
σ_a	Stress amplitude
σ_{el}	Magnitude of the elastic region of a material
σ_m	Mean stress
σ_{max}	Maximum stress
σ_{min}	Minimum stress
ε_p	Plastic strain
τ_{shear}	Particle shear stress
σ_v	Viscous stress
σ_y	Yield stress

Contents

Abstract	i
Acknowledgments	iii
Nomenclature	iv
1 Introduction	1
2 Literature Review	8
2.1 Introduction	8
2.2 Aluminium Alloys Designations and the Solid Solution Strengthening Method	10
2.3 Crystalline Structures in Metals	11
2.3.1 Crystal Lattice Defects	13
2.4 The Effects of Casting and Rolling on the Mechanical Properties of Aluminium Alloys	15
2.4.1 Solidification of Molten Aluminium After Casting	15
2.4.2 Mechanical Deformation - Rolling	17
2.4.3 The Effects of Heat Treatment - Ageing of Aluminium	17
2.5 The 7000 Series Aluminium Alloy	22
2.6 Mechanical Behaviour of Materials	23
2.6.1 Plasticity	23
2.6.2 Constitutive Viscoplasticity Models	27
2.6.3 Numerical and Optimisation Methods	33
2.6.4 Constitutive Models with the Inclusion of Ageing Effects	36
2.6.5 Isothermal Fatigue	37
2.6.6 Thermomechanical Fatigue	42
2.6.7 Creep Deformation	44
2.7 Experimental Techniques	50
2.7.1 Strain Measuring Techniques	50
2.7.2 Sample Heating Methods and Temperature Measurement Techniques	52

2.8	Microscopy Techniques	53
3	Material, Test Methodology and Equipment	59
3.1	Material	59
3.2	General Test Conditions	60
3.3	Hardness Measurements	60
3.3.1	Discrepancy Check in Plate Hardness	60
3.3.2	Plate Hardness After Exposure To Temperature Over Time	62
3.4	Tensile Test Methodology and Equipment	62
3.5	Creep Tests	64
3.6	Fatigue Tests	69
3.6.1	Pyrometer Temperature Measurement Investigation	70
3.6.2	Stress-Controlled Fatigue Tests	72
3.6.3	Isothermal Fatigue Tests with Decaying Strain Amplitude	75
3.6.4	Stress Relaxation Tests	78
4	Material Characterisation	81
4.1	Hardness Discrepancy Check of the 7175-T7351 Plate	81
4.2	Hardness of the Plate After Time at Various Temperatures	82
4.3	Tensile Test Results	84
4.3.1	Definition of a Relationship Between Time at Temperature and Yield Strain	90
4.4	Creep Test Results	91
4.5	Prestrained Creep Test Results	94
4.6	Stress-Controlled Tests Results	103
4.6.1	Isothermal Fatigue	103
4.6.2	Thermomechanical Fatigue	106
5	Microstructural Analysis of the 7175-T7351 Aluminium Alloy	114
5.1	Microstructural Overview	114
5.2	Element Mapping	115
5.3	Particle Identification	120
5.3.1	Particle Spacing and Size Measurements	124

6	Implementation of the Uniaxial Chaboche Model for Stress State Prediction of the Rapidly Ageing 7175-T7351 Aluminium Alloy at Elevated Temperatures	143
6.1	Introduction	143
6.1.1	Initial Comparisons Between Experimental Test Results of the Strain-Controlled Fatigue Tests	144
6.2	The Uniaxial Chaboche Model	146
6.3	Determination of Initial Material Constants	151
6.3.1	Initial Cyclic Yield Stress and Young’s Modulus	151
6.3.2	Mechanical Softening Parameters	153
6.3.3	Kinematic Hardening Parameters	155
6.3.4	Viscous Stress Parameters	158
6.3.5	Material Ageing Parameters	160
6.4	Objective Functions for the Optimisation Process	161
6.5	Numerical Methods and Implementation in MATLAB	162
6.6	Chaboche Model Predictions and Discussion	165
6.6.1	Stress Prediction of the “Fully-Aged” Samples	165
6.6.2	Stress Prediction of the As-Received Samples	171
6.6.3	Complete Chaboche Model Validation - Stress Prediction of “Partially-Aged” and “Fully-Aged” Samples	177
6.6.4	Prediction of Stress Relaxation Tests and Stress-Controlled Isothermal Fatigue Tests	182
6.7	Conclusions	186
7	Discussion	188
8	Conclusions	193
9	Future Work	196
	Bibliography	198
	Appendix	216
9.1	Detailed Schematics of Sample Location from Plate	216

1 Introduction

An increased demand for air transportation has led to the increase of aircraft emissions that are harmful to the global climate (CO_2 , NO_x). It has been established that CO_2 contributes to the greenhouse effect and global warming [1], and the NO_x gases contribute to the formation of smog and acid rain [2]. The Advisory Council for Aviation Research and innovation in Europe (ACARE) have set targets to significantly reduce the environmental impact of aircraft transportation by 2050 in Europe (relative to 2000). Two strategies have been put forward to progress towards those goals: 1) reduce the weight of the aircraft to improve its specific fuel consumption and 2) increase the combustion temperature to increase engine efficiency and reduce CO_2 emissions. Both of these strategies will require insight into the behaviour of the component materials to ensure that they will meet design requirements during operation.

Aluminium alloys are widely used for aerospace applications for its low density, high specific strength and good fatigue properties. Typical components that are made of aluminium are the wings, airframe and fuselage [3]. Their light weight allows for greater range and speed of the aircraft and may also play a role in reducing operational costs. However, aluminium alloys have limited use at elevated temperatures due to the evolution of their metastable microstructure. It is well documented that exposure to elevated temperatures facilitates the coarsening of precipitates (known as material ageing) which can be detrimental to the material's strength. This can be seen in the ageing curves of aluminium alloys where extended time at elevated temperatures will decrease the material's hardness and yield strength (examples of ageing curves of the 2000, 6000 and 7000 series aluminium alloys can be found here: [4-6]).

This work looks into the concept, put forward by Rolls-Royce plc., that the weight of the step-aside gearbox (SAGB) housing could be reduced by replacing the current materials (cast aluminium and cast titanium alloys) with the wrought aluminium alloy 7175-T7351 (provided by Amari-Aerospace ltd). Cast aluminium alloys or titanium alloys are utilised for the housing due to the complexity of its geometry. Some cast aluminium alloys used in aerospace are able to retain their strength at elevated temperatures but have moderate yield strength at those temperatures [7]. Titanium

alloys have relatively high mechanical properties and good thermal stability [8] at the operating temperatures of the step-aside gearbox housing but they are more expensive to manufacture and have a higher density ($4400\text{-}4800\text{kg}\cdot\text{m}^{-3}$) than aluminium [9]. The 7175-T7351 alloy has a room temperature 0.2% proof stress of 454MPa, an ultimate tensile strength of 521MPa, and a similar density to cast aluminium alloys [9]. If the material is suitable for housing applications, then it may be possible to decrease the component weight which would lead to a reduction in fuel consumption. The question of how the wrought material will be fastened or joined together is yet to be explored but precision manufacturing capabilities are available worldwide which could lead to a reduction in manufacturing costs.

The SAGB housing is located on the intermediate fan casing, as shown in Figure 1.1, and a finite element model of the SAGB housing can be found in Figures 1.2 and 1.3, which was provided by Rolls-Royce plc. It is connected to the radial drive shaft and drives the angular drive shaft which ultimately transmits power to the accessory gearbox components such as the hydraulic, oil and fuel pumps, combustors and electric generators [10].

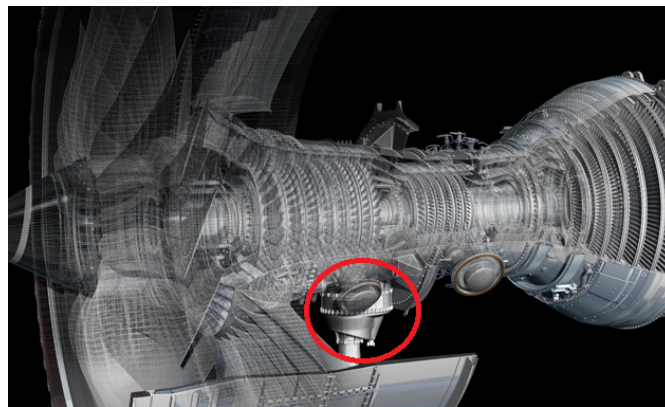


Figure 1.1: An image of the Trent 1000 showing the location of the step-aside gearbox [11].

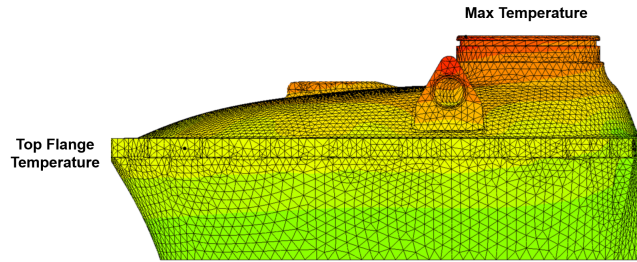


Figure 1.2: FE model image of the step-aside gearbox labelling the 2 areas where operating temperature profiles were obtained (provided by Rolls-Royce plc.).

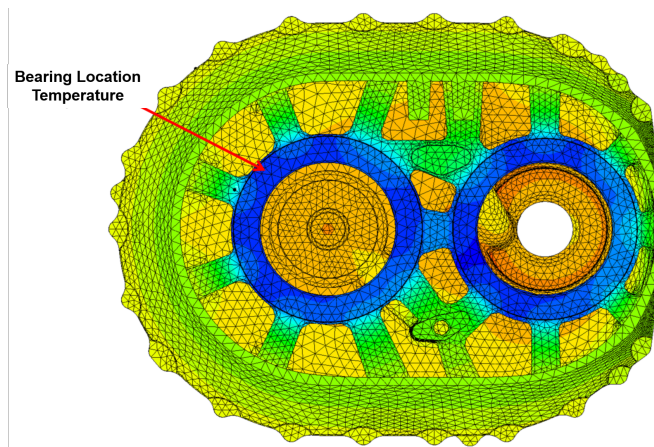


Figure 1.3: FE model image of the step-aside gearbox labelling the third area where operating temperature profiles were obtained (provided by Rolls-Royce plc.).

Figure 1.4 shows the points along the top flange where stress measurements were taken since the top flange will carry the highest load in the housing. Figure 1.5 shows the magnitude of the stresses at some of the points and temperatures of the housing at three different locations during a single excursion. The dashed lines represent a $+30^{\circ}\text{C}$ uncertainty which the component may be subjected to due to operational flexibility.

Stress measurement points On Top Flange

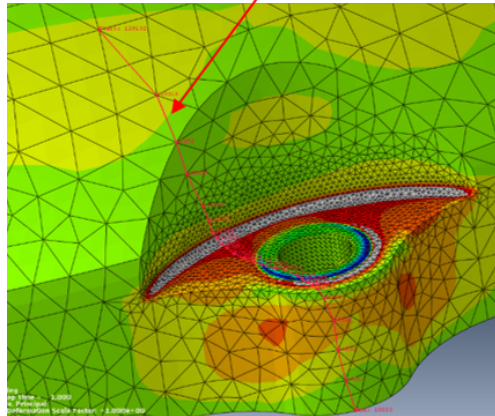
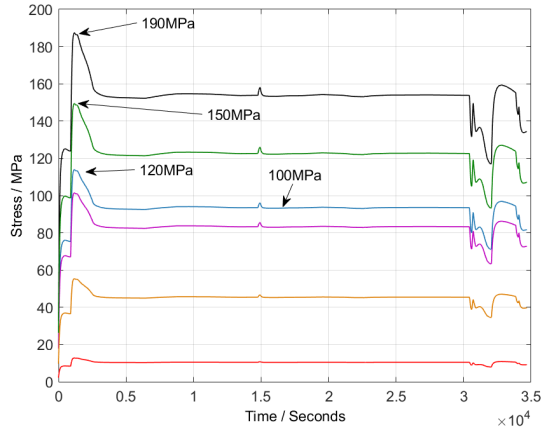
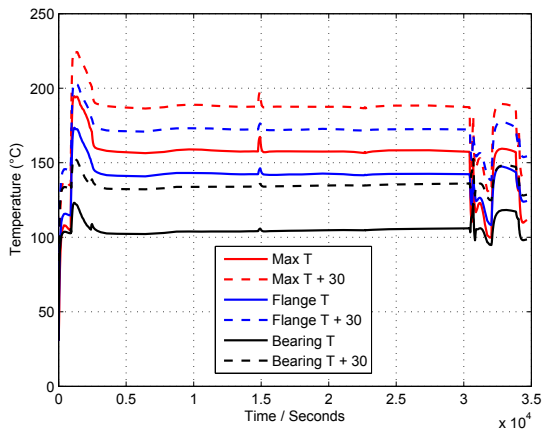


Figure 1.4: The position of the points where the stress was calculated on the top flange (provided by Rolls-Royce plc.).



(a)



(b)

Figure 1.5: (a) Stress profile at several points on the top flange (see Figure 1.3) over a typical flight cycle and (b) temperature profiles of the step-aside gearbox housing over a flight cycle provided by Rolls-Royce plc. The dashed lines represent a $+30^{\circ}\text{C}$ uncertainty at each location.

The first objective was to characterise the 7175-T7351 aluminium alloy through a series of elevated temperature mechanical tests such as tensile, creep and stress-controlled isothermal and thermo-mechanical fatigue tests. This would provide insight to the material's mechanical behaviour under loading conditions that represent simplified flight conditions. The second objective was to develop a constitutive model to predict the stress-state of the aluminium alloy under strain-controlled uniaxial isothermal fatigue conditions. If the stress response can be accurately predicted, then this modified model would be the initial step towards material behaviour prediction. Building a more complex model that incorporates other factors that affect fatigue life such as damage, ratcheting, and anisothermal conditions will require further work but would increase the predictive accuracy for when the material is subjected to more

realistic operating conditions. Further work would also be required for multi-axial stress-strain predictions since uniaxial predictions would not account for potential additional hardening behaviours.

With the ability to predict material behaviour during operation, a design criteria can be implemented to determine if or when the component fails to meet the required strength for safe use. The prediction of material strength would need to be verified by inspection which should be included in the certification procedure. This model could be used for other elevated temperature applications where aluminium alloys could be implemented such as other gearboxes on an aircraft engine and automotive engines. For this objective, the unified, viscoplasticity, Chaboche, model was chosen for stress prediction and its capability to describe cyclic hardening behaviour and stress relaxation due to creep based on multiple material constants [12].

The novelty of this work involved incorporating the material ageing behaviour in the Chaboche model to describe the change in material yield as a function of time at temperature, specifically for the 7175-T7351 aluminium alloy. A bespoke loading waveform of decreasing strain amplitude, where the maximum allowable strain at any time was 10% greater than the monotonic yield strain, was used to induce appreciable plasticity per cycle without exceeding the material's ultimate tensile strength (UTS). This allowed enough data to be obtained so that the material constants could be determined for the modified, ageing-sensitive Chaboche model. If the material behaviour during operation can be accurately predicted, then the possibility for the creation of innovative designs for weight reduction can be made. Hence, improvements in engine performance and efficiency can be gained and harmful emissions and manufacturing costs can be reduced. Previous works by Marquis [13] and Cailletaud [14] have incorporated material ageing in the Chaboche model but were carried out on under-aged aluminium alloys (2024 alloy that was aged at room temperature after quenching and the ASTM 319-T5 alloy).

A literature review is presented in chapter 2. This will set the background of this thesis in greater detail and discuss the applications of the 7175-T7351 in aerospace, the effect on the manufacturing methods on mechanical properties, the phases within the material of interest, and previous works on constitutive models to predict material behaviour subjected to cyclic plasticity. The mechanical behaviour of metals with

reference to the 7000 series alloys, and experimental and microscopy techniques will also be covered.

Chapter 3 will provide a description the equipment and test methodology used for all mechanical testing at elevated temperatures. Details regarding the adjustments needed for temperature measurement of fatigue samples and strain measurement for tensile testing are also presented. Information regarding the effects of ambient temperature control on the strain measurement during stress relaxation tests are given in the appendix.

Chapter 4 presents the results of the material characterisation of the 7175-T7351. The implications of the effects of time at temperature on the material's yield strength are discussed and represented by the hardness, tensile and stress-controlled isothermal fatigue and thermomechanical tests.

A microstructural analysis of the 7175-T7351 alloy is presented in chapter 5, where precipitates within the alloy are identified and measured after the material was soaked at temperature for up to 400 hours. The change in size and spacing of the precipitates are described in detail and how they correlate to the material's monotonic yield stress.

The modification of the Chaboche model to include material ageing effects for the prediction of the material's stress-strain behaviour is detailed in chapter 6. The constitutive equations, optimisation process of material constants, and the implementation in MATLAB are outlined. Furthermore, a comparison between the numerical and experimental stress of the strain-control isothermal fatigue tests, as well as the model's prediction of stress-controlled fatigue tests and stress relaxation tests are provided.

A discussion relating the relevance of this work to elevated temperature applications can be found in chapter 7. Chapters 8 and 9 present the overall conclusions and suggestions for future work that could improve the experimental methods and further develop the current model, respectively.

2 Literature Review

2.1 Introduction

As the demand for air transportation increases, the amount of fuel consumed increases. As a result, there are growing concerns regarding the impact of aviation on air pollution, climate change and community noise pollution. ACARE 2050 have set targets to tackle these concerns in Europe. One of the main goals is to reduce CO₂ emissions per passenger kilometre by 75%, NO_x emissions by 90% and perceived noise emissions by 65%, relative to 2000 emissions, by 2050 [15]. One way to improve the specific fuel consumption is to improve the efficiency of the aero-engine. An increase in the combustion temperature will lead to an improved overall efficiency but as a consequence, the amount of NO_x emissions would also increase. This can be mitigated through the use of various techniques, such as lean premixed prevapourised combustion or water or steam injection, that promote lean combustion and reduce NO_x gas formation [16]. Another way to reduce specific fuel consumption is to reduce the weight of the aircraft as this would result in less fuel being consumed and less emissions being produced [9, 17–20].

In aviation, the improvement of aero-engine performance has been closely linked to the progression of materials and manufacturing processes. Figure 2.1 shows that as new technology was introduced over the years, the fuel consumption decreased and the load factor (ratio of lift to aircraft weight) increased which indicates an improvement in performance indices [21]. The development of titanium and nickel alloys demonstrates this trend by allowing increased engine operating temperature and efficiency [22].

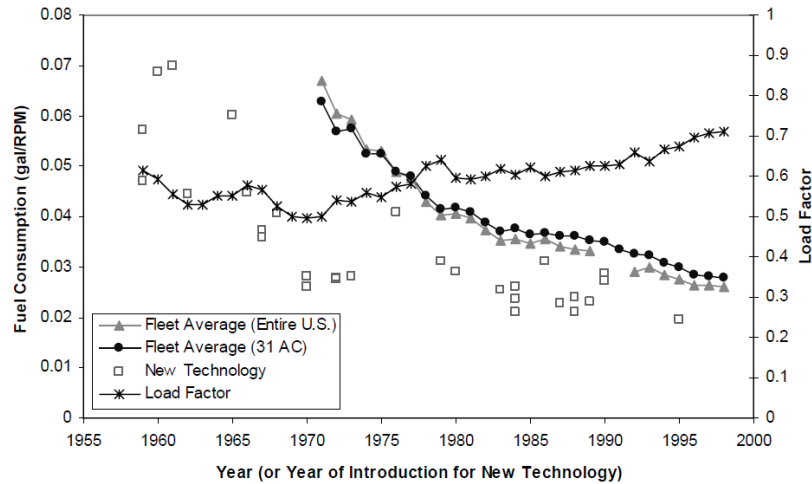


Figure 2.1: Historical Trends in U.S. Fleet Fuel Consumption and Technology Uptake (no data available for entire U.S. fleet during 1990 and 1991)[21].

However, for airline companies, their main concern has been to reduce operating costs and lead times, which causes aircraft design to be more market and customer driven, whereas previously the main design driver was technology [20, 23, 24]. Occasionally during the design stage of a component, a comparison of a few design variables is made, typically with the same manufacturing technology and cost being a secondary concern. This may be due to time and budget constraints [25]. Aircraft manufacturers now realise that the requirement to reduce costs needs to be tackled in the design phase. Burt and Doyle have identified that 70% to 80% of total avoidable cost is controllable within this point [26]. Without a broader range of options, the optimal choice of material and fabrication process to reduce structural weight, manufacturing and operational cost may be overlooked. Therefore, a more critical assessment of materials and manufacturing methods should be conducted.

During the early years of powered flight, the main aircraft design driver was weight minimisation, in order to accommodate for the limited capability of the propulsion system. In general, 75% to 80% of aircraft are made of aluminium alloys and are mainly used in low temperature components such as the fuselage, air frame and wings. These alloys are desirable for aerospace applications due to their low density, relatively high specific strength, moderate cost, good ductility, fracture toughness and corrosion resistance, and ease of control of their properties [24, 27]. The table 2.1 below compares some mechanical properties of titanium and aluminium alloys obtained from CES Edupack 2009 Granta Design software [28]. Titanium alloys have superior tensile

and fatigue strength than aluminium alloys, but their density is 1.5 to 1.9 times greater. Wrought aluminium alloys can possess much greater tensile and fatigue strength than cast aluminium while maintaining the same density. If wrought aluminium alloys can be used for this application, then the weight of the gearbox can potentially be reduced.

Table 2.1: Comparison of a few mechanical properties between titanium and aluminium alloys [28].

Material	Ti Alloys	Wrought Al Alloys	Cast Al Alloys
Density ($\text{kg}\cdot\text{m}^{-3}$)	4400-4800	2500-2900	
Young's modulus (GPa)	110-120	68-80	72-89
Yield Strength (MPa)	750-1200	95-610	50-330
UTS (MPa)	800-1450	180-620	66-386
Fatigue strength, 10^7 cycles (MPa)	589-617	57-210	32-157
Fracture toughness $\text{MPa}\cdot\text{m}^{0.5}$	55-70	21-35	18-35

This chapter will discuss, in general, the manufacturing processes of aluminium alloys, how they are strengthened, and talk more specifically about the 7000 series aluminium alloys to which the 7175 alloy belongs. Aspects of mechanical behaviour such as plasticity, creep, isothermal fatigue and thermomechanical fatigue will also be discussed as well as constitutive models used to predict those behaviours. Lastly, the literature review will cover different types experimental methods (sample heating for hot testing, temperature and strain measurements) and microscopy techniques discussed.

2.2 Aluminium Alloys Designations and the Solid Solution Strengthening Method

Generally, aluminium alloys can be categorised based on two fabrication processes: cast and wrought alloys. The initial stage of manufacturing cast and wrought aluminium products begins either with casting the molten metal directly into moulds with dimensions close to the finished product [29] or semi-continuous casting of ingots for mechanical processing (rolling, forging, extrusion and so on) [30], respectively.

Cast aluminium alloys are identified by a four digit numerical system as shown in Table 2.2. For 2xx.x to 9xx.x the first digit represents the major alloying element and the second two digits serve to identify different alloys in the same series. The final digit

after the decimal point indicates whether the alloy is a casting (.0), or an ingot (.1 or .2) [31].

Table 2.2: Cast aluminium alloy designation system [31]

Main Alloying Element	Current Designation
Aluminium, 99% minimum	1xx.x
Copper	2xx.x
Manganese	3xx.x
Silicon	4xx.x
Magnesium	5xx.x
Unused Series	6xx.x
Zinc	7xx.x
Tin	8xx.x
Other Elements	9xx.x

Table 2.3 shows the wrought aluminium alloy designations. The first digit represents the major alloying element. The second digit indicates alloy modifications of an already existing alloy. For 2xxx, 5xxx, 6xxx, 7xxx and 8xxx, the last two digits identify a specific alloy (without physical significance) [31].

Table 2.3: Wrought aluminium alloy designation system [31]

Main Alloying Element	Current Designation
Aluminium, 99% minimum	1xxx
Copper	2xxx
Manganese	3xxx
Silicon	4xxx
Magnesium	5xxx
Magnesium and Silicon	6xxx
Zinc	7xxx
Other Elements	8xxx

2.3 Crystalline Structures in Metals

When a molten metal has solidified after casting, the atoms self-organise into small solid particles called nuclei. As the nuclei grow, they form grains whose atomic arrangement is described as a crystal lattice. Each grain grows independently and impinges on each

others growth at the interface between grains. Figure 2.2 shows an example of the arrangement of atoms within different grains. It can be seen that there is a mismatch in orientations between each grain which creates a grain boundary. The red circle depicts a triple point which is where all 3 grains share a common boundary.

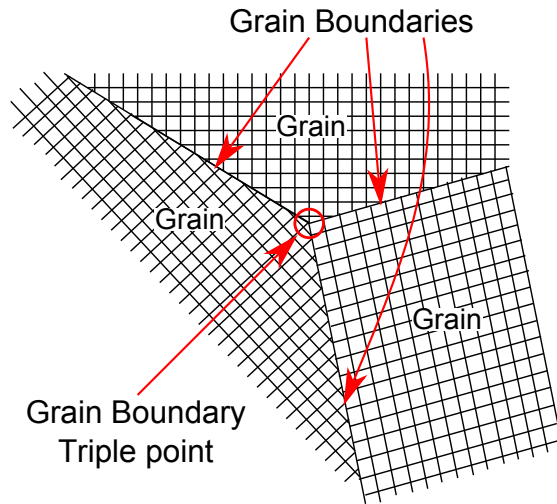


Figure 2.2: A schematic example of grains in different orientations.

A crystal lattice is the periodic array of atoms that is characterised as having translational symmetry. A unit cell is the smallest repetitive arrangement of atoms in 3D space within a crystal lattice. Bravais established 14 types of space lattices but for this review only body-centred cubic (BCC), face-centred cubic (FCC) and hexagonal close packed (HCP) will be covered as examples as shown in Figure 2.3. The length of the cell edges is represented in terms of lattice parameters (a , b and c) and the position of the atoms are measured from a reference lattice point in the form of fractional coordinates based on the unit length of the cell [32].

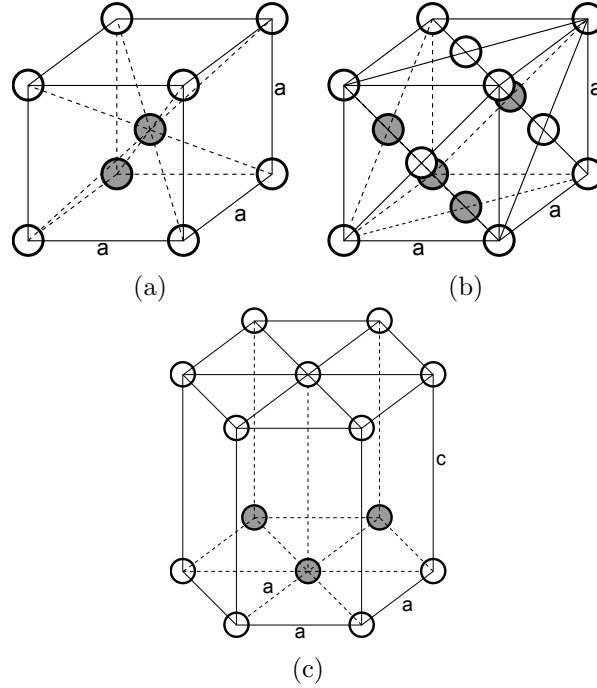


Figure 2.3: A schematic example of (a) body-centred cubic (BCC), (b) face-centred cubic (FCC) and (c) hexagonal close packed (HCP) [32].

Miller indices are a convenient way to specify the planes, directions and the positions of atoms within a crystal lattice. A family of planes are determined by integers h , k , l which are dependent on the type of unit cell within the lattice. For hexagonal and rhombohedral lattice systems, the additional index, i is used. The notation (hkl) denotes the lattice plane and $\langle hkl \rangle$ denotes the lattice direction [32]. This will be used to identify the phase of particles from transmission electron microscopy images (TEM) later in this thesis.

2.3.1 Crystal Lattice Defects

Taylor, Orowan and Polanyi independently proposed the concept of dislocations in 1934 [33–35] and suggested two fundamental types of dislocations: edge dislocation and screw dislocation. An edge dislocation is an extra half-plane in the crystal lattice of the material which distorts the nearby planes of atoms, demonstrated in Figure 2.4. The direction of the dislocation is parallel to the shear stress acting on the lattice. The motion of a screw dislocation, on the other hand, is perpendicular to the direction of the shear stress. Dislocation motion can be impeded by other dislocations, hence, as the dislocation density within the bulk material increases, the amount of obstacles to dislocation motion and the amount of energy required to unlock the dislocations

increases. Note that real dislocations have edge and screw components.

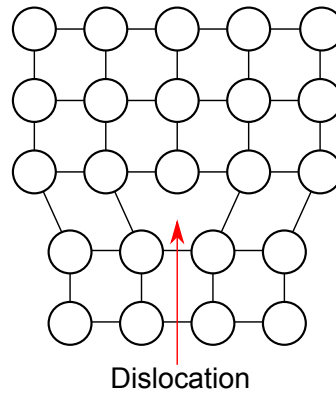


Figure 2.4: A schematic representation of an edge dislocation.

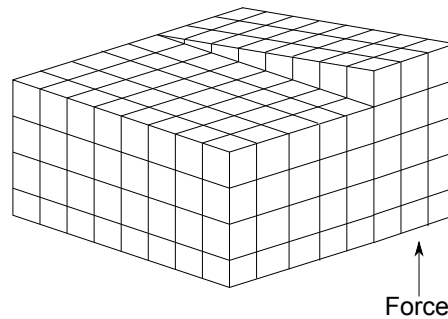


Figure 2.5: A schematic representation of a screw dislocation.

The addition of alloying elements contribute to the material's strength through solid solution strengthening. The foreign element atoms (solute atoms) and are dissolved into the pure material whose atoms are referred to as solvent atoms. The solute atoms replace solvent atoms in the crystal lattice and therefore introducing non-uniformity as shown in Figure 2.6. Higher solubility of solute atoms can be achieved when the solute atoms are of similar atomic size to the solvent atom. Stress fields are created around the solute atoms which obstruct the dislocations (described in the next section) and impedes their motion. An additional stress is required to unlock the dislocation which increases the yield strength of the material in turn [36, 37].

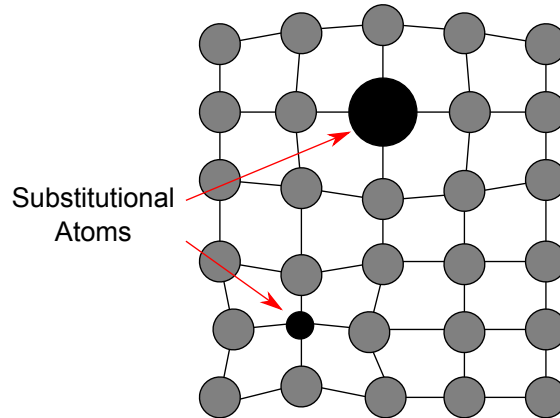
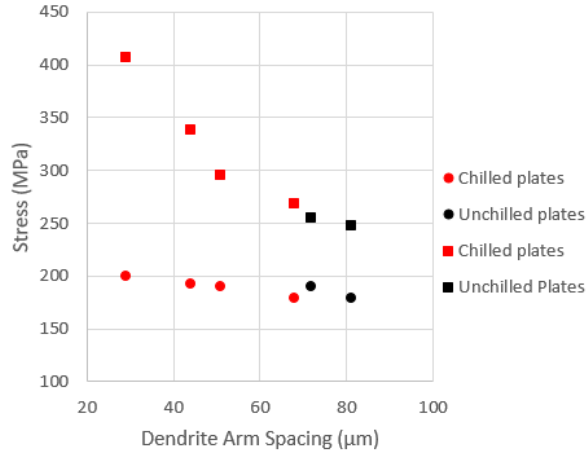


Figure 2.6: A schematic example a substitutional atom and its effect on the surrounding atoms.

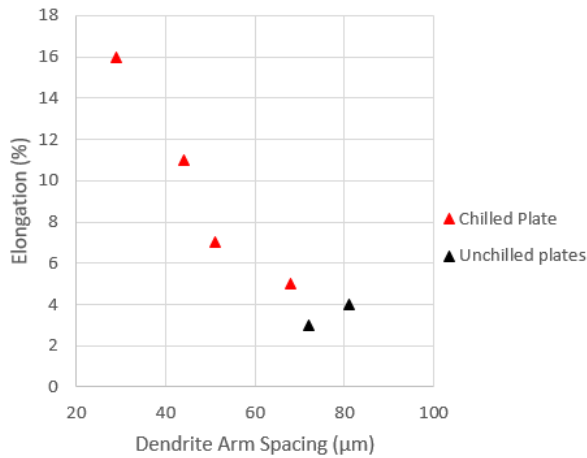
2.4 The Effects of Casting and Rolling on the Mechanical Properties of Aluminium Alloys

2.4.1 Solidification of Molten Aluminium After Casting

The mechanical properties of the two types of aluminium alloys mentioned depend on their microstructure which is derived from their thermomechanical processing and composition [24, 38–41]. Microstructural features and defects that are a result of the casting process can have detrimental effects on the mechanical properties of aluminium alloys. During solidification of the molten metal, dendritic microstructures are formed which create dendrite arm spacing (DAS). Researchers have found that the increased DAS decreases tensile and fatigue properties of cast aluminium [42–45]. Fig. 2.7 shows that as the DAS increases, yield strength, ultimate tensile strength (UTS) and ductility decreases. The magnitude of the spacing is mainly influenced by the solidification rate for a given composition. When dealing with large complex components, it becomes more difficult to maintain strict control over cooling rates.



(a)



(b)

Figure 2.7: Tensile properties of 4.5% Cu alloy versus dendrite arm spacing [42].

Porosity is another inherent feature of castings that arises during solidification, where the two main sources are gas porosity and shrinkage (see [46] for further details). In terms of fatigue properties, it is well documented that an increase in the number and size of the pores and the distance between them in cast alloys reduces the material's fatigue strength [38, 47–51]. Linder et al studied the effect of porosity on fatigue strength for an AlSiMg₁₀ aluminium alloy, manufactured by sand and permanent mould casting. The fatigue strength was compared at 5E+05 cycles for each case. For the sand cast samples, when pore fraction increased from 0.7% to 4.1%, the fatigue strength decreased by 16%. For the permanent mould cast samples, when pore fraction increased from 0.2% to 4.0%, the fatigue strength decreased by 13% [38]. Therefore, it is important to have precision control over the casting process to yield high quality castings for optimal mechanical properties, especially for aerospace applications since components

are subjected to fluctuating stresses.

2.4.2 Mechanical Deformation - Rolling

The rolling process of wrought aluminium alloys (see Figure 2.8) involves passing the of cast ingots through rollers to deform the ingot (reduction in thickness and an increase in length occurs). As a consequence, directionality effects on mechanical properties are induced [52], where the tensile properties are greatest in the rolling direction and are lower in the normal directions. Furthermore, a greater rolling reduction would lead to a greater yield strength and UTS but at a cost of reduced ductility [53, 54].

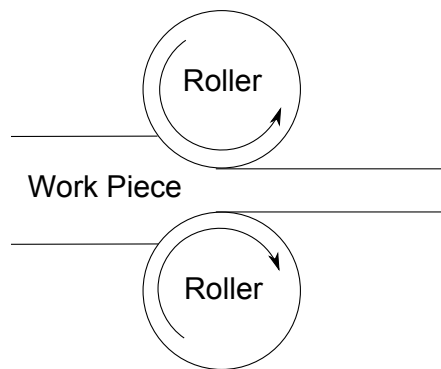


Figure 2.8: A simplified representation of the rolling process for aluminium.

The increased yield strength and UTS from the rolling process is owed to the increased amount of dislocations induced in the material [31].

2.4.3 The Effects of Heat Treatment - Ageing of Aluminium

The alloying elements take the form of second phase particles known as precipitates. Depending on their composition, some wrought and cast aluminium alloys can be heat treated to enhance their mechanical properties. They are referred to as age-hardenable alloys. The ageing process was inadvertently discovered by Alfred Wilm in 1903. It had been well established that quenching steel from a high temperature increased its hardness. Wilm found that applying the same technique to an Al-Cu alloy produced a softer alloy in comparison to the prior untreated alloy. However, days after quenching the alloy, he noticed that the its hardness had increased significantly upon a second measurement, indicating an increase in strength relative to the pre-treated condition [55].

The first stage of the heat treatment process is solution heat treatment, which involves increasing the solubility of the matrix and dissolving the alloying elements into a single phase region. This is achieved by heating and holding the aluminium above the temperature at which only one phase is thermodynamically stable (solvus temperature) for a sufficient amount of time. The solute is redistributed from the precipitate phase into the matrix through diffusion [55].

The alloy is then quenched to form a supersaturated solid solution which retains the soluble elements in a solid solution. The rapid cooling prevents the formation of grain boundary precipitates which increases the amount of available solute during precipitate formation within grains [55].

The final stage is the age-hardening process, where the alloy is held at room temperature or at an elevated temperature below the solvus for an amount of time that is dependent on the desired precipitate form. The solute begins to nucleate and form second phase particles. Table 2.4 shows the temper codes designated for types of thermal treatments. Sometimes supplementary strain-hardening (stretching, compression) is applied to the alloy which can be identified by additional numbers that proceed the first number in the temper code. A simple example of the age hardening process is shown in Figure 2.9 [56].

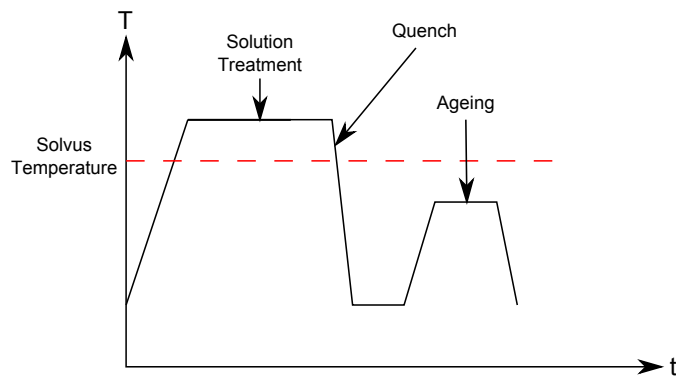


Figure 2.9: A schematic example of the ageing process of aluminium alloys.

Figure 2.10 describes a simplified evolution curve of the material's strength and hardness during age hardening. With a sufficient amount of time at temperature, the alloy will reach peak strength where ductility is at its minimum. If ageing continues after this point, the tensile strength will begin to decrease due to the coarsening of the precipitates and the alloy will be overaged. Ilangoan et al [57] demonstrated this

Table 2.4: The description of heat treatments and their designated codes.

Code	Description
T1	Cooled from an elevated temperature and naturally aged
T2	Cooled from an elevated temperature, cold worked and naturally aged
T3	Solution heat treated, cold worked and naturally aged
T4	Solution heat treated and naturally aged to a substantially stable condition
T5	Cooled from an elevated temperature shaping process and artificially aged
T6	Solution heat treated and artificially aged
T7	Solution heat treated then stabilised
T8	Solution heat treated, cold worked then artificially aged
T9	Solution heat treated, artificially aged and cold worked
T10	Cooled from an elevated temperature, artificially aged then cold worked

phenomena with Al-4.5Cu alloy, although it should be noted that some alloys are purposely overaged to maintain precipitate stability and thus mechanical properties.

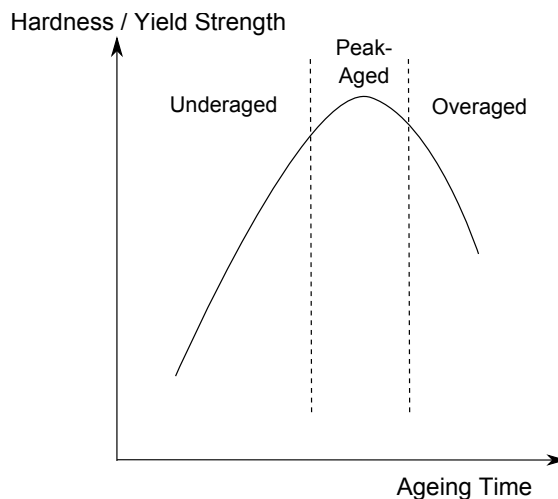


Figure 2.10: Simplified ageing curve for aluminium.

Generally, the age sequence of precipitates are: supersaturated solid solution, transition structures, and finally stabilised aged phase. The initial ageing stage forms Guinier-Preston zones (GPZ), which are metastable coherent clusters of solute atoms. A coherent precipitate will match perfectly at the interface with the metal matrix and the lattice planes cross this interface in a continuous manner. This is only possible if the interfacial plane has the same atomic configuration (orientation and interplane distance) in both phases. Figure 2.11a shows an example of a coherent precipitate where the lines represent the lattice planes. As ageing continues, larger precipitates

grow by “consuming” smaller ones. The strain fields around the precipitates grow and are then reduced by the formation of semi-coherent zones. The mismatch between the crystal lattice planes of the metal matrix and the precipitate particle at the interface causes the strain to increase and forms dislocations. Finally, incoherent, stabilised phase particles are formed where there is no continuity of planes between the particle and the matrix. Figure 2.11 demonstrates the interaction between the different precipitate phases and matrix [32].

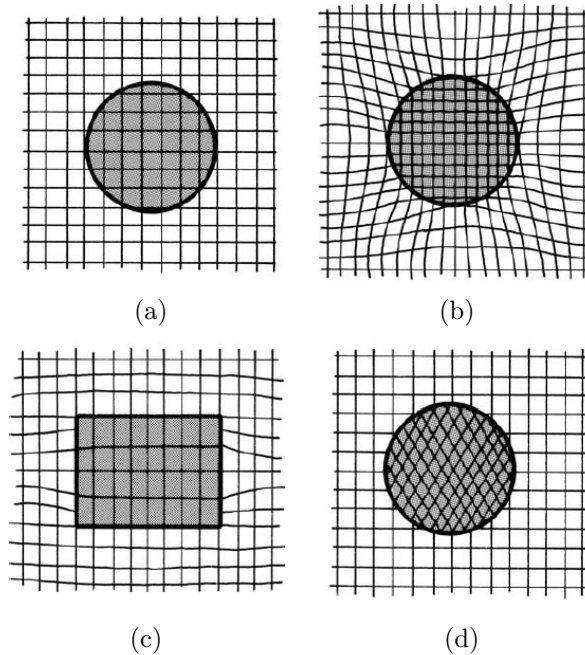


Figure 2.11: Different crystallographic relationships between matrix and second phase particles, where the interface between the two is represented by the bold black line. (a) Complete coherency, (b) coherency with strained, but continuous, lattice planes across the boundary. (c) semi-coherent, partial continuity of lattice planes across the interface. (d) incoherent equilibrium precipitate; no continuity of lattice planes across the interface [32].

The precipitates act as barriers to dislocation motion which has an important role on the strength of the material. However, the strengthening mechanism of the precipitate is dependent on the characteristics of the precipitate and its interface with the matrix. Therefore, two models are used to explain the strengthening mechanism of the precipitates.

$$\tau_{shear} = \frac{\pi r \gamma}{2bL} \quad (2.1)$$

The first model involves dislocations cutting through the particles in the slip plane

which is known as the Friedel effect. The second phase particles are coherent with the matrix and are small enough that they can be sheared by the dislocation. Equation 2.1 presents this model and states that the stress required to shear the particle, τ_{shear} , is proportional to the particle radius, r . γ is the specific energy at the interface, b is the Burgers vector, γ is the surface energy and L is the distance between 2 pinning points.

$$\tau_{Orowan} = \frac{Gb}{2r} \quad (2.2)$$

The second model involves the dislocations circumnavigating around impenetrable second phase particles in slip plane which is known as the Orowan bowing effect. Equation 2.2 presents this model and states that the additional stress is required to bend the dislocation between the particles, τ_{Orowan} , is inversely proportional to the particle radius, r . When the dislocation has completely moved past the particles, a dislocation in the form of a closed loop is left around them [32].

Figure 2.12 shows the relationship between precipitate radius and the shear strength of the material, where r_0 is the critical particle radius. When the particle radii are smaller than r_0 , precipitates are coherent and dislocations are able to shear them (the Friedel effect). Therefore, the increase in particle radii increases the strength of the material up to r_0 . When particle radii are larger than r_0 , precipitates are semi-coherent or incoherent and dislocations pass around or over them (Orowan bowing effect).

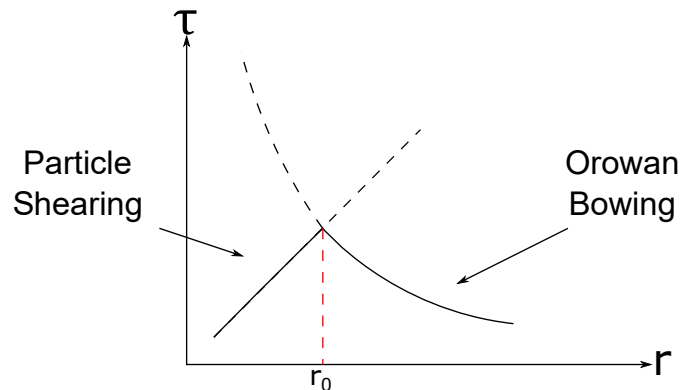


Figure 2.12: The effect of precipitate radius on shear strength [58].

In most cases, the choice of heat treatment for aluminium alloys is driven by the design requirements but there are limitations on what the heat treatment can achieve. Researchers have generally found that either the optimal tensile strength or fatigue

fracture resistance can be only achieved at the cost of the other mechanical property [59–63]. However, heat treatments can be more complex to maximise one mechanical property, for example, fatigue strength, without decreasing tensile strength. Chen et al [64] studied the effect of interrupted ageing for a dwell period at a lower temperature of an Al-Cu alloy. They found that this method produces shearable and shear resistant precipitate phases that lead to an increase in both yield strength and ductility. Lumley et al [65, 66] found that the interrupted heat treatment, T6I6, of the age-hardenable alloys such as the 7050 aluminium alloy could further increase the yield strength and UTS by 10-15% and simultaneously increase fracture toughness.

$$\sigma_y = \sigma_0 + \frac{k}{\sqrt{D}} \quad (2.3)$$

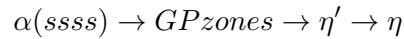
Hall and Petch [67, 68] observed that grain boundaries impede dislocation motion since the slip planes between grains are not aligned. Therefore for a dislocation to move from one grain to another, additional energy is required to unlock the dislocation. The grain size can be controlled by the rate of solidification from the liquid phase and by plastic deformation due to processes such as rolling, forging and extrusion. Equation 2.3 is the Hall-Petch equation where σ_y is the yield strength, D is the grain diameter, k is the strengthening coefficient and σ_0 is the resistance of the lattice to dislocation motion. This equation demonstrates the yield strength increases as the grain size decreases. This is due to a phenomena called dislocation pile-up, where multiple dislocations along the same slip plane build up at the grain boundary and increases driving force for dislocations from one grain to another. The size of the grains limits the number of dislocations that can pile-up at the boundaries which means that smaller grains will increase the yield strength on the material.

2.5 The 7000 Series Aluminium Alloy

In aerospace, the 7000 series alloys are usually used for structural components such as aircraft wing, airframe and fuselage sections because of their remarkable combination of low density, high strength and easy formability [9]. The main alloying elements, in order of weight percentage, are zinc, magnesium and copper. Their composition makes them susceptible to stress corrosion cracking [69, 70] and therefore a trade-off in tensile

strength is usually made to increase corrosion resistance and fracture toughness by over-aging these alloys to produce stable precipitates. It has also been found that decreasing impurity content, increases both strength and fracture toughness. For example, the 7175 and 7475 alloys are based on the 7075 except stricter control of iron and silicon impurities has been achieved [24]. Iron and silicon are inherent within these alloys and are unable to be dissolved in the solid solution. They bond with the aluminium to form coarse intermetallic particles [71].

During heat treatment, the ageing sequence in Al-Zn-Mg-Cu type alloys at temperatures below 190°C is as follows [72]:



The η' phases are rod-shaped and round-shape [73] with a hexagonal closely packed crystal lattice ($a=4.96\text{\AA}$ and $c=14.02\text{\AA}$ [74]). There has been some dispute with regards to the composition of this phase. It is commonly assumed that the composition is MgZn_2 but researchers have found Zn:Mg ratios of 1.2 and higher [74]. The η phase is a stable precipitate with a hexagonal closely packed crystal lattice ($a=5.22\text{\AA}$ and $c=8.57\text{\AA}$ [74]). It should be noted that one of the morphologies mentioned may be a projection of the other in different orientations.

Other intermetallic phases can exist within Al-Zn-Mg-Cu alloys such as the S phase (Al_2CuMg), T phase ($\text{Mg}_3\text{Zn}_3\text{Al}_2$), chromium-rich E phase, Mg_2Si , and Fe-rich phases, where the latter two are caused by impurities. The Fe-rich phases such as the $\text{Al}_7\text{Cu}_2\text{Fe}$ and Al_3Fe are the largest class of particle within this material and be as large as $10\mu\text{m}$ [75]. They known to be detrimental to fracture toughness and in general have a negative impact on mechanical properties [76–78].

2.6 Mechanical Behaviour of Materials

2.6.1 Plasticity

Plasticity refers to the residual deformation in a material after the applied load has been removed. It has been experimentally demonstrated that during plastic deformation, Hooke's law is no longer valid and cannot describe the non-linear relationship between stress and strain. Figure 2.13 shows a schematic example of an engineering stress-strain

curve of a metal loaded uniaxially, where some mechanical properties of a material can be obtained from the graph. σ_y represents the material's yield stress. This is the stress at which plastic deformation occurs within the material. For some metals such as steel, the point of yielding is very distinctive. However, for other metals such as aluminium, the transition between elastic and plastic deformation is gradual. Therefore, it is common to take a proof stress which is the stress that permanently deforms the material by 0.2% strain [32].

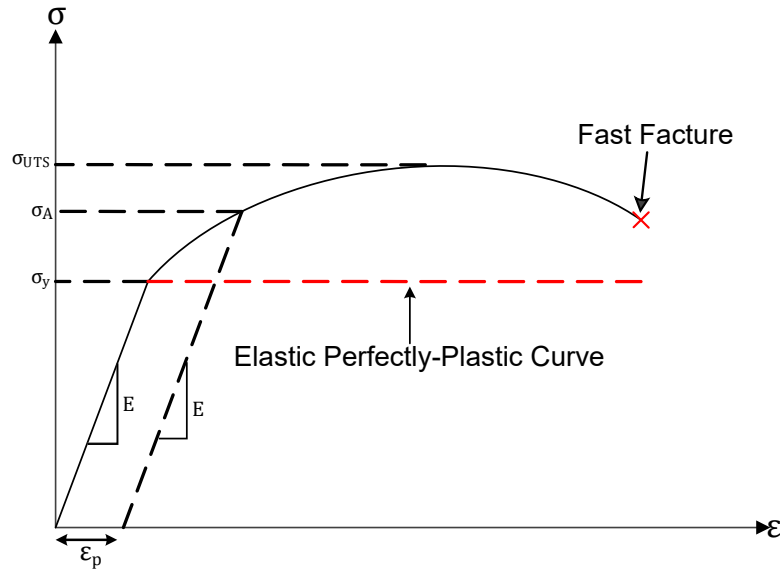


Figure 2.13: A schematic example of a uniaxial stress-strain curve.

Elastic perfectly-plastic materials would exhibit a stress-strain curve that follows the red dashed line following the yield stress. However, metals usually exhibit work hardening or softening, indicated by an increase or decrease in applied load with further straining. The dashed line parallel to the linear elastic curve represents the approximate path that the stress and strain will follow when the metal is unloaded at σ_A assuming no time dependent effects. ϵ_p is the plastic strain in the material when the load is removed. σ_{UTS} is the ultimate tensile strength of the material which is the maximum stress at maximum load before fracture failure occurs. Beyond this point a localised reduction in cross-sectional area occurs which decreases the load-bearing capacity of the material [32].

$$\tau_y = \frac{1}{2} \max(|\sigma_1 - \sigma_2|, |\sigma_2 - \sigma_3|, |\sigma_3 - \sigma_1|) \quad (2.4)$$

$$\sigma_y = \frac{1}{\sqrt{2}} \sqrt{(\sigma_1 - \sigma_2)^2 + (\sigma_2 - \sigma_3)^2 + (\sigma_3 - \sigma_1)^2} \quad (2.5)$$

Several researchers have put forward criteria to determine when yielding occurs in a material. The Tresca criterion [79] states yield occurs in a material when the maximum shear stress, is equal to the yield shear stress of that material, $\tau_{max} = \tau_y$ as shown in equation 2.4. The von Mises criterion [80], shown in equation 2.5, states that yield occurs when the maximum distortional energy within material is equal to the maximum distortional strain energy at yielding under uniaxial tension.

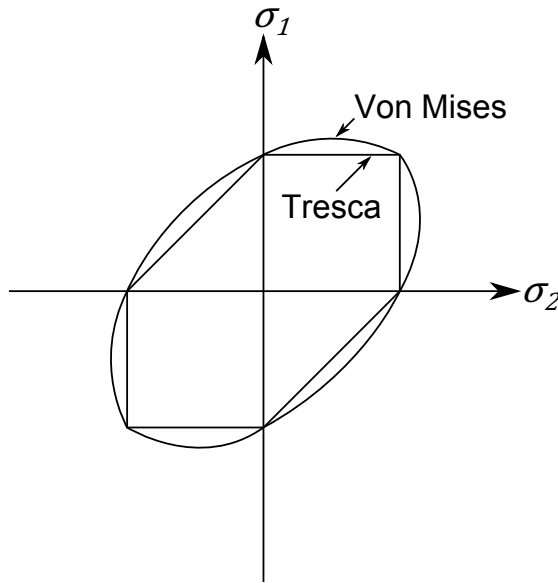


Figure 2.14: A representation of the yield surface predicted by Tresca and von Mises on 2 principle stress axes.

Figure 2.14, shows the boundaries of the yield surfaces predicted by both criteria that determines when plastic flow occurs in a material. The largest difference in their prediction of yielding occurs under pure shear stress. For ductile materials, the choice between von Mises or Tresca yield criterion requires careful measurement of material yield behaviour. Tresca provides a conservative prediction of yielding since it describes plastic deformation at regions where von Mises still predicts elastic behaviour. Therefore, von Mises may be more accurate depending on the application of the material and is generally used in design. Other works on yield criteria such as the maximum principal stress yield criterion (William Rankine), maximum principal strain yield criterion (Adhemar Jean Claude Barre de Saint-Venant) have been documented. These criteria state that yield occurs when one of the principal stresses or strains

exceeds the material's yield stress or strain which is unsatisfactory when describing yield under pure shear stress conditions [81].

When plastic deformation under uniaxial loading has occurred, some materials exhibit hardening behaviour that is usually described as isotropic and kinematic hardening [82]. Other forms of hardening (e.g. hardening due to torsional loading) can occur under multiaxial stress-states but for this thesis only uniaxial stress-states are considered. Isotropic hardening depicts the expansion of the yield surface radius, increasing by a magnitude of R (drag stress). During kinematic hardening, the size of the yield surface remains constant but the surface translates in the direction of the maximum principal stress by a magnitude of χ (back stress).

Figure 2.15a and 2.15b show examples of how the yield surface can change during isotropic and kinematic hardening respectively, where σ_1 , σ_2 and σ_3 are the principal stresses. The black and red circles represent the initial yield surface and the new yield surface after hardening respectively. The expansion and translation of the yield surface results in different material properties in the 3 principal stress directions.

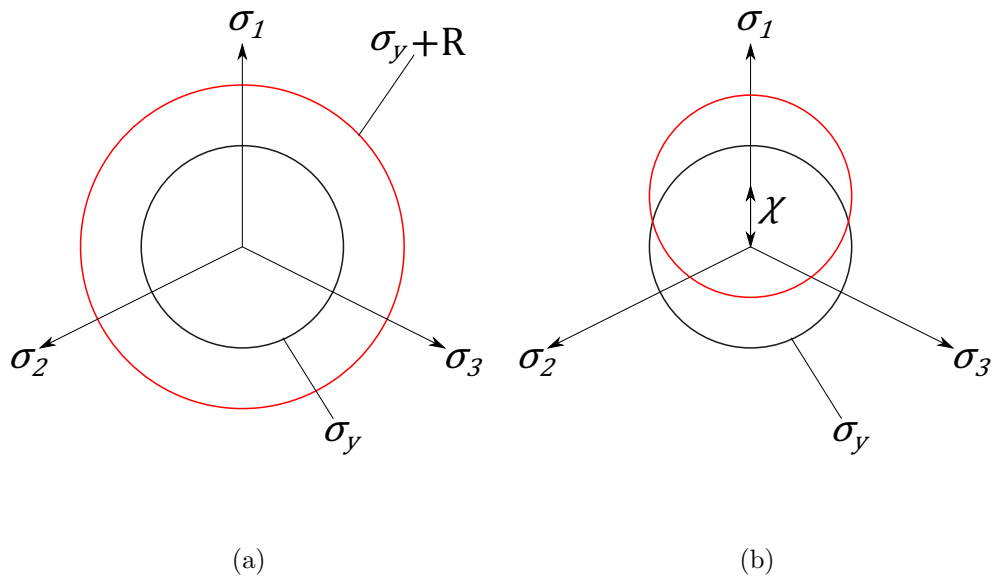


Figure 2.15: (a) Isotropic hardening and (b) kinematic hardening [32].

A phenomena called the Bauschinger effect [83] can occur in polycrystalline metals, where the increase of tensile yield strength due to work hardening decreases the compressive yield strength. During the reverse loading from tension into compression after hardening had occurred, as shown in Figure 2.16, dislocations are able to glide more easily, aided by a back stress generated around the points of dislocation

resistance. Thus, the yield stress level in the reverse direction is reduced by the magnitude of the back stress, and the size of the yield surface remains $2\sigma_y$.

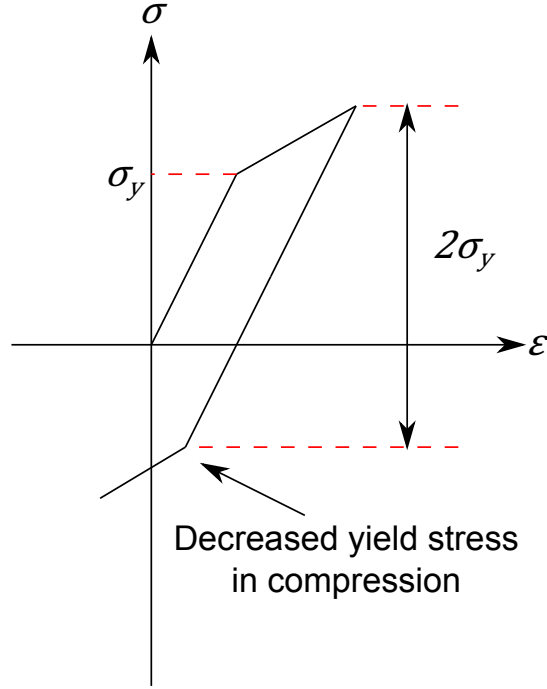


Figure 2.16: A schematic example of the Bauschinger effect.

2.6.2 Constitutive Viscoplasticity Models

The Chaboche model [82, 84] is comprised of a set of constitutive equations (shown below) that utilises temperature dependent material parameters to predict stress-strain behaviour of a material and single yield surface. It has the capacity to describe a wide range of inelastic material behaviour such as cyclic hardening or softening, the Bauschinger effect, stress relaxation behaviour, stress ratcheting and creep behaviour.

$$\varepsilon_{total} = \frac{\sigma}{E} + \varepsilon_p \quad (2.6)$$

The total strain can be described by equation 2.6, where E is the Young's modulus, σ is the total stress and ε_p represents both the plastic and viscoplastic strains.

$$\dot{\varepsilon}_p = \left\langle \frac{f}{Z} \right\rangle^n \text{sgn}(\sigma - \chi) \quad (2.7)$$

$$\text{sgn}(x) = \begin{cases} 1 & x > 0 \\ 0 & x = 0 \text{ and } \langle x \rangle \\ -1 & x < 0 \end{cases} = \begin{cases} x & x \geq 0 \\ 0 & x < 0 \end{cases} \quad (2.8)$$

$\dot{\varepsilon}_p$ is the plastic strain rate demonstrated by the flow rule equation below:

$$f = |\sigma - \chi| - R - k \quad (2.9)$$

k is the initial cyclic yield strength and Z and n are viscous parameters that describe the stress relaxation behaviour. f is the yield function that determines when plastic strain occurs (equation 2.9). The material is elastic when $f \leq 0$ and plastic when $f > 0$.

$$R = Q(1 - e^{-bp}) \quad (2.10)$$

R is the isotropic drag stress that determines the expansion or reduction of the yield surface (see equation 2.10). b is the rate at which the isotropic drag stress saturates to the value Q . p is the accumulated plastic strain as shown in equation 2.16.

$$d\chi = cd\varepsilon_p \quad (2.11)$$

$$d\chi = da(\varepsilon_p)(\sigma - \chi) \quad (2.12)$$

$$\dot{\chi} = C(a\dot{\varepsilon}_p - \chi\dot{p}) \quad (2.13)$$

χ is the total back stress due to kinematic hardening. Prager [85] and Ziegler [86] (see equations 2.11 and 2.12) introduced the linear kinematic hardening model (using plastic moduli) where χ is collinear with the evolution of plastic strain. However, this behaviour is not typical. Armstrong and Frederick [87] modified the linear kinematic hardening model as shown in the equation 2.13. χ is the back stress, C and a are temperature-dependent material parameters, $\dot{\varepsilon}_p$ is the plastic strain rate and \dot{p} is the equivalent plastic strain rate. The key modification to Prager's equation is the second term $\chi\dot{p}$ which is known as dynamic recovery. This term changes the evolution of χ

from linear to an exponential relationship for monotonic uniaxial loading and enables the prediction of non-linear kinematic hardening. Furthermore, the back stress has a saturation value, caused by the balance between the rate of dislocation annihilation and production [12, 88].

$$\chi = \sum_i^M \chi_i \quad (2.14)$$

$$\dot{\chi}_i = C_i(a_i \dot{\varepsilon}_p - \chi \dot{p}) \quad (2.15)$$

$$p = \Sigma |d\varepsilon_p| \quad (2.16)$$

Chaboche proposed the use of multiple Armstrong-Frederick equations to describe the back stress since it was found to have greater control over the back stress saturation rate for uniaxial cases [89, 90]. M is the total number of back stresses as shown in equation 2.14 and $\dot{\chi}_i$, in equation 2.15, represents a back stress rate component where C_i is the rate at which the kinematic hardening saturates to the value a_i . However, this rule has been known to over-predict uniaxial and multiaxial ratcheting [12].

When a material is subjected to stress-controlled cyclic loading with a non-zero mean stress, ratcheting may occur. This is a cyclic accumulation of inelastic strain which is characterised by the translation of the hysteresis loops in the direction of the applied mean stress.

$$d\chi_i = C \left(\frac{2}{3} a_i d\varepsilon_p - H(f_i) \left\langle d\varepsilon_p \cdot \frac{\chi_i}{\bar{\chi}_i} \right\rangle \chi_i \right) \quad (2.17)$$

$$d\chi_i = C \left(\frac{2}{3} a_i d\varepsilon_p - \left(\frac{\bar{\chi}_i}{a_i} \right)^{m_i} \left\langle d\varepsilon_p \cdot \frac{\chi_i}{\bar{\chi}_i} \right\rangle \chi_i \right) \quad (2.18)$$

This behaviour is dependent on the loading conditions and the loading history of the component. Ohno-Wang [91, 92] directly modified the Armstrong-Frederick rule by introducing a critical state of dynamic recovery. Equation 2.17 (Ohno-Wang rule I) assumes that each back stress component χ_i remains linear until the critical value, a_i is reached, and after that χ_i remains constant. H is a Heaviside step function ($H(x) = 1$

if $x \geq 0$, $H(x) = 0$ if $x < 0$) and $\bar{\chi}_i$ is the magnitude of χ_i . However, this rule produces closed hysteresis loops and cannot predict ratcheting so Ohno-Wang modified the rule as shown in equation 2.18 (Ohno-Wang rule II). The Heaviside step function is replaced with a power law which allows for the partial activation of the dynamic recovery term before the critical state. The exponent, m_i , controls the rate of ratcheting where smaller values of m_i lead to increased ratcheting. Furthermore, as m_i tends to positive infinity, the equation reduces to Pragers' rule. Similarly to the rule I, each back stress component simulates non-linear kinematic hardening until it reaches a critical value a_i . After that, it has no effect. An review on the extensive work on prediction of ratcheting by Abdel-Karim can be found here [93].

$$\sigma = \chi + (R + k + \sigma_v) \text{sgn}(\sigma - \chi) = E(\varepsilon - \varepsilon_p) \quad (2.19)$$

$$\sigma_v = Z\dot{p}^{1/n} \quad (2.20)$$

The total stress is summarised by equation 2.19 which is the sum of the stresses due to hardening and viscous effects. Equation 2.20 is a power law used to describe the relationship between the viscous stress, σ_v , and the equivalent plastic strain rate.

Tong and Zhan [94–97] have applied the Chaboche model to nickel-based super-alloys and highlighted the importance of implementing an optimisation process to improve the predictive accuracy on the material parameters. Works to predict the isothermal and thermomechanical fatigue behaviour of 316 steel [98] and P91 steel [99–102] have been carried out by Hyde and Rouse. Kyaw and Rouse [103] coupled a continuum damage model [104] with the Chaboche model to predict stress-strain behaviour and fatigue life of a P91 steel. They estimated the material parameters for isotropic hardening, kinematic hardening and viscous stress using Cottrell's stress partitioning method [105] as shown in Figure 2.17.

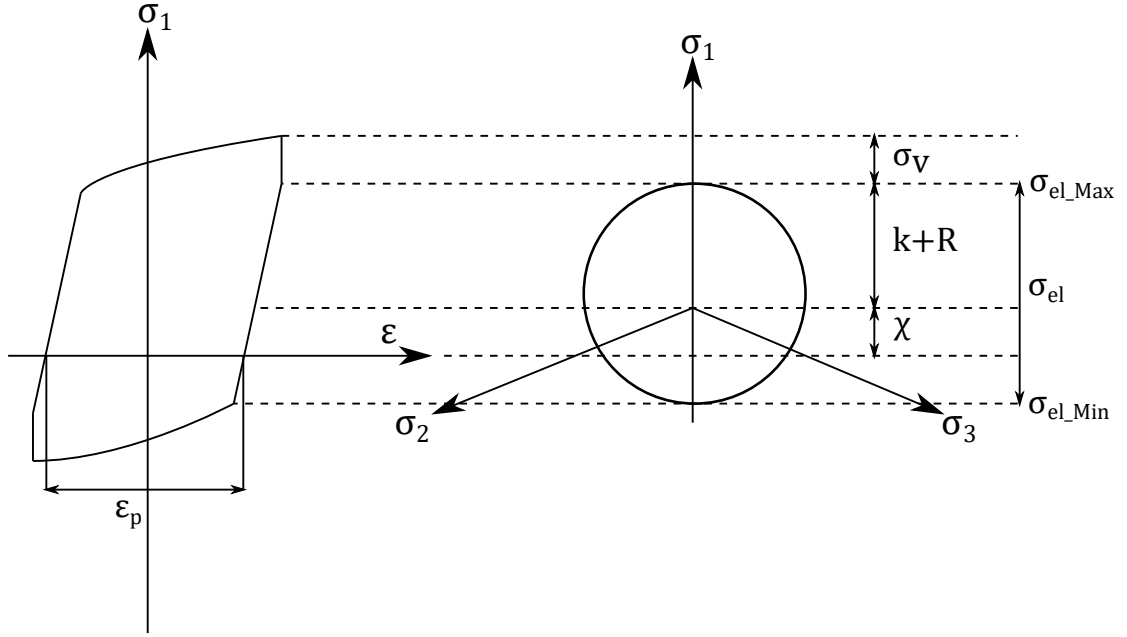


Figure 2.17: A representation of Cottrell's stress partitioning method [105].

Examining a single branch of a hysteresis loop, the total stress can be decomposed into stress components: viscous stress, σ_v , isotropic drag stress, R , initial cyclic yield stress, k , and the kinematic back stress, χ . σ_{el} is the magnitude of the elastic region which can be determined where the linear stress-strain relationship begins and ends. k is usually calculated from the second tensile branch from the 0% level to the yield stress value. Since R is the expansion of the yield surface, the radius of the yield surface is therefore $k + R$. χ is translation of the yield surface which can be determined by subtracting the radius of the yield surface, $k + R$ from the greatest stress value that lies of the radius, σ_{el_Max} . The total plastic strain can be obtained by measuring the width of the hysteresis loops where the stress-strain relationship is linear.

Other models have been proposed to describe monotonic and cyclic plasticity of materials such as the Mroz model [106]. This involves the use of multiple "hypersurfaces" as shown in Figure 2.18. The inner most surface, S_1 , represents the elastic region. As the stress point increases within the inner surface and comes into contact with its radius, the point joins to the surface and together they linearly move with the stress point with a new modulus. In order to predict the material response accurately, many surfaces are required where each surface is assigned a linear plastic modulus (represented by E_1 , E_2 and E_3). This model is able to estimate piecewise linear stress-strain loops under stable cyclic loading and the Bauschinger effect. However, the size of each surface must vary

in such a way that the surfaces do not intercept in order to avoid non-unique solutions. This creates a difficulty in describing isotropic hardening behaviour [107]. Furthermore, the model is computationally tedious since entire families of surfaces must be tracked and it does not accurately predicted ratcheting behaviour [108].

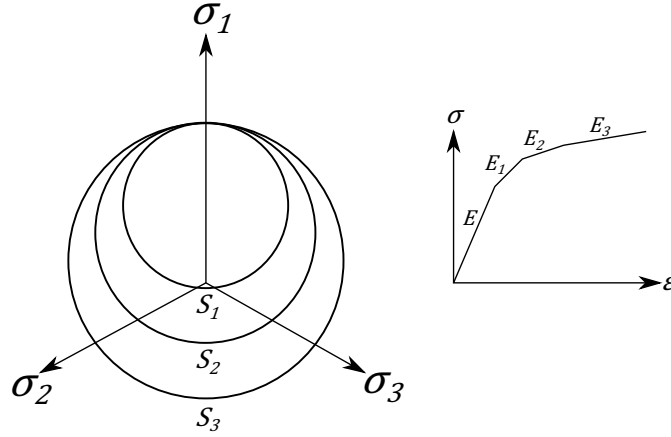


Figure 2.18: A representation of the Mroz Model [109] showing the multiple surfaces and the assigned plastic modulus for each surface.

The Dafalias and Popov model [110] uses the same kinematic hardening rule as the Mroz model but they utilised a non-linear hardening modulus that allowed them to reduce the number of surfaces to two: a yield surface and bounding surface. The current stress state lies on the yield surface and the limiting stress state lies on the bounding surface. The modulus is derived from the distance between the surfaces as opposed to the Mroz model that utilises multiple moduli. Both surfaces are of the same shape and are allowed to isotropically and kinematically harden. One deficiency in this model arises during the unloading or reloading, or sudden change in load direction. As a result, it fails to account for complex loading histories and produces unrealistic predictions [108].

Physically-based constitutive models are an alternative method to predict cyclic viscoplasticity, where key microstructural features and micro-mechanisms that are directly correlated to the material's strength are incorporated into the model. Estrin et al [111, 112] established a unified elastic-viscoplastic constitutive model based on dislocation density. Cailletaud [113] developed a constitutive micromechanical model for the 2024 aluminium alloy and 316L stainless steel under monotonic and cyclic multiaxial loading at room temperature. Sauzay et al [114, 115] established that cyclic softening of the martensitic 9Cr1Mo steel was related to the degradation of the microstructure (lath and sub-grain boundary elimination) and the reduction in

dislocation density. Using the Hall-Petch and Taylor models [116], the macroscopic backstresses were calculated. Barrett et al [117] implemented a dislocation-based for the cyclic viscoplastic behaviour of 9-12Cr steels. Their model described cyclic softening due to the decrease in overall dislocation density, loss of low angle boundary dislocations, the coarsening of the microstructure, and kinematic hardening due to precipitate strengthening and dislocation substructure hardening. They later extended their model to simulate grain boundary strengthening by incorporating lath widening, high angle grain boundary strengthening due to the formation of dislocation pile-up, accounting for precipitate strengthening of carbides along grain boundaries and carbonitrides in the microstructure, and modelling the evolution of edge and screw dislocations [118]. The advantage of physically-based models are that they are based on microstructurally driven phenomena which enables prediction of material behaviour across a wider range of loading conditions. However, this approach requires an understanding of the evolution of the strengthening mechanisms which means taking extensive measurements of the key microstructural features.

2.6.3 Numerical and Optimisation Methods

To solve the ODEs presented in the Chaboche model, either explicit or implicit numerical methods could be used. Both require the use of iterations to advance a solution through a sequence of steps from an initial state to a final converged state.

$$Y(t + \Delta t) = F(Y(t)) \quad (2.21)$$

In an explicit method, the system status of the next time step would be directly evaluated from the currently known quantities of the dependent variables, demonstrated in Equation 2.21. $Y(t + \Delta t)$ is the state of the system in the later time step and $Y(t)$ is the current system state. The explicit method is easier to program and can be calculated within a shorter time. However, the stability of such a method requires a step size small enough to prevent divergence from the conditionally stable solution [119].

$$G(Y(t), Y(t + \Delta t)) = 0 \quad (2.22)$$

In implicit methods, the dependent variables are defined by sets of equations and an

iteration technique or matrix is needed to obtain a solution. Implicit methods are more complex to program but larger time-step sizes are possible, especially for "stiff" equations where a convergence can only be made possible for an explicit methods if very small time steps are used. An implicit method evaluates some or all of the terms in Y with regards to unknown quantities at the new time step, $t + 1$, and of the previous current step, t . Implicit methods have high stability and converge if appropriate parameters are set, but, as a set of equations needs to be solved every step, the computational time required for the calculations may be larger than explicit methods [119]. For this reason, an explicit method was chosen to solve the ODEs as ODE45.

The material parameters for the Chaboche model are derived from experimental data, using assumptions to simplify the hardening and viscous behaviours. However, the prediction of material behaviour may be limited by such assumptions and as the model increases in complexity, the number of material parameters will also increase. This has led to the introduction of optimisation techniques to identify a new set of material parameters that improve the accuracy of the model predictions.

A gradient-based search method for finding the solution for a local minima was chosen to optimise the material constants. There are derivative-free approaches that use genetic-based algorithms to iterate towards the solution (discussed by Chaparro [120]) but it has been found that a number of works have successfully utilised the Levenberg-Marquardt method [121, 122] to optimise the material constants in the Chaboche model [94–97, 100–103, 123].

Gradient-based search methods are able to converge to a solution in a relatively short amount of time but the convergence to the local minimum is strongly dependent on the proximity of the initial trial solution [120]. This is because the gradient at any local minima or maxima is zero. If the function, $f(x_k)$ contains a minimum at $x_k = x_m$, where x is the set of variables, k is the iteration number, and x_m is the solution at the minimum, then how can x_k be found? The most basic approach is called the steepest descent method [124] which calculates the direction for the fastest decrease of a function at a given point. The steps of this approach are shown below:

1. Start with an initial guess of the solution, x_{k0} , and set a tolerance on the gradient so that a convergence to the solution is possible.

2. If the current iteration does not contain the solution, then compute the next direction (a vector called p_k) that should be taken towards the direction of steepest descent.
3. Calculate the size of the step length, α_k , within the specified time span so that $f(x_k + \alpha_k p_k) < f(x_k)$.
4. Update the variables by setting $x_{k+1} = x_k - \alpha_k p_k$ and repeat from step 2.
5. If the conditions are satisfied, then the current solution to $x_k = x_m$, then x_k is the solution.

This method is a first order method which means that it produces a linear convergence rate. A solution can be found but may take a “zig-zag” approach to finding a minimum which can be time consuming for a large scale problem.

Newton’s method for optimisation is a second order approach which tries to find where the derivative, $\nabla f(x_m)$, equals to 0 and the updated variables now becomes $x_{k+1} = x_k - \frac{f'(x_k)}{f''(x_k)}$. This function minimises the second order approximation at a given point in the function but the drawback to this approach is that for every iteration, the second order derivatives (the Hessian) needs to be calculated which again, can be time consuming [120].

The Gauss-Newton method for non-linear least-squares method attempts to minimise the residuals differences of the sum of squares between the predicted and observed results demonstrated by the equation below:

$$r_k(x)^2 = \sum_{k=1}^m (p^{exp} - f_k(x))^2 \quad (2.23)$$

where r is the residuals differences, p^{exp} is the experimental observations and $f_k(x)$ is the predicted results. This can only be used to minimise the sum of squares but unlike Newton’s method, it has the benefit of not required to compute the second derivatives but instead approximates them using the residuals [125].

The Levenberg-Marquardt method has the advantage of interpolating between the steepest descent method (first order) and the Gauss-Newton method [125] (second order) approaches depending on the closeness between the initial and final solution and does

not need to calculate the second partial derivatives which reduces computational time. For these reasons, this work also used this method for optimisation purposes.

2.6.4 Constitutive Models with the Inclusion of Ageing Effects

Little research has been carried out to incorporate the material ageing behaviour into the Chaboche model when the material is subjected to elevated temperatures and cyclic stresses. It is understandable that this behaviour would not be necessary to characterise for high temperature materials such as steel and nickel-based superalloys but this phenomenon does occur in aluminium alloys. Their microstructure will evolve over time at temperature and will directly affect their load-bearing capacity.

$$R = Kp^{1/M} + Ca \quad (2.24)$$

$$\dot{a} = (c - \beta \exp(-\gamma p))(a_\infty(\varepsilon_p) - a) \quad (2.25)$$

Marquis et al [13] modified the Chaboche model to include material ageing. They chose to predict the stress state of the 2024 aluminium alloy that was aged at room temperature after solution heat treatment and quenching. The change in the elastic region was measured at different age times of the material under monotonic and cyclic loading up to 0.2% strain. Since a small variation in back stress was induced by ageing, it was assumed that the material ageing only affects isotropic hardening, represented in equation 2.24, where C , K and M are material constants, p is the accumulated plastic strain, and a is the material ageing term. The ageing rate, \dot{a} , is defined in equation 2.25 where c , β and γ are temperature-dependent material constants, ε_p is the plastic strain, and a_∞ is the asymptotic ageing value of a that is dependent on plastic strain. They found that the cyclic straining increases the rate of ageing and were able to accurately predicted the stress range versus accumulated plastic strain of the material under fully reversed fatigue conditions at room temperature.

Cailletaud et al [14] carried out a similar study on a cast aluminium, heat treated to the T5 condition, where the alloy was soaked at various temperatures and times and its Vickers hardness was measured at certain time intervals. They correlated Vickers hardness readings to the elevated temperature yield strength of the material as a function

of time at temperature described the rate of decay from an initial yield strength to the final asymptotic yield strength caused by ageing.

The step-aside gearbox housing is mounted close to the engine and will be subjected to elevated temperatures. This can have detrimental effects on the strength of the candidate material being considered for this thesis. Therefore, the novelty of this work was developing a constitutive model for the 7175-T7351 aluminium alloy with the inclusion of ageing terms. The isotropic softening was decoupled into mechanical cyclic softening due to the load and material ageing due to time at temperature during the fatigue tests. Generally, it would be important to consider this material behaviour for all candidate age-hardenable aluminium alloys. Furthermore, the test method used was novel in the sense that a variable strain-amplitude test was used to gain enough experimental data to accurately predict material response. By decreasing the strain amplitude according to the decrease in monotonic yield strength with time, plastic strain was induced per cycle while remaining below the UTS. This prevented early failure of the samples.

2.6.5 Isothermal Fatigue

Fatigue is the progressive decrease of material strength as a result of dynamic mechanical loading. Isothermal fatigue (IF) involves varying loads at constant temperature (noting that dynamic mechanical systems will see varying temperatures). This mode of failure is the most dominant in mechanical systems and structures [126]. Figure 2.19 demonstrates a schematic example of a cyclic loading curve.

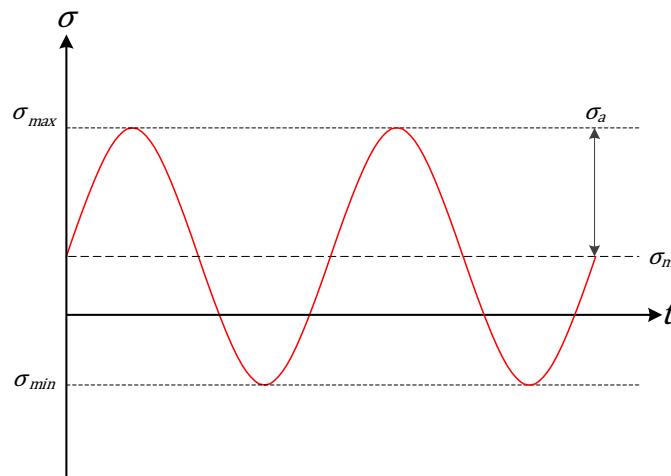


Figure 2.19: A schematic example of fatigue loading curve.

The main features from this curve are the stress amplitude (σ_a) and mean stress (σ_m) which are described by equations 2.26 and 2.27, respectively.

$$\sigma_a = \frac{\sigma_{max} - \sigma_{min}}{2} \quad (2.26)$$

$$\sigma_m = \frac{\sigma_{max} + \sigma_{min}}{2} \quad (2.27)$$

$$R_\sigma = \frac{\sigma_{min}}{\sigma_{max}} \quad (2.28)$$

σ_{max} and σ_{min} are the maximum and minimum applied stresses. The R-ratio, R_σ , is described by equation 2.28 which is the ratio between the maximum and minimum stress.

The first published paper regarding fatigue dates back to 1837 where W. A. J. Albert investigated into the continuous failure of the conveyor chains used in the Clausthal mine [127]. Rankine discovered the effect stress concentrators in machined components on fatigue fracture behaviour [128]. In 1860, Wöhler carried out the first systematic study of metal fatigue on railway axles using a stress-life approach [129]. It was not until Basquin plotted fatigue results using a logarithmic scale that produced the well known S-N curve [130]. A schematic example of an S-N curves for ferrous and non-ferrous metals is shown in Figure 2.20, plotting the log of the strain amplitude, $\Delta\varepsilon/2$, against the log of the number of cycles to failure, N_f . An inverse relationship between the two variables can be seen. Ferrous metals have a fatigue limit, demonstrated by the horizontal section of the curve, which indicates that fatigue failure will not occur below a certain stress amplitude value. Non-ferrous metals do not exhibit a fatigue limit [32].

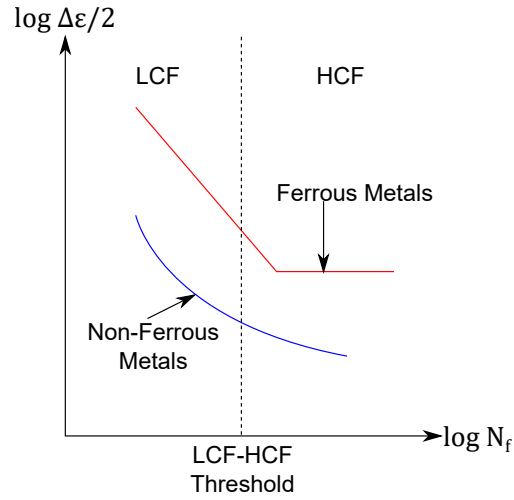


Figure 2.20: A schematic representation of S-N curves for ferrous and non-ferrous metals.

$$\frac{\varepsilon_e}{2} = \frac{\sigma_a}{E} = \sigma'_f (2N_f)^b \quad (2.29)$$

The fatigue life of a material can be categorised into two groups: low cycle fatigue (LCF) and high cycle fatigue (HCF). In the HCF region, Basquin's equation (see equation 2.29) is used to relate the elastic strain amplitude $\frac{\varepsilon_e}{2}$ to the number of reversals to failure, $2N_f$ which is twice the number of cycles to failure, N_f . σ'_f is the fatigue strength coefficient and b is the fatigue strength exponent; both parameters can be obtained graphically from Figure 2.20 [32].

$$\frac{\varepsilon_p}{2} = \frac{\sigma_a}{E} = \varepsilon'_f (2N_f)^c \quad (2.30)$$

In the LCF region, fatigue life is characterised as a function of plastic strain range. This behaviour is typically found in components operating at elevated temperatures, where a component expands and or contracts. Coffin and Manson [131, 132] described the relationship between the plastic strain amplitude, $\frac{\varepsilon_p}{2}$ and the number of reversals to failure $2N_f$. ε'_f is the ductility coefficient in fatigue and c is the ductility exponent in fatigue which can be obtained graphically from the SN curve [32].

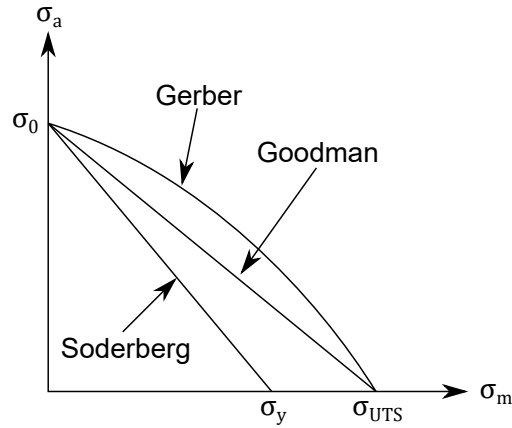


Figure 2.21: A schematic example of the constant life design curves for fatigue loading.

$$\sigma_a = \sigma_0 \left(1 - \frac{\sigma_m}{\sigma_{UTS}}\right) \quad (2.31)$$

$$\sigma_a = \sigma_0 \left(1 - \left(\frac{\sigma_m}{\sigma_{UTS}}\right)^2\right) \quad (2.32)$$

$$\sigma_a = \sigma_0 \left(1 - \left(\frac{\sigma_m}{\sigma_y}\right)\right) \quad (2.33)$$

The mean stress can have a significant effect on component fatigue lifetime. Goodman [133], Gerber [134], and Soderberg [135] developed models (see equations 2.31 to 2.33 respectively) that relates the mean stress, σ_m , to the stress amplitude that will provide safe operating conditions, σ_a . These models are demonstrated graphically in Figure 7.2, where σ_0 is the fatigue strength in terms of stress amplitude when $\sigma_m = 0$, and σ_y and σ_{UTS} is the yield stress and UTS of the material respectively. It has been found that most experimental data falls between the Goodman and Gerber lines which suggests that the Goodman model is a more conservative estimate of the mean stress effect [32].

Typically there are 3 stages of fatigue failure: crack initiation, crack propagation (also known as the Paris region [136]) and fracture as shown in Figure 2.22.

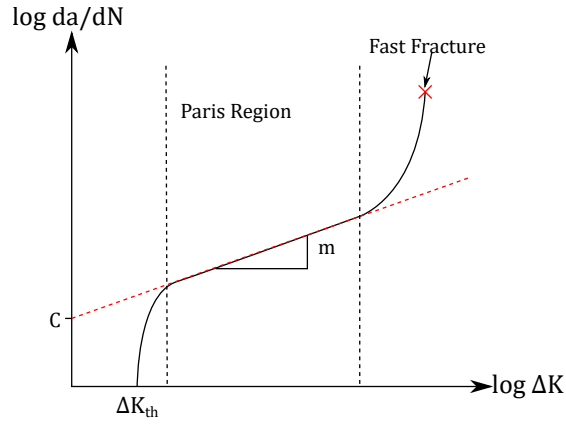


Figure 2.22: A schematic example of a crack growth rate graph.

da/dN is the crack growth rate, ΔK is the stress intensity factor range and m and C are material constants used in Paris' Law to determine stage II crack growth (see equation 2.34). An important feature in Figure 2.22 is the fatigue threshold, ΔK_{th} . Stress intensity factor range below this value will be insufficient to cause crack propagation to occur.

$$\frac{da}{dN} = C(\Delta K)^m \quad (2.34)$$

The majority of fatigue life is spent in the Paris region which may be used to determine the component lifetime of a material for SAGB housing applications.

Vratnica et al [137, 138] studied the effect of compositional variation of over-aged 7000 series forged alloys on fracture toughness. They found the alloys with the lowest impurity levels had the greatest fatigue threshold (resistance to crack initiation). Crack initiation and nucleation always occurred at coarse intermetallic (IM) particles (Fe and Si containing particles about $2.0\mu\text{m}$ in size or greater). They also found that the Mg_2Si and soluble phase particles that were smaller than the Fe-containing particles retarded crack growth by making the crack growth path more tortuous. The fracture surface of the samples they tested contained both Mg_2Si and Fe-containing particles, where the Fe particles cracked more readily. Therefore, the Fe-containing particles were not effective at resisting crack propagation.

Alpay [139] had similar findings to Vratnica. Almost all $\text{Al}_7\text{Cu}_2\text{Fe}$ particles on the crack path were fractured, with no evidence of plastic deformation. However, Mg_2Si and CuAl_2Mg particles were found unfractured and believed to impede crack growth by

either causing the crack to branch or by increasing the crack growth path.

Jian et al [140] studied fatigue behaviour of an Al-Zn-Mg-Cu alloy heat treated to T7451 temper. The initiation of fatigue damage occurred at Fe-rich particles found near or at the free surface. The fracture of the inclusion particles was induced when the accumulation of cyclic loading reaches the ultimate tensile strength.

Lindigkeit et al [141] studied the effect of microstructure on fatigue crack propagation of Al-Zn-Mg-Cu alloys in various heat treatments within a vacuum. They found that underaged alloys containing shearable precipitates possessed a greater crack propagation resistance in comparison with overaged alloys that contained impenetrable precipitates. Crack propagation resistance also increases with ductility and decreased precipitate size.

Desmukh et al [142] found that for the 7010 alloy, the overage heat treatment gave lower tensile strength but the highest value of fatigue crack propagation threshold. However, it also yielded the highest fatigue crack growth rate compared to near-peak age and peak age heat treated alloys; a similar finding to Lingigkeit. They attributed this to homogeneous deformation in the Paris region of crack growth and easy void nucleation at the coarse, non-shearable η precipitates.

2.6.6 Thermomechanical Fatigue

Thermomechanical fatigue (TMF) is the synergistic damage process caused by fluctuating thermal and mechanical loading. In the past, isothermal LCF data was used to predict the life of components under TMF loading. Researchers such as Thomas et al have found that TMF can be more detrimental to component lifetime than isothermal fatigue at maximum temperature [143].

TMF is usually described as either in-phase (IP), or out-of-phase (OP). IP TMF is where maximum and minimum temperature are synchronised with maximum and minimum mechanical loads, shown in Figure 2.23. OP TMF is where maximum temperature corresponds with the minimum mechanical loading and vice versa, shown in Figure 2.24.

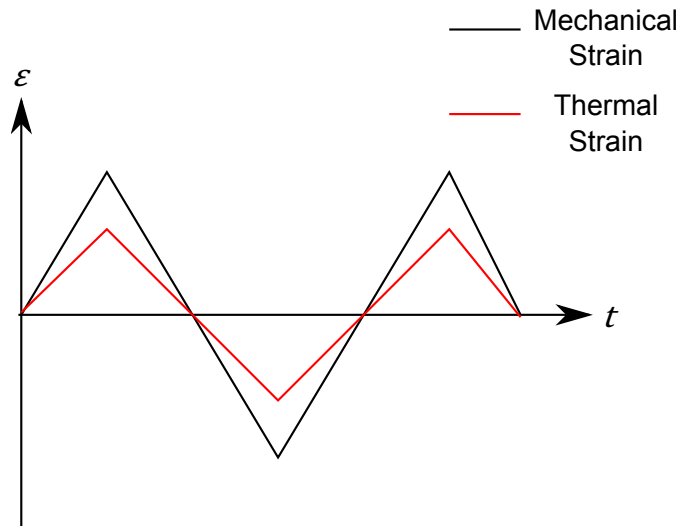


Figure 2.23: In-Phase TMF loading conditions.

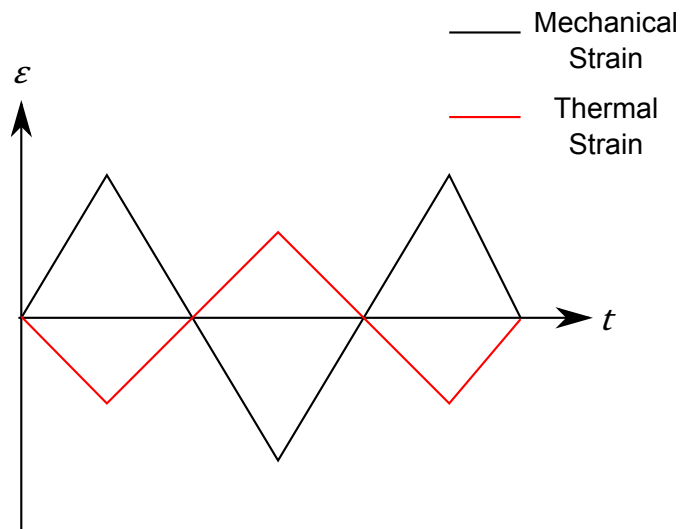


Figure 2.24: Out-of-Phase TMF loading conditions.

Halford [144] describes the effects of phasing and states that phasing effect is material dependent. Many researchers have found oxidation can heavily contribute to damage during out-of-phase thermo-mechanical fatigue. At high temperature and compression, an oxide layer forms in the initiated or propagating crack. When the material experiences lower temperatures under tension, an interfacial strain between the oxide layer and bulk material is induced which causes spallation of the layer and thus removal of bulk material. This phenomena will continue to occur until failure of the material [145, 146]. Many works have been carried out on high temperature materials such as nickel-based superalloys [123, 147–152] and steels [123, 153–157].

As far as the author is aware, the study of TMF behaviour in 7000 series aluminium

alloys has not been explored and the majority of work on the TMF of aluminium alloys has been carried out with automotive engine applications in mind. The cast aluminium alloys A356 and A357 have been thoroughly studied. Bose-Filho et al [158] investigated the effects of the microstructure and defects on TMF life for various Al-Si alloys via the following manufacturing processes: thixoforming, injection moulding and permanent mould casting. They found that the casting processes and chemical composition that produced a reduction in porosity and have an absence of secondary dendrite arm spacing had greater lifetimes under TMF loading.

Azadi et al [159] found that varying the strain ratio (maximum strain to minimum strain), R_ϵ , had no significant effect on high temperature LCF or OP-TMF lifetime of A356. However, the high temperature LCF lifetime of A357 was more influenced by strain ratio due to its different strain hardening behaviour as a result of its composition. The high temperature LCF lifetime was greater than OP-TMF lifetime due to severe conditions under TMF loadings with variable temperatures.

Merhy et al [160] characterised the crack growth of the A357 heat treated to the T7 specification. They found that at high temperatures and low frequencies, time-dependent crack growth highly influences crack advancement. Furthermore, the crack path largely depended on microstructural features such as the secondary dendritic arm spacing and the size and shape of Si particles. The cracks remained perpendicular to loading direction within the matrix and either debonded or fractured the Si particles in its path. This created mixed cracking mechanisms.

Huter et al [161] found that aluminium alloys with high copper content contained hard particle phases that caused crack initiation independent of applied mechanical loading. On the other hand, alloys with low copper content had greater global deformations throughout the specimens. Furthermore, heat treatments that caused large overageing decreased the TMF life compared to a limited overaged heat treatment.

2.6.7 Creep Deformation

Creep is a time-dependent, thermally activated plasticity under constant stress where permanent deformation can take place below the yield stress of the material. Since the term “high temperature” is relative to different metals, the temperature is expressed as

a homologous temperature which is a ratio of the actual temperature, T , and melting temperature, T_m . Creep generally occurs in aluminium at $T > 0.3T_m$ [162].

There are typically 3 stages of creep as shown in Figure 2.25, where $\dot{\epsilon}_c$ is the creep strain and t is time. Stage I (primary creep) is caused by the applied load to the specimen. The creep rate decreases and the material enters stage II (secondary creep) where the creep strain rate is at a minimum. At this point the rate of work hardening is balanced by the rate of recovery (eg. the reduction of dislocation density) and the creep strain, increases linearly with time. An Arrhenius equation is usually used to calculate the minimum creep rate in terms of activation energy required for creep (equation 2.35).

$$\dot{\epsilon}_{c,min} = Ae^{-Q/RT} \sigma^n \quad (2.35)$$

where A is a material constant, Q is the activation energy for the controlling mechanism, T is absolute temperature and R is the universal gas constant.

During stage III (tertiary creep), an acceleration in creep strain rate is observed caused by the accumulation of voids and microcracks. As a result, the cross sectional area of the material is reduced, leading to full fracture [32, 163].

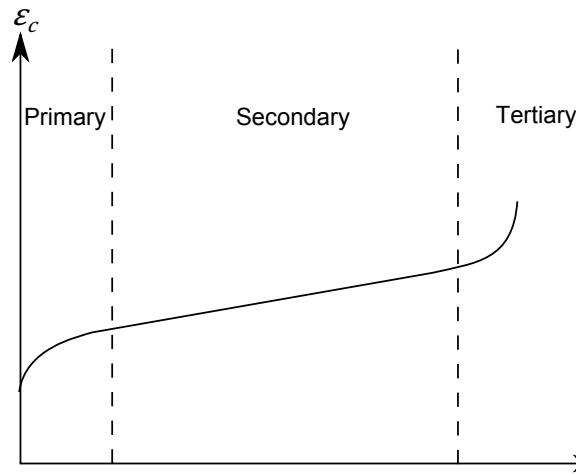


Figure 2.25: A schematic example of a creep curve.

The evolution of creep deformation depends on the temperature and stress conditions. Creep deformation mechanisms are categorised into the following: grain boundary sliding, diffusion creep, dislocation creep and dislocation gliding. Multiple mechanisms may occur at any time but usually one mechanism is dominant. Ashby [164] created deformation maps for various materials to schematically demonstrate

which conditions will produce the dominant creep mechanism as shown in Figure 2.26. For different materials, the type of dominant creep deformation mechanism will depend on the homologous temperature and applied normalised shear stress (σ/G).

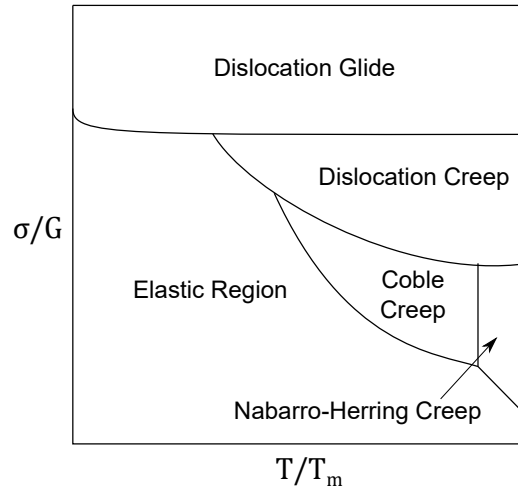


Figure 2.26: A schematic example of an Ashby creep deformation map [164].

Coble [165] proposed a diffusion mechanism known as Coble creep which occurs at lower homologous temperatures. This is when the diffusion of atoms at the grain boundaries is greater than the diffusion through the lattice. When he measured the diffusion coefficient of aluminium and oxygen ions in alumina, he found that the coefficient for aluminium was several orders of magnitude greater than oxygen. If the creep rate was limited to the lattice diffusion of atoms, then the least mobile species would control the diffusion rate. However, he observed that the diffusion of oxygen ions was enhanced along the grain boundaries and controlled the overall creep of the material.

Nabarro-Herring creep [166] involves mass transport of vacancies through the grains over grain boundaries. Excess vacancies are created at grain boundaries perpendicular to the tensile axis with a uniaxial tensile stress and eventually diffuse towards grain boundaries that are parallel to the stress. The grains elongate without the aid of dislocation slip or climb.

Dislocation creep is a time dependent process where dislocations are able to climb over obstacles assisted by the diffusion of vacancies to the dislocation. This mechanism is enhanced with increasing temperature. At higher stresses, dislocations are able to

glide on slip planes [167].

$$\dot{\varepsilon}_{min}^c = A\sigma^n \quad (2.36)$$

Equation 2.36 is the Norton creep power law [168] which predicts the minimum creep strain rate, $\dot{\varepsilon}_{min}^c$, for a creep stress at a particular temperature. This relationship describes a linear correlation may be found by plotting the logarithmic secondary creep rate against the logarithmic applied stress. The material constants A and n can then be deduced from the equation of the straight line.

$$\omega = A_D/A \quad (2.37)$$

Kachanov [169] initiated the development of continuum damage models (CDM) to predict creep behaviour in a phenomenological way and present it from the viewpoints of mechanics. He suggested that the strain rate and damage rate (void formation and crack growth) of a material are both dependent on stress, temperature and damage. He defined damage as the reduction of the load-bearing area as shown in equation 2.37. ω is a damage variable that ranges from 0 (no damage) and 1 (full fracture), A is the undamaged cross-sectional area and A_D is the effective area where the area of the voids are subtracted from the damaged area. By selecting the equations to describe those two rates, the duration of the tertiary creep stage can be predicts and the creep life can be approximated.

$$\sigma_e = \sigma/(1 - \omega) \quad (2.38)$$

This variable was used by Robotnov [170] to describe the effective stress that is applied to a damaged cross sectional area (equation 2.38) which in turn allowed strain and damage to be coupled.

$$\dot{\varepsilon}_{cr} = d\varepsilon_{cr}/dt = A \left(\frac{\sigma_{eq}}{(1 - \omega)} \right)^n \quad (2.39)$$

$$\dot{\omega} = d\omega/dt = \frac{M\sigma_r^X}{(1 - \omega)^\phi} \quad (2.40)$$

The Kachanov-Robotnov model is described by equations 2.39 and 2.40, where A , M , n , χ , and ϕ are time and temperature material constants, σ_{eq} is the von Mises equivalent stress and $\dot{\varepsilon}_{cr}$ is the creep strain rate. To account for multi-axial behaviour, the uniaxial creep law can be written in terms of von Mises stress in equation 2.40, where ω can be expressed in terms of rupture stress, σ_r , in equation 2.41 [171, 172].

$$\sigma_r = \alpha\sigma_1 + (1 - \alpha)\sigma_{eq} \quad (2.41)$$

where σ_1 is the maximum principal stress, σ_{eq} is the von Mises equivalent stress and α is the triaxiality material constant which lies between 0 and 1. Other researchers such as Liu and Murakami [173] and Sdobyrev [174] have also worked on creep damage models.

$$\phi = \frac{\dot{\varepsilon}_{min}^p}{\dot{\varepsilon}_{min}^0} \quad (2.42)$$

Prior plastic deformation has been found to have varying effects on creep behaviour which was dependent on the material and the prestrain treatment. To quantify creep resistance or enhancement, the parameters ϕ (equation 2.42) and ψ (equation 2.43) represent the ratio between the minimum secondary creep rate and rupture time, respectively, of prestrained samples and the virgin (non-prestrained) samples [175]:

$$\psi = \frac{t_f^0}{t_f^p} \quad (2.43)$$

where $\dot{\varepsilon}_{min}^p$ and $\dot{\varepsilon}_{min}^0$ are the minimum creep rate of prestrained and virgin sample, respectively. When $\phi > 1$, prestrain causes creep enhancement and when $\phi < 1$, creep resistance occurs.

Similarly, ψ is ratio of the rupture time of the virgin sample t_f^0 , to the rupture time of the prestrain sample, t_f^p . Similar to the parameter, ϕ , when $\psi > 1$, prestrain causes a reduction in creep life and when $\psi < 1$, creep life is extended [176].

Researchers have studied the effect of creep on 7000 series aluminium alloys and have observed microstructural features that interact with creep damage. Park et al [76] studied the effect of static and cyclic creep on 7075-T6 alloy. They found a greater amount of void formation in the statically-loaded creep samples. Fracture was transgranular and appeared to nucleate at Cr-rich dispersoids (E-phase) for both cases.

This agrees with the previous work conducted by Ludtka and Laughlin [177]. These dispersoids were located within the grain and acted as void formation sites that led to ductile fracture. The larger sized E-phase in the static crept surface increased the rate of creep strain. Ludtka also found that the stress exponent, n , of Norton's creep law increased as temperature decreased indicating the increasing influence of stress on creep behaviour. On the other hand, this ductile fracture behaviour might explain the increase in toughness of the 7075 aluminium alloy.

Embury et al [178] studied the effects of substructures and orientation on creep behaviour of 7075-T6 alloy. They found that samples containing a dense uniform dislocation structure had a greater creep rate than samples with elongated subgrains. However, as temperature increases, the secondary creep rate within the two types of microstructure become similar. Grain orientation had no effect up to 150°C but had considerable influence at 450°C. They suggested that grain orientation was only important when grain boundary sliding was the dominant mechanism for deformation. Fine GPZs were found to be the major factor that contributes to creep strength and unstable grains may facilitate dislocation motion which enhance creep rate. Howard et al [179] studied grain anisotropy on creep resistance of 7075 alloy. They found that a substantial strengthening effect is observed when the material is deformed parallel to the major axis of the grains.

Wilshire and Willis [180] studied the effect of prestraining on both partially-solution treated and fully-solution treated 316 stainless steel. They found that under each heat treatment, the minimum creep rate and creep ductility decreased. However, the failure time for the partially solution treated samples decreased whereas the opposite occurred for the fully solution treated samples. The effects of prestrain treatment depends on the microstructure of the material. Oshashi et al [181] applied pretension up to 3% on 316 steel at 650°C. They found that creep resistance under both axial tension and torsional loading increased with prestrain. Previous studies by Kikuchi and Ilschner [182] found that small pre-strains at room temperature of AISI 304 stainless steel had improvements on creep strength. As prestrain increases, creep life increases but the strain to failure decreases. Kowaleski et al [183] found that room temperature deformation of copper will decrease secondary creep rate but decrease overall creep life.

While some researchers have noted increased creep resistance after prestraining

others had found that in other materials, creep resistance decreased. Zhang [184] found that prestraining in nickel based C263 superalloy, creep life and rupture strain was reduced with increasing plastic prestrain at room temperature. The minimum creep rate also slightly increased with prestrain. Djakovic et al [185] studied creep behaviour in the aluminium alloy 2650-T8. After prestraining to 4.9% at room temperature, creep life was reduced by a factor of 5 which was caused by grain boundary cavitation. Tai and Endo [175] prestrained a chrome steel at 600°C and concluded that the greater the prestrain, the greater the creep enhancement.

Cortellino et al [176] studied small punch creep tests of P91 steel to assess whether creep life data could be obtained from small pieces of material. The initial impression of the small punch essentially induced a prestrain into their samples before it was crept. They used a modified Liu-Murakami creep damage model to account for the initial plastic strain and utilised the two parameters, ϕ and ψ to describe the variation of the minimum creep rate and failure time induced by prestraining, respectively.

2.7 Experimental Techniques

This project involved conducting a range of uniaxial mechanical testing at elevated temperatures. This section will briefly discuss the different techniques used for strain and temperature measurement, and heating techniques used for elevated temperature testing.

2.7.1 Strain Measuring Techniques

The machine cross-head motion can be tracked with the load as a function of time, where the displacement of the cross-head is assumed to be the displacement of the specimen. However, errors in strain and stiffness are introduced through the deflection of the entire load frame under the applied stress. Compared to other strain measurement techniques mentioned in this section, the machine cross head displacement provides the least accuracy [186].

Strain gauges are often used for strain measurement for their accuracy and ease of use. However, accurate strain measurement of strain gauges are highly dependent on the quality contact and adhesion between the gauge and test specimen. For this reason, strain gauges are mainly used to obtain information regarding the elastic region

of the material since debonding of the gauge may occur in the plastic region. There are other systematic errors that have an effect on the global accuracy of strain gauges, for example, errors due to transverse sensitivity and temperature [186].

Extensometers are also used to measure strain and there two types: contact (clip-on and sensor arm) and non-contact (video and laser) extensometers. Clip-on extensometers are mounted onto the gauge section where the extension of the sample is transferred to the internal transducer within the clip, as shown in Figure 2.27a. The movement range of the clip-on extensometer is limited to a few millimetres. Therefore, the clip must be removed before the failure of the sample to avoid damage [187]. Usually, the clip gauge measures the initial elastic region of the material before it is manually removed and the machine cross-head is used for the remaining stress-strain measurement. This minimises the initial error caused by the deflection of the test frame.

Unlike clip-on extensometers, sensor arm extensometers offer a high movement range while maintaining accurate measurements and the automation during measurement (manual removal of the extensometer is not required). A small load is applied to the sample by the extensometer which creates a microindentation for precise positioning at the contact point (see Figure 2.27b). However, if the extensometer is placed on just one side of the sample, the accuracy in strain measurement may be compromised due to bending or crack propagation in the sample [187].

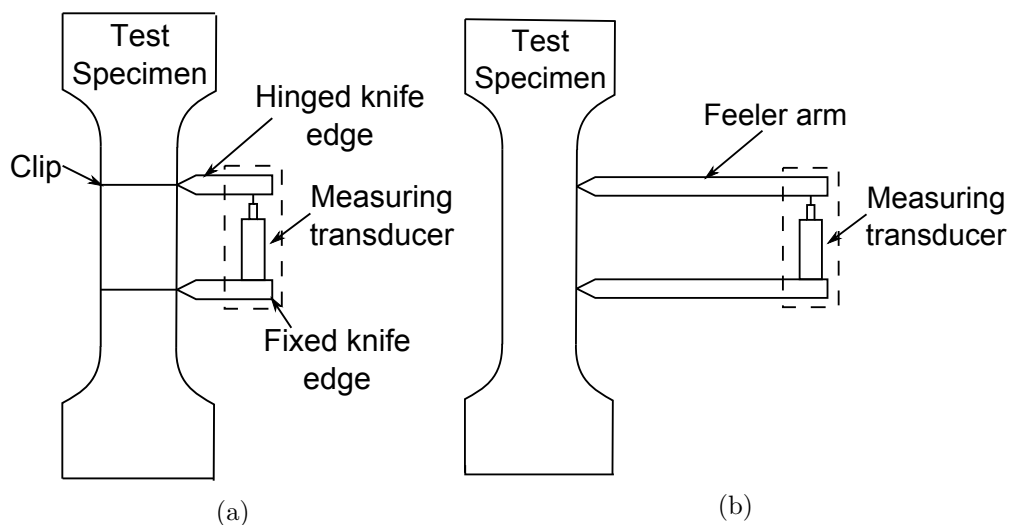


Figure 2.27: A schematic representation of (a) a clip extensometer and (b) a sensor arm extensometer measuring the strain of a sample.

For cases where contact extensometers are an unsuitable for strain measurement, non-contact extensometry can be an alternative to accurately measure the strain. Video extensometers require markings on the sample to distinguish the tracking areas from the surrounding area for strain measurement (see Figure 2.28). The distance between the tracking areas becomes the gauge length and the movement of the areas are outputted as signals that are converted into strain [187].

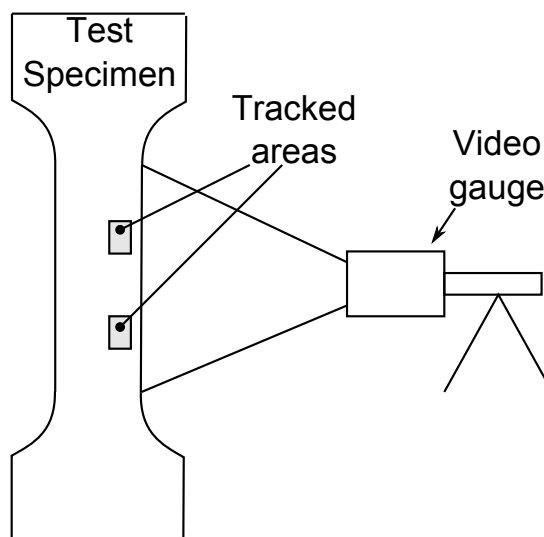


Figure 2.28: A schematic representation of a video extensometer measuring the strain of a sample.

Laser extensometers evaluate the reflections of the lasers and continually tracks selected measurement points on the sample which is then used to calculate strain. This technique does not require markings on the sample and the strain of very small gauge sections can be measured with high accuracy [187].

2.7.2 Sample Heating Methods and Temperature Measurement Techniques

Environmental chambers encase the sample, grips and the test frame (partially) and heats the sample via convection. A circulation system maintains uniform temperature within the chamber to keep a temperature tolerance of about $\pm 1^\circ\text{C}$ (but a significant amount of time is required to preheat the furnace depending on the size of the test rig and desired test temperature [188]). A window can be installed for a line of sight to the sample in case visual measurement techniques are required.

Split furnaces encases the sample and grips, and it is common practice to use a low heating rate. It requires the sample be mounted in the test machine before heating,

meaning that the sample will experience a temperature soak before testing [188]. This technique would be inappropriate if the material is temperature sensitive, resulting in changed mechanical properties.

An induction furnace heats an electrically conductive material through electromagnetic induction. A high-frequency alternating current is passed through a coil surrounding the sample and heat is generated by internal eddy currents in the material. Faster heating rates can be achieved compared to the previous heating techniques. However, the design of the coil is test material dependent and crucial for uniform temperature distribution across the gauge section of the sample. Therefore, thermal calibration can be time consuming since it is dependent on the specimen's magnetic properties and the manufacture of a bespoke induction coil specific for the specimen. Additionally, accurate temperature control is required to avoid overshoot [188].

Thermocouples are commonly used for contact temperature measurement and are usually welded to the sample. However, it has been found that the heat affected zone can affect fatigue properties of materials by forming a crack initiation site at the area of the weld [123]. Alternatively, a pyrometer can be used, which is a non-contact temperature measurement equipment that detects the energy from the infra-red radiation emitted from the heated sample. Dual laser beams are sometimes used to obtain the correct distance between the pyrometer and sample. It is critical that the emissivity of the sample is known for accurate temperature measurement which may require additional preparation and calibration before testing [189]. This can be achieved by heating the material and measuring its temperature using a thermocouple for example, and adjusting the emissivity on the pyrometer until it matches the temperature readings from the thermocouple.

2.8 Microscopy Techniques

Scanning electron microscopy (SEM) is capable of producing images for topography and fractography scanning the sample surface with a focused beam of electrons. The electrons interact with atoms of the sample at various depths and can produce signals such as secondary electron (SE) and back-scattered electrons (BSE). SE images are produced by signals of the electrons emitted from close proximity to the surface, while

BSE images are produced from electron signals from deeper locations within the sample. The electrons slow down as they circle around the element nucleus and exit the sample. The greater the nucleus size, the greater the number of BSE meaning that different elements within a sample can be presented. These imaging techniques do not require the sample to be flat but it must be a conductive material. The benefit of SEM is that a large area, maybe the entire sample, can be focused and imaged and greater magnifications can be achieved (up to 1,000,000x) compared to optical microscopy (1,000x) [190].

If more information regarding the composition of the material is required then techniques such as energy-dispersive X-ray spectroscopy (EDX or EDX) can be used. The incident beam excites an electron from an inner (higher energy) shell of an atom which leads to it being ejected and replaced by an electron from an outer (lower energy) shell. This results in an energy difference between the higher-energy and lower-energy shell being released in the form of an X-ray. This energy level is dependent of the element of the material and the level of the electron shell (labelled K, L and M in Figure 2.29). The energy detected can be used to identify the element (see Figure 2.30) [191]. There are a number of limitations to this method such as an overlap in energy peaks from different elements (occur when the emission from different electron shells of different elements are similar in energy), or low concentrations of elements within a spectrum [192]. EDX cannot provide structural information regarding the material or particle within it but there are other techniques that have this capability described below.

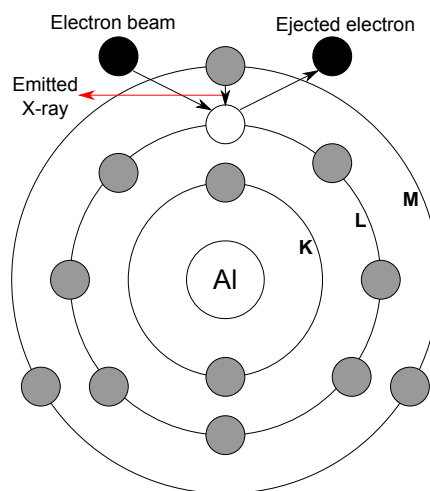


Figure 2.29: A schematic example of an X-ray emission from an aluminium atom induced by the interaction with an electron beam.

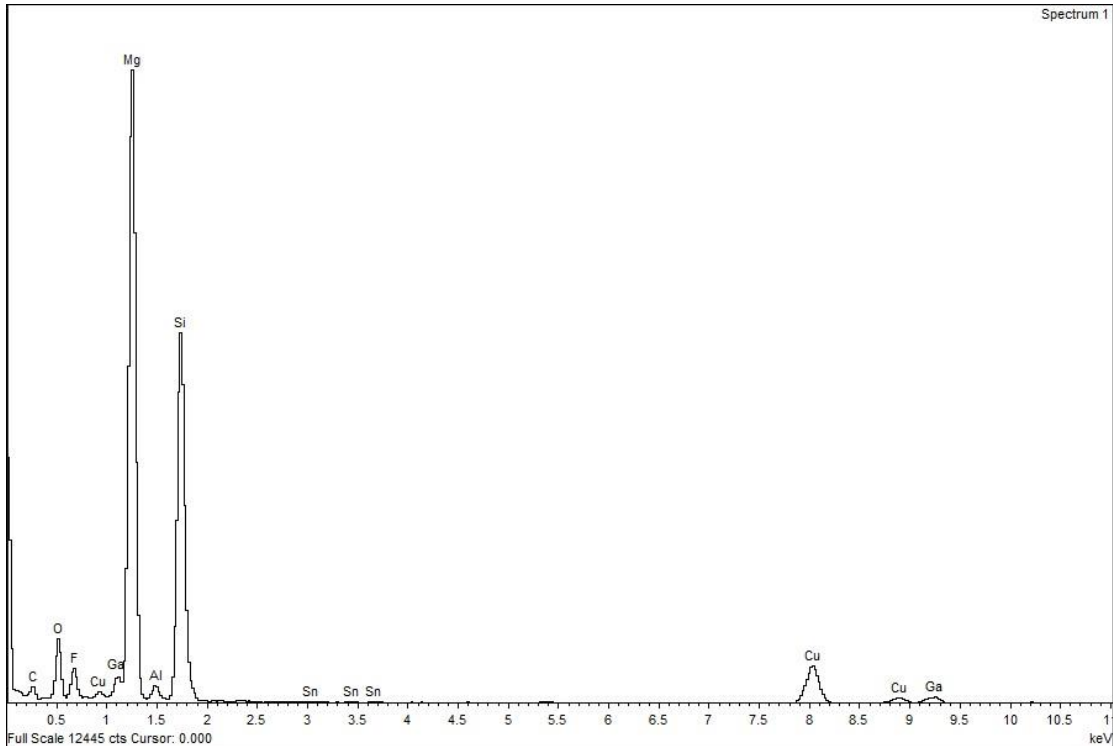


Figure 2.30: The results of an EDS spectrum showing the detected elements.

Transmission electron microscopy (TEM) is a technique used to transmit an electron beam through the sample to form an image. The specimen must be electron transparent which can be achieved through various preparation techniques such as: mechanical milling, chemical etching, ion milling or ion etching. In recent years, the latter two techniques have been used for sample preparation [193, 194] though the sample may become contaminated by the ion beam. TEM is able to obtain image the grains, grain boundaries and particles within the microstructure. Additionally, selected-area diffraction patterns can be obtained which can be used identify the phase of a particle. Figure 2.31 shows a schematic representation of a diffraction pattern from a particle. The brightest spot appear in the centre of the pattern and the surrounding spots provides two axes of the lattice parameters. Each spot corresponds to atom positions in the crystal lattice, hence, the distribution of diffraction spots depends on the crystal structure and orientation of the crystal [195].

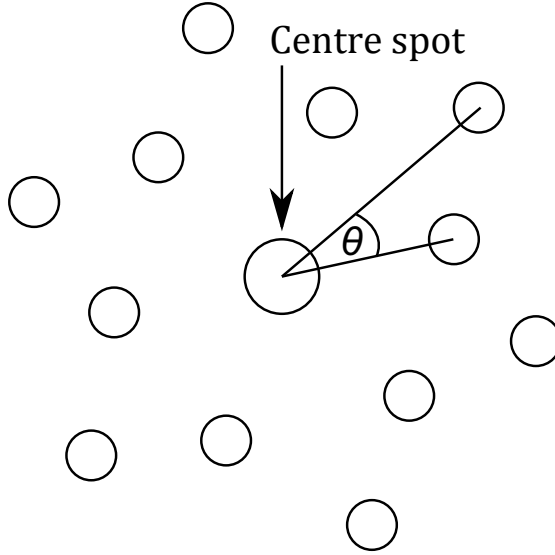


Figure 2.31: An example of a diffraction pattern showing how the angle between planes were measured.

The first step is to measure the d-spacing between the centre spot and those that surround it and the angle between them (θ). Afterwards, a materials database, such as the International Centre for Diffraction Data (ICDD), can be used to obtain the lattice parameters, a , b , and c (depending of the type of Bravis lattice of the particle). If the phase of the particle is not known, then EDX can be used to determine the composition of the particle as a starting point for searching for possible phases in a materials database. Then it is required to index the diffraction pattern and determine the lattice position of the atoms to determine the phase of the particle [196].

$$\cos\theta = \frac{4}{3a^2} \left[h_1h_2 + k_1k_2 + 0.5(h_1k_2 + h_2k_1) + \frac{3a^2}{4c^2}l_1l_2 \right] d_{h_1k_1l_1}d_{h_2k_2l_2} \quad (2.44)$$

$$\frac{1}{d_{hkl}^2} = \frac{4}{3} \left(\frac{h^2 + hk + k^2}{a^2} + \frac{l^2}{c^2} \right) \quad (2.45)$$

If the crystal structure of a particle is hexagonal, then the angle between planes, θ can be calculated using Equation 2.44, where h , k , and l are the Miller indices that are assigned to spots in the diffraction pattern, and a and c are the lattice parameters as described in Figure 2.3. d_{hkl} is the distance between a family of planes (hkl) which can be calculated using Equation 2.45 [195].

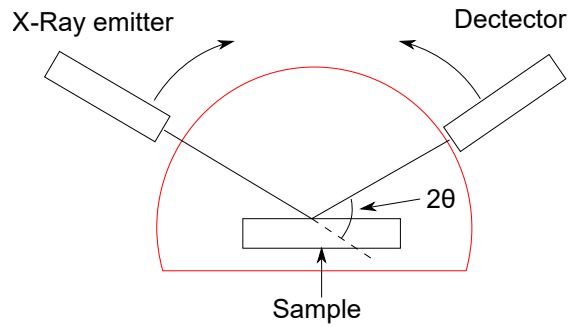


Figure 2.32: A schematic representation of the X-ray powder diffraction process.

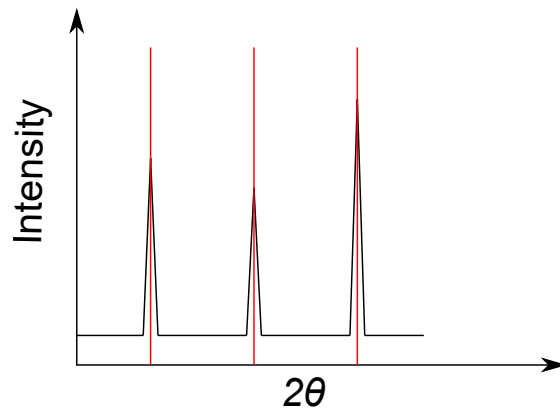


Figure 2.33: A schematic example of intensity versus diffraction angle of an X-ray powder diffraction pattern where the peaks represent a plane of atoms.

$$2d\sin\theta = n\lambda \quad (2.46)$$

Another method for particle identification is called X-ray powder diffraction which is used to determine the crystal structures and atomic spacing of a material, where the diffracted intensity is plot against the diffraction angle 2θ . The diffraction behaviour of the X-rays is characterised by Bragg's law [197], which relates the wavelength to the distance between planes and the angle of incidence. The positions of the peaks in a powder pattern are determined by the size, shape and symmetry of the unit cell. They also identify the planes of atoms that are parallel to each other. The peak intensities shows how much of a particular atoms lie in the structure, or how much of a phase is present in a sample. Therefore, the powder pattern is a fingerprint of the phase.

Electron backscatter diffraction (EBSD) is a SEM-based microstructural crystallographic characterisation technique used to study polycrystalline materials. The obtained diffraction pattern are in the form of Kikuchi bands (see Figure 2.34)

that are used to identify different grain orientations within the material and different phases, where the lattice spacing is found by measuring the space between the band edges [198]. The main drawback of using EBSD is that the samples may require further preparation since the technique requires that a small, flat sample of a particular size due to 70° tilt positioning in the SEM chamber.

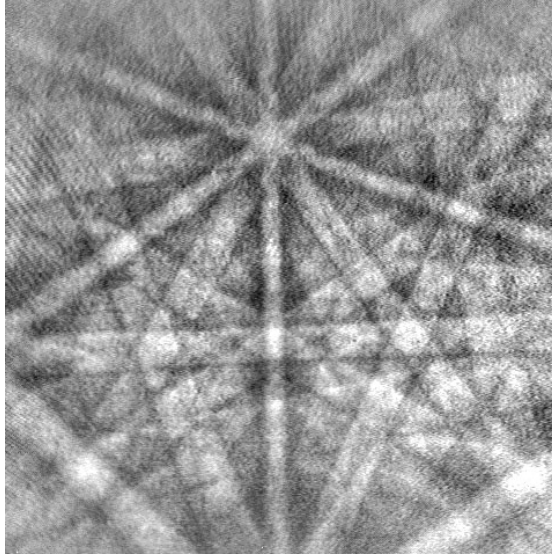


Figure 2.34: An example of the pattern Kikuchi bands obtained from EBSD.

3 Material, Test Methodology and Equipment

3.1 Material

A wrought 7175 aluminium alloy, heat treated to the T7351 specification according to the SAE AMS2772F procedure, was purchased from Amari-Aerospace ltd. in the form of 1.5m X 1.0m X 0.03m hot rolled plate. The chemical composition of this alloy is shown in Table 3.1. The melting temperature of this alloy ranges between 532°C to 635°C [28].

Table 3.1: Element composition of the 7175-T7351 aluminium alloy provided by Amari-Aerospace ltd.

	Zn	Mg	Cu	Cr	Ti	Fe	Mn	Si	Other	Al
wt %	5.7	2.5	1.6	0.2	0.04	0.06	0.02	0.03	0.02	Bal

The plate was mapped and cut according to Figure 3.1 so that a record of each type of test specimen could be traced back to a position in the plate before they were manufactured. Figures 9.1 and 9.2 demonstrates the coordinate systems used to designate sample names for fatigue and creep samples. Tensile samples were labelled either “L” or “T” to specify that the sample axis was parallel or perpendicular to the rolling direction respectively, followed by a number.

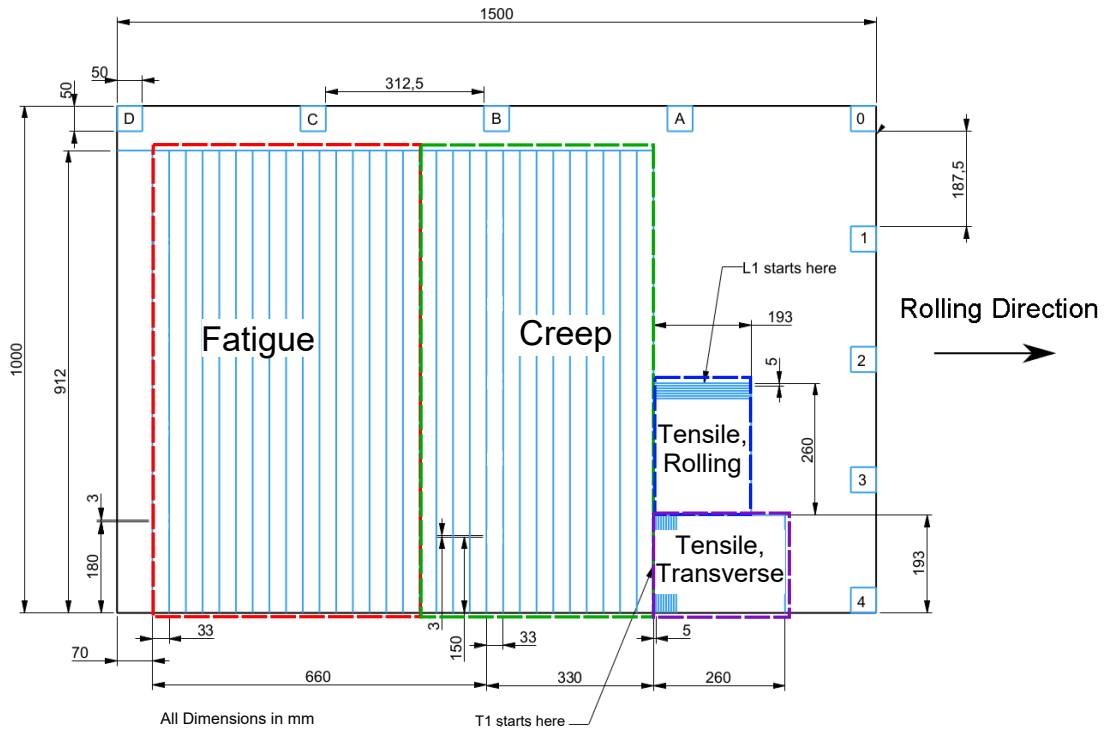


Figure 3.1: A schematic of the plate used to manufacturing samples.

3.2 General Test Conditions

The choice of temperatures and stresses used for mechanical testing were based on the simplified operating conditions of the SAGB housing during flight. Figure 1.5a characterises this stress variation at several positions on the top flange of the housing during flight. From this profile, the minimum and maximum stress for the testing was chosen to be 100MPa and 190MPa. Similar to the stress flight profile, Figure 1.5b shows the operating temperatures over a flight cycle at the top flange, “flange T”, the area closest to the engine, “max T”, and the bearing housing location, “bearing T”. The subsequent test temperature range used was therefore 120°C to 230°C.

3.3 Hardness Measurements

Hardness is a measure of resistance to deformation which provides an indication of a material’s strength. Vickers hardness testing was used to measure the room temperature hardness of the samples for reasons that will be explained in sections 3.3.1 and 3.3.2. A square-based pyramid diamond indenter, with opposing indenter faces set 136° from one another was used. The indenter was pressed into the samples with a specified load for 10 to 15 seconds. The indenter was then removed, leaving a square impression in the sample. The sample was to be flat to obtain accurate readings and the surface roughness was not an issue for macro Vickers hardness tests. However, for micro Vickers hardness tests, it was required to polish the surface before testing. The average length of the diagonal lines, d , was measured in millimetres and the Vickers hardness was calculated using equation 3.1, where F is the applied kilogram force [199].

$$HV = \frac{2F \sin\left(\frac{136}{2}\right)}{d^2} \quad (3.1)$$

3.3.1 Discrepancy Check in Plate Hardness

Hardness measurements were recorded to check for any major discrepancies in material properties throughout the plate. Sections A to D and 0 to 4 were water-jet cut from the plate, as shown in Figure 3.1, along the length and width of the plate. Macro-scale Vickers hardness (using a 10kg load) was measured, using the machine shown in Figure 3.2, along the length and width on the top surface, and depth of the 7175-T7351 plate.



Figure 3.2: The machine used for macro-scale Vickers hardness testing.

Micro-scale Vickers hardness testing (using a 1kg load on a Buehler Instrument Model 1600-6400 in Figure 3.3) was used to generate a depth profile of sections 0 and 2. The reason for using this measurement scale was that once the sample height was set (in the y axis direction per-se), the platform could then traverse in the x and z axis directions with a $\pm 0.05\text{mm}$ uncertainty to acquire micro Vickers measurements at desired positions on the sample's face. The depth profile would reveal whether there were significant differences in hardness through the thickness of the plate between the edge and the mid-width of the plate. The first indentation was taken about 1mm from the bottom edge, followed by indentations every 2mm. Macro-Vickers hardness measurements were taken at various depths to verify the micro-Vickers hardness measurements. The surface was polished to a 1mm finish for a clear image of the indentation to measure the diagonal length of the impression made by the indenter.



Figure 3.3: The machine used for micro-scale Vickers hardness testing.

3.3.2 Plate Hardness After Exposure To Temperature Over Time

A requirement from Rolls-Royce plc. was to obtain tensile data after the material was “soaked” for 1000 hours at test temperature prior to testing. However, this would not provide insight into the rate at which the mechanical properties would change over time at temperature. A simple method to observe this behaviour using hardness testing was devised. Rectangular blocks cut from the sections 0, 2, B and D as shown in Figure 3.1 were placed in furnaces set to 120°C, 160°C, 180°C, 200°C and 230°C. Room temperature Vickers hardness (using a 10kgf load) was measured on all planes of the samples (described in Figure 3.4) at intervals over a period of 1000 hours (6 weeks).

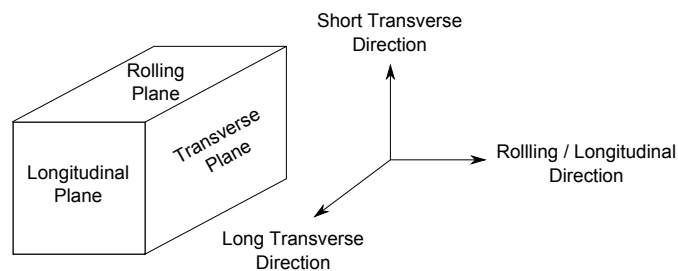


Figure 3.4: Drawing of a sample used to measure Vickers hardness of each plane of the samples and the assigned plate directions.

3.4 Tensile Test Methodology and Equipment

Figure 3.5 shows the geometry of the flat dog-bone test specimens used for tensile testing. The samples were manufactured in such a way that the applied load acted parallel or

perpendicular to the rolling direction of the plate. This was to examine the effects of plate directionality on tensile properties.

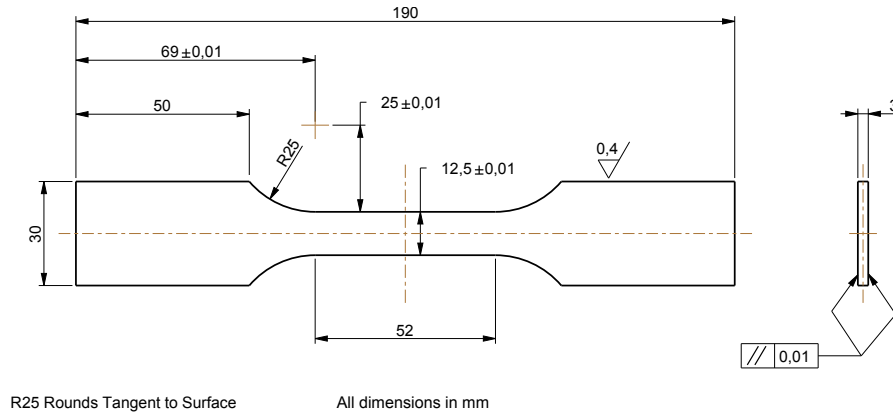


Figure 3.5: Geometry of tensile test specimens.

Room and elevated temperature (20°C, 120°C, 160°C, 180°C, 200°C and 230°C) tensile tests were conducted on an Instron 5985, using an environmental chamber for temperature control (Figure 3.6). The tensile samples were either as-received or soaked at elevated temperature for up to 1000 hours. K-type thermocouples were used to ensure the Instron grips reached test temperature before testing commenced.

Contact extensometers (clip or sensor arm extensometer) could not be used since the tests continued until failure of the sample and the extensometer would not be able to be removed during the test. Therefore, strain measurements were recorded using an Imetrum video gauge. Black specks were sprayed on a white baron nitride coating on the samples to produce distinguishable features for the video gauge to track that did not discolour during heat exposure. The strain was calculated in real time by producing a signal proportional to strain measured over the gauge length between 2 tracked areas on the sample. One potential disadvantage with using this technique was that if the pattern of the target tracking area change significantly (for example the pattern was close to the necking area), the video gauge would not be able to recognise the original pattern of the tracked areas and would stop calculating the strain of the sample. Therefore, the full monotonic stress-strain curve could not always be obtained.

An attempt was made to spot weld a K-type thermocouple onto a used test piece, as a means of measuring the surface temperature of the samples, but this could not be done. The thermocouple would attach to the spot welder instead of the sample which may have been due to the insufficient power to melt the area of the sample to where

the thermocouple should have joined. Flash tape (adhesive tape capable of being used at 250°C) was used instead to attach thermocouples to the top, bottom and centre of the sample's gauge section. It was found that the temperature difference between the bottom and centre of the gauge section, and the centre and top of the gauge section was within the 1°C limit. According to the standard BS EN ISO 6892-2:2011, the maximum permissible difference along the test sample is 3°C, and the permissible difference between the test sample and the test temperature was $\pm 3^\circ\text{C}$. Once the test temperature was reached, the sample was left for an extra 3 minutes to ensure temperature uniformity. Samples were pulled in tension at a rate of $1\text{mm}\cdot\text{min}^{-1}$.

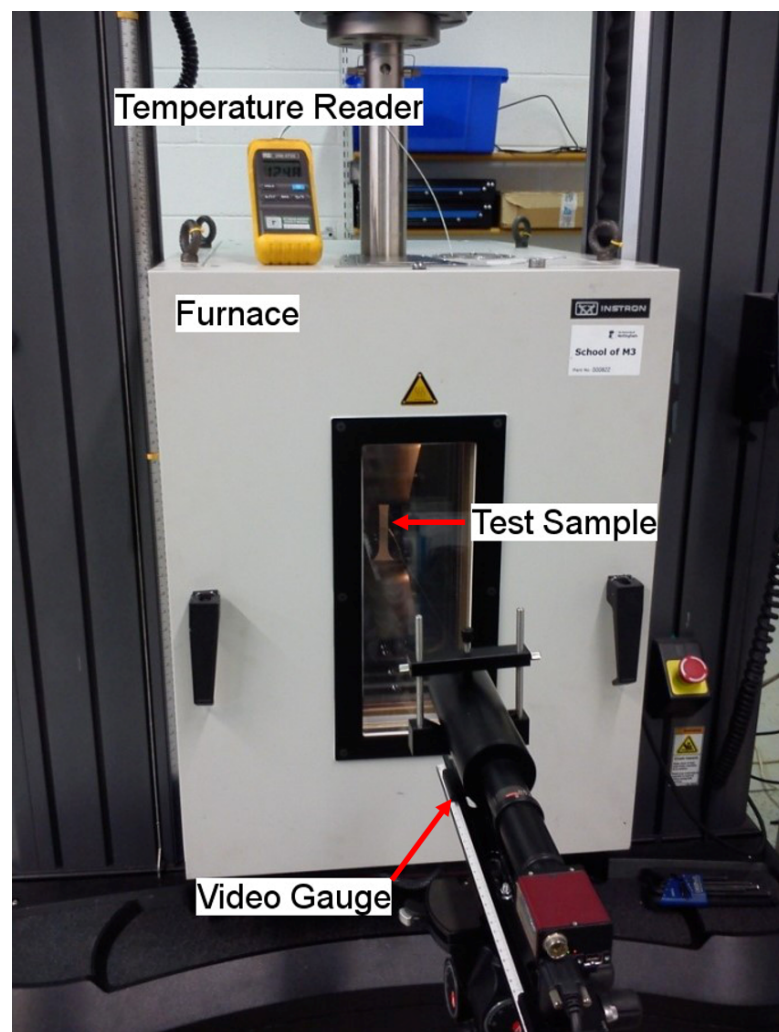


Figure 3.6: Tensile test setup on the Instron 5985 with an environmental chamber.

3.5 Creep Tests

Denison dead weight machines were used to carry out creep tests (test parameters can be found in Figure 3.2). The applied stress and temperature ranged from 100MPa to

190MPa and 160°C to 200°C respectively. Strain was measured using an extensometer that mounted onto the knife-edges of the sample. The sample temperature was measured with 3 thermocouples; one at the top, bottom and centre of the gauge section (see Figure 3.7). The deviation in sample temperature was within $\pm 3^\circ\text{C}$ of the specified test temperature and along the gauge length which was in accordance to BS EN ISO 204:2009. The geometry of the test samples can be found in Figure 3.8. Samples were placed in the machine and heated to the specified temperature before the test commenced for 80 minutes in total.

Table 3.2: Test parameters used for creep tests.

Temperature ($^\circ\text{C}$)	Stress (MPa)
160	100
	120
	150
	190
180	100
	120
	150
	190
200	100
	120
	150
	190

The Mayes 250 machine was used to prestrain and creep test samples at 180°C. The temperature and strain measurements were conducted in the same manner as the creep tests on the deadweight Denison machines (see Figure 3.7). The aim was to study how creep behaviour changes in the event of a component being overloaded. The values of engineering prestrains for this test was based on the full monotonic stress-strain curve obtained from the Mayes 250 at 180°C (Figure 3.9a). The monotonic yield strain was found to be 0.4% and the UTS strain was 0.96%. Therefore, the chosen prestrains were 0.6%, 1%, 2.5%, 5% and 10%, and the creep stresses ranged from 120-190MPa. Full test parameters can be found in Table 3.3.

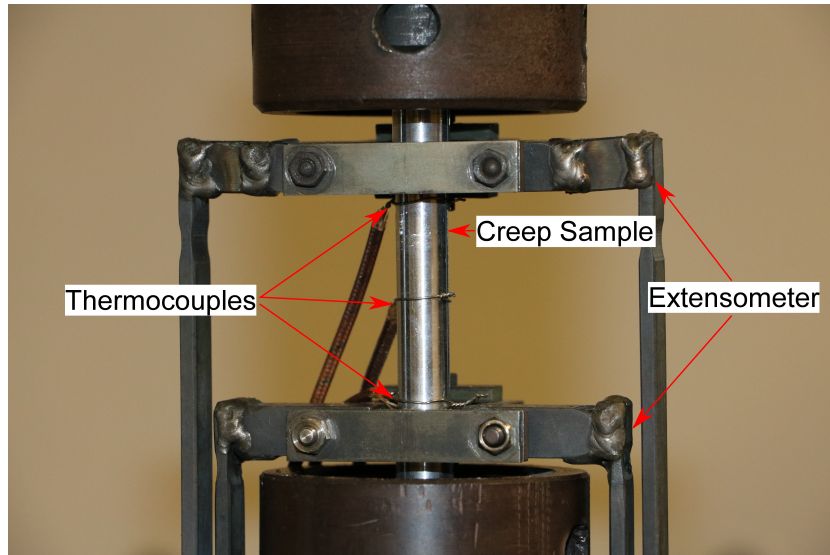


Figure 3.7: A demonstration of the creep test setup. This section would then be encased in a split furnace to be tested at elevated temperatures.

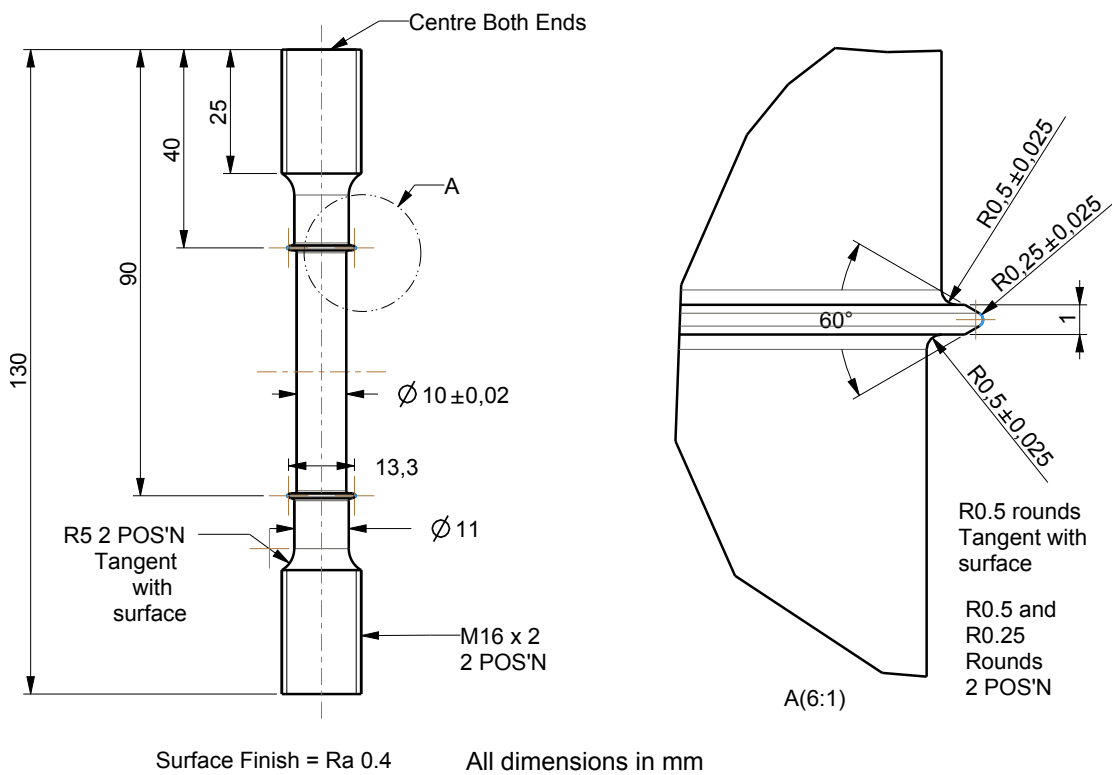


Figure 3.8: Geometry of creep and prestrained creep test specimens.

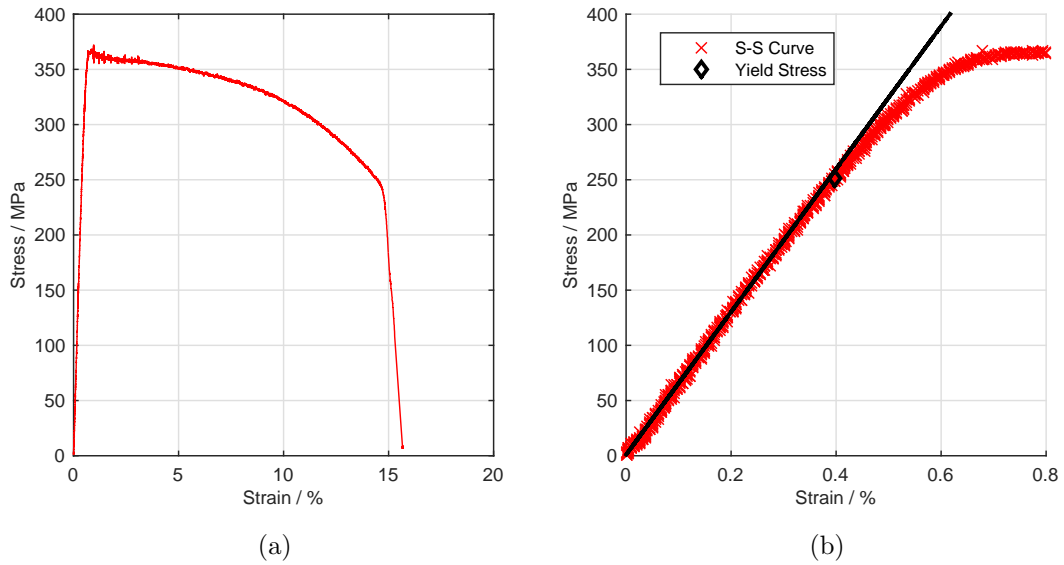


Figure 3.9: (a) Full $\varepsilon - \sigma$ curve at 180°C obtained on the Mayes 250 and (b) a close up of the $\varepsilon - \sigma$ noting the yield stress).

Table 3.3: Test parameters used for prestrained creep tests at 180°C .

Stress (MPa)	Engineering prestrain (%)
120	0.6
	1
	2.5
	5
	10
150	0.6
	1
	2.5
	5
	10
90	0.6
	1
	2.5
	5
	10

Significant necking occurred when samples were prestrained at 5% and 10%. Since it was not possible to measure the minimum cross section while the sample was mounted on the Mayes 250, spare samples also prestrained to 5% and 10% were then removed and

the cross section of these measured instead. The surface of the strained samples were coated with white paint and imaged against a black background as shown in Figure 3.10 using a low resolution microscope. After the image was converted to black and white, the boundary of the neck regions was then traced in MATLAB and used to calculate the diameter (see Figures 3.12 and 3.13). The “height” on the y-axis refers to the height of the boundary that was traced around the necked region (see Figure 3.11). The applied load was adjusted to ensure the correct creep stresses were applied to the samples after the prestrain loading.

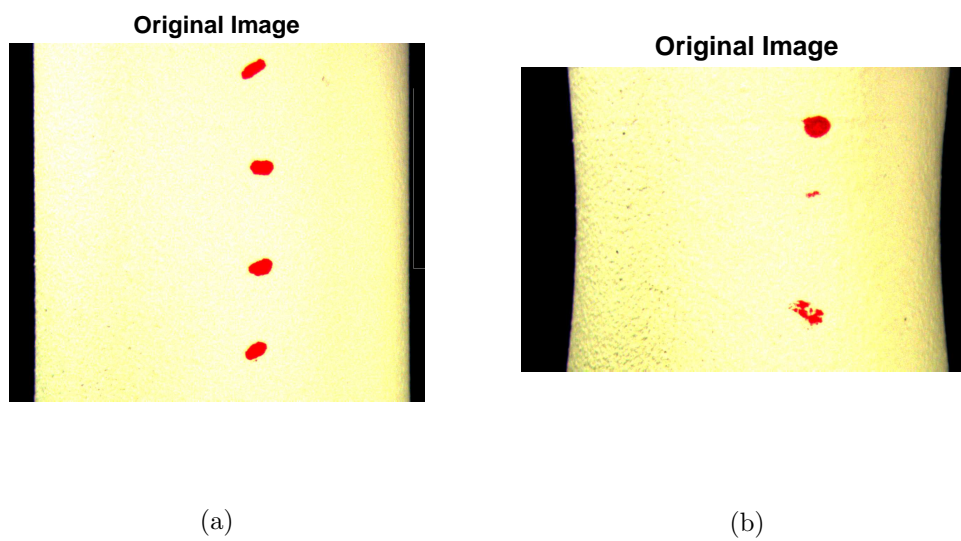


Figure 3.10: (a) The necked region of 5% prestrained sample and (b) Necked region of 10% prestrained sample at 180°C (166 pixels per mm). (The red dots can be ignored).

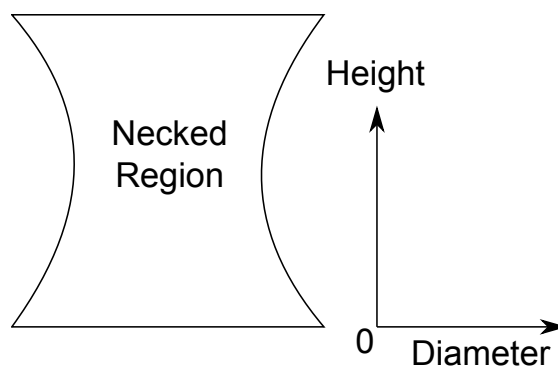


Figure 3.11: A schematic example showing how the definition of height and diameter of the prestrain samples.

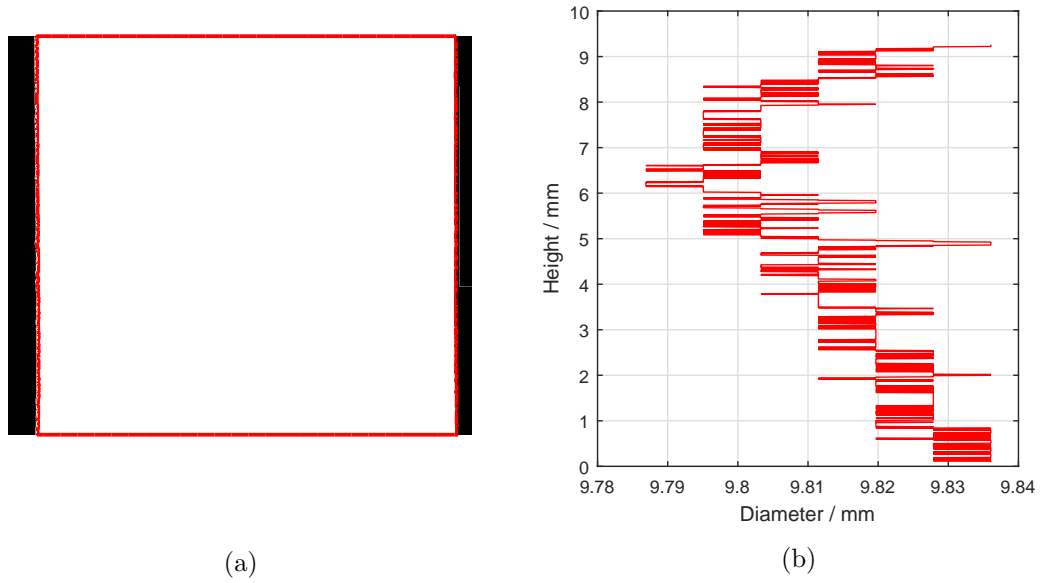


Figure 3.12: (a) The traced boundary of 5% prestrain sample and (b) the measured diameter along the gauge length shown in (a) (166 pixels per mm).

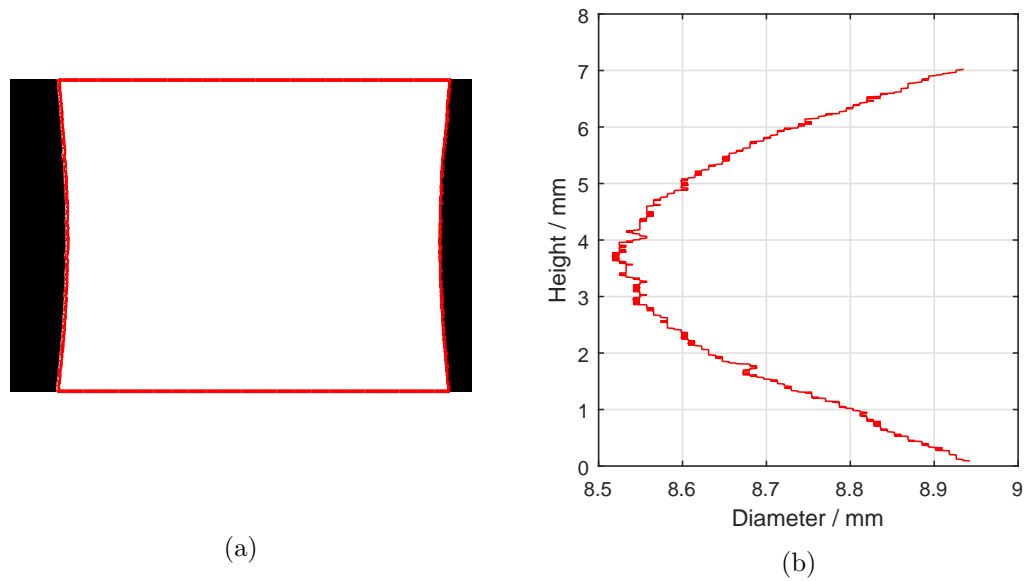


Figure 3.13: (a) The traced boundary of 10% prestrained sample and (b) the measured diameter along the gauge length shown in (a) (166 pixels per mm).

3.6 Fatigue Tests

IF and TMF tests, under both stress and strain control, were conducted on an Instron 8862 TMF thermomechanical fatigue system and heated using a radio-frequency induction furnace. An extensometer was used for sample strain measurement and external forced air cooling was used for anisothermal test conditions. Figure 3.14

shows the specimen geometry. Thermocouples failed to join to the samples for temperature measurement which was most likely due to the insufficient power from the spot welder to locally melt the sample. The thermocouples would often join to the spot welder instead. Therefore, a study was carried out to see whether a pyrometer could be used for non-contact thermal measurements, as discussed in section 3.6.1

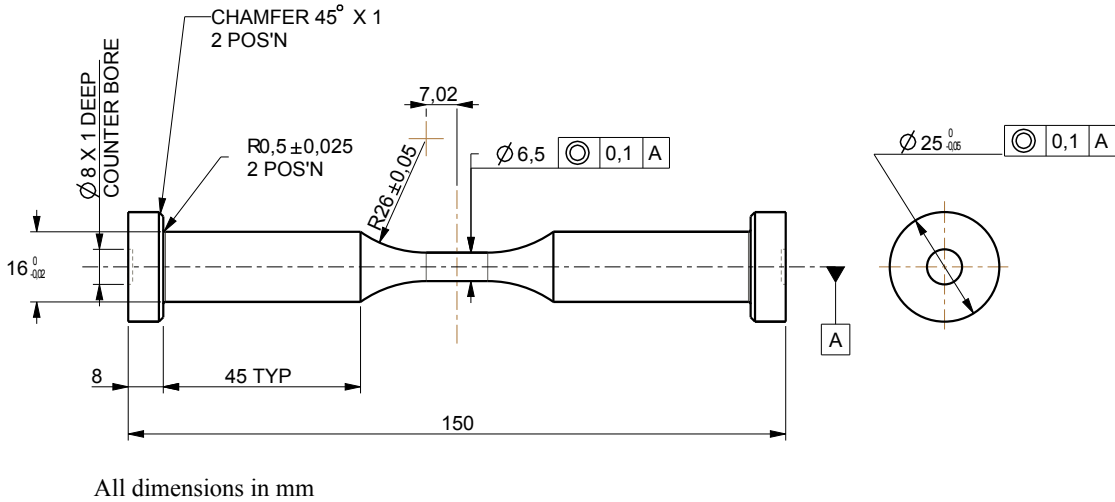


Figure 3.14: Isothermal and thermomechanical fatigue test specimen geometry.

3.6.1 Pyrometer Temperature Measurement Investigation

Emissivity is a measurement of the efficiency with which a surface emits thermal energy in comparison to a perfect black body surface, which has a emissivity value of 1. In order to take accurate temperature measurements, the emissivity of the test specimens must be known. To obtain a consistent emissivity value for each sample, the surface of their gauge sections was abraded parallel to the sample axis using SiC grit papers P2500 and P4000, followed by an application of black stove spray paint from PlastiKote. According to the ISO/FEPA standards, P2500 and P4000 abrasion papers have average particle sizes of 8.4µm and 5µm [199]. To check for emissivity consistency, the gauge sections of 3 fatigue samples were removed and a hole was made using an electrode to a depth about half way down the gauge length for the placement of a thermocouple. These sections were then raised to various temperatures using a heating plate as shown schematically in Figure 3.15. A thermal camera was used to manually set the emissivity value to match the thermocouple reading. Ultimately, an emissivity of 0.88 was determined for this material as shown in Figure 3.16 by the close temperature reading match between the pyrometer and the thermocouple. The CTLF-CF2-C8 high performance pyrometer

shown in Figure 3.17 was used for temperature measurement, has a working distance of 150mm and a 1.9mm diameter spot size and was capable of measuring temperatures from -50°C to 975°C .

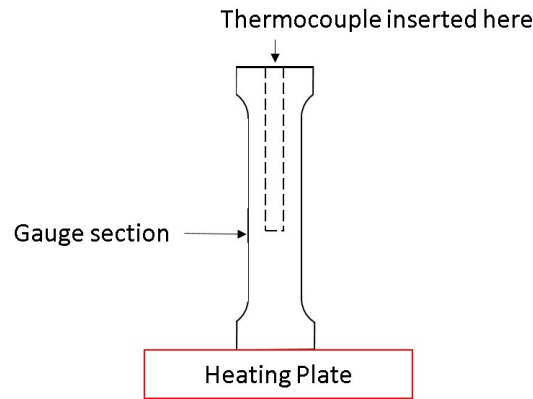


Figure 3.15: A schematic representation of the setup used to obtain the emissivity of a coated sample.

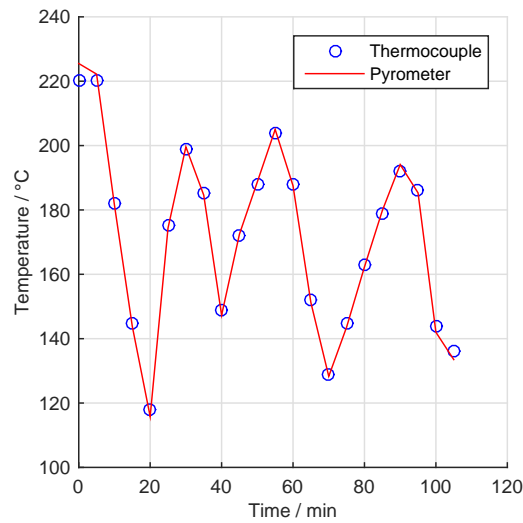


Figure 3.16: The emissivity on the pyrometer was set to 0.88 to match the temperature measured by the thermocouple.

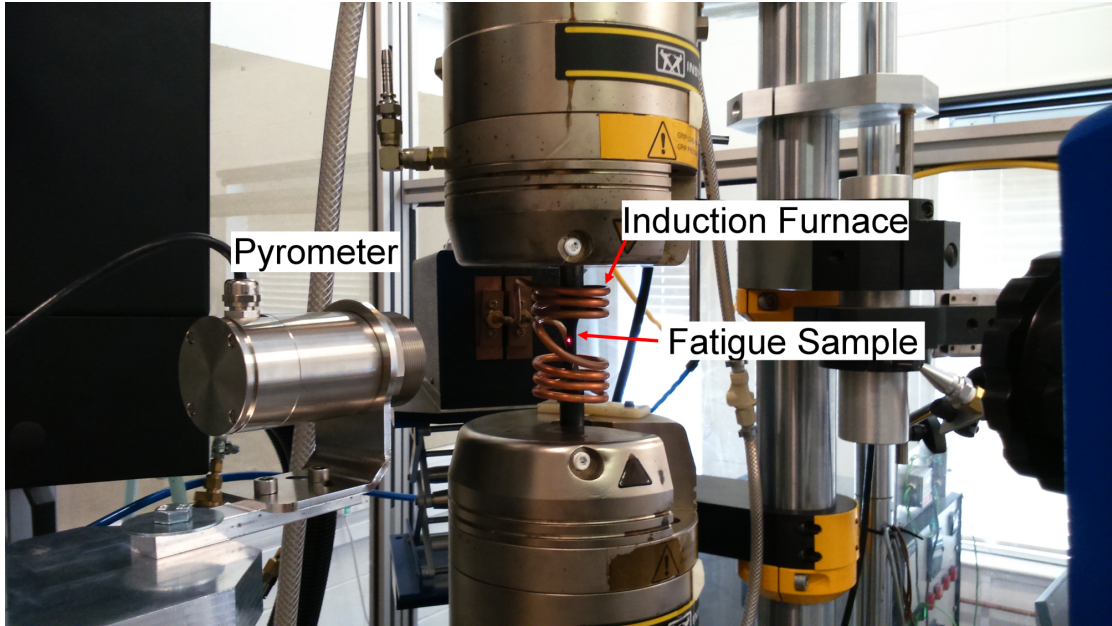


Figure 3.17: Experimental setup used for fatigue testing.

3.6.2 Stress-Controlled Fatigue Tests

Stress-controlled IF and TMF tests were first carried out to determine the initial material behaviour under simulated operating conditions of the SAGB housing. In order to make comparisons between both types of tests, the loading rates must remain the same. The maximum loading rate was controlled by the maximum achievable cooling rate during thermal cycling between 200°C to 120°C for TMF tests. Table 3.4 shows the IF test parameters.

Table 3.4: Stress-controlled isothermal fatigue test matrix.

Temperature (°)	σ_{max} (MPa)	R-ratio	Frequency (Hz)
160	190	0.25	0.01
200	120, 190		

TMF tests were carried out either in-phase or completely out-of-phase and the minimum temperature was set to 120°C. Table 3.5 shows the test parameters used for TMF testing. The same waveform and stress range was implemented as the isothermal fatigue tests.

According to BS ISO 12111-2011, the maximum allowable indicated temperature variation over the gauge section is $\pm 10^\circ\text{C}$ axially. Thermal calibration of the induction furnace was carried out with the aid of the SC7500M FLIR IR camera. A sample

Table 3.5: Stress-controlled thermomechanical fatigue test matrix.

Temperature Range (°C)	Phase (°)	R-ratio	Frequency (Hz)	σ_{max} (MPa)
120-160	IP	0.25	0.01	190
120-160	OP			
120-200	IP			
120-200	OP			

was raised to static temperatures of 100°C, 150°C and 200°C, and the gauge section temperature was measured with the thermal camera. The red line in Figure 3.18a shows where the temperature measurements were taken starting from pixel height 194 to 329 (full image size = 640x512px). Thereafter, the same sample was thermally cycled between 120-160°C and 120-200°C. For both cases, the temperature remained between $\pm 10^\circ\text{C}$ of the target temperature across the sample gauge section. It was also found that the maximum frequency to produce a stable thermal cycle was 0.01Hz. Figures 3.18 and 3.19 show the measured temperature under constant and dynamic heating conditions respectively.

To protect the extensometer, an upper and lower strain limit of $\pm 3\%$ was set. This was to prevent complete fracture of the sample which could cause the extensometer to fall. Once this strain level was met, the test was terminated and it assumed that the sample was going to fracture had the test continued.

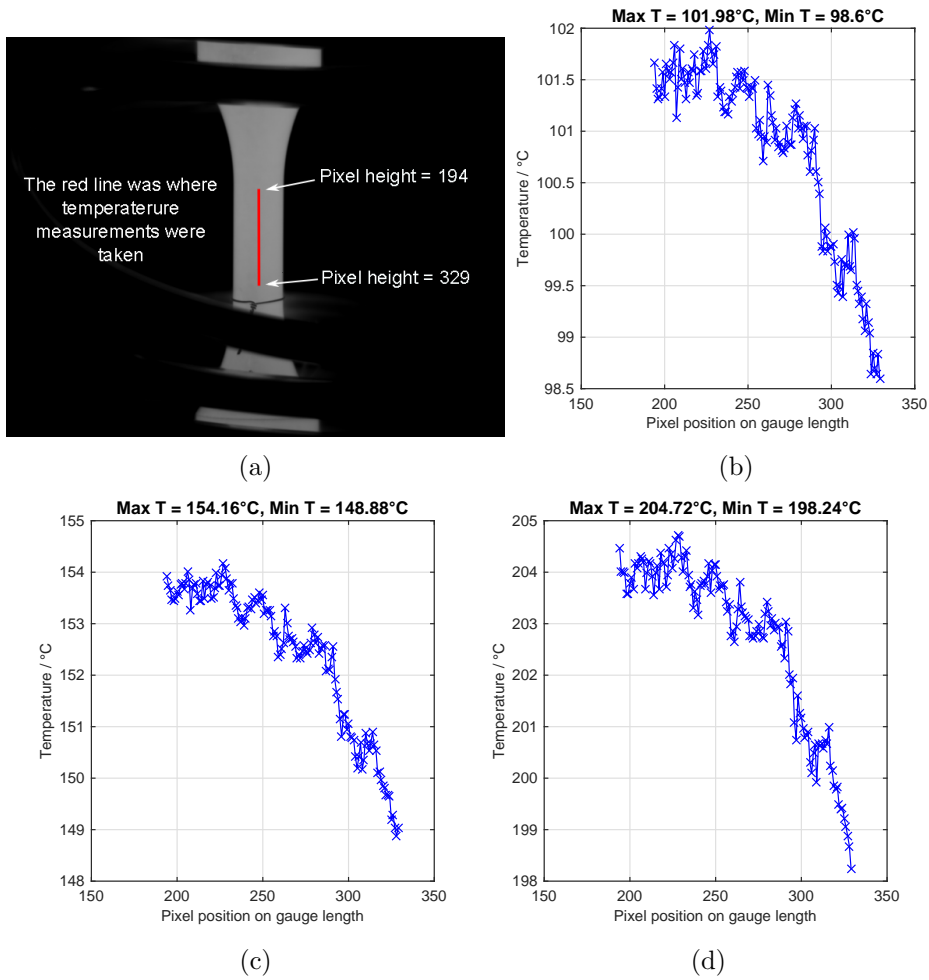


Figure 3.18: An image showing the heated sample and where temperature measurements were taken (a) and the recorded static temperature measurements at (b) 100°C, (c) 150°C and (d) 200°C.

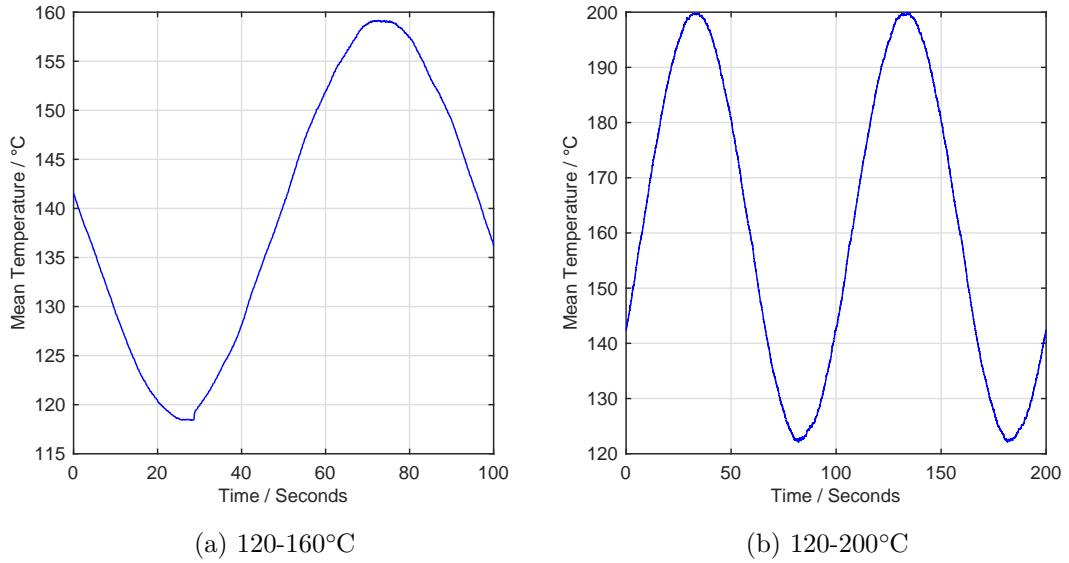


Figure 3.19: The measured dynamic temperature along the gauge length between (a) 120-160°C and (b) 120-200°C.

3.6.3 Isothermal Fatigue Tests with Decaying Strain Amplitude

In order to predict the material's stress response during isothermal thermal fatigue at elevated temperatures, it was useful to understand the material's stress response and its hardening and creep behaviours, as well as account for the material's change in strength as a function of time at temperature. The Chaboche model was chosen for the purpose of this work, which utilises temperature-dependent material parameters for stress-strain prediction. These parameters are a function of plastic strain and are estimated from experimental data. Therefore, plastic strain in the test specimens must be induced per cycle.

It was demonstrated in the tensile tests that the yield stress of the material initially decreases rapidly with time at temperature. This suggested that large amounts of plastic strain would be accumulated during a constant amplitude isothermal fatigue test at 200°C, due to the decreasing yield stress. Failure of the sample would occur rapidly and insufficient material data may be acquired to accurately predict the material behaviour. Therefore, a method was designed to induced appreciable plasticity per cycle while remaining below the material's UTS to avoid failure.

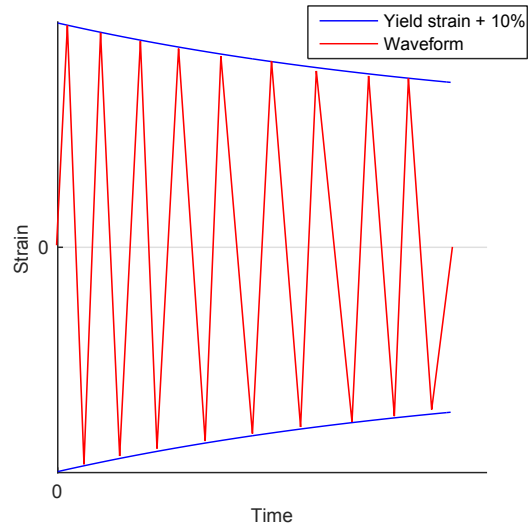


Figure 3.20: Ideal fully reversed load profile for the strain-controlled tests.

A relationship that describes the sample's monotonic yield strength and time at temperature was first established which was obtained from tensile data. This allowed a novel triangular waveform of decreasing amplitude to be created for fully reversed ($R_\sigma=-1$) fatigue tests, where the maximum allowable strain at any time was +10% greater than the sample's monotonic yield strain as shown in Figure 3.20.

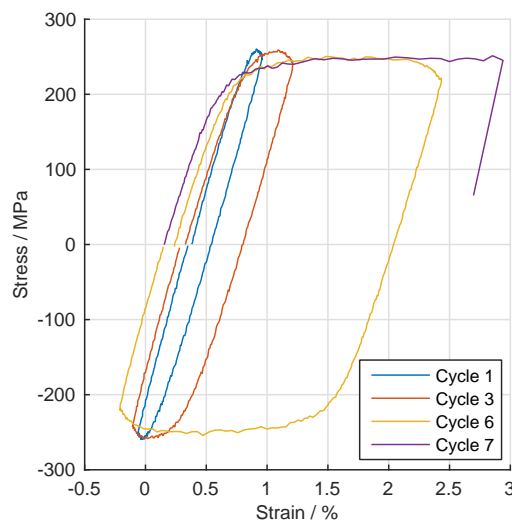


Figure 3.21: A demonstration of the initial result of stress-controlled isothermal fatigue with decreasing stress amplitude.

Initially, these tests were carried out under load controlled but the results showed that due to the lack of work hardening, the test machine struggled to meet the maximum and minimum target load and excessively strained the sample in the process. This

behaviour is demonstrated in Figure 3.21.

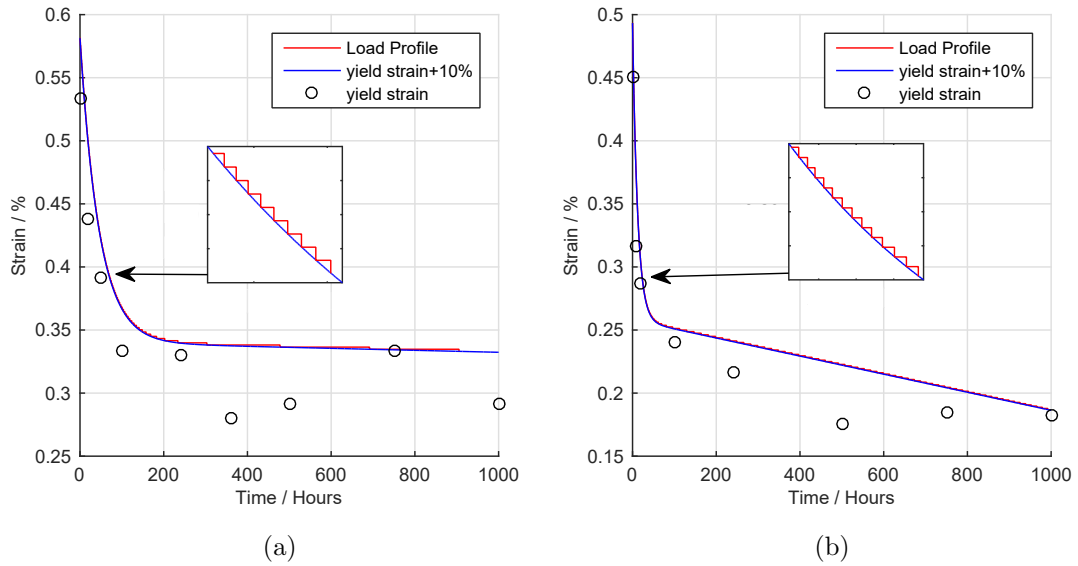


Figure 3.22: The load profile at (a) 160°C and (b) 200°C. The red stepped line represents the duration at a certain amplitude before stepping down.

Due to the restrictions of the Instron’s software, simulating a smooth decreasing strain amplitude was not possible. Instead, multiple “test blocks” of constant strain amplitude were programmed, where the strain amplitude of each successive test block was lower than the previous one. The termination of a test block occurred when the applied strain was +0.5% greater than the desired strain profile. For example, the blue line in Figure 3.22a represents the ideal test maximum strain amplitude for the 160°C isothermal strain-controlled fatigue test, which is +10% greater than the monotonic yield strain at 160°C. The red “stepped” line represents the test blocks of constant strain amplitude which show the magnitude of the strain amplitude and the time at which the test block begin and finish.

To make comparisons with the stress-controlled fatigue data with a positive R-ratio ($R_\sigma=0.25$), the loading rate was kept constant to avoid strain-rate effects on material behaviour by varying the frequency of the waveform as the strain amplitude decreased.

Samples were soaked at 160°C and 200°C for 0 hours, 75 hours, 100 hours or 400 hours. The sample name designations indicate the soak temperature (“160°C” or “200°C”) and soak time in hours (“0h”, “75h”, “100h” or “400h”). The samples were tested under fully reversed isothermal strain-controlled fatigue conditions at 160°C and 200°C. A summary of test conditions for each sample can found in Table 3.6.

Table 3.6: Strain-controlled isothermal fatigue test matrix

Sample ID	Soak time (Hours)	Test and Soak Temperature (°C)	Frequency (Hz)	Strain-ratio R_ϵ
160°C-0h	0	160	Variable	-1
160°C-100h	100			
160°C-400h	400			
200°C-0h	0	200		
200°C-75h	75			
200°C-400h	400			

To avoid problems with a changing mean strain level between the changes in strain amplitude, the mean strain was set to 0% in the control software. As a result, the controller would force the sample to 0% strain at the beginning of each cycle. To achieve this, the extensometer was placed on the sample and the strain reading on the extensometer was reset to 0% after the sample had reached test temperature. However, the original distance between the extensometer arms at 0% was used to calculate the change in strain, rather than the new distance between the arms caused by the thermal expansion of the sample. Therefore, to reduce the error in the strain measurement, the extensometer was placed on the samples to give a reading of -0.37% or -0.47% before heating the sample to 160°C or 200°C respectively. After the thermal expansion, this brought the extensometer reading close 0% before it was reset to 0%. The extensometer was recalibrated before each test.

3.6.4 Stress Relaxation Tests

Stress relaxation tests were carried out to obtain the viscous stress parameters that describes the creep behaviour of the material. The samples were either as-received or soaked at 160°C or 200°C for 75 hours or 400 hours. The samples were strained to +10% above their monotonic yield strain corresponding to the strain profile previously obtained for the strain-controlled fatigue tests (Figure 3.22) at a rate of $5\text{E-}03\%.\text{s}^{-1}$ and crept for 2 hours as shown in Figure 3.23a. The sample's geometry was identical to the creep sample as shown in Figure 3.8 and the tests were carried out on the Mayes 250. The duration for the sample temperature to become uniform before testing was 80 minutes.

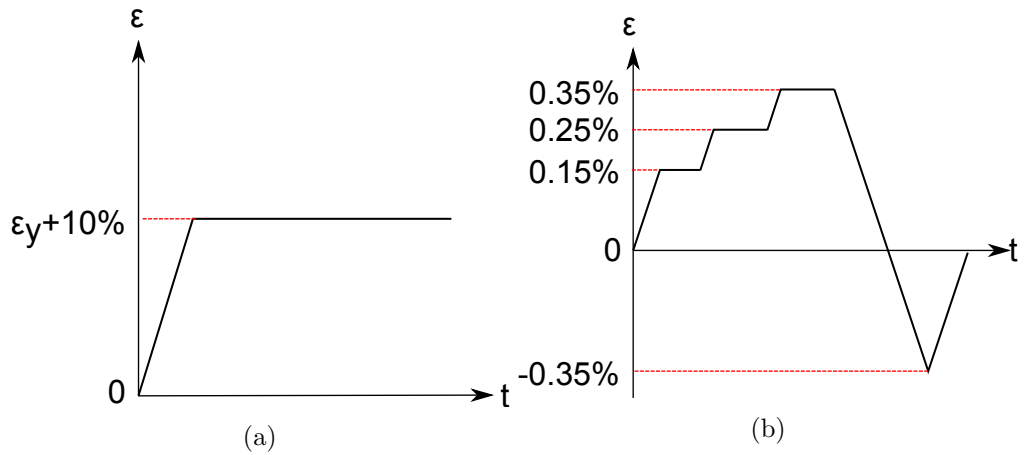


Figure 3.23: The strain profile used for (a) static stress relaxation tests and (b) cyclic stress relaxation tests.

Fully reversed stress relaxation tests were carried on the Instron 8862, as shown in Figure 3.24, using samples soaked 75 hours at 200°C prior to testing. Each test cycle had a 1 hour dwell period at 0.15%, followed by two dwells periods each for 2 hours at 0.25% and 0.35%. The ramping rate in between dwell periods was $5\text{E-}03\%.\text{s}^{-1}$. Afterwards, the samples were fully reversed to -0.35% (see Figure 3.23b). The sample geometry for this type of test is shown in Figure 3.14.

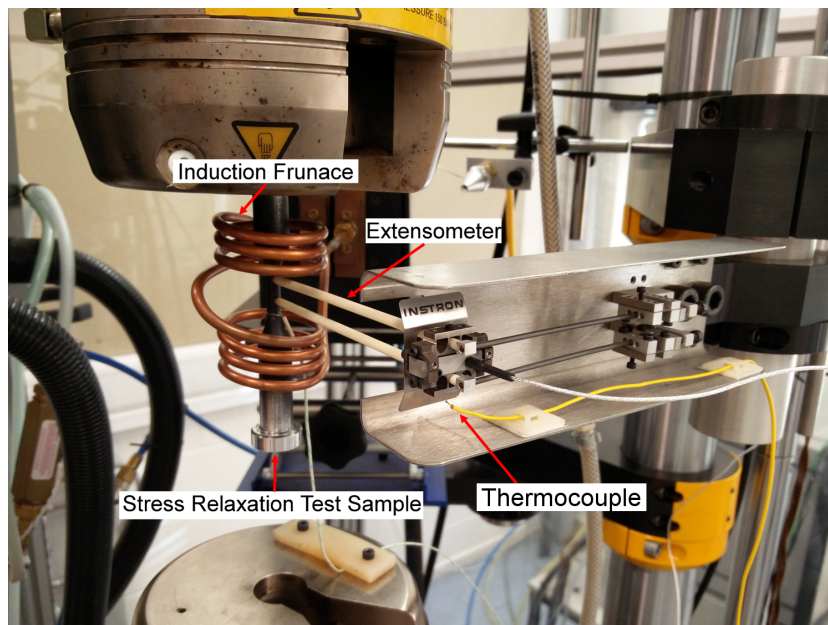


Figure 3.24: The experimental setup of the cyclic stress relaxation tests before the sample was fully mounted.

Adjustments had to be made to the testing environment for the fully reversed stress relaxation tests. Drops in the stress level during the dwell periods occurred which did

not reflect material behaviour and had to be corrected. For more details regarding this test method, refer the appendix.

4 Material Characterisation

4.1 Hardness Discrepancy Check of the 7175-T7351 Plate

Hardness tests were conducted on the top surface along the length and width of the plate at locations 0-4 and A-D as shown in Figure 3.1 in section 3.1. Figure 4.1 shows the Vickers hardness along the width and length of the plate. The variation in hardness at these locations on the plate was not significant, where the range of mean values lied between 150HV_{10} and 156HV_{10} .

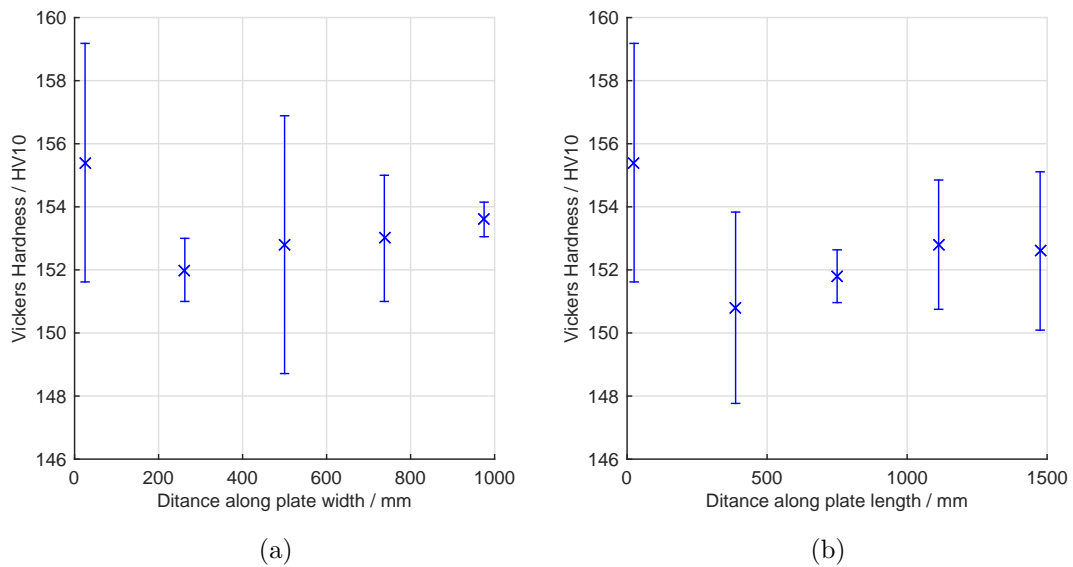


Figure 4.1: Hardness measurements on the rolling plane of various locations along the (a) width and (b) length of the 7175-T7351 plate.

The micro-Vickers hardness readings throughout the depth of the plate at locations 0 and 2 (the edge and middle of the plate) are displayed in Figure 4.2 shows that the overall mean hardness and standard deviation did not vary significantly between the two sections of the plate, and the hardness readings shown in Figure 4.1 lie within the scatter of the depth hardness. It was therefore valid to assume that there was no obvious discrepancy in strength along the length, width and depth of the plate that would affect the subsequent mechanical testing results.

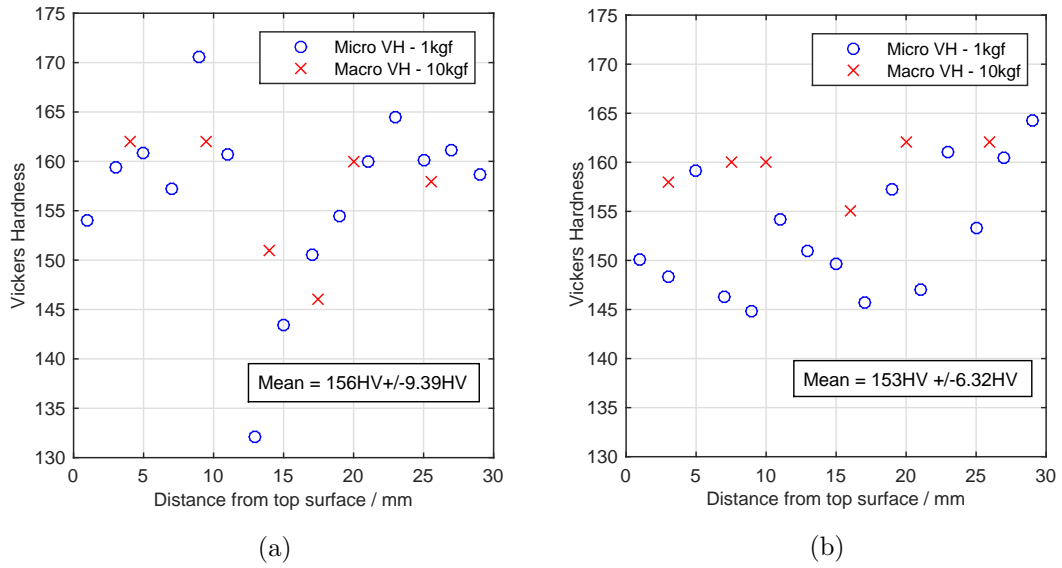


Figure 4.2: Hardness depth profiles of (a) section 0 and (b) section 2 using macro and micro Vickers hardness measurements showing the mean and standard deviation of the micro-Vickers measurements.

4.2 Hardness of the Plate After Time at Various Temperatures

A requirement for tensile testing was to expose the samples up to 1000 hours at a range of elevated temperatures before testing. However, this did not provide insight into how the aluminium alloy evolves with time at temperature. Therefore, room temperature hardness measurements were obtained from samples that were soaked between 0-1000 hours at temperatures ranging between 120°C and 230°C.

It was found that the hardness was homogeneous between each plane (as described in Figure 3.4 in section 3.3.2) for each soak temperature, as demonstrated in Figure 4.3. Therefore, the hardness measurements from transverse plane was used to represent the plate and used for comparative purposes.

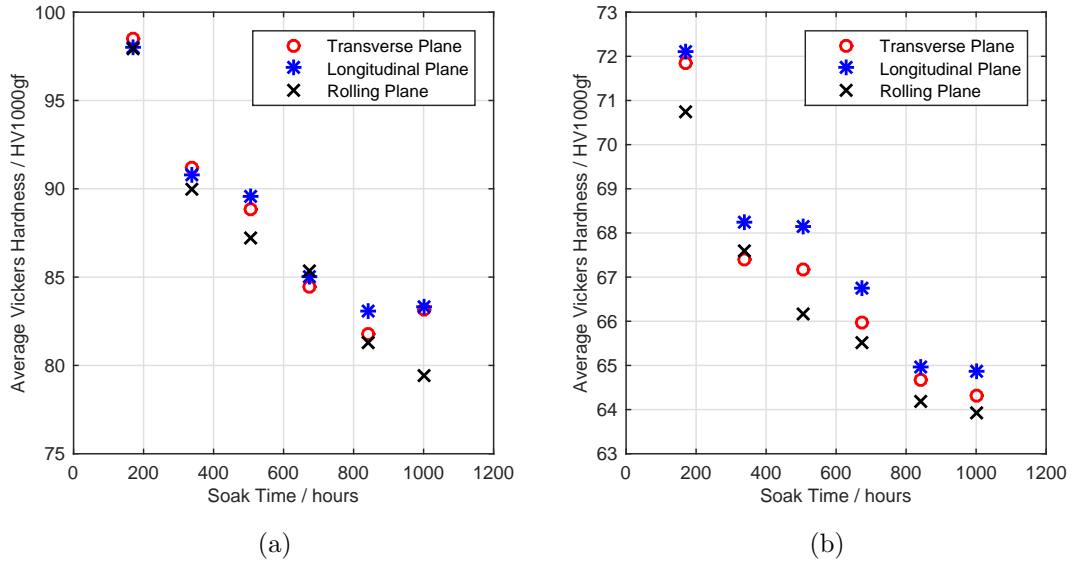


Figure 4.3: The hardness readings of all 3 planes of the samples up to 1000 hours of exposure at (a) 180°C and (b) 230°C.

The initial room temperature hardness ranged between 156HV₁₀ and 160HV₁₀. It can be observed in Figure 4.4 that the rate of decrease in hardness was greater at higher soak temperature. Figure 4.4a shows the hardness on the transverse plane up to 24 hours of soaking at each temperature. The decrease in hardness at 24 hours at 200°C and 230°C was 34% and 48% respectively, which indicates that the reduction in material yield strength is initially rapid. At 120°C, the alloy retained its initial hardness, indicating that the microstructure of the alloy was stable at this temperature. Figure 4.4b shows the change in hardness readings after an extended period of time at elevated temperatures. Up to 1000 hours, the hardness reached an asymptotic value which is dependent on the soak temperature. The asymptotic values, from lowest to highest soak temperatures, are 154HV₁₀, 102HV₁₀, 83HV₁₀, 70HV₁₀ and 64HV₁₀ (3%, 36%, 48%, 56% and 60% decrease from the initial hardness value for each temperature). This suggests that the rate of change in material strength greatly reduced as time at temperature increased.

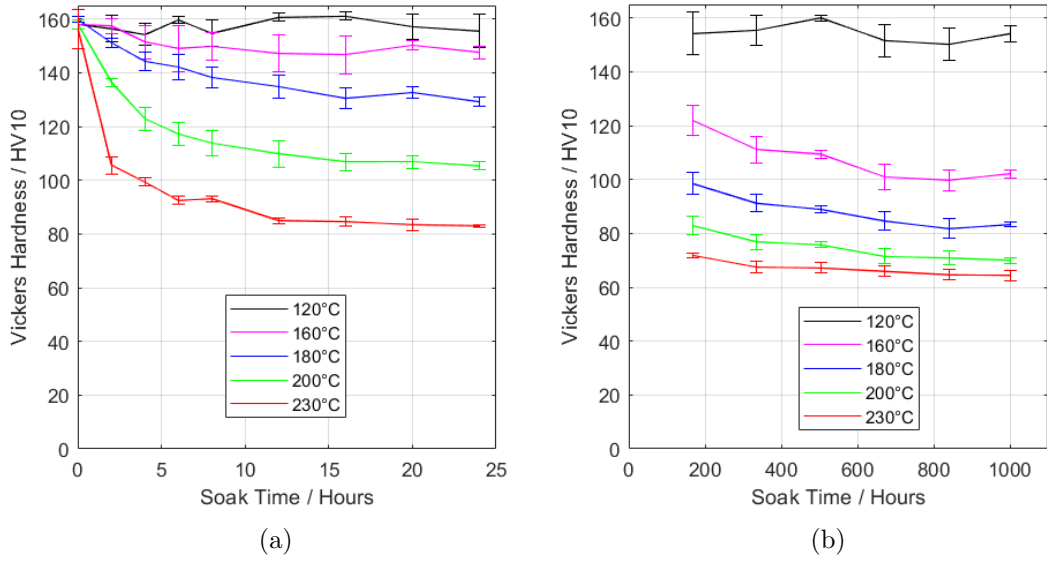


Figure 4.4: The room temperature Vickers hardness after exposure to various temperatures up to (a) 24 hours and (b) from 168 hours up to 1000 hours.

4.3 Tensile Test Results

Figure 4.5 shows the yield stress and UTS of 5 as-received samples tested at room temperature and 230°C. Referring to the directions names chosen for the plate in Figure 3.4, the gauge length of the samples were either parallel (“Longitudinal”) or perpendicular (“Long Transverse”) to the rolling direction. It can be seen that the tensile properties are similar in both directions at both temperatures.

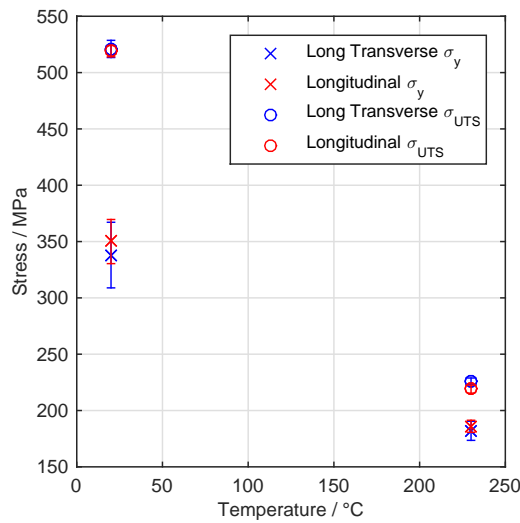
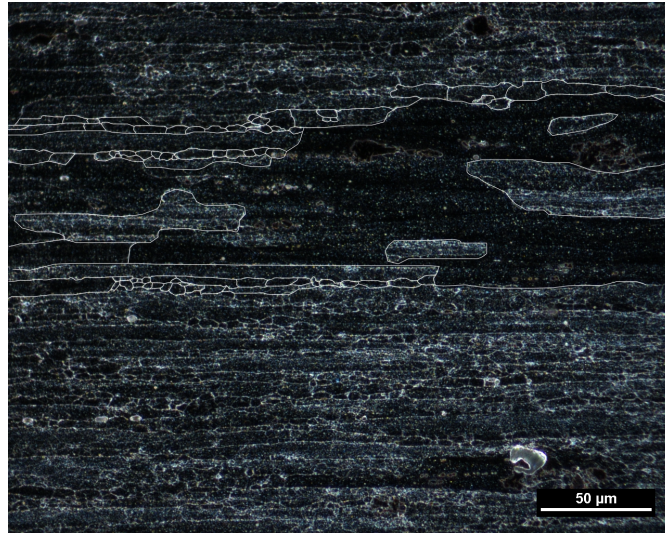
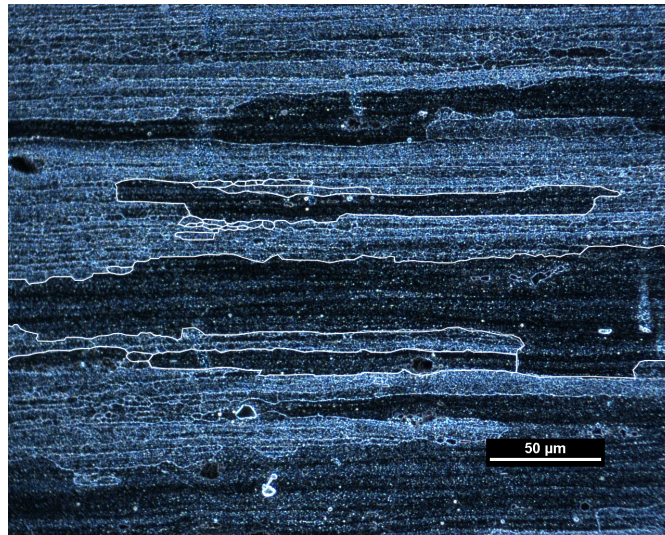


Figure 4.5: A comparison of 7175-T7351 mechanical properties in the longitudinal and long transverse directions at room temperature and 230°C.



(a)



(b)

Figure 4.6: The microstructure of the 7175-T7351 plate revealed by a chemical etchant (5ml HF, 20ml HCl, 20ml HNO₃, 60ml H₂O) - (a) dark field image parallel to the rolling direction and (b) dark field image perpendicular to rolling direction (some grains are outlined in white).

Figure 4.6 shows the microstructure in the longitudinal (Figure 4.6a) and transverse (Figure 4.6b) planes of the as-received material. It can be seen that the grain size and arrangement are very similar which would explain the similarities in mechanical properties. In both figures a large variation in grain size is shown, ranging from small grains, approximately $3.42\mu\text{m}^2$, to coarse grains, approximately $14960\mu\text{m}^2$. The 7175 plate was hot-rolled, specifying that the material was raised above the its recrystallisation temperature before it was mechanically deformed. This would have allowed for grain growth and recrystallisation to occur before the elongation and

alignment of the grains caused by the rolling process. The black particles that can be seen are distributed throughout the plate and are aligned in the rolling direction. Figure 4.7 shows a backscatter image of one of those black particles and where an EDX spectrum was acquired. The EDX analysis shown in Table 4.1 identified the composition of the particle as being high in aluminium, iron and copper. These intermetallic particles have been found to be detrimental to the fracture toughness of the material.

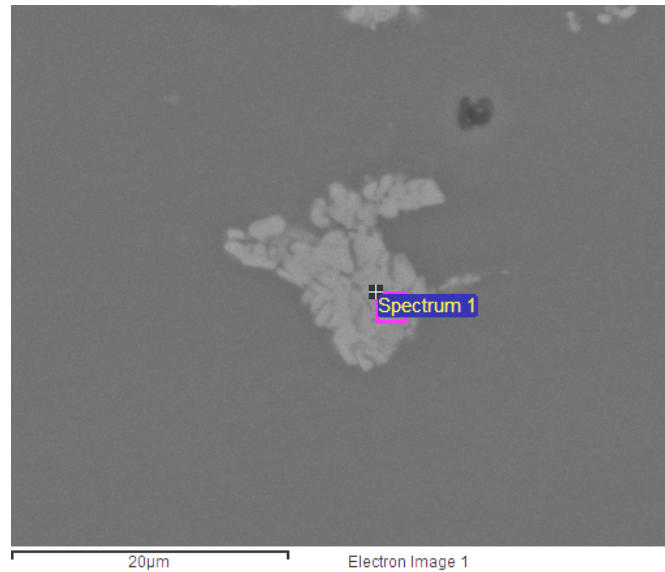


Figure 4.7: A back-scatter electron image of a Al-Cu-Fe rich particle on the longitudinal plane.

Table 4.1: EDX analysis results of the spectrum acquired in Figure 4.7.

Element	weight %
O	1.47
Mg	0.69
Al	54.43
Si	0.33
Cr	0.76
Fe	11.73
Ni	0.76
Cu	27.93
Zn	1.9
Total	100

Figure 4.8 shows tensile properties of the as-received material at elevated temperatures up to 230°C. At 120°C, the yield stress was unaffected by temperature

this (similar to the unchanged room temperature hardness readings observed after soaking at 120°C, validating that the microstructure is thermally stable), but the UTS decreased by 20.15%, demonstrating a reduction in material hardening. As test temperature rose significantly above 120°C, the yield stress and UTS decreased. At 200°C and 230°C, the yield stress dropped by 31.36% and 46.15% respectively.

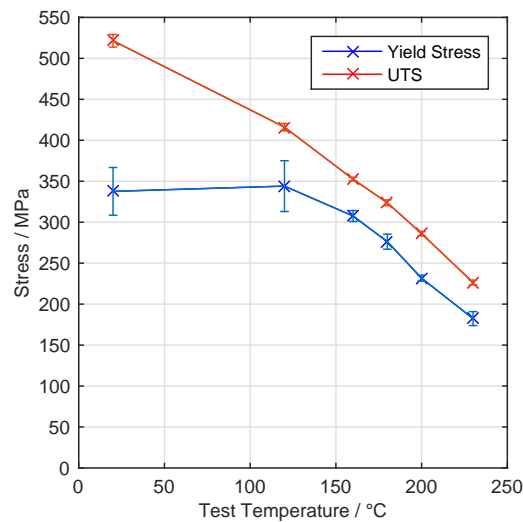


Figure 4.8: The mechanical properties of the 7175-T7351 at elevated temperatures.

Figure 4.9a shows the tensile properties of the samples that were soaked at temperatures ranging from 120°C to 230°C for 1000 hours before being tested at room temperature. Compared to the as-received material, the material yield stress at 120°C soak remained virtually unchanged, but a permanent decrease in both yield and UTS can be seen at higher soak temperatures. Both observations correlate to those from the hardness test data. Figure 4.9b shows that when samples were tested at the respective soak temperature, the yield stress and UTS had decreased significantly. Referring back to the loading conditions of the gearbox housing (see Figure 1.5a), this shows that the strength of the material would eventually decrease below the maximum operating stress of 190MPa.

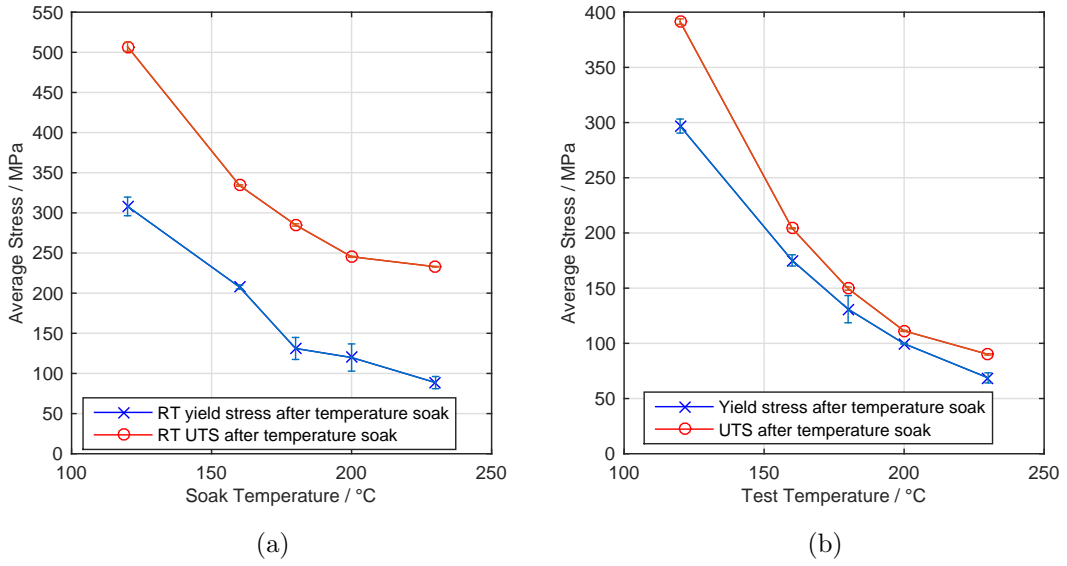


Figure 4.9: The average yield stress and UTS of the 7175-T7351 at (a) room temperature and (b) elevated temperatures after temperature soak for 1000 hours. The soak temperature in part b was the same as the test temperature.

Figure 4.10 are EBSD images that show the grains of the 7175-T7351 plate in the as-received condition and after it had been soaked for 1000 hours at 120°C, 180°C and 230°C. Despite the duration and soak temperature, the grain structure remains similar to the dark field images shown in Figure 4.6, suggesting that the change in strength was correlated to the change in size and or spacing of the precipitates. More details regarding this will be covered in section 5.

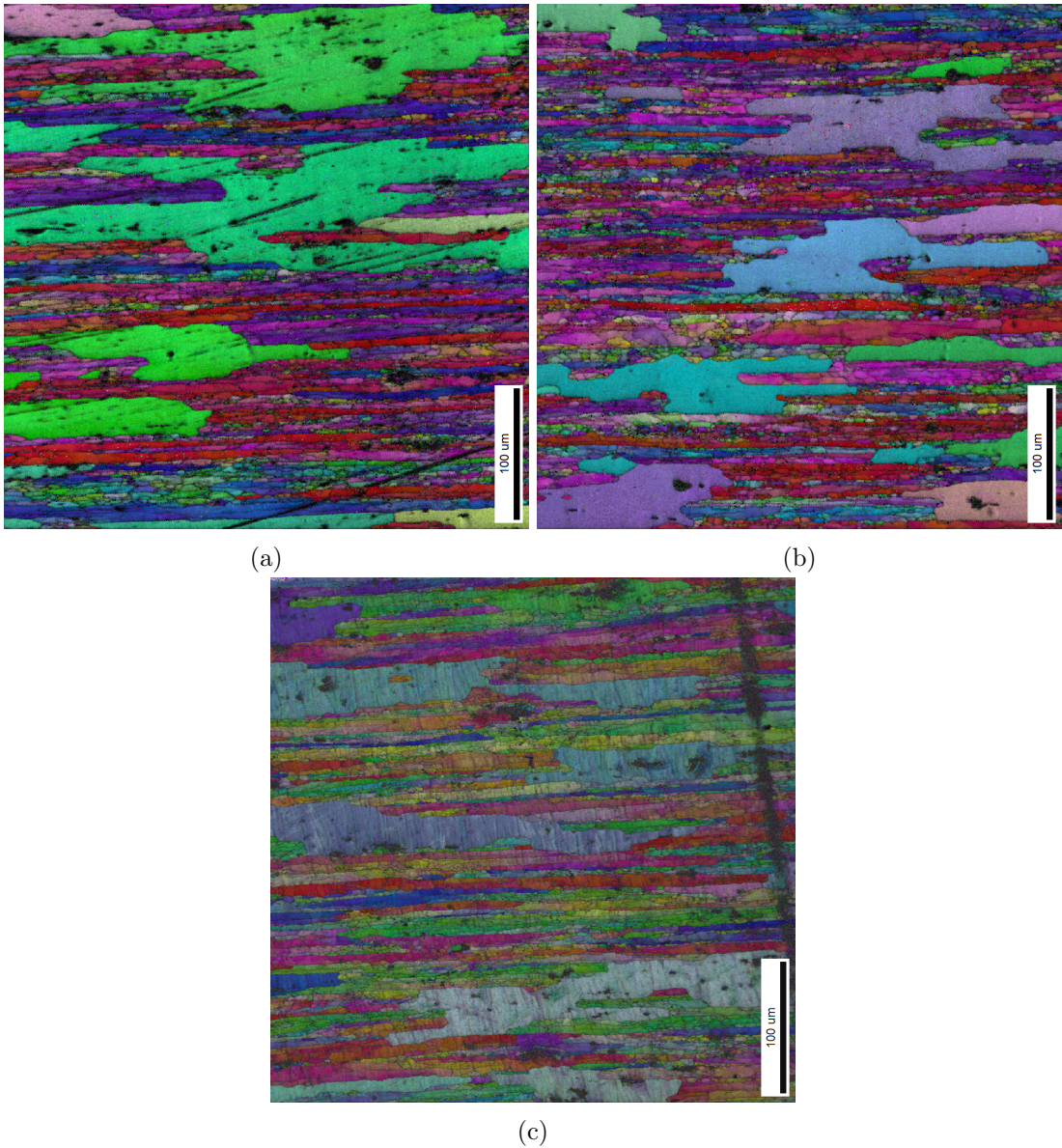


Figure 4.10: EBSD images of the 7175-T7351 microstructure of (a) the as-received and the material after 1000 hours soak at (b) 120°C and (c) 230°C.

The yield stress of the material was studied more closely after it was soaked at 160°C and 200°C for up to 1000 hours. Figure 4.11 shows that the rate of decrease in yield stress was much greater at 200°C than 160°C. For example, after 20 hours of soaking at 200°C the yield stress decreased by 29%, whereas at 160°C the decrease was only 8%.

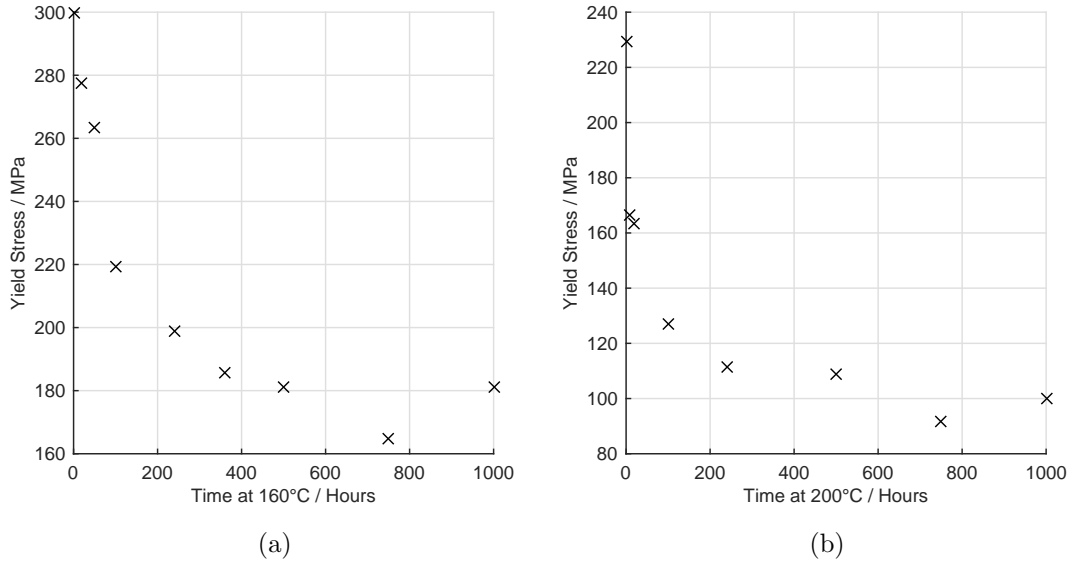


Figure 4.11: The yield stress after soaking at (a) 160°C and (b) 200°C.

4.3.1 Definition of a Relationship Between Time at Temperature and Yield Strain

For the fatigue test data obtained for chapter 6, an expression that described the yield strain as a function of time was required for the 7175-T7351 alloy at 160°C and 200°C (where samples were loaded at a rate of $1\text{mm}\cdot\text{s}^{-1}$) to design a novel loading waveform. The data presented in Figure 4.12 shows the monotonic yield strain at 160°C and 200°C after periods of soaking at those temperatures. The fitted curve in the graphs, determined by equation 4.1, was used to assume the monotonic yield strain of the alloy after spending t hours at temperature.

$$\varepsilon_y(t) = \varepsilon_{y0} + A(1 - \exp(-Bt)) + Dt \quad (4.1)$$

ε_{y0} is the initial yield strain and A , B and D are fitting constants used to describe the rate of decrease of yield strain. An initial estimate of the constants obtained from MATLAB's curve fitting function was used to find an optimal set of constants that provided a better fit to the experimental data using a non-linear least squares method. Table 4.2 shows the numerical values for the material constants at 160°C and 200°C. The magnitude of the maximum strain during the fully reversed fatigue test was $\varepsilon_y + 10\%$ (for example, strain was consistently around 10% above the monotonic age-dependent yield point).

Table 4.2: The constants obtained to describe the yield stress of the material after temperature soak at 160°C or 200°C.

Constants	ε_{y0}	A	B	D
160°C	0.5285	-0.2193	0.0218	-7.12E-06
200°C	0.4485	-0.2139	0.0828	-6.51E-05

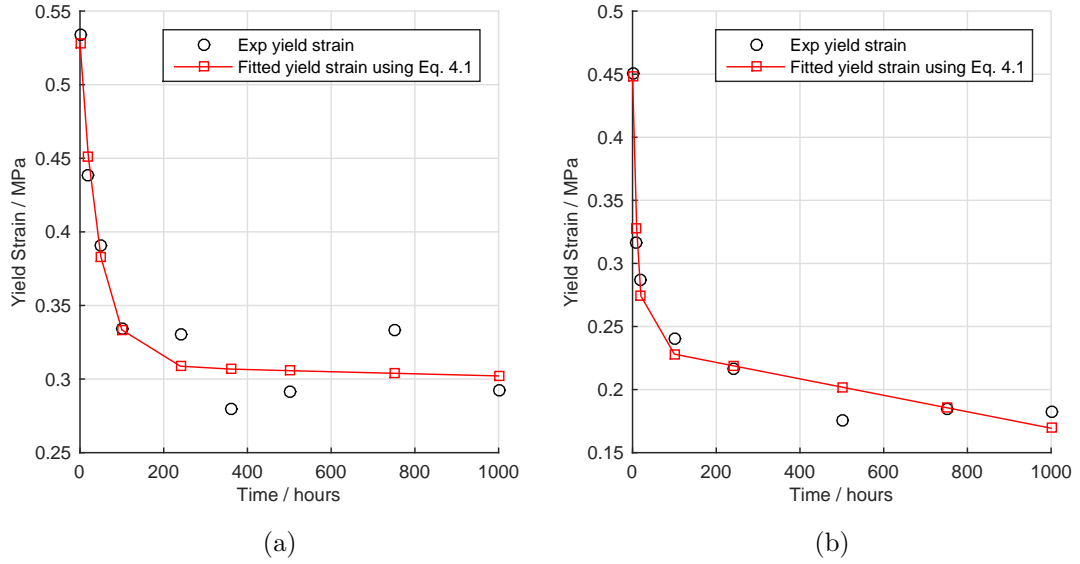


Figure 4.12: Yield strain vs time at (a) 160°C and (b) 200°C.

4.4 Creep Test Results

The creep test results of the as-received material are demonstrated in Figure 4.13 below.

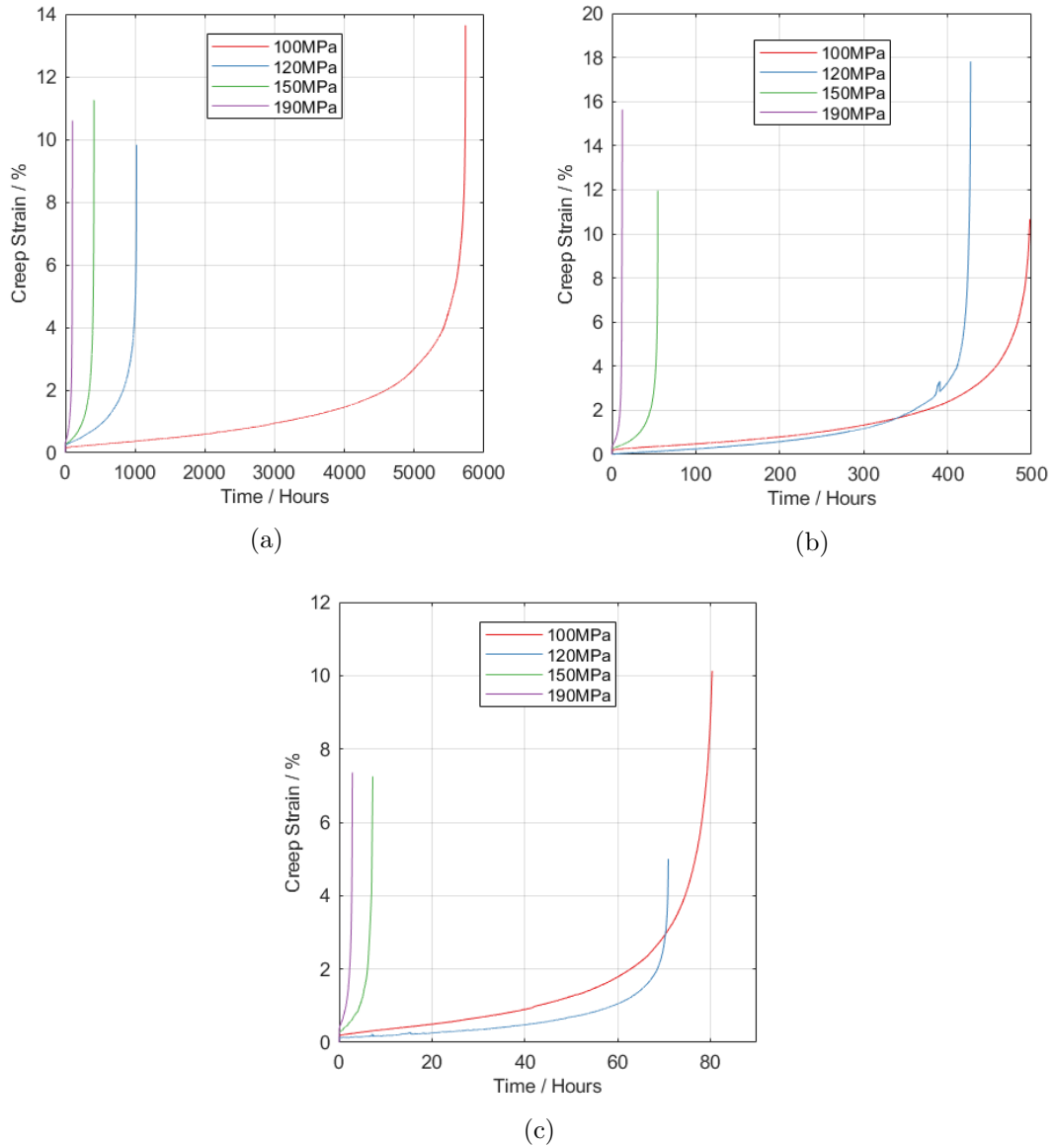


Figure 4.13: Creep test results at (a)160°C, (b)180°C and (c) 200°C.

By taking the natural log of the secondary creep rate and applied stress and fitting a linear line to the data (see Figure 4.14), the constants A and n for Norton's creep law can be obtained. Table 4.3 shows that the stress exponent, n , did not vary greatly between each temperature, suggesting that the creep mechanism did not change for each test condition.

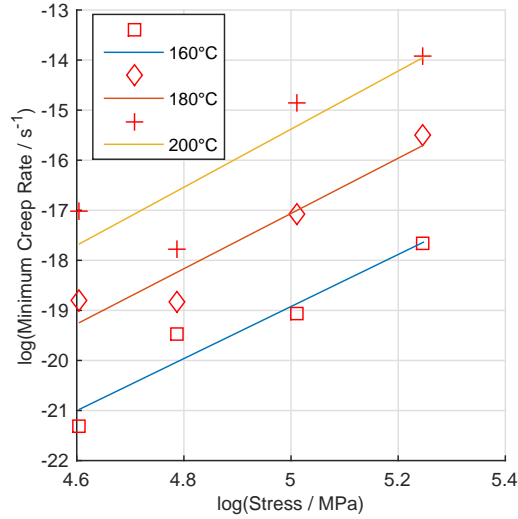


Figure 4.14: The natural log of applied stress plotted against the natural log of the secondary creep rate for each temperature.

Table 4.3: Norton creep power law constants at 160°C, 180°C and 200°C.

Temperature (°C)	160	180	200
n	5.20	5.52	5.80
A (MPa ^{1/n} .s ⁻¹)	3.11E-20	4.05E-20	5.25E-20

Table 4.4: A comparison between the experimental and predicted minimum creep rate at 160°C.

Stress (MPa)	100	120	150	190
Experimental min creep rate (s ⁻¹)	7.81E-10	2.02E-09	6.43E-09	2.20E-08
Predicted min creep rate (s ⁻¹)	5.61E-10	3.50E-09	5.26E-09	2.11E-08

Table 4.5: A comparison between the experimental and predicted minimum creep rate at 180°C.

Stress (MPa)	100	120	150	190
Experimental min creep rate (s ⁻¹)	4.44E-09	1.21E-08	4.16E-08	1.54E-07
Predicted min creep rate (s ⁻¹)	6.93E-09	6.57E-09	3.87E-08	1.87E-07

Tables 4.4 to 4.6 compares the experimental and estimate minimum creep rates using the obtained power law constants. It can be seen that the predicted results can accurately predict the experimental minimum creep rate.

Table 4.6: A comparison between the experimental and predicted minimum creep rate at 200°C.

Stress (MPa)	100	120	150	190
Experimental min creep rate (s^{-1})	2.09E-08	6.02E-08	2.20E-07	8.65E-07
Predicted min creep rate (s^{-1})	4.09E-08	1.90E-08	3.58E-07	9.04E-07

4.5 Prestrained Creep Test Results

An initial investigation into the effect of prestrain on secondary creep rate was carried out to simulate the overload of the SAGB housing during flight. Figure 4.15 shows the creep life of each sample with varying engineering prestrain levels. In Figure 4.15c the magnitude of the scatter is quite significant, where the material exhibited both enhancement and reduction in secondary creep rate at the same prestrain level. The minimum creep rate for each stress was plotted against the true prestrain levels in Figure 4.16 and it shows that no obvious relationship can be seen between the two variables.

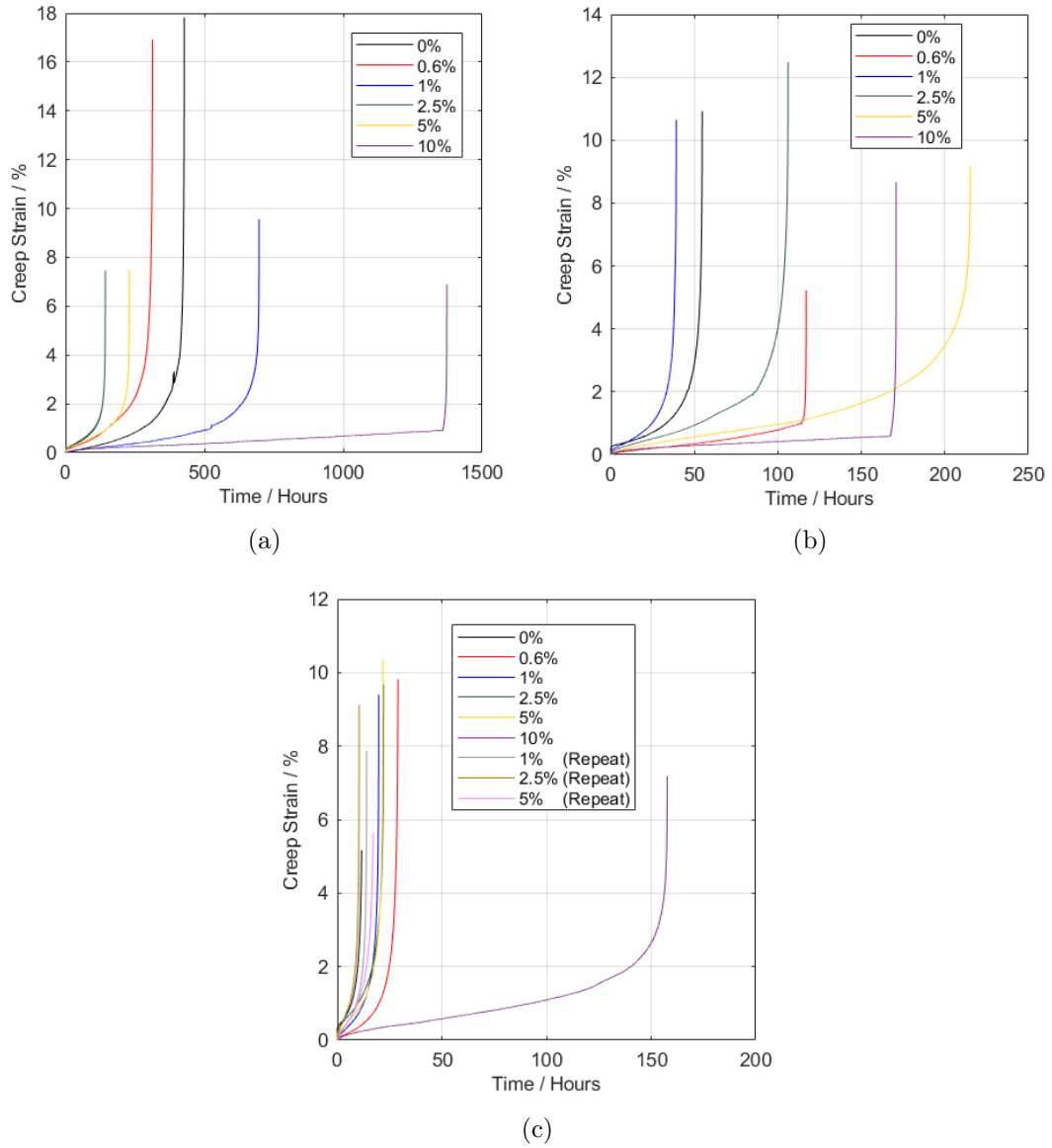


Figure 4.15: The creep life of the samples with a prior engineering prestrain at 180°C and stressed at (a) 120MPa, (b) 150MPa and (c) 190MPa.

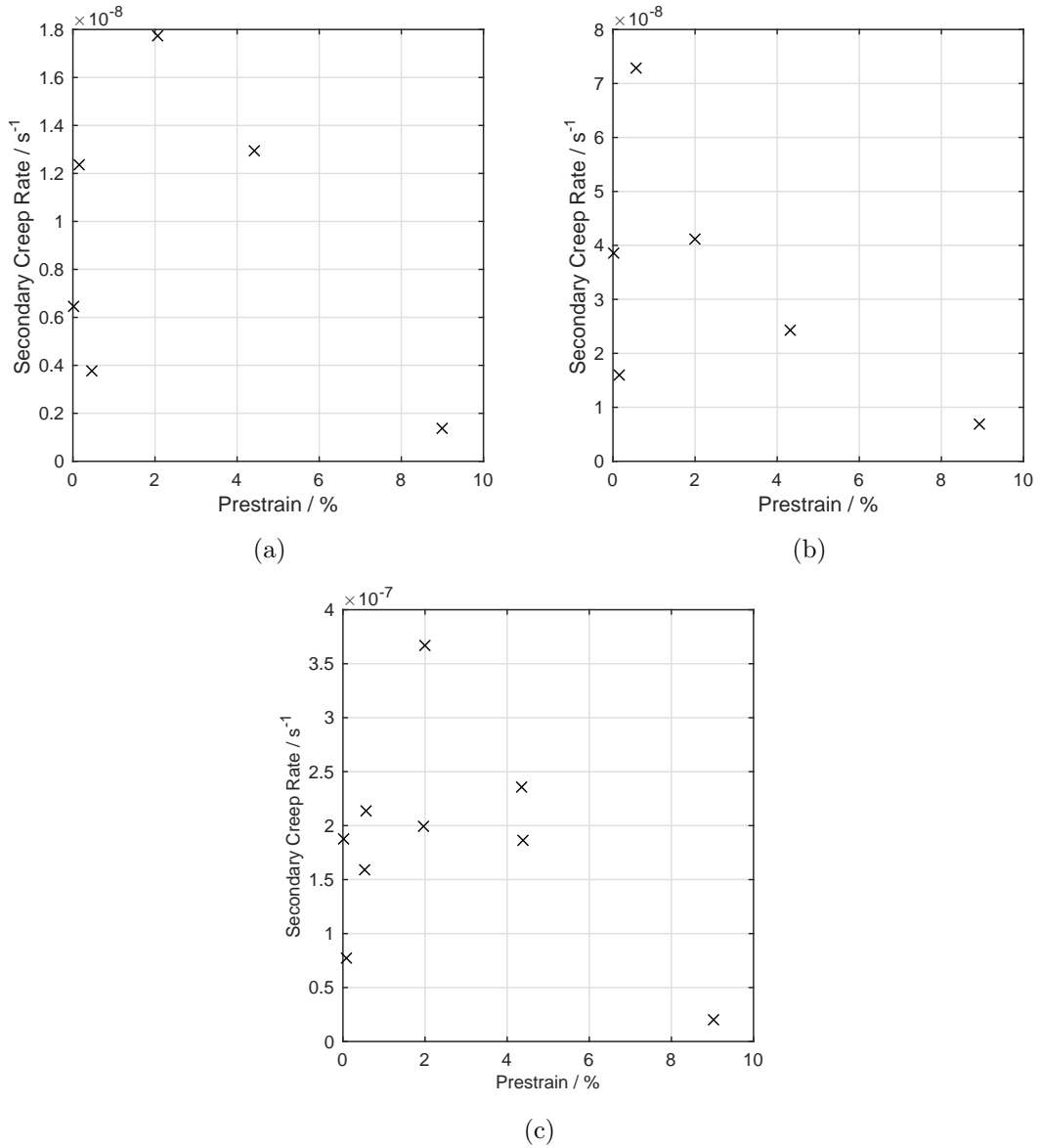


Figure 4.16: The minimum creep rate versus true prestrain at 180°C and stressed at (a) 120MPa, (b) 150MPa and (c) 190MPa.

A large increase in creep life can be seen when the sample was loaded to an engineering strain of 10%, and 5% when stressed at 150MPa prior to creep. It was previously shown in section 3.5 that a significant necked region developed in the gauge section after the sample was prestrained to 10%. However, after the 5% prestrain, only a slight decrease in gauge diameter was observed. The possibility that the neck may have created a notch effect and introduced a multiaxial stress state in the material was investigated later in this section. It should be noted that experimental validation of a multiaxial stress-stress was not carried out.

The measured diameter profiles obtained previously were used to create an

axisymmetric FE model of the 5% and 10% prestrained samples (assuming the necking was symmetrical halfway along the gauge length). A uniaxial load was applied to the model to induce a 190MPa pressure to the minimum cross-sectional area and the maximum principal stress, σ_1 , equivalent von Mises stress, σ_{eq} , and the rupture stress (see equation 2.41 in section 2.6.7), σ_r , was calculated along its radius, demonstrated in Figure 4.17c. The coefficient of multiaxiality, α , was assumed to be 0.3 since this is a typical value used for ductile materials (eg. P91 steel at 600°C [176]). This was a simple study to determine the stress distribution along the radius of the prestrained samples. Figure 4.18 shows the magnitude of the three stresses with distance along the path of interest highlighted in Figure 4.17c. Figure 4.17a shows that the 5% prestrain on the sample produces a relatively uniform stress distribution along the radius of the minimum cross-section. This suggests that a multiaxial stress state was not in effect while the samples were loaded. Therefore, the creep behaviour of the sample prestrained at 5% and crept at 150MPa should be considered an anomaly. Figure 4.17b shows that when the sample was prestrained by 10%, there was a high stress concentration (192-196MPa) at the radius of the cross-section which decreased to a minimum (166-172.5MPa) at the centre of the sample. This indicates that the necked region may act as a significant stress concentrator in the sample and introduce a multiaxial stress state under load but future work should be undertaken to verify this.

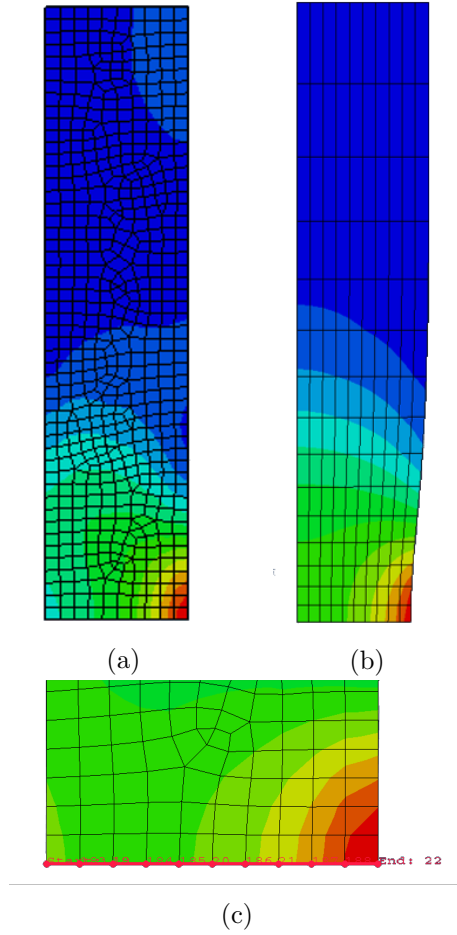


Figure 4.17: The FE model used to predict the maximum principal stress, equivalent von Mises stress and the rupture stress ($\alpha=0.3$) for (a) 5% and (b) 10% prestrained sample. (c) Shows the profile where the stress was calculated.

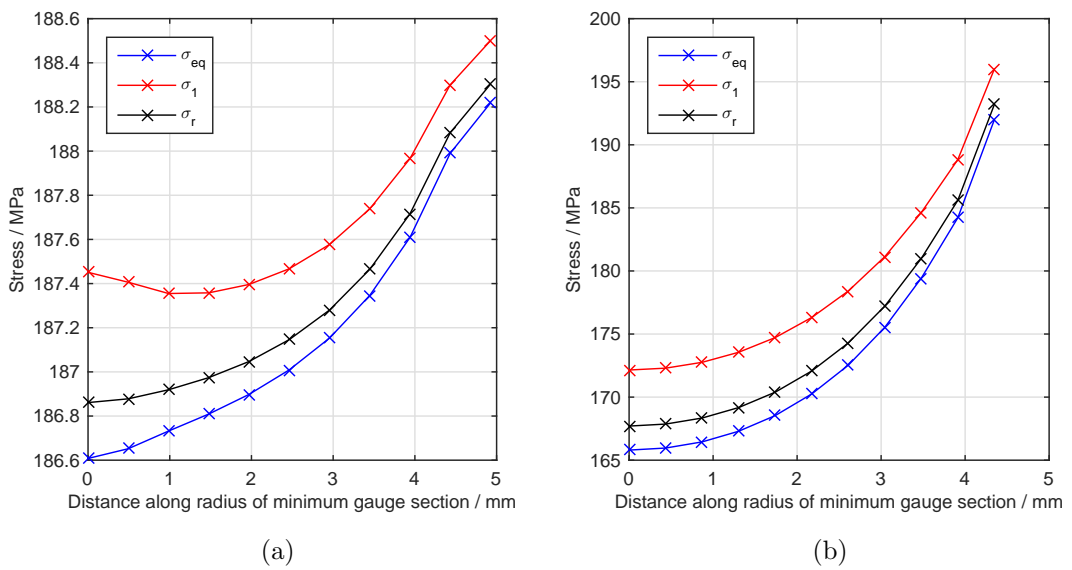
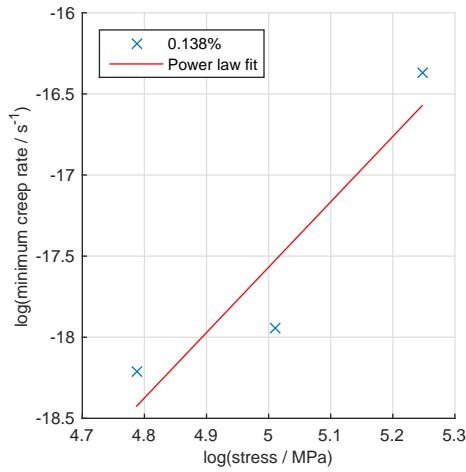
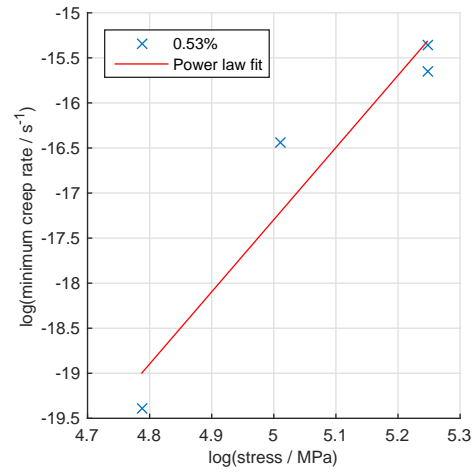


Figure 4.18: The FE predicted stress distributions for samples prestrained at (a) 5% and (b) 10%.

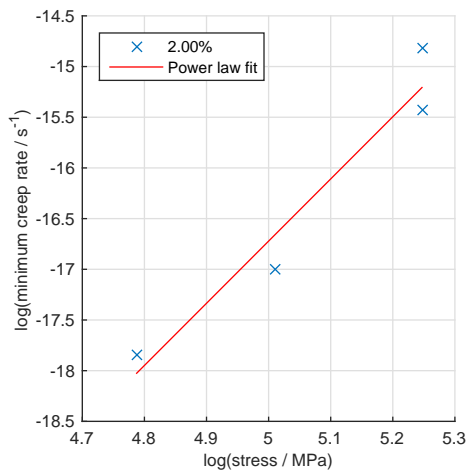
Since the relationship between the amount of prestrain and the minimum creep rate was not clear, stress relaxation tests were carry out to determine whether the viscous stress parameters were similar to those obtained from Norton's creep law prediction of the minimum creep rate of the prestrain samples. Figure 4.19 shows plots of the natural logarithm of minimum creep rate versus the applied stress for each true prestrain level to obtain the constants Z and n from Norton's creep power law (presented in Table 4.7).



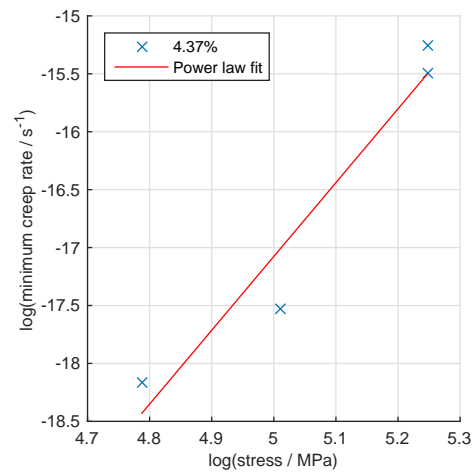
(a)



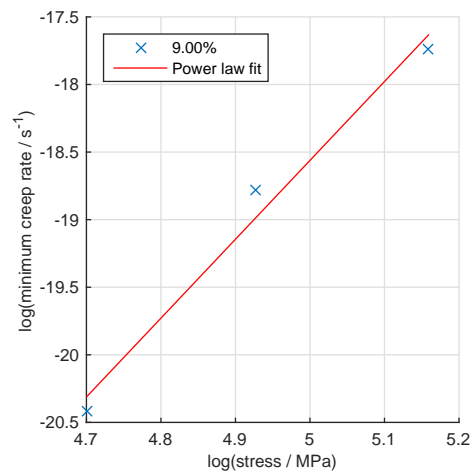
(b)



(c)



(d)



(e)

Figure 4.19: Plots showing the natural log of the minimum creep rate versus the natural log of the creep stress for the true prestrains levels at (a) 0.138%, (b) 0.530%, (c) 2.000%, (d) 4.370% and (e) 9.000%.

Table 4.7: The viscous stress parameters obtain from the prestrained creep tests at 180°C

Average true prestrain (%)	n	Z
0.138	4.03	4.17E-17
0.530	8.01	1.26E-25
2.000	6.13	2.63E-21
4.370	6.37	5.64E-22
9.000	5.84	1.85E-21

$$\sigma = \sigma_v + \sigma_y \quad (4.2)$$

To calculate the viscous stress of the stress relaxation tests (with dwell periods at 0.5%, 4% and 8% engineering strains), it was assumed that the stress relaxation period below the material's yield surface was linear and that hardening was negligible. By fitting a line of best fit to the linear region, the upper boundary of the yield surface was chosen to be the first stress value that deviates from the fitted line by 3MPa, displayed by the red diamond in Figure 4.20. The total stress was assumed to the sum of the yield stress and the viscous stress as shown in equation. σ is the total stress, σ_v is the viscous stress and σ_y is the yield stress (the red diamond in Figure 4.20). Therefore, by rearranging the equation, the viscous stress can be calculated.

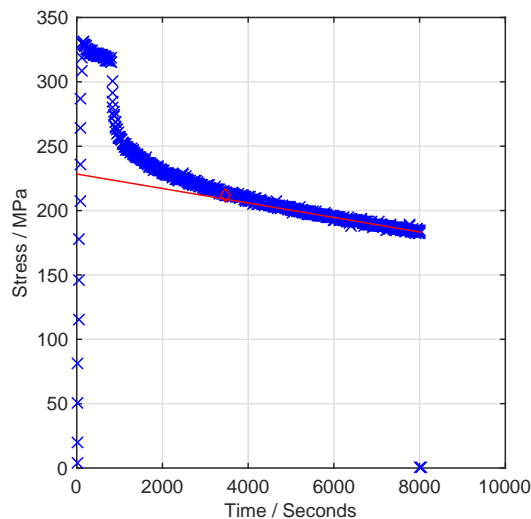


Figure 4.20: Calculation of the yield surfaces

Figure 4.21 shows the plots of the natural log of equivalent plastic strain rate versus

the viscous stress to acquire Z and n presented in Table 4.8. It can be seen that the creep constants are not similar. The crept samples after they were prestrained were stressed within its elastic region while during the stress relaxation tests, the dwell period of the sample occurred above its yield surface. As a result, different creep mechanisms may have taken place for each type of creep tests, indicated by the difference in creep parameters.

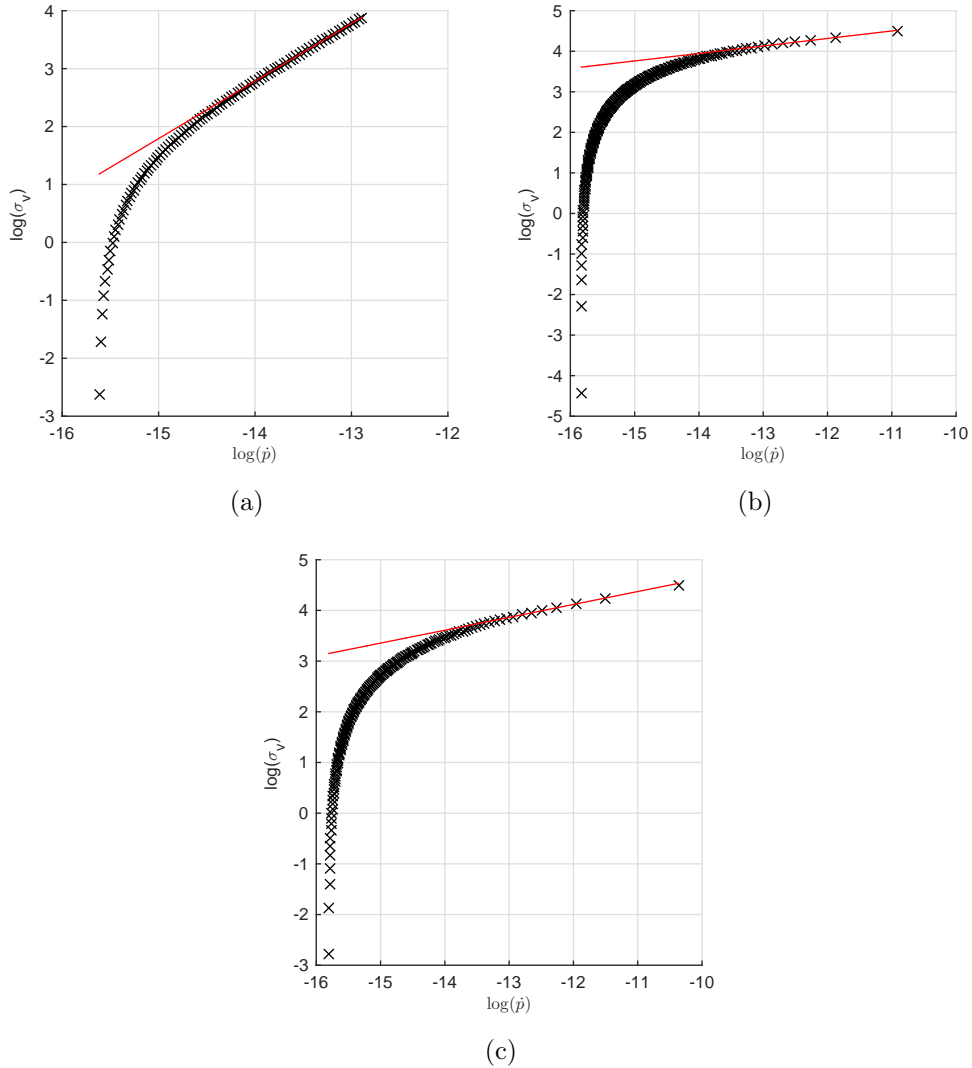


Figure 4.21: A plot of the natural log of the accumulated plastic strain rate and viscous stress during dwell periods at engineering strains of (a) 0.5%, (b) 4% and (c) 8%.

$$\sigma = \sigma_v + R + \chi + k \quad (4.3)$$

A different method was used when calculating Z and n for the stress relaxation tests at 160°C and 200°C (see section 6.3), which accounted for the material hardening

Table 4.8: The power law constants obtained from the stress relaxation tests at 180°C.

Dwell strain %	n	Z (MPa.s ^{1/n})
0.5	1.01	5.04E-08
4.0	5.41	4.50E-16
8.0	3.93	5.71E-13

behaviour, from the strain-controlled isothermal fatigue tests at those temperatures. The total stress was calculated using equation 4.3, where R is the isotropic drag stress and χ is the kinematic back stress. Therefore, the method used to obtain viscous stress parameters for the stress relaxation test at 180°C was repeated for the tests at 160°C and 200°C. Table 4.9 demonstrates a significant difference in Z and n .

Table 4.9: A comparison of viscous stress parameters with and without the inclusion of the material hardening behaviour.

Sample name	160°C-400h without $R + \chi$	160°C-400h with $R + \chi$	200°C-400h without $R + \chi$	200°C-400h with $R + \chi$
n	3.53	1.48	3.74	1.17
Z (MPa.s ^{1/n})	2.67E-12	1.12E-08	1.44E-11	1.95E-07

4.6 Stress-Controlled Tests Results

The stress-controlled fatigue were carried out using a non-zero positive mean stress to represent the cyclic stress conditions of the SAGB housing during cruise. It should be noted that the tests that lasted more than 10000 cycles or reached 3% strain were interrupted at this point (whichever came first).

4.6.1 Isothermal Fatigue

Stress controlled isothermal fatigue (IF) tests were carried out at 160°C and 200°C. Figure 4.22 show the sample strain evolution with cycle number at 160°C. It can be seen in part a that the hysteresis loops translate in the positive strain direction (ratcheting) as the number of cycles increase. The hysteresis loops also show that no appreciable plasticity took place and that the applied stress was less than the sample's yield stress.

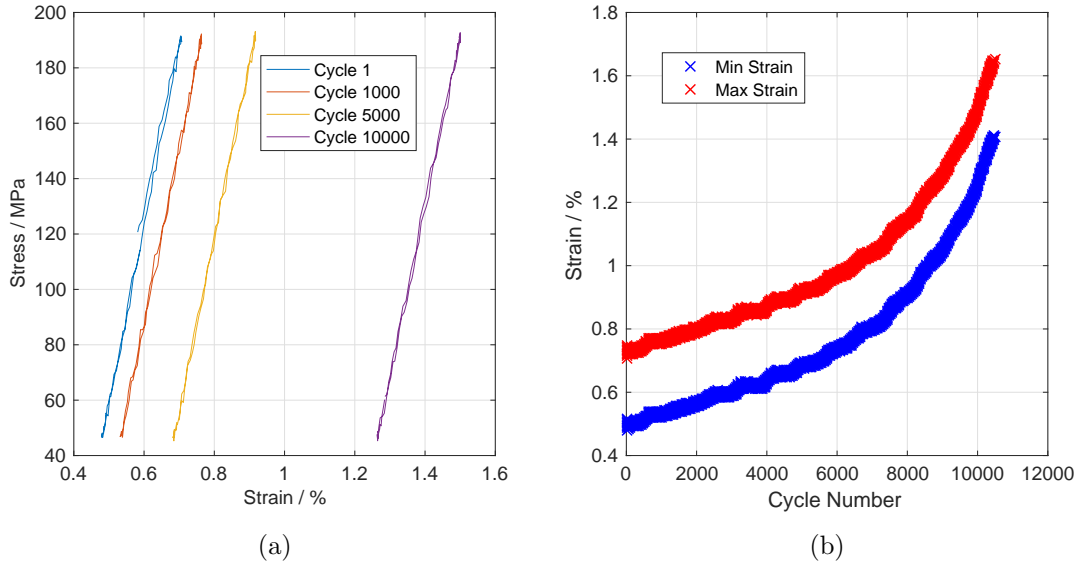


Figure 4.22: (a) Stress-strain data of selected cycles tested under IF conditions ($\sigma_{max}=190\text{MPa}$, $T=160^\circ\text{C}$) and (b) the maximum and minimum strain per cycle. The test was interrupted after 10,486 cycles.

Figure 4.23 shows that at 200°C , the test was terminated after 306 cycles since it reached 3% strain which represented failure of the sample. Figure 4.23a shows that a small amount of plastic strain took place in the first cycle but was followed by elastic loading for the next successive cycles. Eventually, the sample began accumulating plastic strain, demonstrated by the non-linear stress-strain behaviour similar to cycle 300. Also, ratcheting in the positive strain direction took place at 200°C . The accumulation of plastic strain accounts for the accelerated increase in maximum and minimum strain shown in Figure 4.23b. This suggests that the material has aged and eventually the yield strength decreased below the applied stress. This test result, as well as the hardness and tensile data, supports the notion that simple exposure to elevated temperature is detrimental to the mechanical strength of this alloy. This is an important material behaviour to account for if this aluminium alloy is considered for the step-aside gearbox housing application since it will directly affect the lifetime of the component.

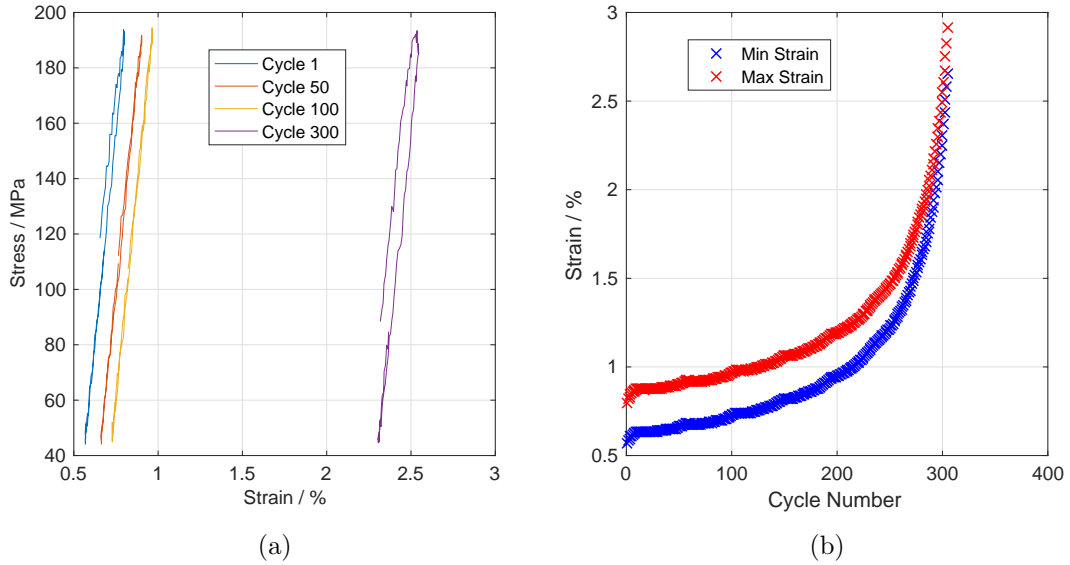


Figure 4.23: (a) Stress-strain data of selected cycles tested under IF conditions ($\sigma_{max}=190\text{MPa}$, $T=200^\circ\text{C}$) and (b) the maximum and minimum strain per cycle. The test was interrupted at cycle 306 when 3% strain was reached.

When the maximum stress was reduced to 120MPa, the number of cycles before test termination greatly increased as shown in Figure 4.24, from 306 cycles at $\sigma_{max}=190\text{MPa}$, to 4,242 cycles. This was to be expected but it should be noted that a similar material strain response was observed. Initially, the sample was ratcheting while remaining elastic under the applied load. Eventually, the sample began to accumulate plastic strain before reaching the 3% strain limit as demonstrated in Figure 4.24b. This also supports the idea that the material's strength had decreased below the applied stress due to ageing. This occurrence was at a much later time than the previous test because of the lower maximum stress.

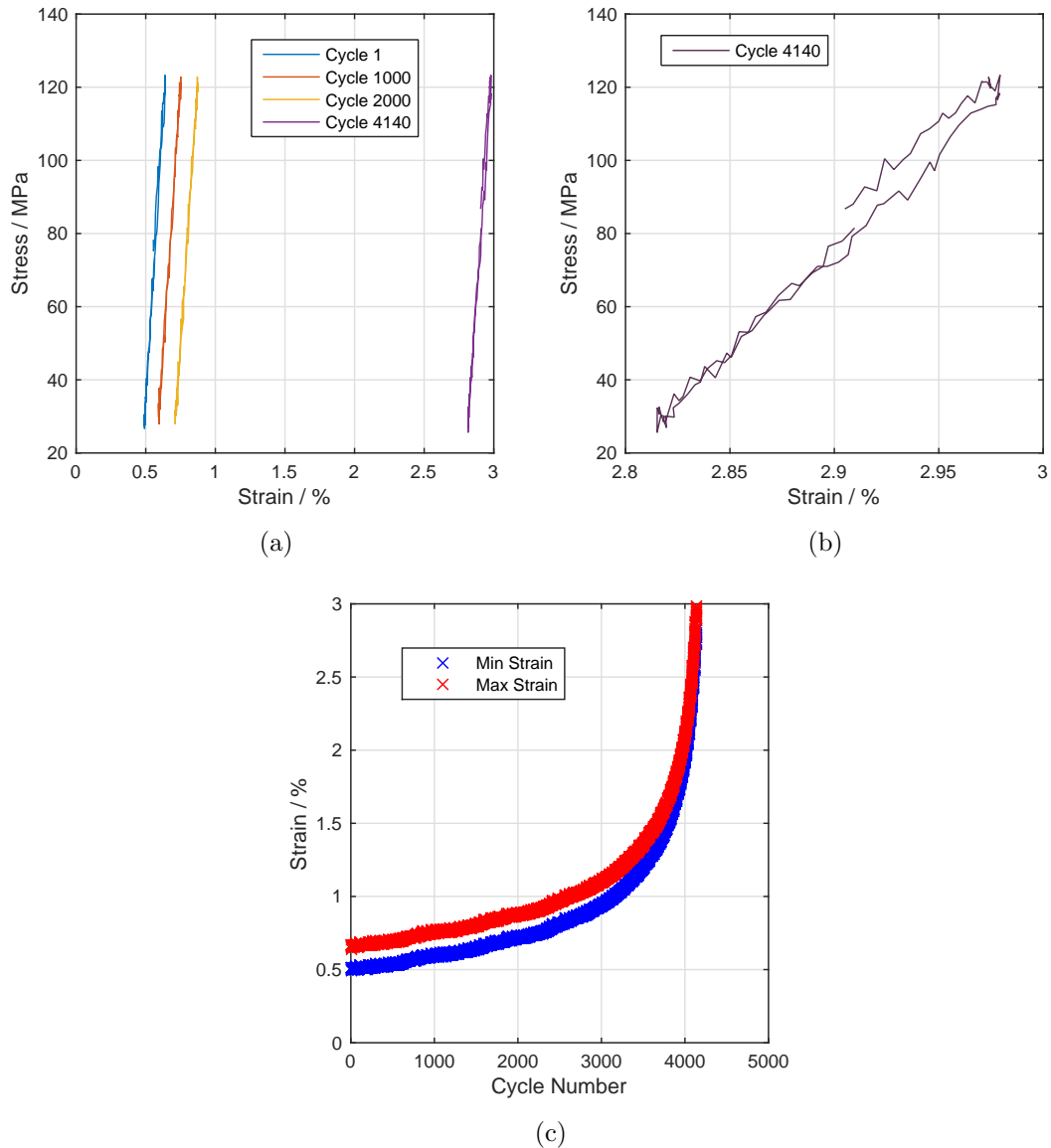


Figure 4.24: (a) Stress-strain data of selected cycles tested under IF conditions ($\sigma_{max}=120\text{MPa}$, $T=200^\circ\text{C}$), (b) the hysteresis loop of cycle 4,140 and (c) the maximum and minimum strain per cycle. The test was interrupted at cycle 4,242 when 3% strain was reached.

4.6.2 Thermomechanical Fatigue

Thermomechanical fatigue (TMF) tests were carried out in-phase (IP) and out-of-phase (OP) conditions to investigate the effect of those loading conditions on fatigue life with a positive R-ratio of 0.25 (as with isothermal testing). Figure 4.25 shows the results of the IP TMF test with a temperature range of 120-160°C and $\sigma_{max}=190\text{MPa}$. The amount of plasticity for each hysteresis loop was minimal which was similar to the IF condition at 160°C. However, the ratcheting behaviour was greater than the isothermal

fatigue condition (shown in Figure 4.22) which reached the 3% strain limit (terminating the test).

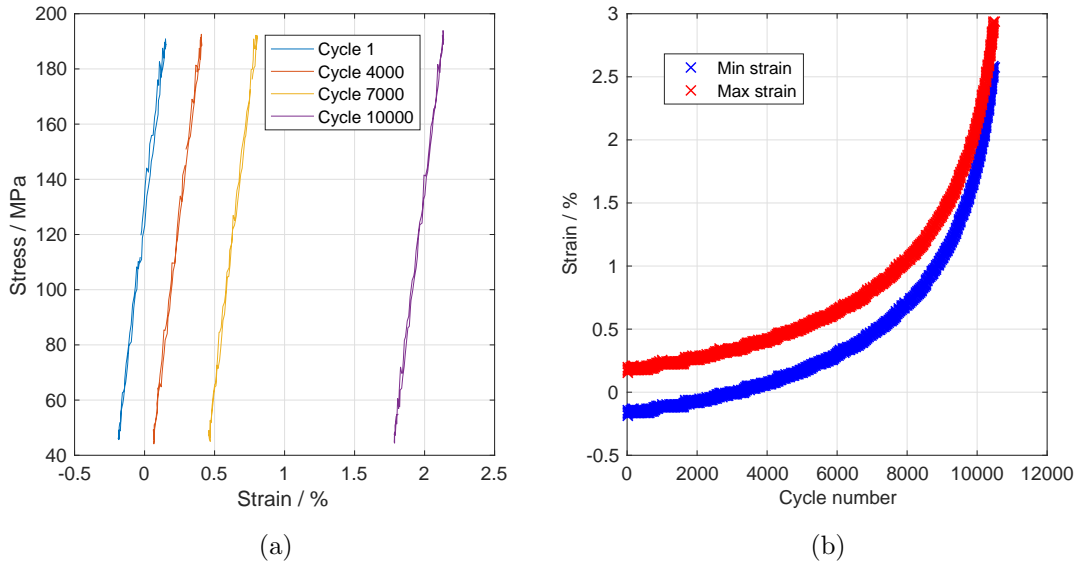


Figure 4.25: (a) Stress-strain data of selected cycles tested at under IP TMF conditions ($\sigma_{max}=190\text{MPa}$, $T=120\text{-}160^\circ\text{C}$) and (b) the maximum and minimum strain per cycle. The test was interrupted at cycle 10486.

Figure 4.26a shows that when the sample was tested in the OP TMF condition (temperature range = $120\text{-}160^\circ\text{C}$, $\sigma_{max}=190\text{MPa}$), p-shaped hysteresis loops were formed. This complex behaviour started after the first cycle, where Figure 4.27 displays a schematic representation of the hysteresis loop. As the sample was approaching the maximum stress, it was simultaneously pulled in tension mechanically and thermally contracting due to the decreasing temperature. Cycle 10 was examined in Figure 4.28 to see how the strain, stress and temperature change with time. A spike in strain level from 0.42% to 0.52% occurred about 14 seconds before the maximum stress. During that time, the strain rapidly decreased and synchronised with the stress waveform. It would be unlikely that the thermal contraction would become dominant while the stress was still increasing towards 190MPa. One possible explanation would be that the extensometer arms experienced slippage but the reason behind the phenomena remains unclear. The test was stopped at just over 5,000 cycles since it was clear that the sample would have continued to 10,000 cycles before hitting the 3% strain limit as the maximum strain level was relatively stable at about 0.525%.

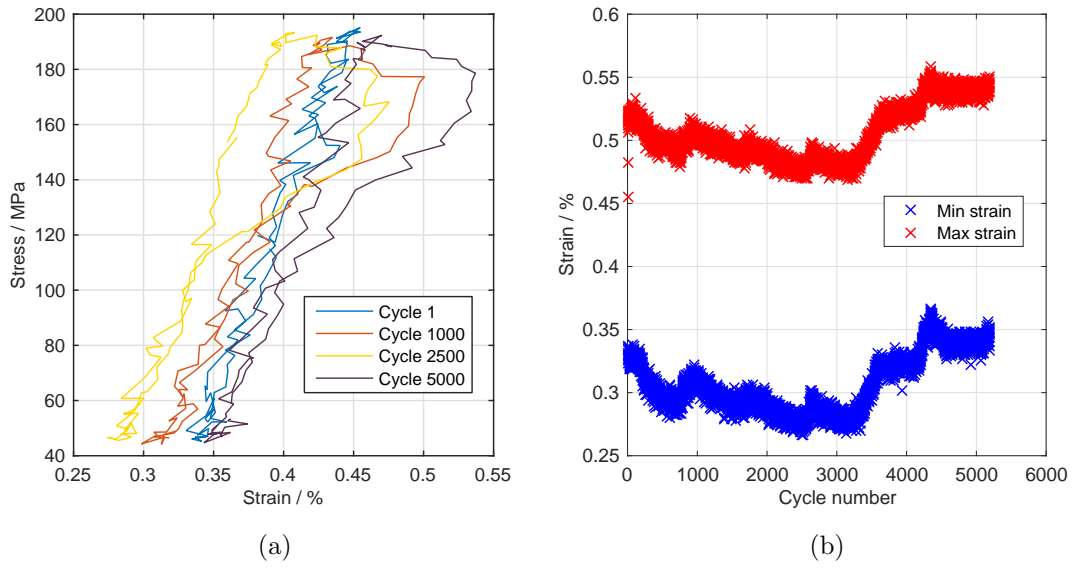


Figure 4.26: (a) Stress-strain data of selected cycles tested under OP TMF conditions ($\sigma_{max}=190\text{MPa}$, $T=120\text{-}160^\circ\text{C}$) and (b) the maximum and minimum strain per cycle. The test was interrupted at cycle 5194.

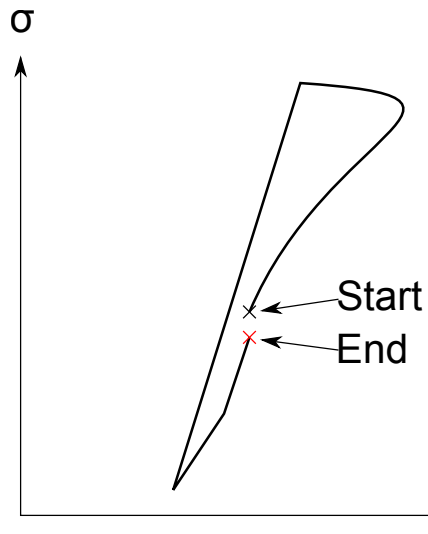


Figure 4.27: A schematic example of a hysteresis loop of the TMF OP condition shown in Figure 4.26.

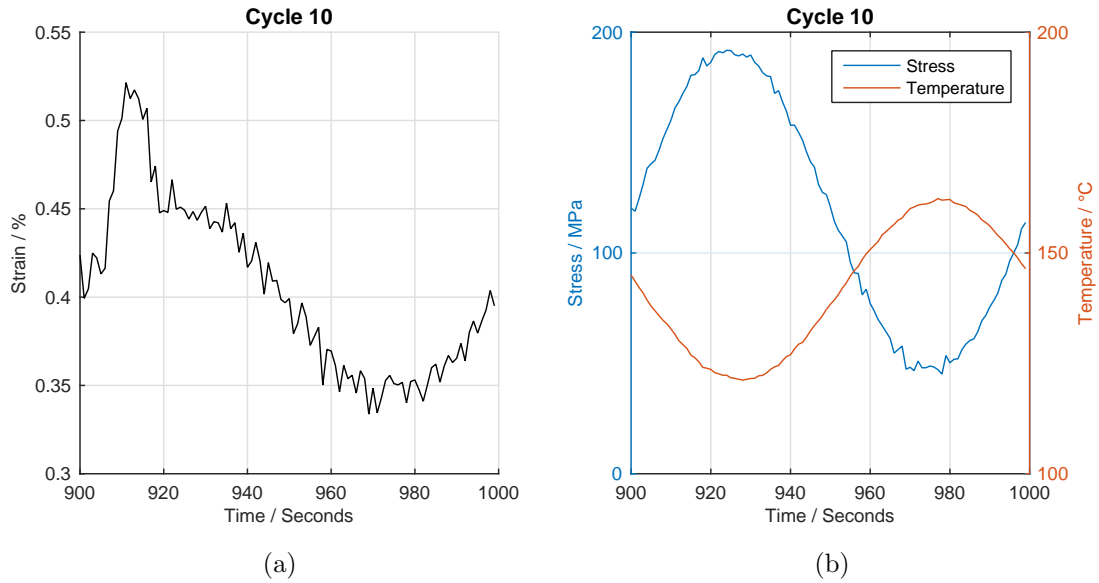


Figure 4.28: (a) Strain vs time and (b) stress and temperature vs time of cycle 10 of the OP TMF test at 120-160°C.

When the sample was subjected to IP TMF conditions with a temperature range of 120-200°C, the fatigue life decreased from 10,486 cycles to 600 cycles compared to the test with a temperature range of 120-160°C. However, when compared to the IF test at 200°C (Figure 4.23) the number of cycles before the test was terminated for the IP TMF condition was double compared to IF condition. Similarly to the IF condition, plastic strain was induced in the first cycle, followed by elastic loading and ratcheting until the last few cycles where significant plastic strain was accumulated as shown in Figure 4.29a. Figure 4.30a shows the material strain response during OP TMF loading. As the load approached maximum stress, the strain due to thermal contraction increased. Eventually in each cycle, the strain due to thermal contraction became more dominant than the mechanical tensile strain, which led to a decrease in the total strain before maximum stress was reached. The opposite behaviour occurred as the sample approached minimum stress where the temperature approaches its maximum. From Figure 4.31, it can be seen that the stress value of maximum strain increases with the number of cycles. This behaviour may also be attributed to the material ageing. Initially, the sample's yield strength was greater than the applied load and the strain due to thermal contraction of the sample evenly opposed the tensile strain (more or less). However, as the yield strength decreased with time at high temperature, the maximum strain per cycle began to increase because the sample began to yield and the amount of plastic strain per

cycle increased before thermal contraction became dominant. This phenomena was also responsible for the ratcheting of the hysteresis loops in the positive strain direction.

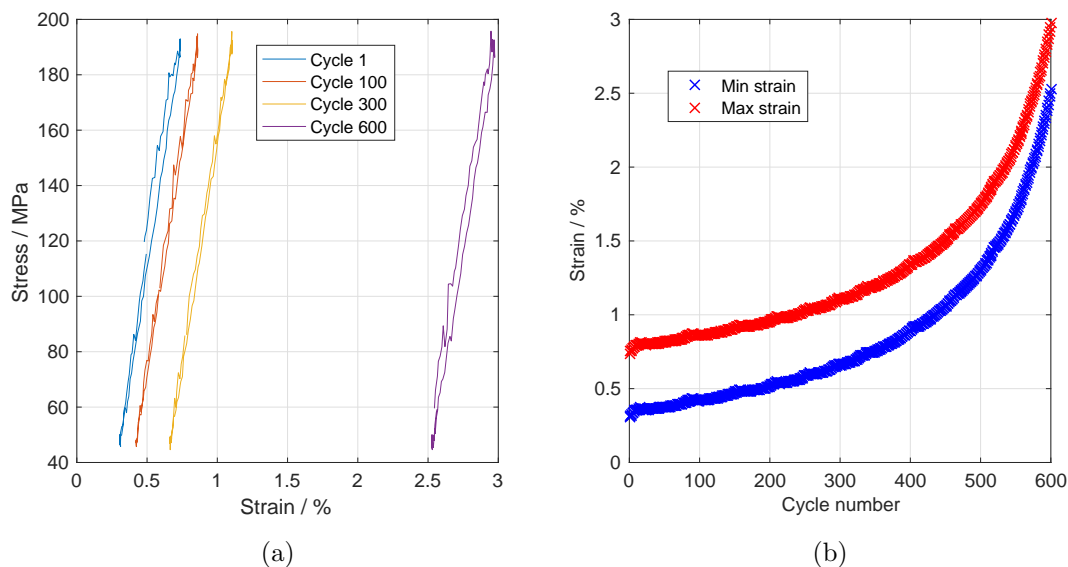


Figure 4.29: (a) Stress-strain data of selected cycles tested under IP TMF conditions ($\sigma_{max}=190\text{MPa}$, $T=120\text{-}200^\circ\text{C}$) and (b) the maximum and minimum strain per cycle. The test was interrupted at cycle 600 when 3% strain was reached.

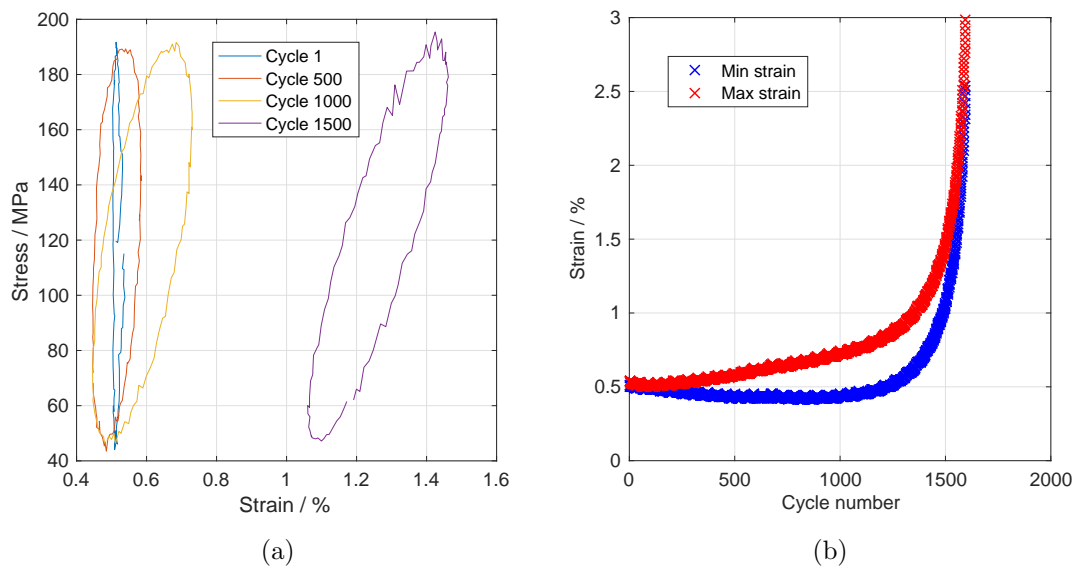


Figure 4.30: (a) Stress-strain data of selected cycles tested under OP TMF conditions ($\sigma_{max}=190\text{MPa}$, $T=120\text{-}200^\circ\text{C}$) and (b) the maximum and minimum strain per cycle. The test was interrupted at cycle 1,598 when 3% strain was reached.

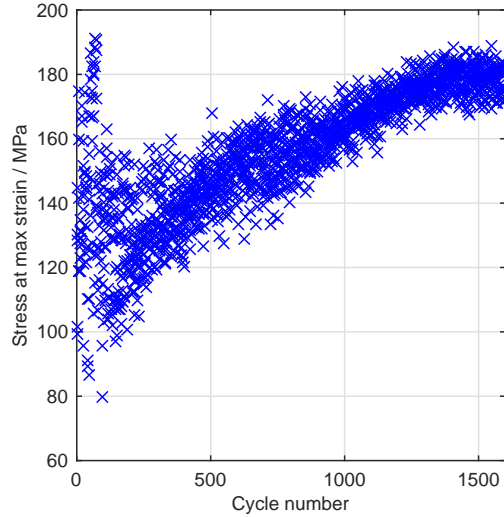


Figure 4.31: The stress at which maximum strain occurs per cycle for the OP TMF condition at 120-200°C.

When $\sigma_{max}=120\text{MPa}$, the number of cycles to test termination under IP TMF increased compared to $\sigma_{max}=190\text{MPa}$, from 600 to 6,062 cycles, which is to be expected. The IP TMF condition in Figure 4.32 exhibited ratcheting behaviour but no apparent plastic strain was induced. As shown in Figure 4.33, the material behaviour in the OP TMF test showed that the strain response was highly influenced by the out-of-phase thermal straining of the material. The maximum strain level in Figure 4.33b remained stable compared to the other test conditions.

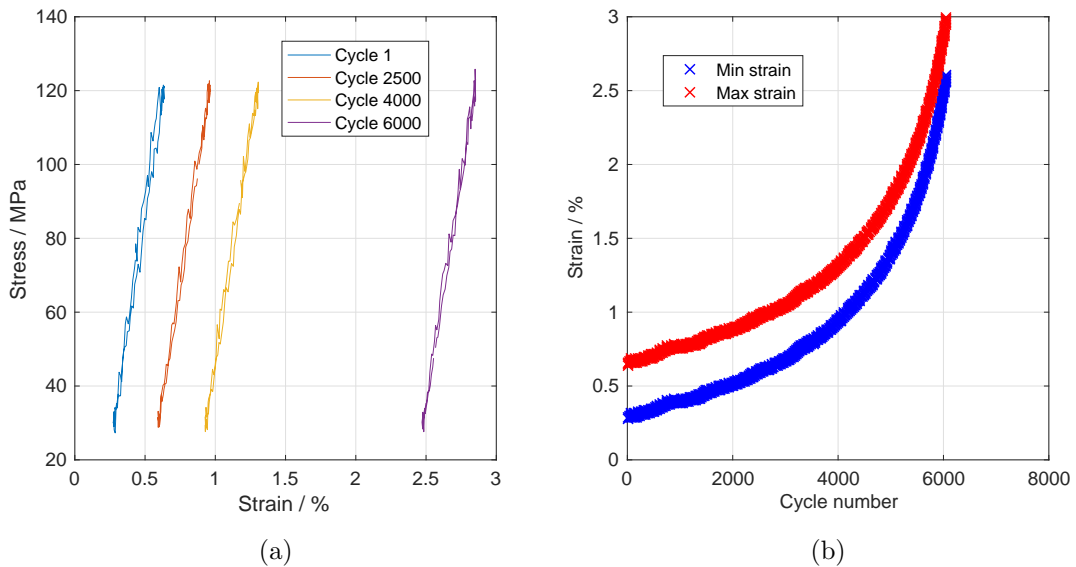


Figure 4.32: (a) Stress-strain data of selected cycles tested under IP TMF conditions ($\sigma_{max}=120\text{MPa}$, $T=120\text{-}200^\circ\text{C}$) and (b) the maximum and minimum strain per cycle. The test was interrupted at cycle 6,062 when 3% strain was reached.

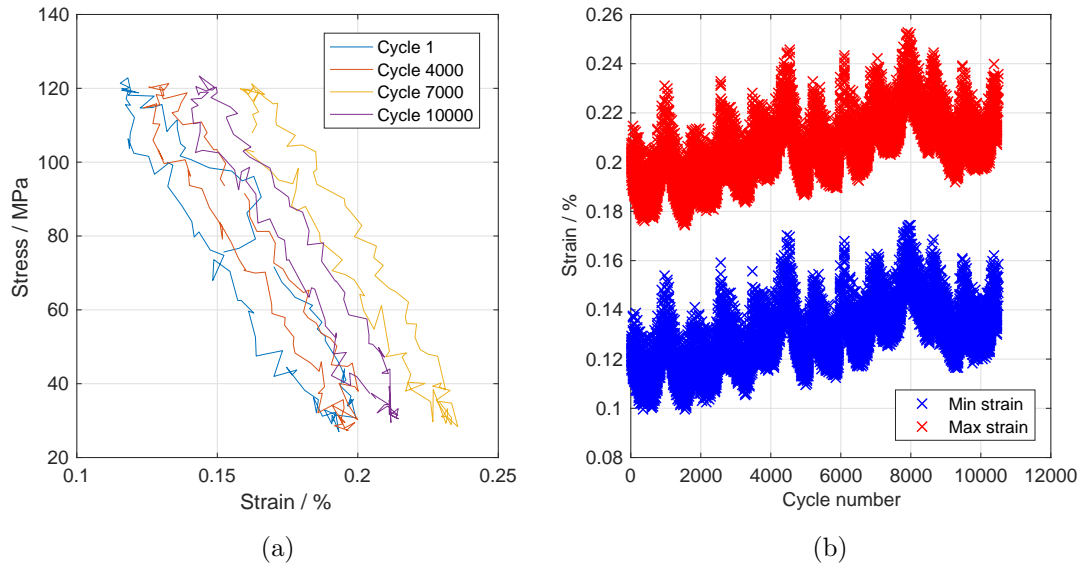


Figure 4.33: (a) Stress-strain data of selected cycles tested under OP TMF conditions ($\sigma_{max}=120\text{MPa}$, $T=120\text{-}200^{\circ}\text{C}$) and (b) the maximum and minimum strains per cycle. The test was interrupted at cycle 10,486.

Figure 4.34 shows the lifetime of all fatigue test conditions with a maximum temperature of 200°C versus stress amplitude. Under IF conditions, the samples were constantly subjected to elevated temperatures where the material was continually ageing. This produced the shortest test duration since the material's yield stress decreased with time at test temperature and quickly reached the 3% strain limit. During IP TMF testing, the temperature was cycling in phase with the stress meaning that maximum temperature corresponded to maximum stress. Under these conditions, the amount of time spent at high temperature and stress was less than the IF condition, which in turn decreased the rate of material ageing. When the stress was out of phase with the temperature, the samples would have aged at the same rate as the IP TMF samples. However, at maximum stress the samples' yield strength was greater since the temperature was at a minimum and therefore accumulated much less damage. The OP TMF condition resulted in the greatest fatigue life. It can be seen that regardless of the stress amplitude, the fatigue life is directly dependent on the amount of time the samples were at high temperature, and whether they were highly loaded at high temperature.

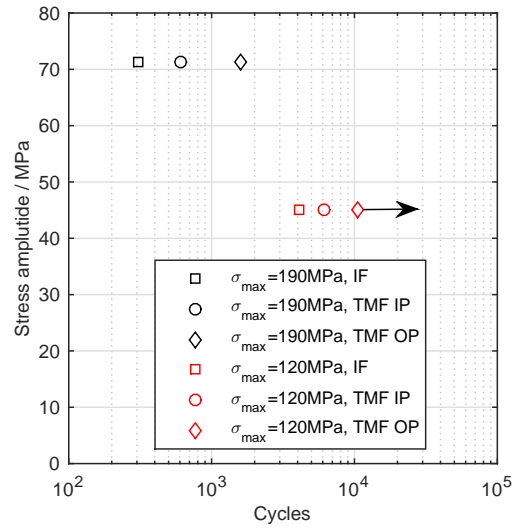


Figure 4.34: The cycles to test termination versus the stress amplitude of IF and TMF tests for test with a maximum temperature of 200°C.

5 Microstructural Analysis of the 7175-T7351 Aluminium Alloy

5.1 Microstructural Overview

Figure 5.1 shows an overview of the microstructures of the samples that were soaked at 200°C from 0-400 hours. The dark patches that obscure the particles in Figures 5.1a and 5.1b are diffraction shadows (circled in red). These were caused by the absence of electron detection, which is dependent on the grain orientation and sample tilt. It can be seen that the particle sizes generally increases along with inter particle spacing as the soak time increases (measurements are detailed in section 5.3.1). Also, relatively large particles can be seen on the grain boundaries outlined by the red lines.

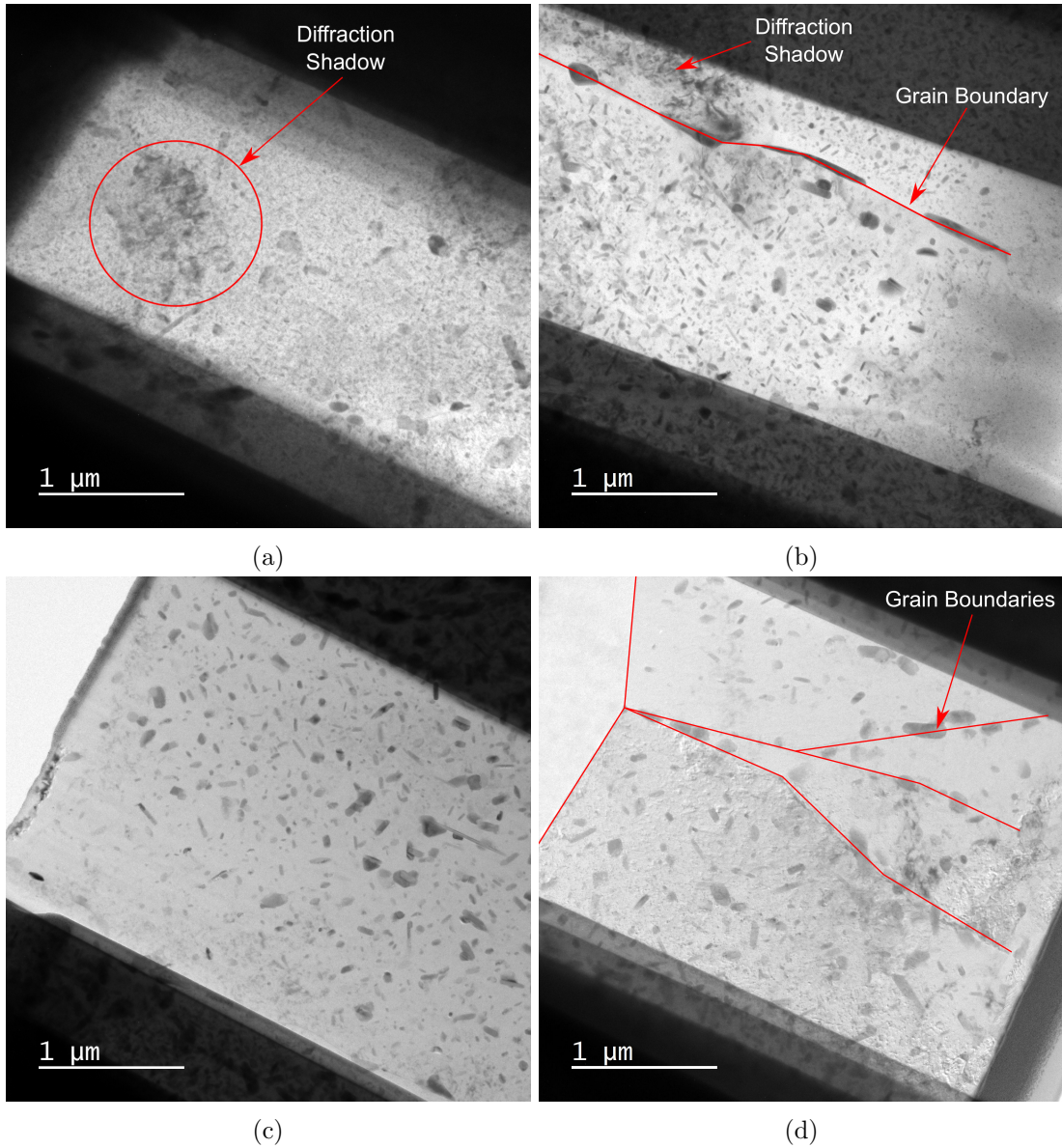


Figure 5.1: TEM images showing and overview (x6000 magnification) of the 7175-T7351 microstructure after soaking at 200°C for (a) 0 hours (as-received material), (b) 24 hours, (c) 75 hours and (d) 400 hours.

5.2 Element Mapping

Obtaining diffraction patterns for particle phase identification proved to be problematic as the matrix pattern would frequently interfere with the particle pattern. Therefore, element maps of the samples that were soaked for 0 hours, 24 hours and 75 hours were used to show the concentration of elements at the positions of the particles using SEM. With this information, an inference can be made on the phase composition of the observed particles based on the phase identification in Section 5.3.

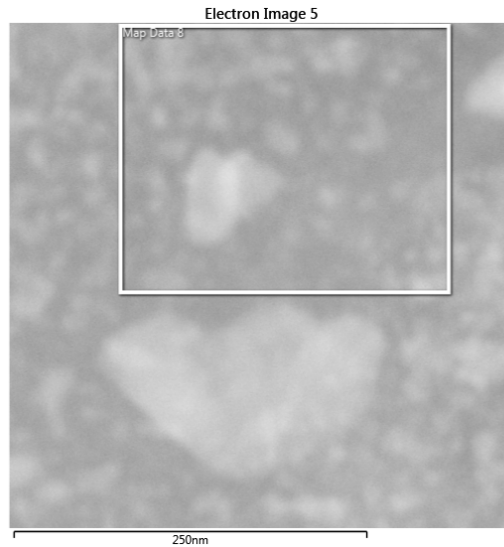


Figure 5.2: An SEM image of the as-received material showing the area inside the white box where element mapping took place.

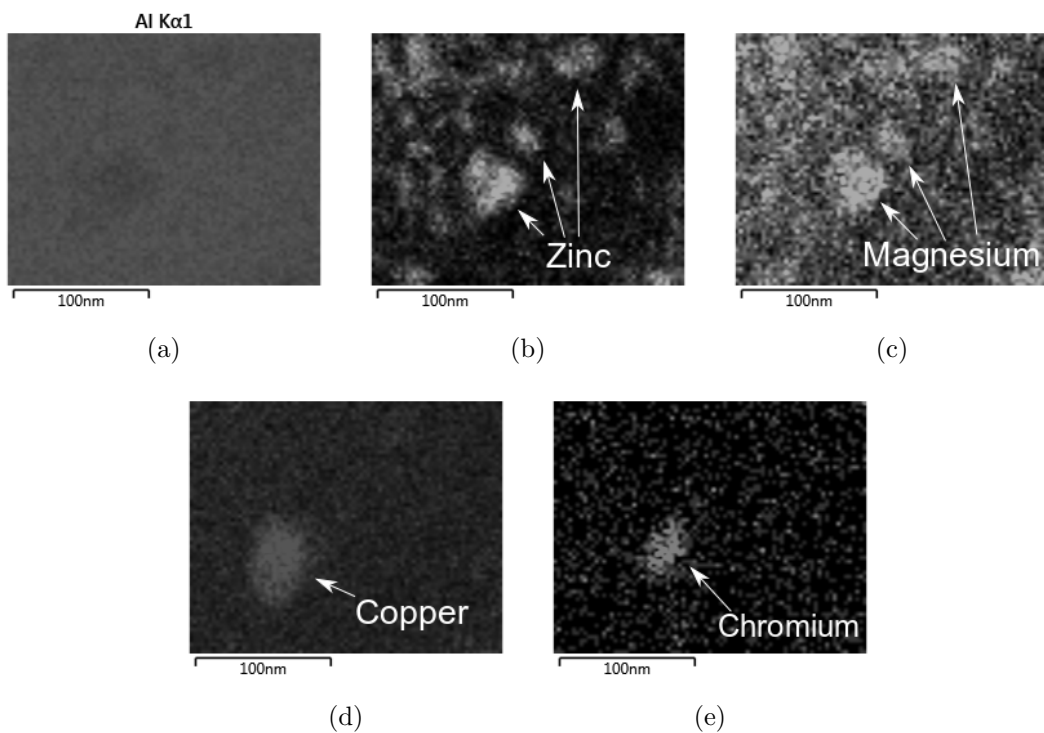


Figure 5.3: Element mapping of “Map Data 8” shown in Figure 5.2, where the white areas represent the element locations of (a) aluminium, (b), zinc, (c) magnesium, (d) copper and (e) chromium.

Figure 5.2 shows the electron image of the as-received material, highlighting the area that was mapped. Figure 5.3 shows that the concentrations of zinc and magnesium can be seen at the positions of the particles. Furthermore, an overlap of a zinc-magnesium rich area and a copper-chromium rich area occurs at the position of the larger particle.

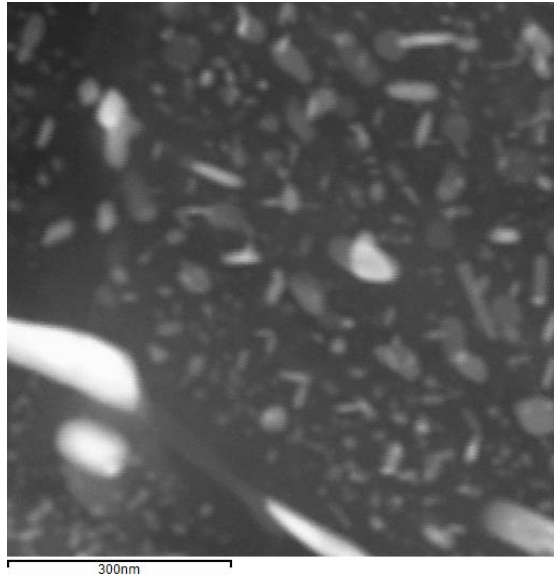


Figure 5.4: An SEM image used for element mapping of the material after it was soaked for 24 hours at 200°C.

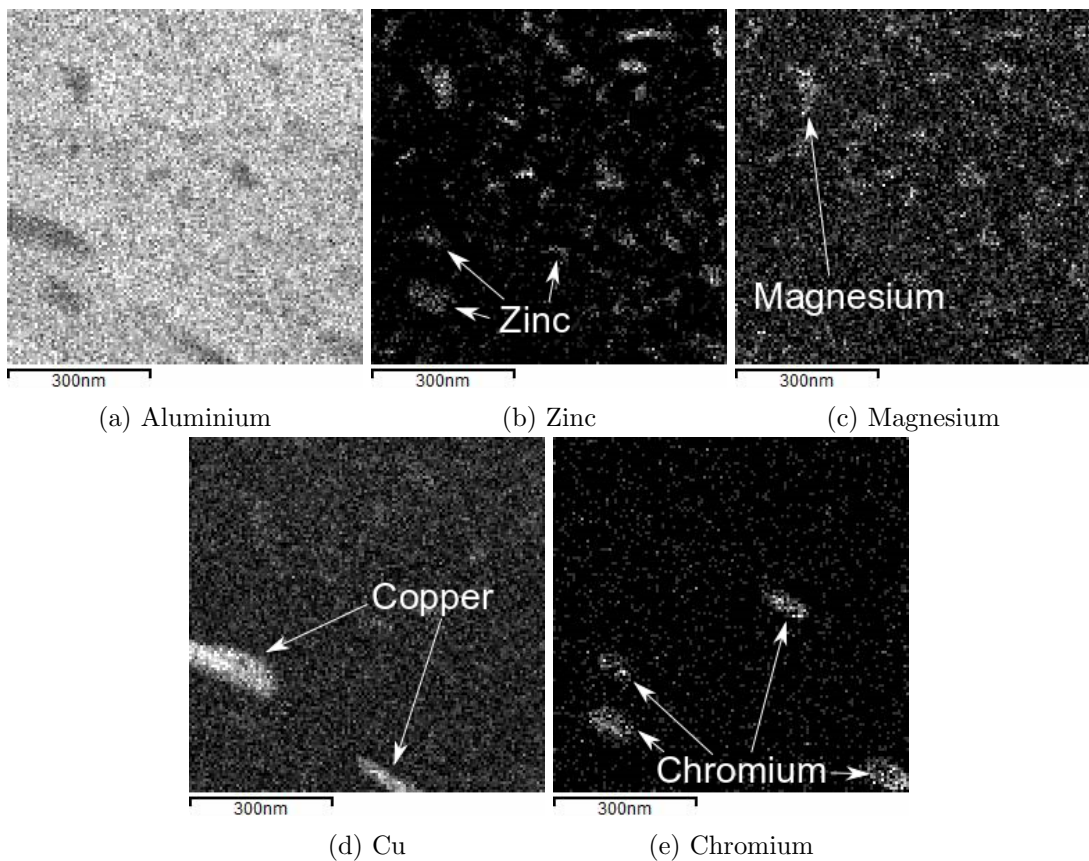


Figure 5.5: Element mapping of the microstructure in Figure 5.4, where the white pixels represent the atom locations of (a) aluminium, (b), zinc, (c) magnesium, (d) copper and (e) chromium.

Similar observations can be seen for the sample that was soaked for 24 hours in Figures 5.4 and 5.5. Zinc and magnesium are finely dispersed particles within the

matrix. Copper-rich particles lie on the grain boundaries and chromium-rich particles are also seen within the grains near the boundary.

Figure 5.6 shows the electron image of the sample that was soaked for 75 hours and the areas used to obtain element maps. The larger particles shown in Figure 5.7 are rich in zinc, magnesium and copper whereas the smaller particles in Figure 5.8 are only rich in zinc and magnesium. Chromium-rich particles can also be seen in Figure 5.7.

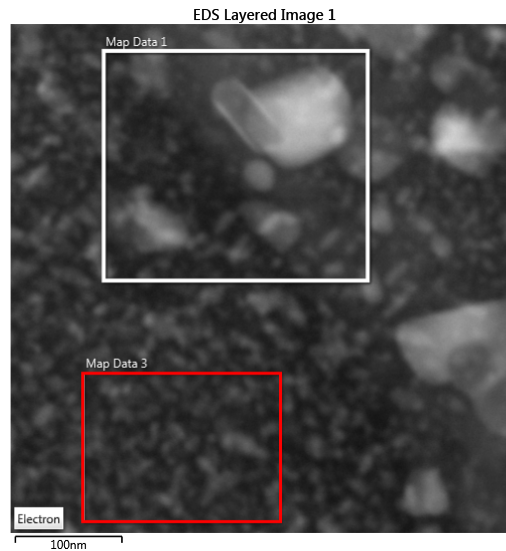


Figure 5.6: An SEM image highlighting two areas used for element mapping of the material after it was soaked for 75 hours at 200°C.

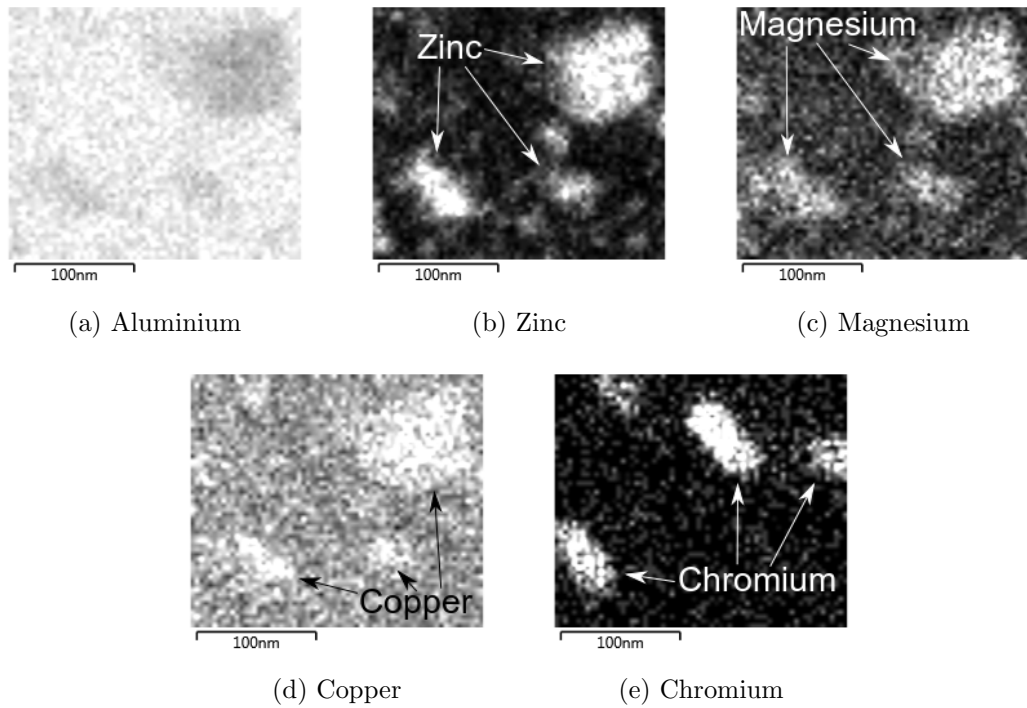


Figure 5.7: Element mapping of “Map Data 1” highlighted by the white box in Figure 5.6, where the white pixels represent the atom locations of (a) aluminium, (b), zinc, (c) magnesium, (d) copper and (e) chromium.

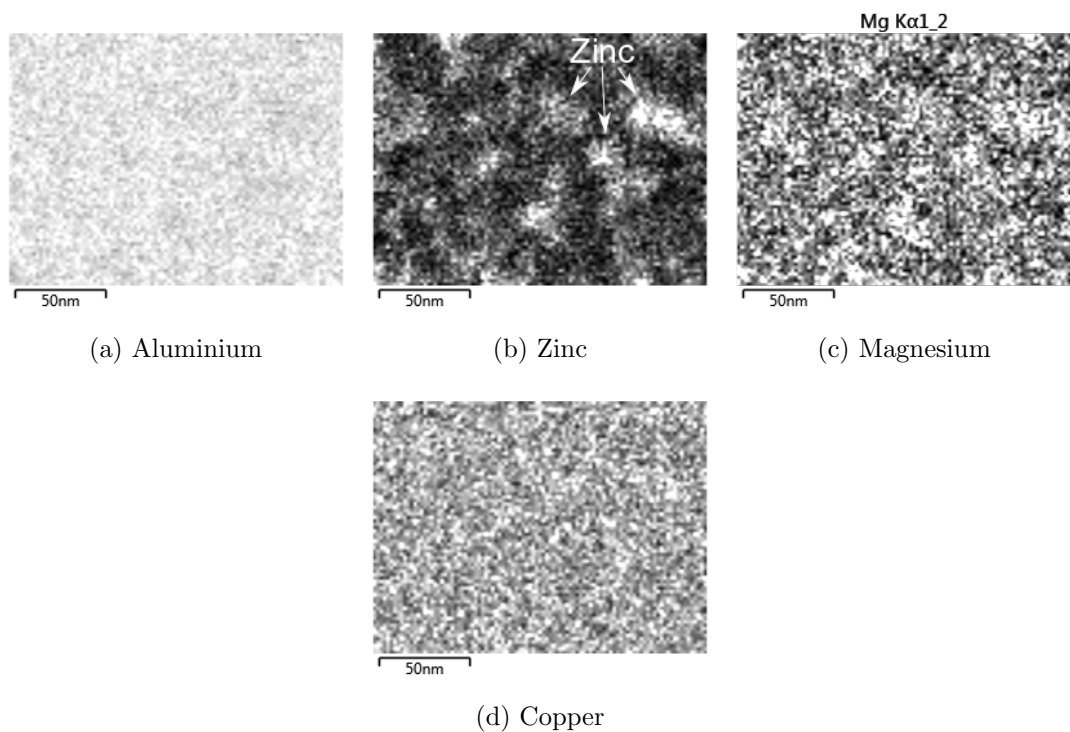
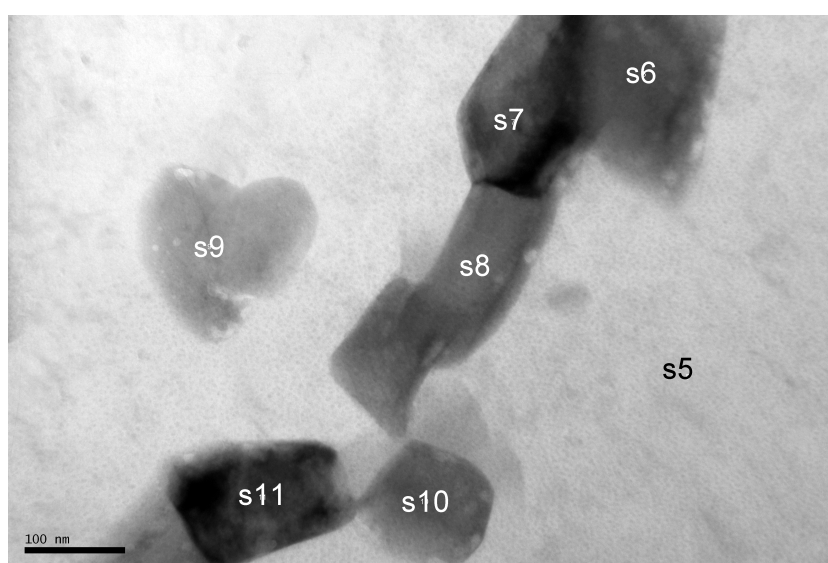


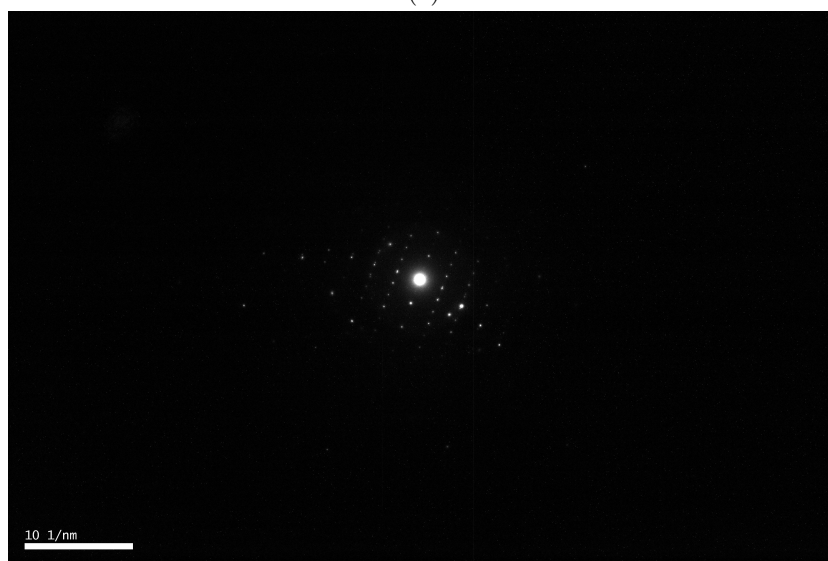
Figure 5.8: Element mapping of “Map Data 3” highlighted by the red box in Figure 5.6, where the white pixels represent the atom locations of (a) aluminium, (b), zinc, (c) magnesium and (d) copper.

5.3 Particle Identification

A TEM image of a sample that was soaked for 400 hours at 200°C is shown in Figure 5.9a. An EDX analysis was performed on the particles labelled s6, s7, s8, s10 and s11 and they were found to be rich in zinc and magnesium. A diffraction pattern was obtained for particle s8 as shown in Figure 5.9b. It revealed the crystal lattice structure and the atomic spacing of that particle which was used to determine its phase. The d-spacing between the atoms from the centre spot and the angle between first spot anti-clockwise from the horizontal and the other detected spots (the angle between planes as shown in Figure 2.31) were measured (see Table 5.1).



(a)



(b)

Figure 5.9: (a) A TEM image of a sample soaked at 200°C for 400 hours and (b) the diffraction pattern of the “s8” particle.

The MgZn_2 phase has a hexagonal close packed lattice. The Miller indices, lattice vectors and d-spacings were obtained from the International Centre for Diffraction Data (ICDD), Powder Diffraction File (PDF) 00-034-0457 [200]. The angle between planes in the lattice was calculated (see Table 5.1). The lattice vectors are a and c are 5.2225 and 8.5684 respectively for the MgZn_2 phase.

Both the angles and d-spacing were compared to the measurements obtained from the diffraction pattern to see whether the values correspond to the database values for MgZn_2 . It can be seen that the d-spacing and angles of the particle and phase database match reasonably well. Hence, the particles with high concentrations of zinc and magnesium are likely to be the MgZn_2 phase.

Table 5.1: The d-spacing and the angle between the planes relative to the first spot anti-clockwise from the horizontal of the particle compared to the database measurements for the MgZn_2 phase.

Particle measurements		PDF database for MgZn_2 phase					
d-spacing (\AA)	θ ($^\circ$)	h	k	i	l	d-spacing (\AA)	θ ($^\circ$)
4.014	0.0	-1	0	1	1	3.990	0
2.007	-0.2	-2	0	2	2	1.997	0
3.116	18.4	-1	0	1	2	3.105	18.7
2.424	29.7	-1	0	1	3	2.411	29.9
4.300	62.0	0	0	0	2	4.270	62.2
2.149	62.1	0	0	0	4	2.138	62.2
2.421	94.3	1	0	-1	3	2.411	94.4
3.124	105.5	1	0	-1	2	3.105	105.6
4.011	124.4	1	0	-1	1	3.990	124.3
2.195	137.3	2	0	-2	1	2.184	137.4
4.532	152.1	1	0	-1	0	4.510	152.2
2.268	151.8	2	0	-2	0	2.260	152.2
2.193	166.8	2	0	-2	-1	2.184	167.0

The same method was used to identify other particles. Figure 5.10 shows a long dark particle lying on a grain boundary and its diffraction pattern of the sample that was soaked for 24 hours. Table 5.2 shows a comparison between the d-spacings and angles between planes of atoms and the excerpt from the ICDD database (PDF 01-072-9560) for the Al_2Cu phase [200].



(a)



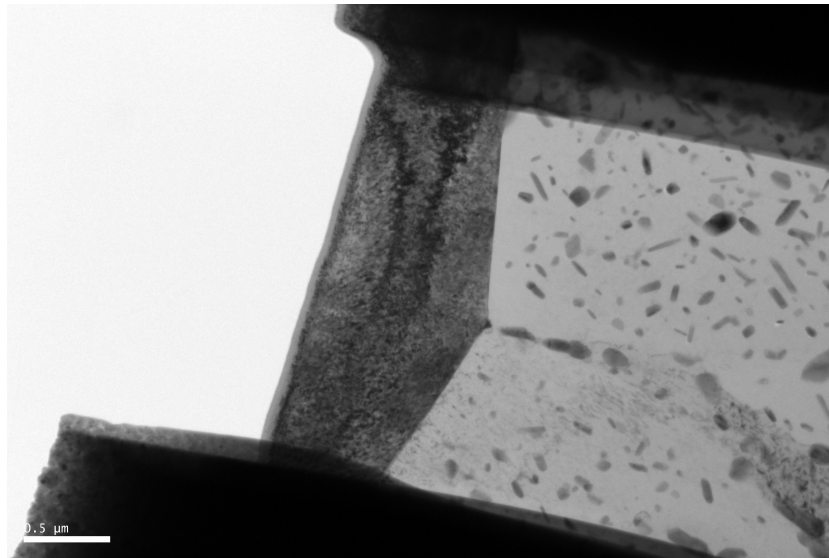
(b)

Figure 5.10: (a) A TEM image of a sample soaked at 200°C for 24 hours and (b) the diffraction pattern of the dark particle on the grain boundary.

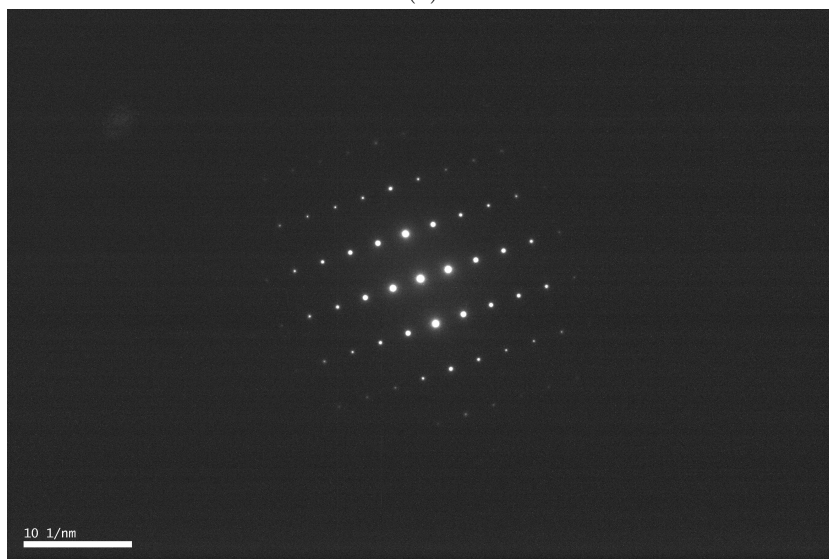
Figure 5.11 shows a very coarse dark particle and its diffraction pattern of the sample that was soaked for 24 hours. Table 5.3 shows a comparison between the d-spacings and angles between planes of atoms and the Mg_2Si lattice parameters (PDF 01-075-5955) [200].

Table 5.2: The d-spacing and the angle between the planes relative to the first spot anti-clockwise from the horizontal of the particle compared to the database measurements for the Al_2Cu phase.

Particle measurements		PDF database of Al_2Cu				
d-spacing (\AA)	θ ($^\circ$)	h	k	l	d-spacing (\AA)	θ ($^\circ$)
3.846	0.0	1	1	1	3.832	0
2.394	29.8	1	3	1	2.380	29.7
4.343	63.8	0	2	0	4.295	63.5
2.359	97.7	-1	3	-1	2.380	97.3
3.831	127.4	-1	1	-1	3.832	127.0
2.141	153.6	-2	0	-2	2.141	153.5



(a)



(b)

Figure 5.11: (a) The large dark particle chosen for identification and (b) the diffraction pattern of that particle.

Table 5.3: The d-spacing and the angle between the planes relative to the first spot anti-clockwise from the horizontal of the particle compared to the database measurements for the Mg₂Si phase.

Particle measurements		PDF database for Mg ₂ Si				
d-spacing (Å)	θ (°)	<i>h</i>	<i>k</i>	<i>l</i>	<i>d</i> (Å)	θ (°)
3.712	0.0	1	1	1	3.690	0.0
1.851	0.0	2	2	2	1.845	0.0
1.234	0.0	3	3	3	1.230	0.0
1.087	30.8	5	1	3	1.080	28.6
1.439	41.6	4	0	2	1.429	39.2
1.947	60.8	3	-1	1	1.927	58.5
1.089	75.1	5	-3	1	1.080	73.0
2.284	92.2	2	-2	0	2.260	90.0
1.141	92.2	4	-4	0	1.130	90.0

5.3.1 Particle Spacing and Size Measurements

Figures 5.12-5.34 show the TEM images at 3 locations of the samples that were soaked at 200°C for 0 hours, 24 hours, 75 hours and 400 hours. These images were used to measure the average particle size and the spacing between the 4 nearest neighbours for each particle. To prevent diffraction shadows from reducing the contrast between the particles and the matrix, the images were cropped to remove them. Once the images were converted to black & white and a threshold was set, the particle analysis tool in Imagej [201] was used to calculate the particle area and positions of the centroids of the particles. However, TEM revealed particles at various depths of the sample that overlap with other particles on different planes. Consequently, the particle analysis tool could not distinguish between 2 particles that were overlapping. Therefore, the measurements obtain by this method were only used for comparisons between the other images analysed with this method and should not be considered as absolute measurements. Particles in the cropped images were a mixture of zinc-magnesium particles and aluminium-copper particles.

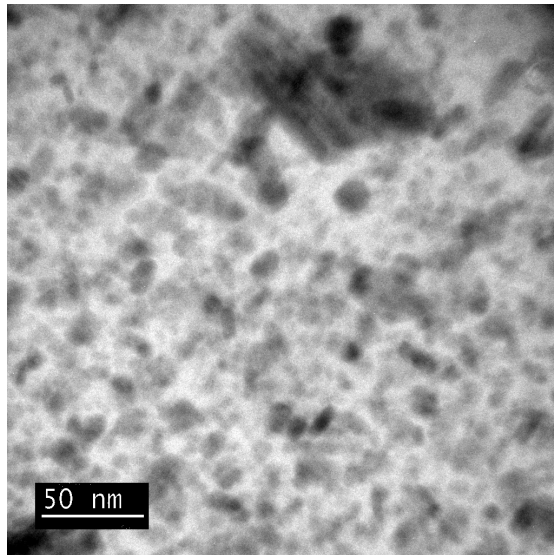


Figure 5.12: The first TEM image used to measure particle spacing and size for the as-received material (0 hours of soak time at temperature).

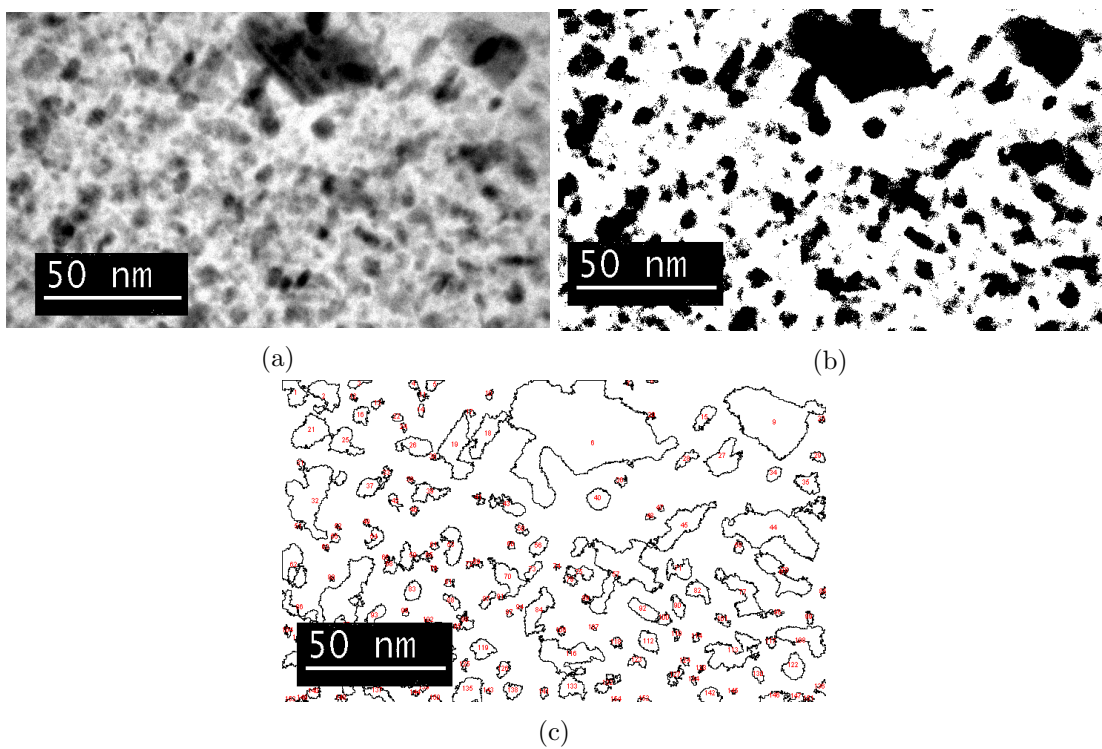


Figure 5.13: (a) A cropped image from Figure 5.12 (as-received sample) which was (b) set to binary (black & white) after setting a threshold. (c) The drawing of particles detected by ImageJ which were used for particle spacing and size measurements.

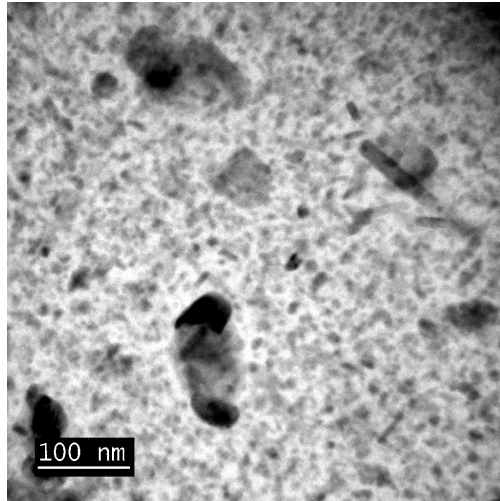


Figure 5.14: The second TEM image used to measure particle spacing and size for the as-received material (0 hours of soak time at temperature).

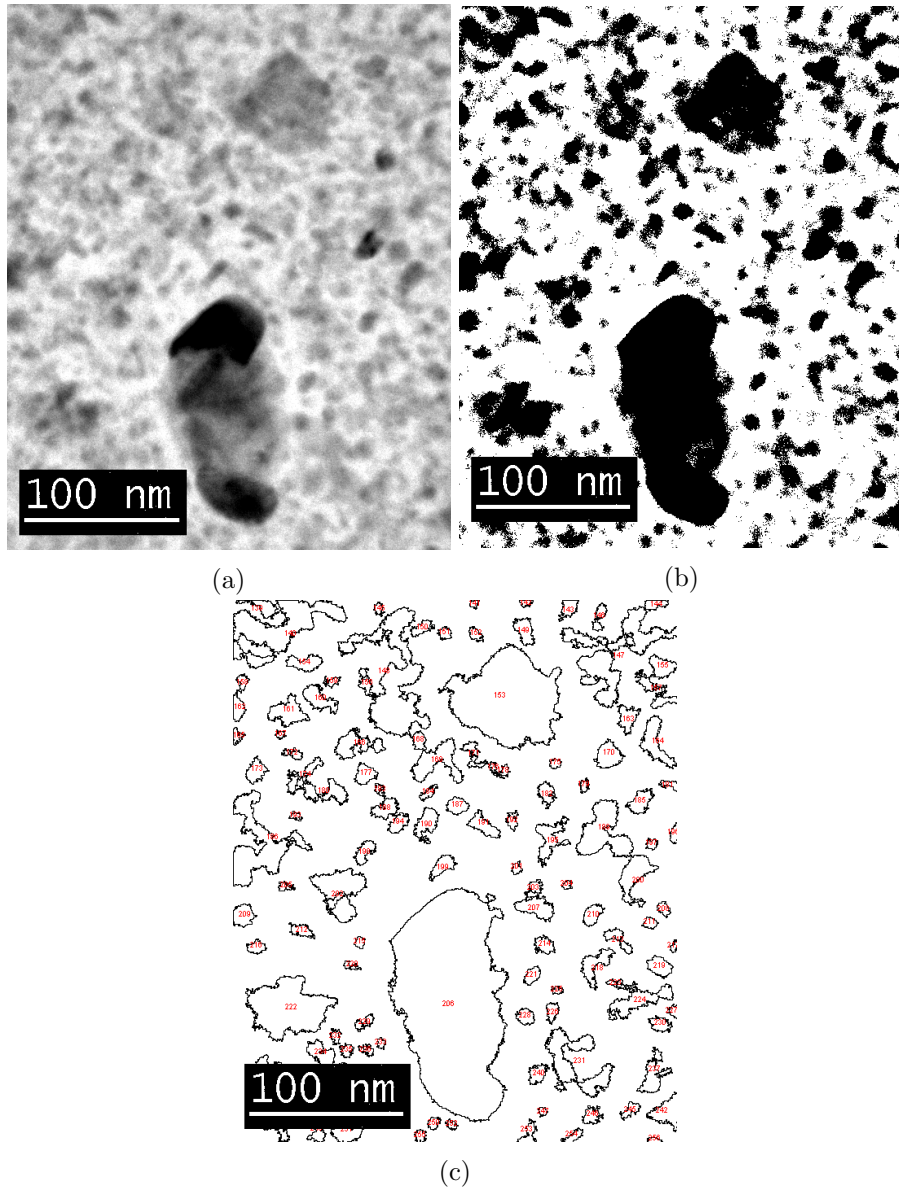


Figure 5.15: (a) A cropped image of Figure 5.14 (the as-received sample) which was (b) set to binary (black & white) after setting a threshold. (c) The drawing of particles detected by ImageJ which were used for particle spacing and size measurements.

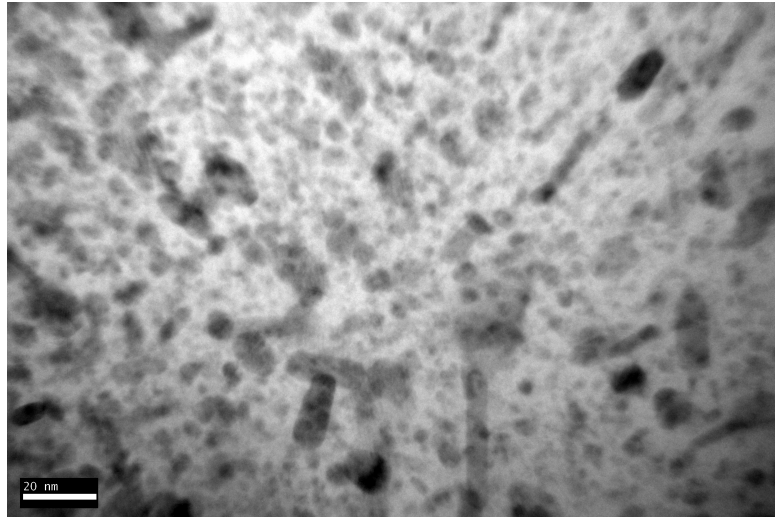


Figure 5.16: The third TEM image used to measure particle spacing and size for the as-received material (0 hours of soak time at temperature).

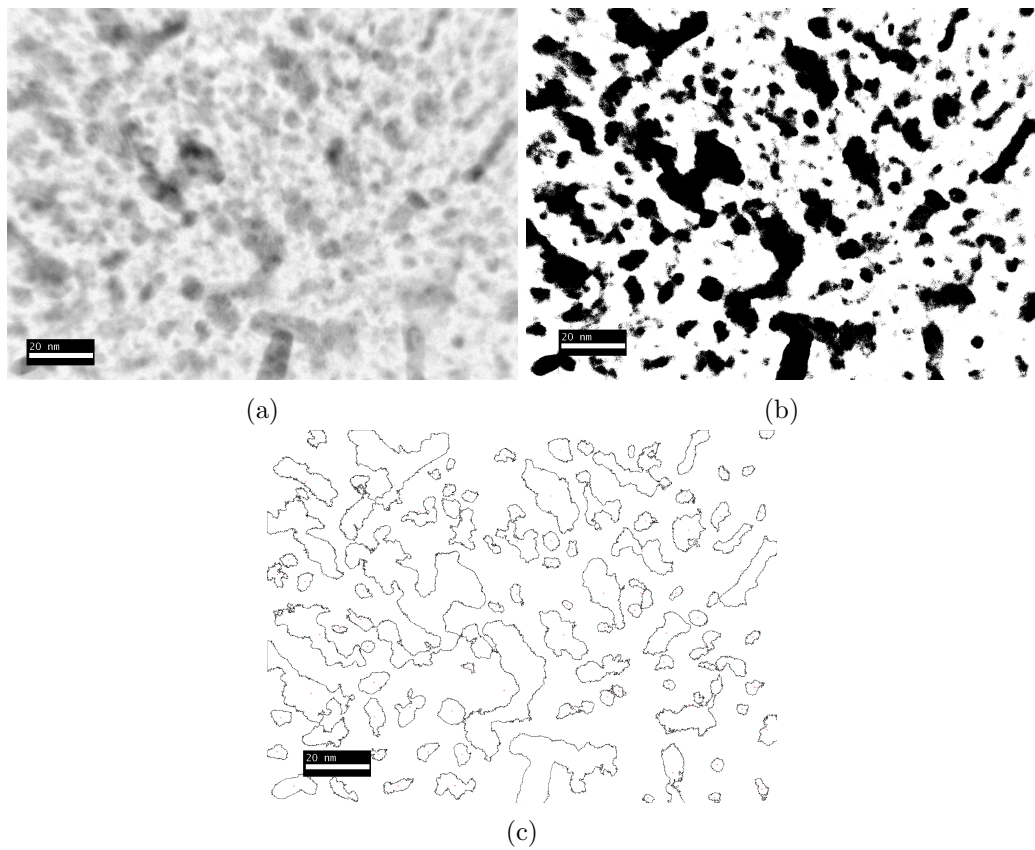


Figure 5.17: (a) A cropped image from Figure 5.16 (as-received sample) which was (b) set to binary (black & white) after setting a threshold. (c) The drawing of particles detected by ImageJ which were used for particle spacing and size measurements.

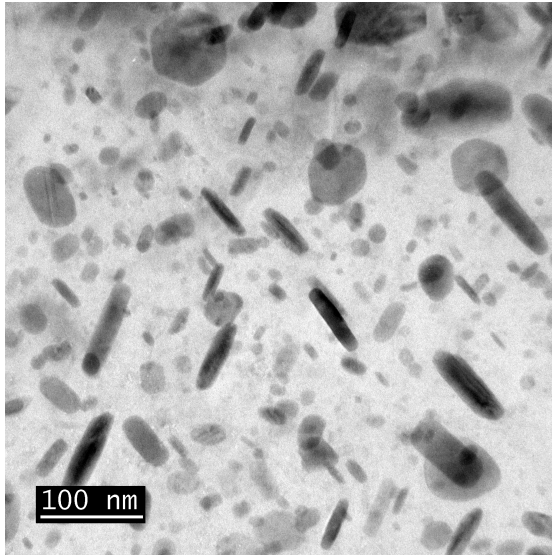


Figure 5.18: The first TEM image used to measure particle spacing and size for a sample soaked for 24 hours at 200°C.

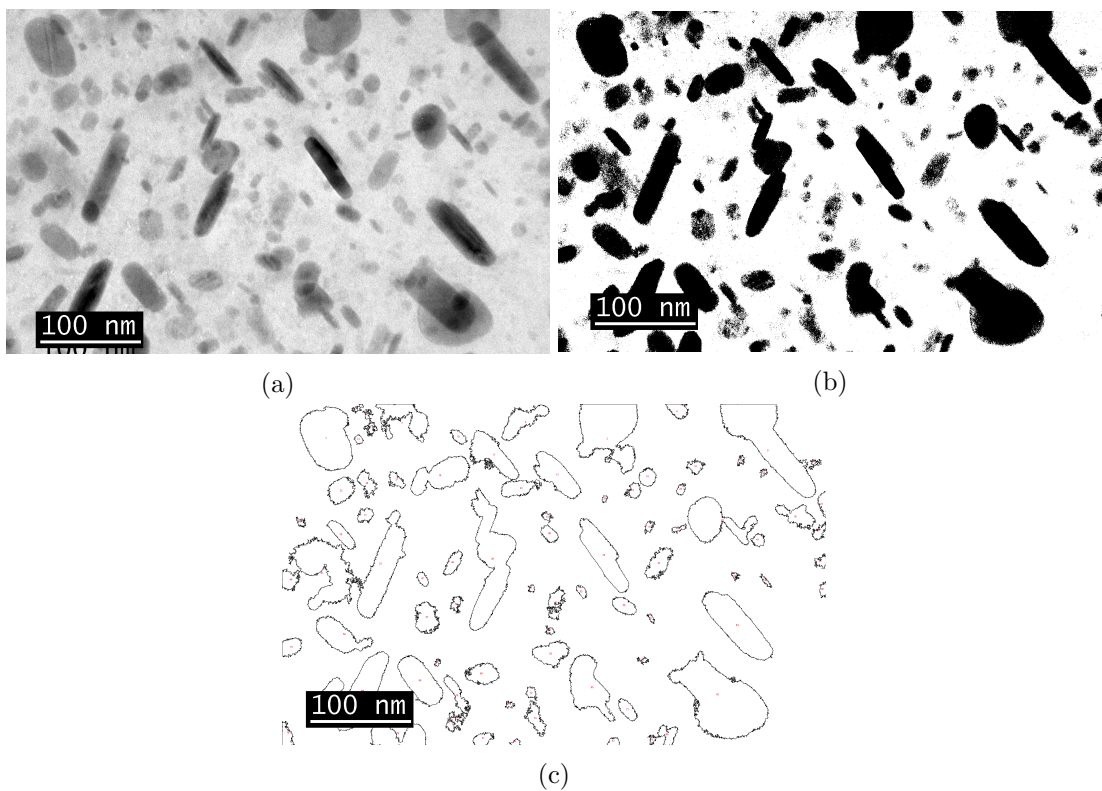


Figure 5.19: (a) A cropped image from Figure 5.18 (a sample that was soaked for 24 hours at 200°C) which was (b) set to binary (black & white) after setting a threshold. (c) The drawing of particles detected by ImageJ which were used for particle spacing and size measurements.

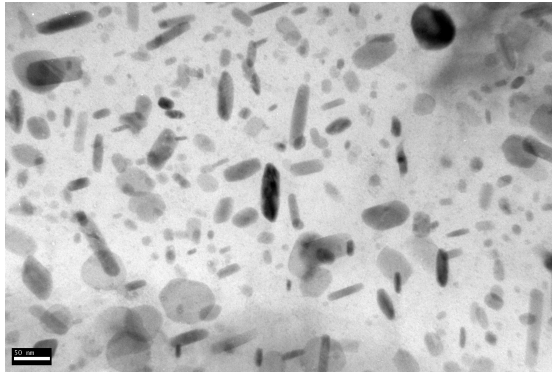


Figure 5.20: The second TEM image used to measure particle spacing and size for a sample soaked for 24 hours at 200°C.

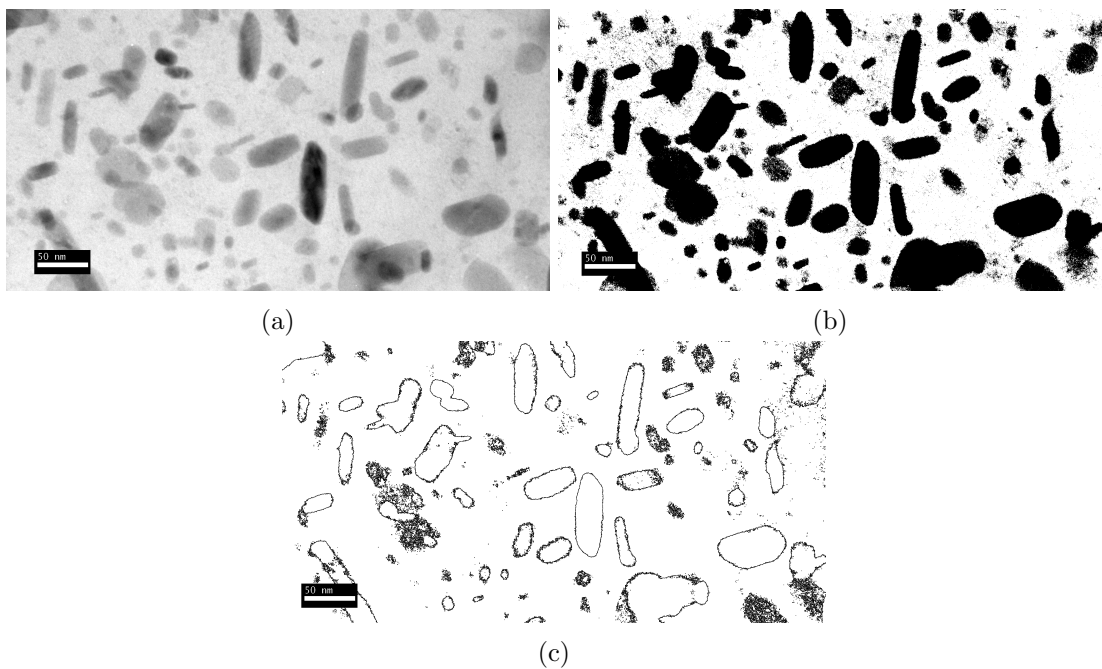


Figure 5.21: (a) A cropped image from Figure 5.20 (a sample that was soaked for 24 hours at 200°C) which was (b) set to binary (black & white) (black & white) after setting a threshold. (c) The drawing of particles detected by ImageJ which were used for particle spacing and size measurements.

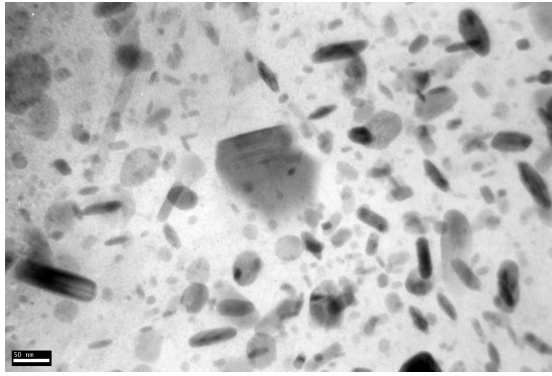


Figure 5.22: The third TEM image used to measure particle spacing and size for a sample soaked for 24 hours at 200°C.

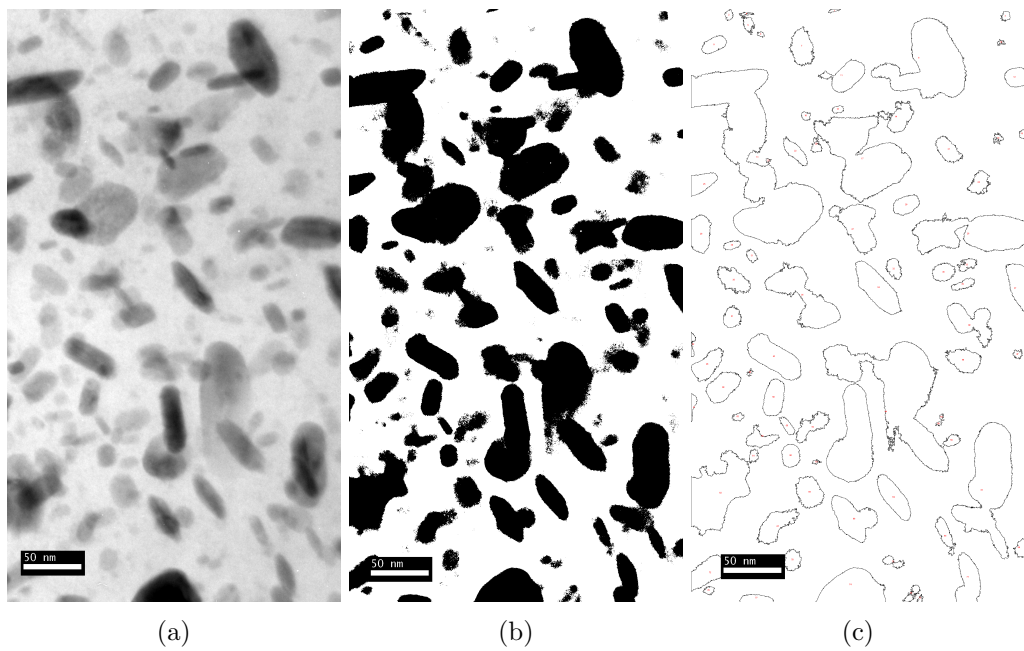


Figure 5.23: (a) A cropped image from Figure 5.22 (a sample that was soaked for 24 hours at 200°C) which was (b) set to binary (black & white) after setting a threshold. (c) The drawing of particles detected by ImageJ which were used for particle spacing and size measurements.

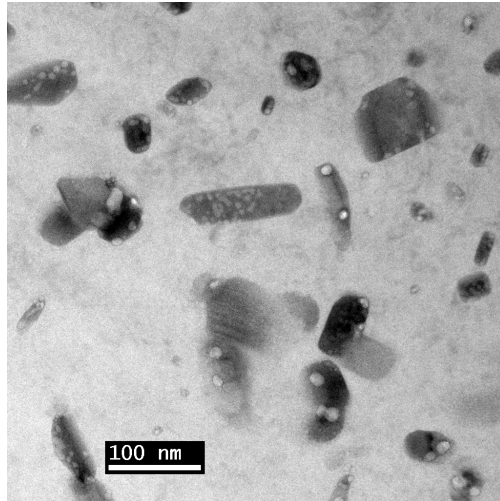


Figure 5.24: The first TEM image used to measure particle spacing and size for a sample soaked for 75 hours at 200°C.

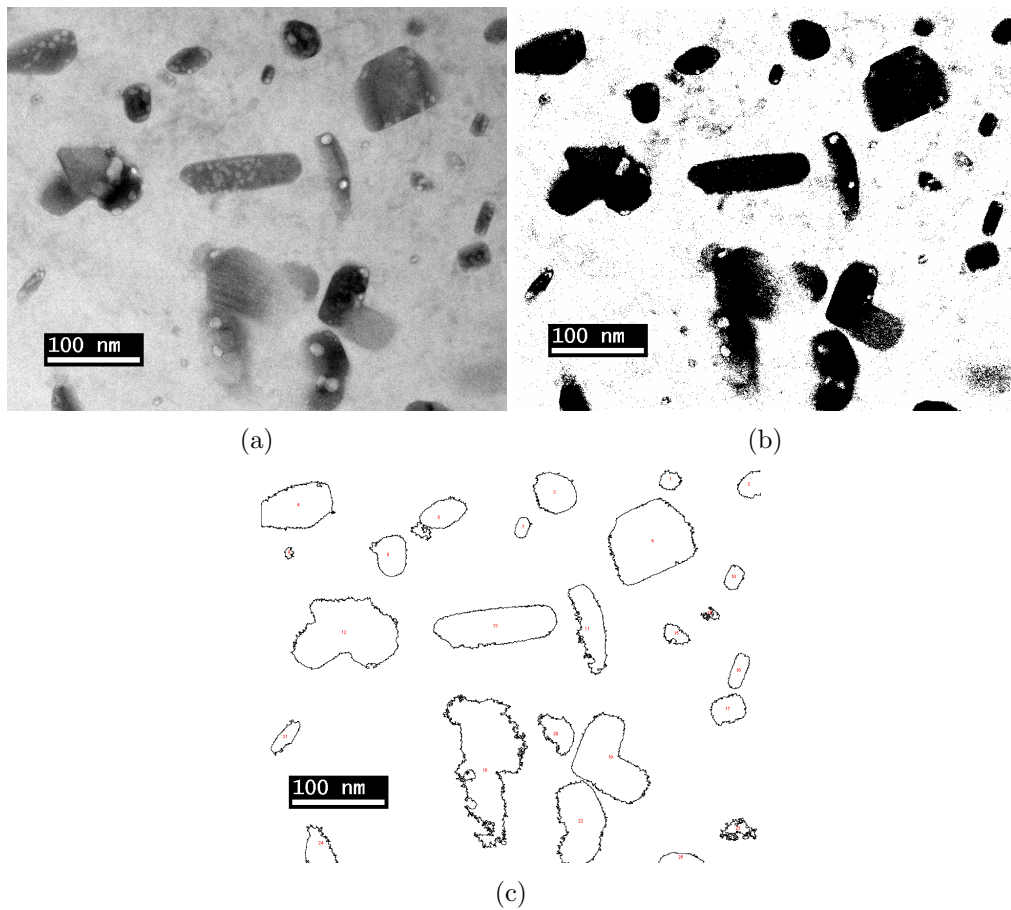


Figure 5.25: (a) A cropped image from Figure 5.24 (a sample that was soaked for 75 hours at 200°C) which was (b) set to binary (black & white) after setting a threshold. (c) The drawing of particles detected by ImageJ which were used for particle spacing and size measurements.

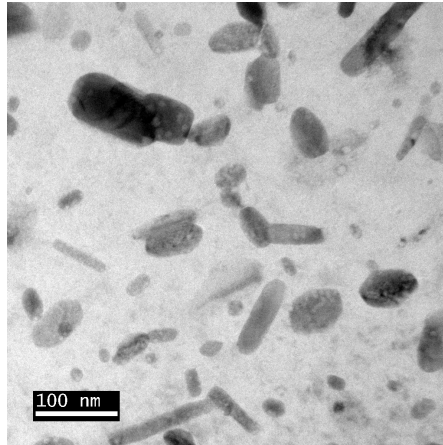


Figure 5.26: The second TEM image used to measure particle spacing and size for a sample soaked for 75 hours at 200°C.

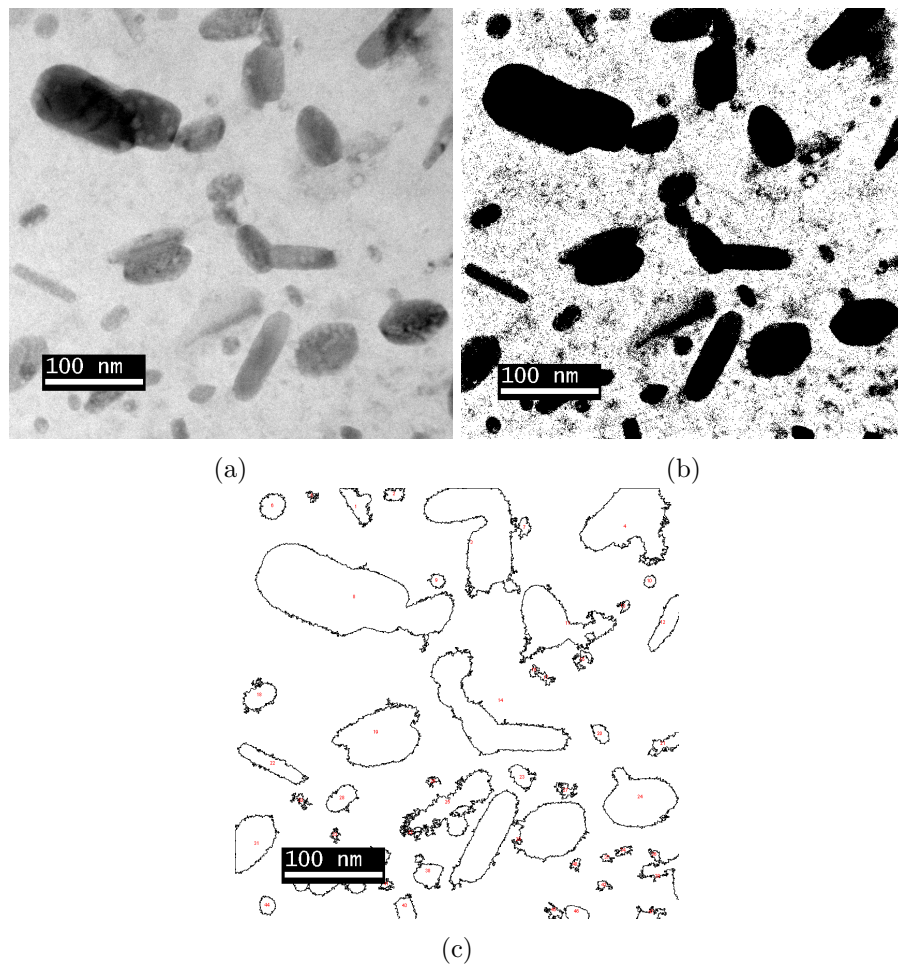


Figure 5.27: (a) A cropped image from Figure 5.26 (a sample that was soaked for 75 hours at 200°C) which was (b) set to binary (black & white) after setting a threshold. (c) The drawing of particles detected by ImageJ which were used for particle spacing and size measurements.

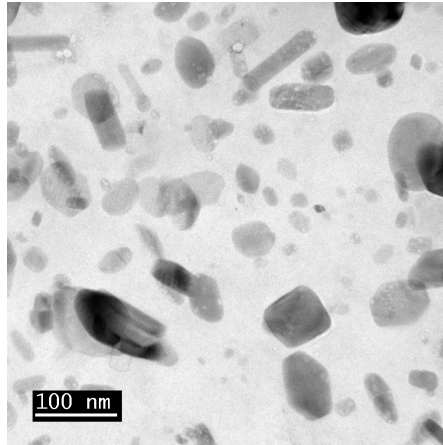


Figure 5.28: The third TEM image used to measure particle spacing and size for a sample soaked for 75 hours at 200°C.

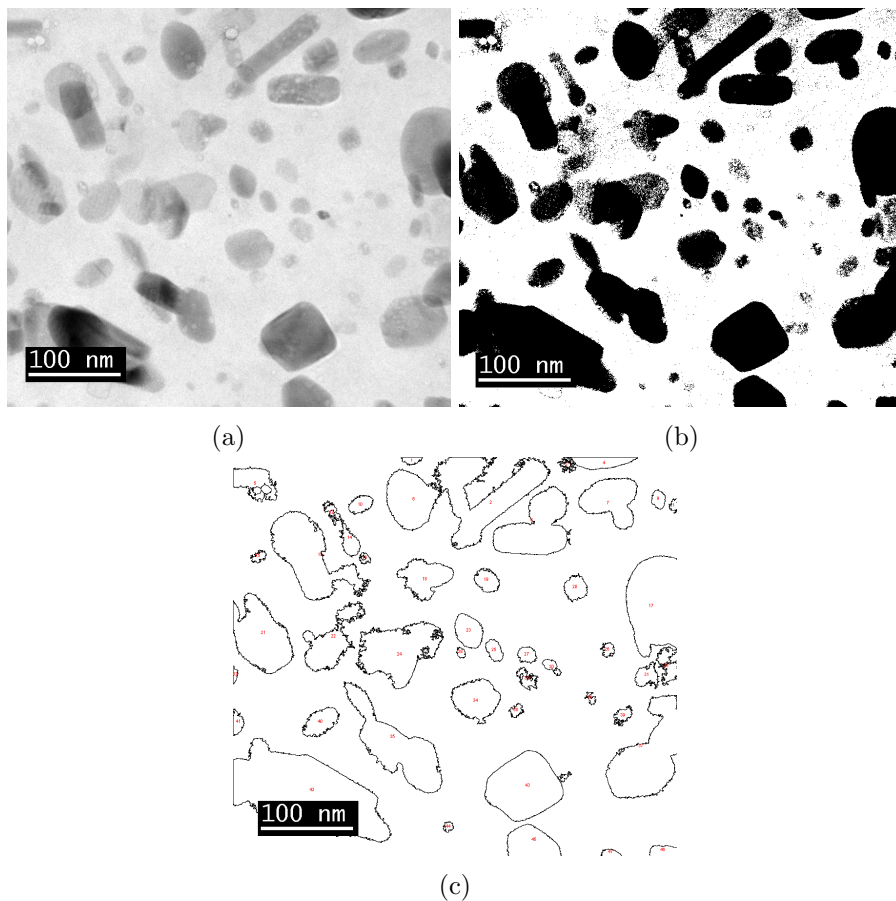


Figure 5.29: (a) A cropped image from Figure 5.28 (a sample that was soaked for 75 hours at 200°C) which was (b) set to binary (black & white) after setting a threshold. (c) The drawing of particles detected by ImageJ which were used for particle spacing and size measurements.

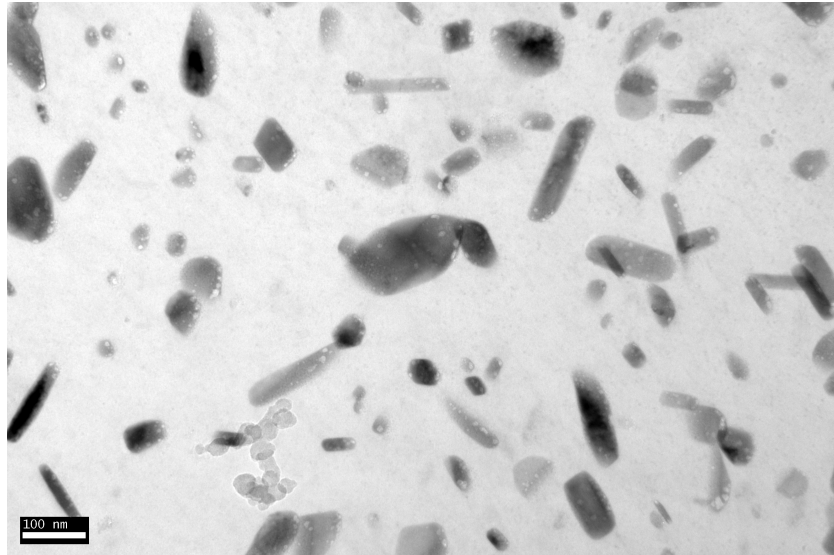


Figure 5.30: The first TEM image used to measure particle spacing and size for a sample soaked for 400 hours at 200°C.

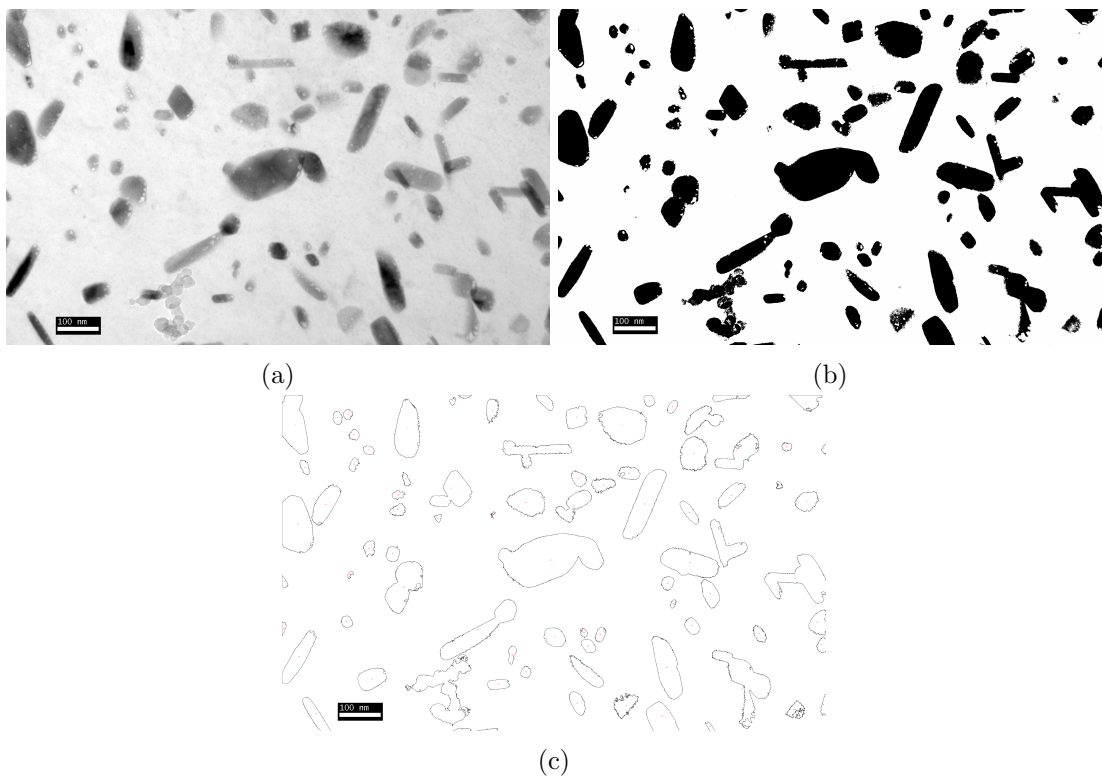


Figure 5.31: (a) A cropped image from Figure 5.30 (a sample that was soaked for 400 hours at 200°C) which was (b) set to binary (black & white) after setting a threshold. (c) The drawing of particles detected by ImageJ which were used for particle spacing and size measurements.

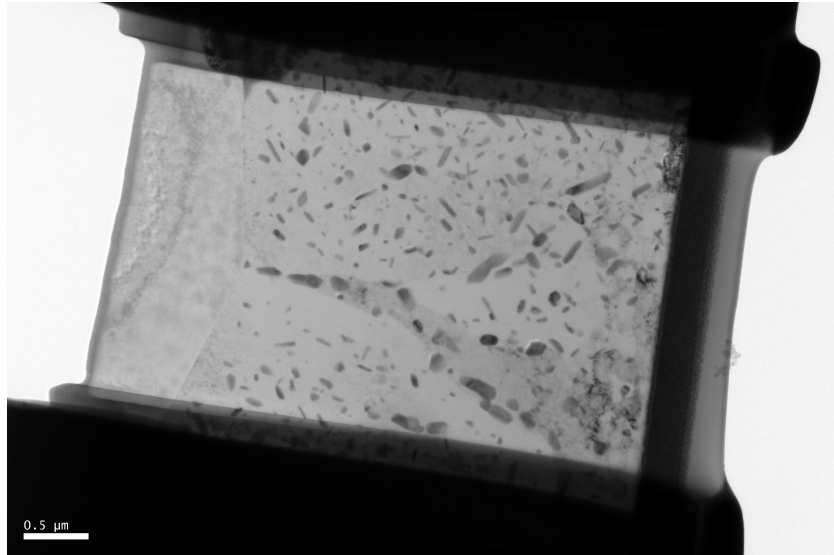


Figure 5.32: The second TEM image used to crop 2 images to measure particle spacing and size for a sample soaked for 400 hours at 200°C.

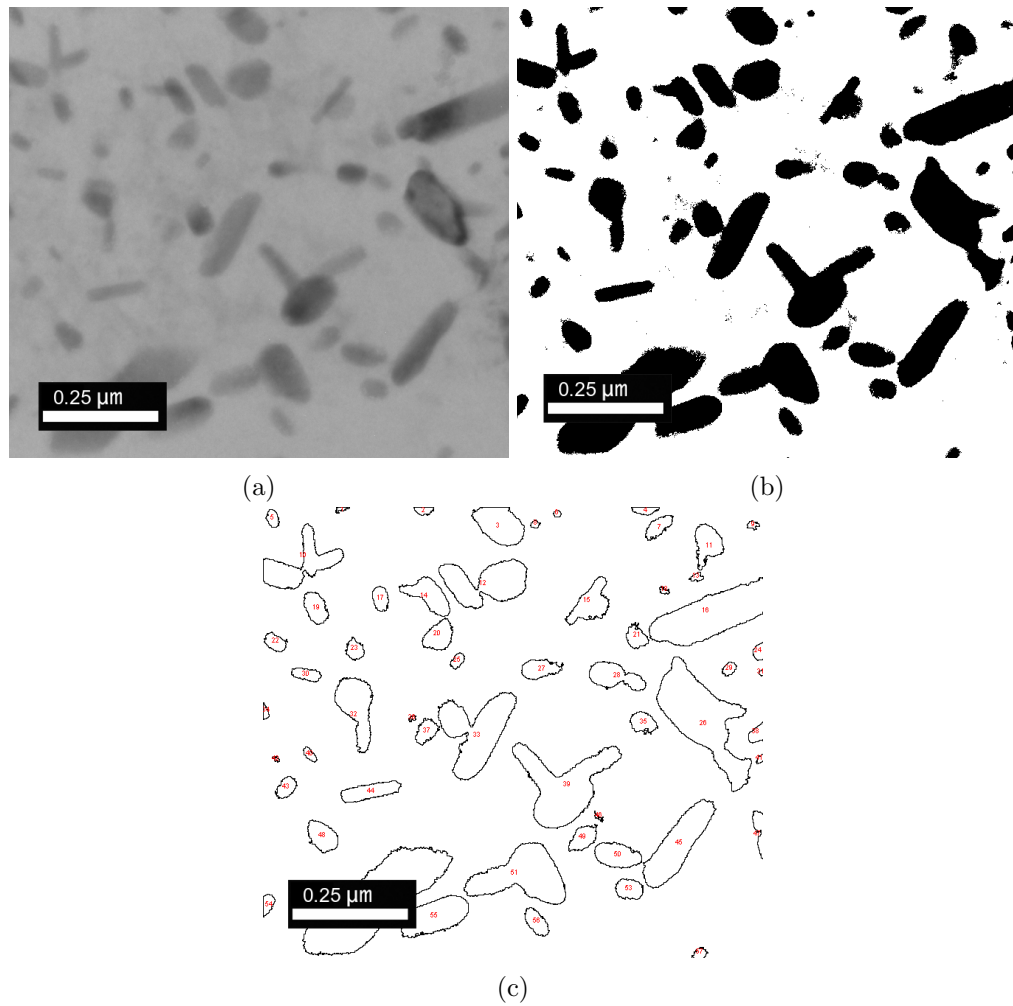


Figure 5.33: (a) The first cropped image from Figure 5.32 (a sample that was soaked for 400 hours at 200°C) which was (b) set to binary (black & white) after setting a threshold. (c) The drawing of particles detected by ImageJ which were used for particle spacing and size measurements.

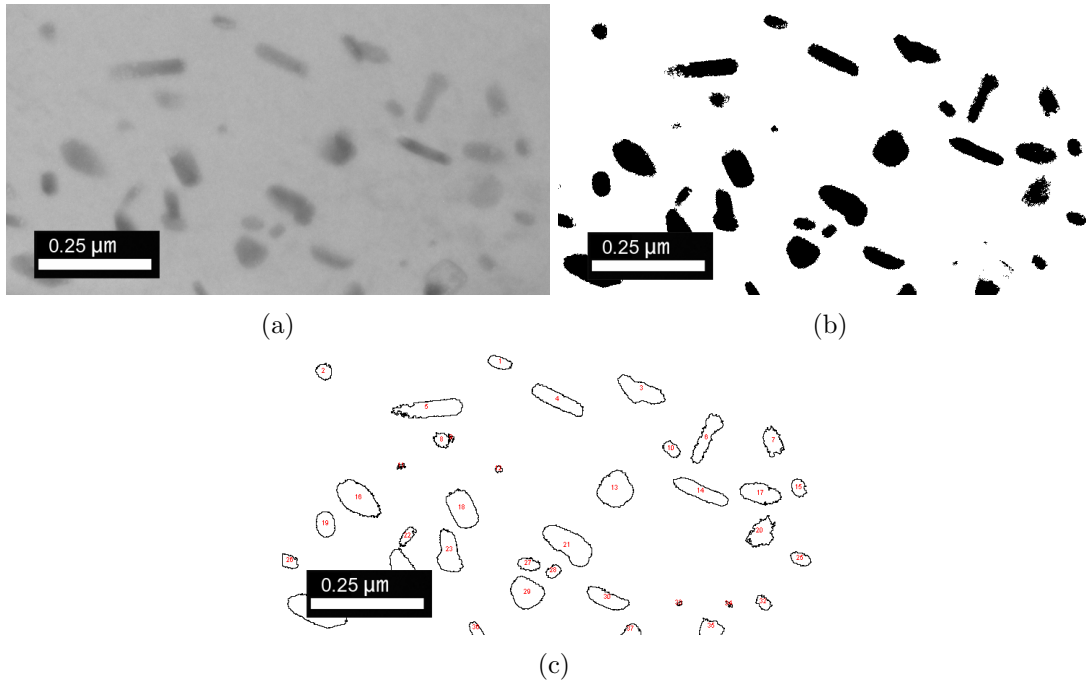


Figure 5.34: (a) A second cropped image from Figure 5.32 (a sample that was soaked for 400 hours at 200°C) which was (b) set to binary (black & white) after setting a threshold. (c) The drawing of particles detected by ImageJ which were used for particle spacing and size measurements.

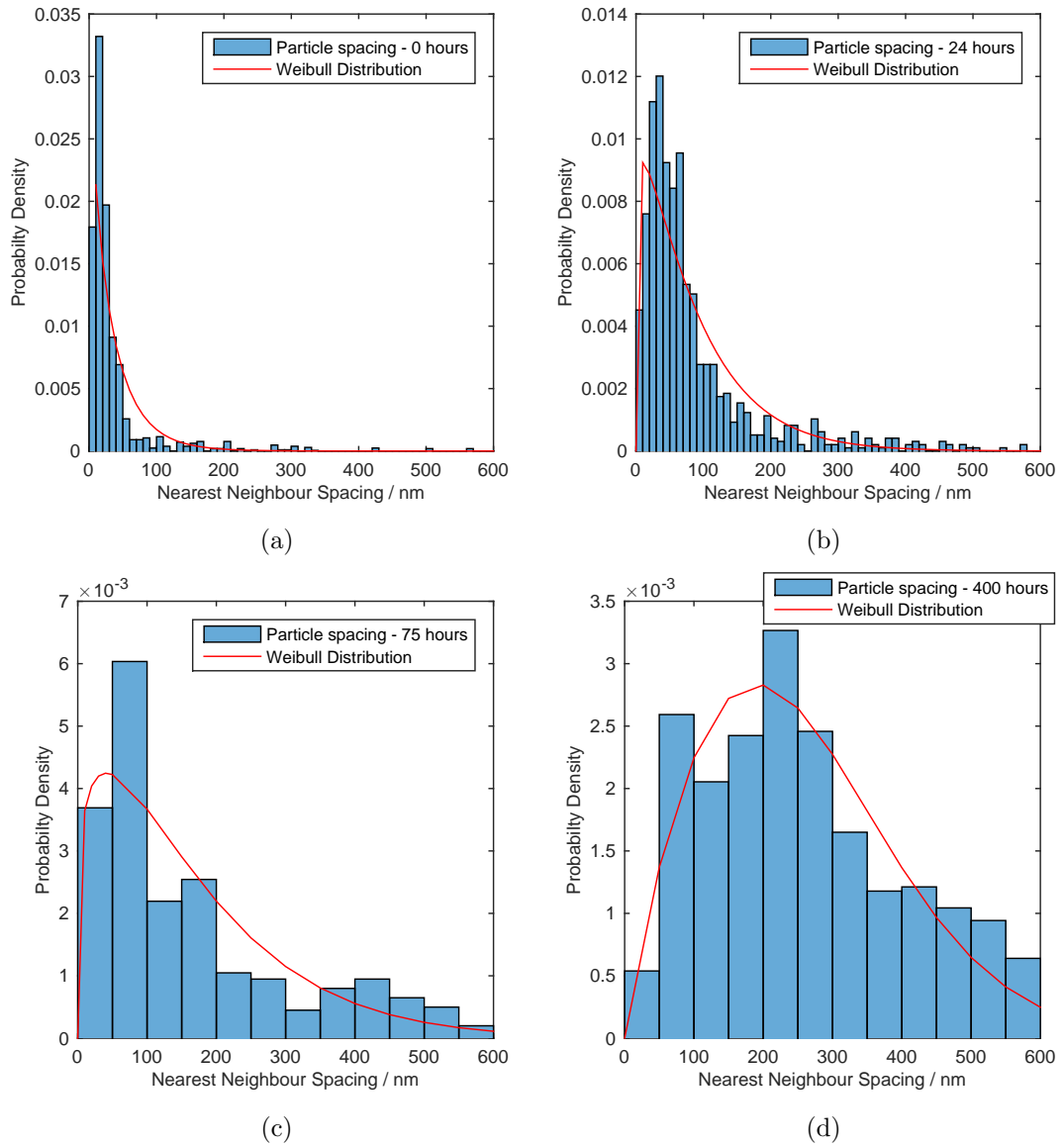


Figure 5.35: The particle spacing between the four nearest neighbours of each particle after soaking at 200°C for (a) 0 hours, (b) 24 hours, (c) 75 hours and (d) 400 hours.

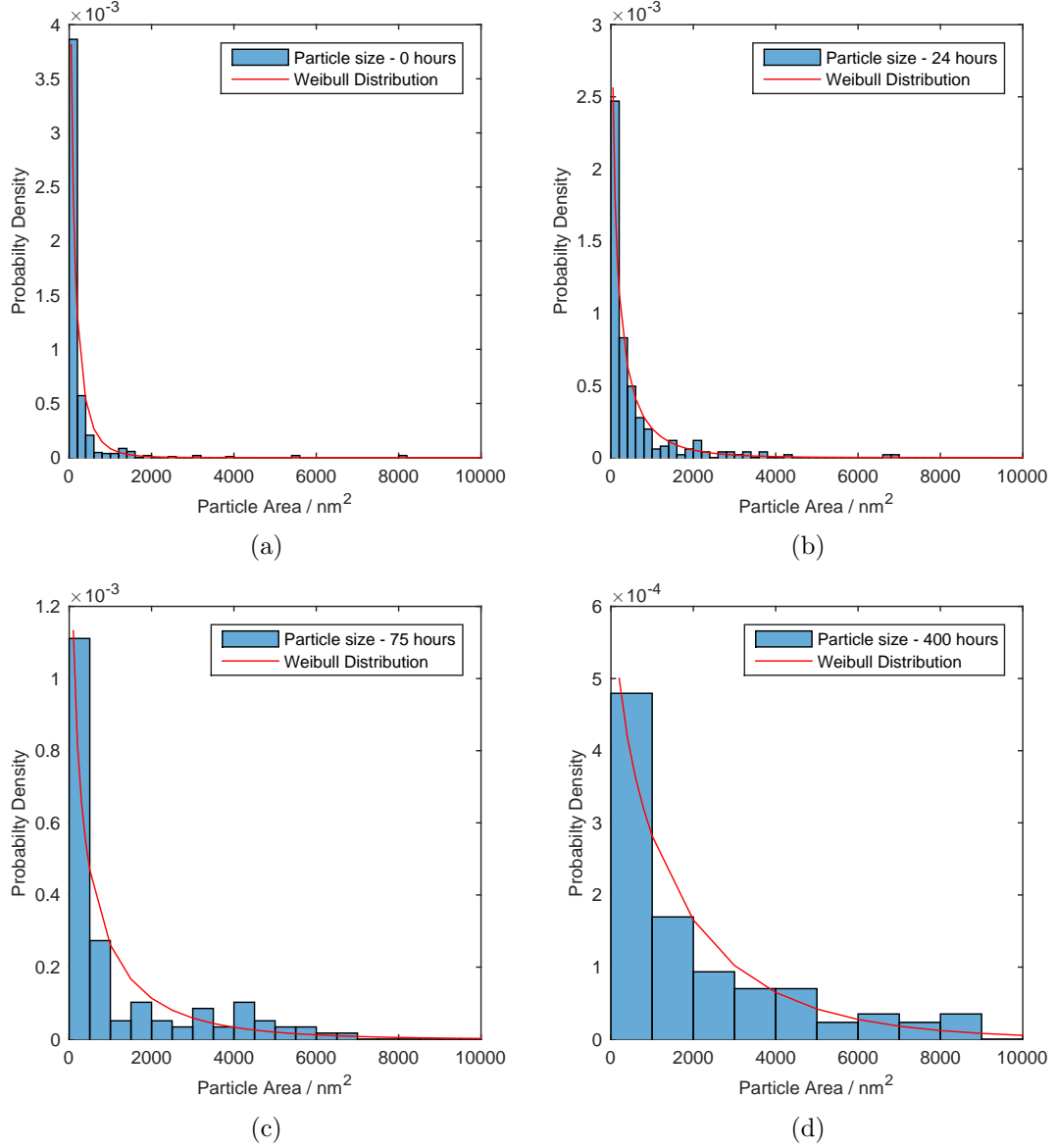


Figure 5.36: The particle size after soaking at 200°C for (a) 0 hours, (b) 24 hours, (c) 75 hours and (d) 400 hours.

$$Binsize = 2 \frac{IQR(x)}{n^{1/3}} \quad (5.1)$$

Figures 5.35 and 5.36 show histograms of the inter-particle spacing of the 4 nearest neighbours and the particle size, respectively. A Weibull distribution was fitted to the histograms to demonstrate the change in probability density function that the particle spacing and size falling within a certain range. The bin width for each sample was determined using the Freedman-Diaconis rule [202] (see equation 5.1), which minimises the difference between the area under the empirical probability distribution and the area

under the theoretical probability distribution. $IQR(x)$ is the interquartile range (the difference between the 75th and 25th percentiles of the data set) and n is the number of observations in the data set x .

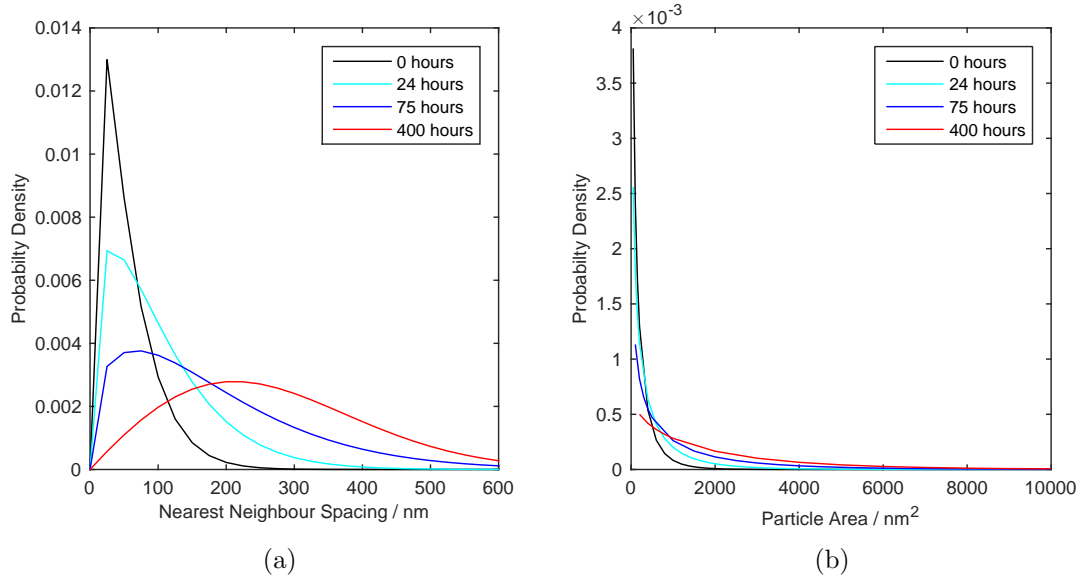


Figure 5.37: A comparison of the distribution curves of (a) the particle spacing between the four nearest neighbours and (b) the particle size.

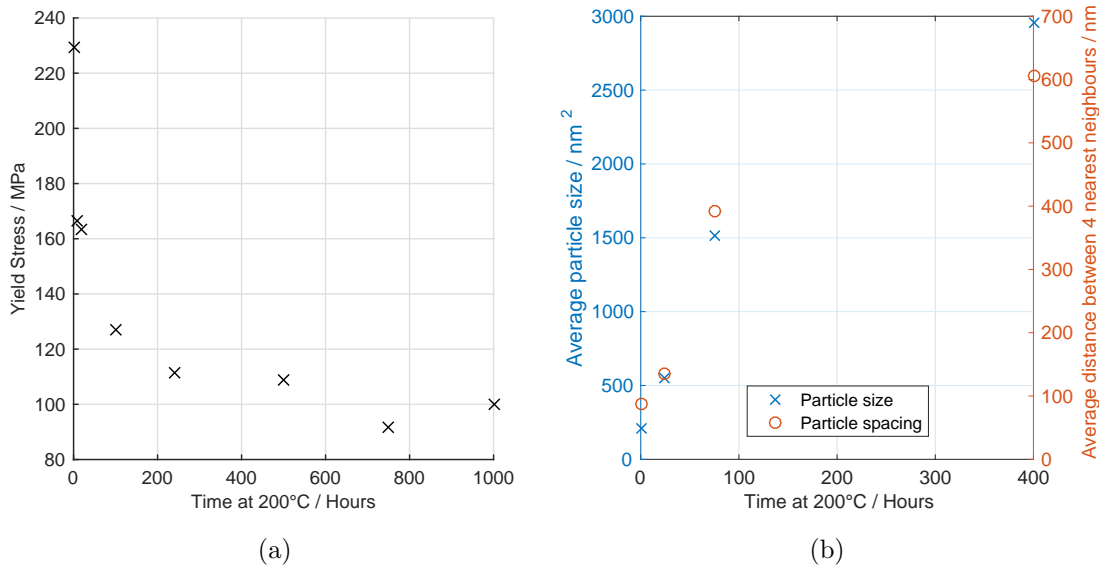


Figure 5.38: The change in (a) monotonic yield stress and, (b) average particle size and distance between the 4 nearest neighbours after time at 200°C.

Figure 5.37 compares the Weibull distribution curves for the inter-particle spacing and particle size. It can be seen in Figure 5.37a that as the soak time increases, the peak of the probability density shifts more to the right, indicating that the particle spacing

is more likely to increase. Additionally, Figure 5.37b shows that the probability density of smaller particle size decreases as soak time increases, indicating that the particles were coarsening with time at temperature. According to the Orowan Bowing equation, the increase of particle size and spacing are correlated to the decrease in yield strength which is shown in Figure 5.38.

The element map of the samples soaked for various times at 200°C showed that the majority of the particles within the 7175-T7351 are composed of zinc-magnesium particles. The TEM particle identification analysis revealed that the phase of the zinc-magnesium particle was most likely MgZn_2 since the d-spacing and angle between planes matched well with the powder diffraction data of that phase. Therefore, it was assumed that the particles observed in the TEM images were MgZn_2 particles. The particle size and spacing measurements suggest that as the soak time increases, the particle size and spacing increases. Furthermore, it was shown that the yield stress decreases with time at temperature which suggests that the size of the particles and the spacing between them directly correlates to the material's strength.

6 Implementation of the Uniaxial Chaboche Model for Stress State Prediction of the Rapidly Ageing 7175-T7351 Aluminium Alloy at Elevated Temperatures

6.1 Introduction

Results in Chapter 4 show that the 7175-T7351 aluminium alloy ages rapidly between 180-230°C. This phenomenon makes the 7175 most likely to be unsuitable for the gearbox housing application due to its rapid ageing at temperatures potentially experienced in the gearbox area of an engine. However, if other candidate aluminium alloys are considered, then their ageing rate will be dependent on the elevated temperature and the composition of the alloy. It would be difficult to determine if or when the material fails to meet design requirements while it is subjected to both elevated temperatures and cyclic mechanical loading. Therefore, it would be beneficial to have some capability to predict the material's fatigue life and in turn, determine its suitability for aerospace gearbox housing applications. The design of the SAGB housing could then be optimised for the greatest weight reduction possible to improve the specific fuel consumption of the aircraft.

Samples were soaked and tested under fully reversed isothermal fatigue conditions at 160°C and 200°C. The soak times were 0 hours (as-received plate condition), 75 hours, 100 hours and 400 hours as described in chapter 3. The sample name designations (specified in section 3.6.3) indicate the soak and test temperature ("160°C" or "200°C"), and soak time in hours ("0h", "75h", "100h" or "400h"). The yield stress data in Chapter 4 showed that after 400 hours, the variation of yield stress with time at temperature (both at 160°C and 200°C) was small. Therefore, the samples soaked for 400 hours were assumed to be "fully-aged", meaning that the sample was thermally stable. Samples that were soaked between 0 hours and 400 hours were considered to be "partially-aged". The partially-aged samples were used to validate model once the material constants were established. Tests were interrupted if the sample exhibited a rapid decrease in stress amplitude leading to failure or the test duration exceeded 300 hours. A novel waveform was used to induce numerically identifiable plasticity per cycle while remaining below

the UTS of the 7175-T7351 aluminium alloy. This allowed the material behaviour to be modelled as a function of plastic strain.

This chapter proposes that the modified unified, uniaxial, viscoplasticity Chaboche model can be used to predict the 7175-T7351 aluminium alloy's stress responses at 160°C and 200°C with the addition of an isotropic function that accounts for material ageing. Two key assumptions that were made for the model were that; the material ageing only affects isotropic hardening and the isotropic hardening can be de-coupled into two components: mechanical softening (due to the mechanical straining) and material ageing (due to exposure at temperature that allows for the diffusion of soluble atoms in the metal matrix). If this behaviour can be predicted, then this model would be a step forward into the development of the assessment of ageing materials for gearbox housing application. The modified model will be able to predict the decrease in strength while subjected to operating temperatures and mechanical straining. It should be noted that this chapter does not attempt to predict the damage accumulated in the samples during fatigue that would lead to sample failure.

Section 6.2 will cover the constitutive equations that comprise the Chaboche model, followed by a description of how the initial material constants of the model were determine in section 6.3. The objective functions used in the optimisation of the material constants is described in section 6.4. The implementation of the Chaboche model and the optimisation process in MATLAB is described in section 6.5.

A comparison between the Chaboche model predictions and the experimental stresses and the validation of the Chaboche model will be covered in section 6.6. The model was used to predict the behaviour of a cyclic stress relaxation test and stress-controlled fatigue tests in section 6.6.4. These findings illuminate the deficiencies in the model that would need to be addressed for future improvements to the model if predictions of material behaviour under gearbox housing operating conditions is required.

6.1.1 Initial Comparisons Between Experimental Test Results of the Strain-Controlled Fatigue Tests

Figure 6.1 shows stress amplitude versus time plots of the isothermal fatigue tests at 160°C and 200°C. It also indicates when the fatigue test began for each sample; for example, the test for sample 160°C-100h began after soaking for 100 hours at

temperature. It can be seen that the stress amplitudes of the as-received and 200°C-75h and 160°C-100h samples were initially different but they eventually converge to stress amplitude values of the as-received samples.

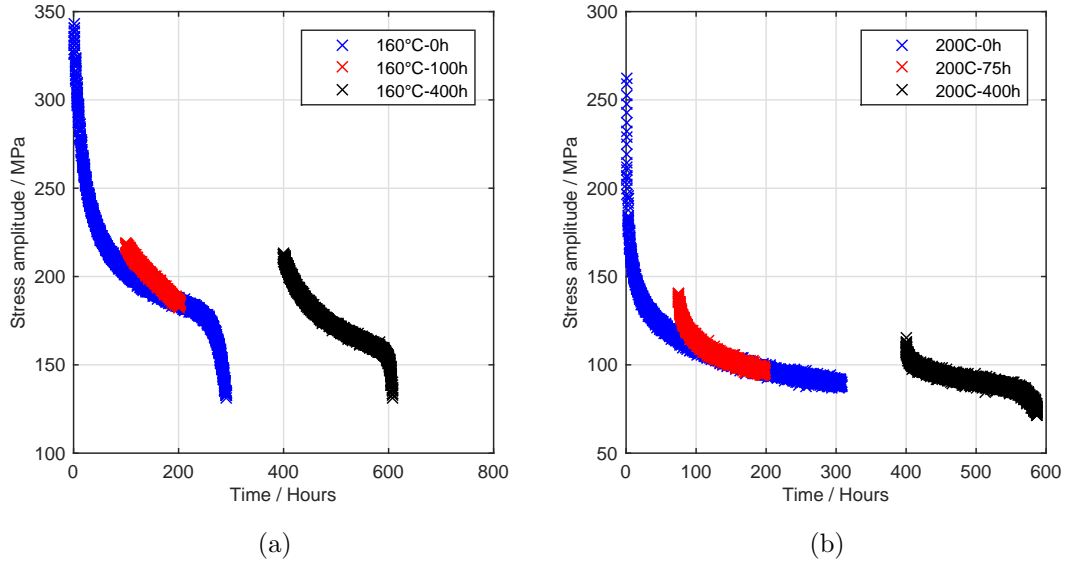


Figure 6.1: A comparison of the stress amplitude versus time at (a) 160°C and (b) 200°C.

In Figure 6.2, the hysteresis loops of samples 160°C-0h, 160°C-100h, 200°C-0h and 200°C-75h were examined after 100 hours and 160 hours at 160°C and 75 hours and 160 hours at 200°C. The as-received samples (200°C-0h and 160°C-0h) underwent mechanical loading and material ageing for the entire test duration. However, samples 160°C-100h and 200°C-75h had only experienced material ageing before they were mechanically loaded. A difference in the stress range and induced plastic strain can be seen between the first cycle of samples 160°C-100h and 200°C-75h (Figures 6.2a and 6.2c) and the as-received samples at the corresponding time at temperature. Eventually the response stabilises and the hysteresis loops are similar (Figures 6.2b and 6.2d). This suggests that the material’s stress response was dependent on both the accumulated plastic strain and the amount of time spent at temperature. Hence, the stress amplitude of the “75h” and “100h” samples were greater than the “0h” samples due to the lack of cyclic softening (a mechanical contribution).

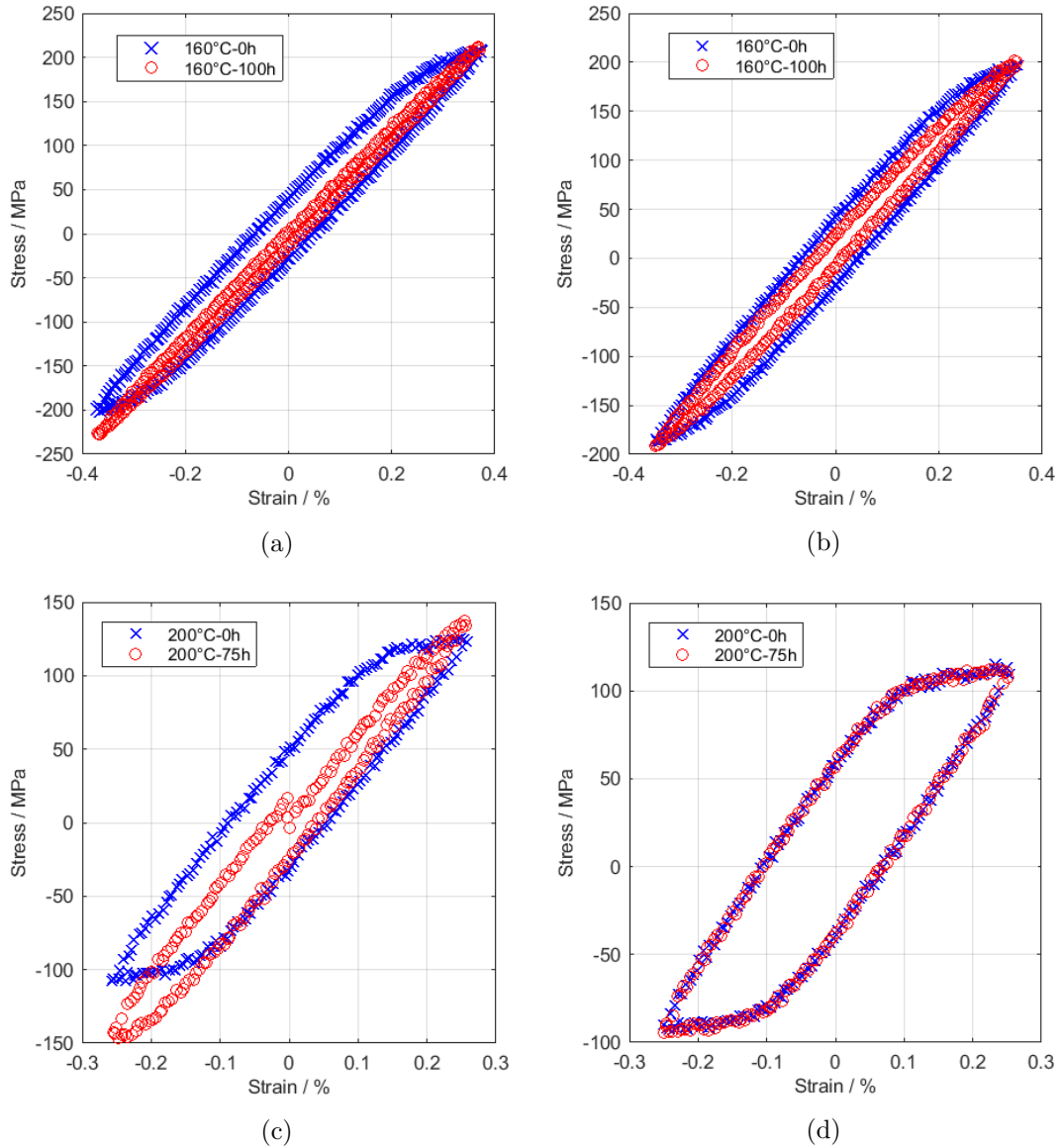


Figure 6.2: A comparison of hysteresis loops of samples 160°C-0h and 160°C-100h after (a) 100 hours and (b) 160 hours at 160°C, and samples 200°C-0h and 200°C-75h after (c) 75 hours and (d) 160 hours at 200°C.

6.2 The Uniaxial Chaboche Model

The unified, uniaxial Chaboche model is a set of constitutive equations that can be used to predict changes in the material's yield surface (kinematic and isotropic hardening or softening) whilst taking viscoplastic behaviour into consideration (stress relaxation). The material parameters were obtained sequentially, assuming that isotropic softening due to mechanical softening and material ageing could be decoupled. First, the mechanistic material parameters were obtained from the samples that were soaked for 400 hours at test temperature before being subjected to

isothermal fatigue conditions, working on the assumption that the material had “fully-aged”. The implications of this was that the microstructure was assumed to have stabilised (no further ageing) and that the isotropic softening behaviour was caused by mechanical straining only. Once these material parameters were established, the ageing parameters were obtained from the as-received (“0h”) samples, where the mechanical softening was subtracted from the overall isotropic hardening. The material parameters were obtained for the equations shown below for this constitutive model.

$$\varepsilon_{total} = \frac{\sigma}{E} + \varepsilon_p \quad (6.1)$$

The total strain can be described by equation 6.1, where E is the Young’s modulus, σ is the total stress and ε_p is the total plastic and viscoplastic strains.

$\dot{\varepsilon}_p$ is the plastic strain rate demonstrated by the flow rule equation below:

$$\dot{\varepsilon}_p = \left\langle \frac{f}{Z} \right\rangle^n \text{sgn}(\sigma - \chi) \quad (6.2)$$

$$\text{sgn}(x) = \begin{cases} 1 & x > 0 \\ 0 & x = 0 \text{ and } \langle x \rangle = \begin{cases} x & x \geq 0 \\ 0 & x < 0 \end{cases} \\ -1 & x < 0 \end{cases} \quad (6.3)$$

Z and n are viscous parameters that describe the stress relaxation behaviour. f is the yield function that determines when plastic strain occurs (equation 6.4). The material is elastic when $f \leq 0$ and plastic when $f > 0$.

$$f = |\sigma - \chi| - R - k \quad (6.4)$$

For this modified mode, k is the initial cyclic yield strength of the “fully-aged”, thermally stable material and χ is the kinematic back stress which is the total sum of the back stresses.

$$\chi = \sum_i^M \chi_i \quad (6.5)$$

$$\dot{\chi}_i = C_i(a_i\dot{\varepsilon}_p - \chi\dot{p}) \quad (6.6)$$

$$p = \Sigma|d\varepsilon_p| \quad (6.7)$$

M , as shown in equation 6.5. For this model, $M = 2$ since it has been shown in previous works that 2 back stresses allows for short and long term dynamic effects for various metals such as the ASTM 319 aluminium alloy, and P91 and P92 steels [14, 98, 100, 103, 153]. $\dot{\chi}_i$ in equation 6.6 represents a back stress rate component where C_i is the rate at which the kinematic hardening saturates to the value a_i . p is the accumulated plastic strain as shown in equation 6.7.

$$R = R_m(p) + R_a(t) \quad (6.8)$$

$$R_m(p) = Q_m(1 - e^{-b_m p}) + H_m p \quad (6.9)$$

$$R_a(t) = Q_{a1}e^{b_{a1}t} + Q_{a2}e^{b_{a2}t} \quad (6.10)$$

$$R_a(t) = \frac{\sigma_{el}}{2} - k \quad (6.11)$$

R is the isotropic drag stress that determines the expansion or reduction of the yield surface. The decomposition of the isotropic hardening or softening is described in equation 6.8, where R_m is mechanical softening and R_a is material ageing. In equation 6.9, the term H_m is the gradient of the linear secondary region of the drag stress, R_m . b_m is the rate at which the drag stress due to mechanical softening saturates to the value Q_m . In equation 6.10, the material ageing is expressed as the sum of two exponential terms, using the material constants Q_{a1} , b_{a1} , Q_{a2} and b_{a2} . The equation determines an additional stress required to accurately describe the material's yield stress at time t before the microstructure has stabilised. R_a was approximated by equation 6.11 (where $\frac{\sigma_{el}}{2}$ is the radius of the yield surface) which ensures that R_a eventually decays to $\approx 0MPa$ when the material's yield locus size equals k (the

asymptotic yield stress). These constants were obtained after the base model for mechanical effects only was established.

$$\sigma = \chi + (R + k + \sigma_v) \text{sgn}(\sigma - \chi) = E(\varepsilon - \varepsilon_p) \quad (6.12)$$

The total stress is summarised by equation 6.12 which is the sum of the stresses due to hardening and viscous effects.

$$\sigma_v = Z\dot{p}^{1/n} \quad (6.13)$$

σ_v is the viscous stress as shown in equation 6.13. This describes the linear relationship between the logarithmic viscous stress and logarithmic equivalent plastic strain rate.

The flowchart in Figure 6.3 demonstrates how the Chaboche model was implemented in MATLAB. After specifying input values (i.e. Number of cycles, initial material constants, etc), the algorithm calculates the state variables that determines material behaviour for the i_{th} cycle. The ‘‘Solve ODEs’’ step utilises the function ODE45 which is explained in more detail in Figure 6.4. This calculates the state variables for the j_{th} data point in the current cycle. At the end of the cycle, the last calculated set of state variables were specified as the first set of state variables of the next cycle and the process repeats.

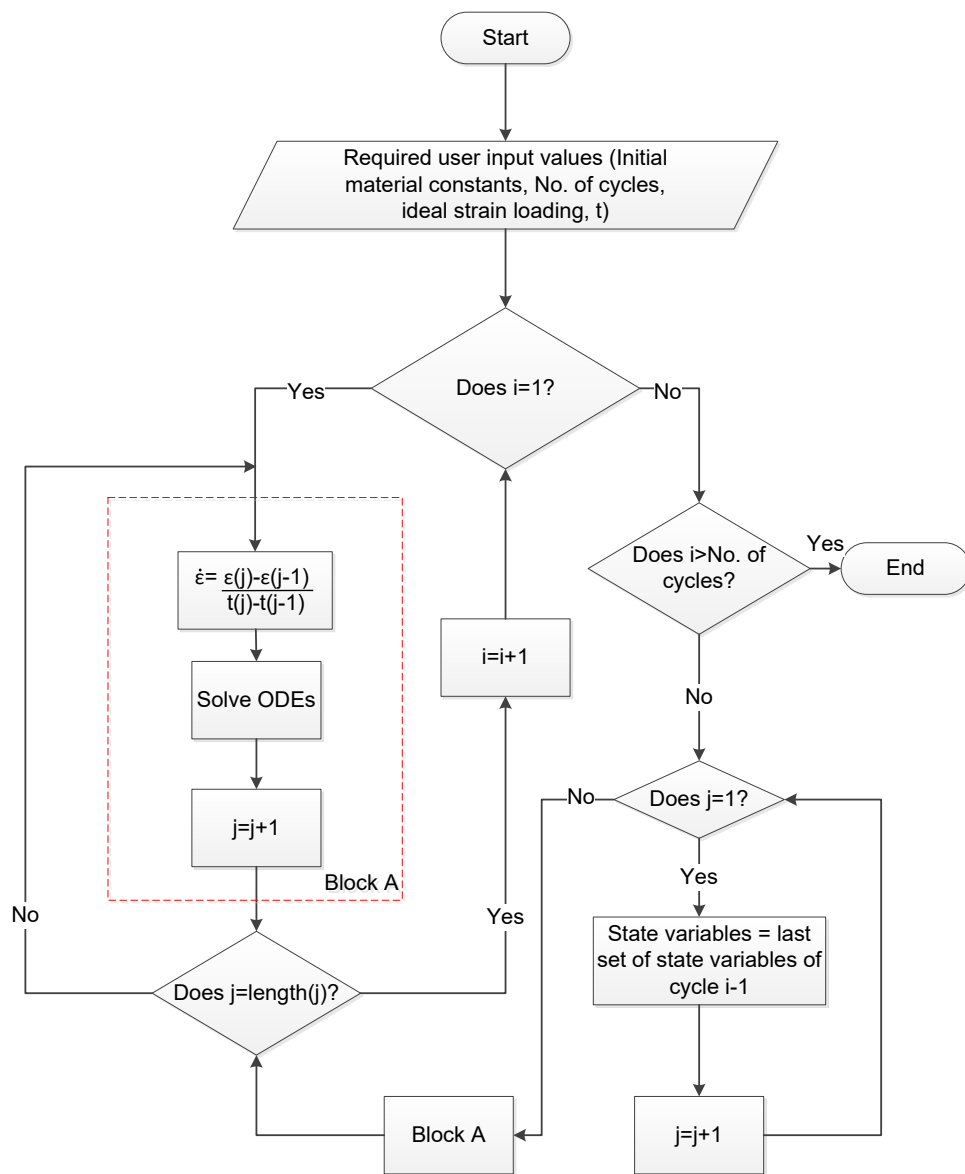


Figure 6.3: Flowchart of Chaboche model implemented in Matlab [123].

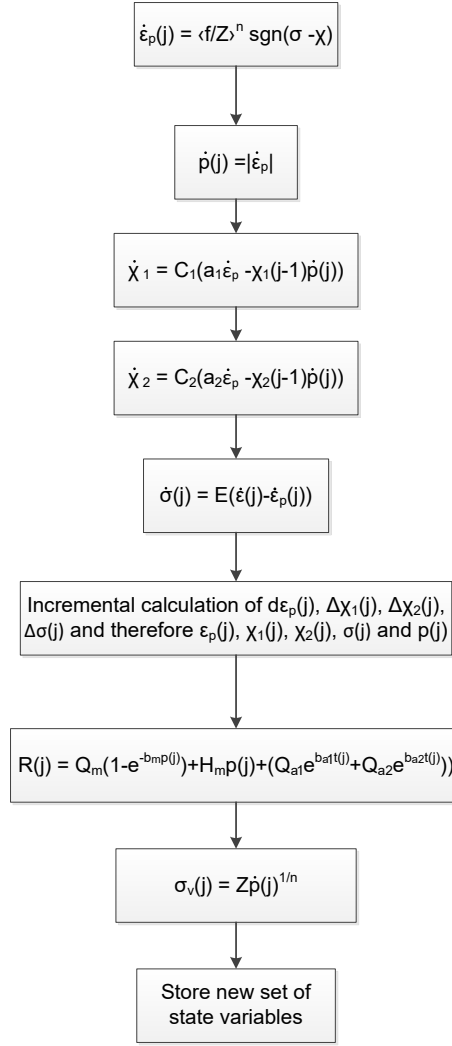


Figure 6.4: The flowchart showing the “Solve ODEs” step.

6.3 Determination of Initial Material Constants

This section will explain how the material constants for the Chaboche model were obtained. Additionally, it will explain how the upper and lower bounds for each constant were obtained for the optimisation process detailed in section 6.5.

6.3.1 Initial Cyclic Yield Stress and Young’s Modulus

For each tensile and compressive branch of the samples soaked for 400 hours, the Young’s modulus and the elastic region of the material was statistically determined as part of Cottrell’s stress partitioning as described in section 2.6.2. This was to obtain the material constants for isotropic and kinematic hardening, and viscous stress. The stress-

strain data was divided into $\varepsilon \geq 0$ and $\varepsilon \leq 0$. For each sub-set of data, a line of best fit was evaluated (using the coefficient of determination, r^2 as an error estimator) for an increasing number of data points, starting with the first 15 data points to the end of the tensile branch. The linear regression that yielded the greatest r^2 value was chosen to represent the linear elastic region. If the starting number of data points is too few, the calculated r^2 value from the linear regression may already be at a maximum and misrepresent the elastic region. Figure 6.5 represents the change of the line of best fit as the number of data points increase and that as the stress becomes non-linear, the goodness of the fit of the linear regression will begin to decrease significantly. The stress value that deviated 5MPa from this linear region was considered to be the elastic limit of the sample. It was found that if the stress difference was less than 5MPa, then a stress value within the elastic region would be chosen due to the scatter in the experimental data. The same approach was used to find the elastic region for $\varepsilon \leq 0$. The Young's modulus of each loading branch was the average of the 2 gradients obtained for that branch. The initial estimate of Young's modulus was measured from the first tensile branch. The upper and lower bounds for Young's modulus were set to the maximum and minimum moduli calculate from this method for the optimisation process.

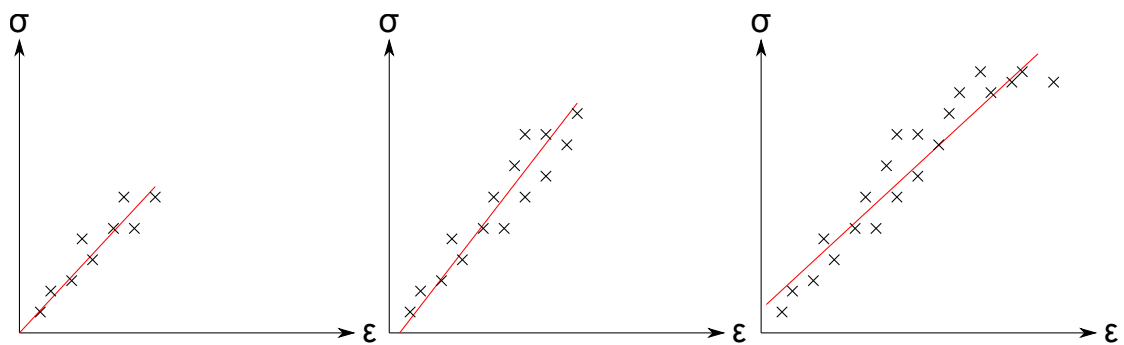


Figure 6.5: A representation of how the line of best fit changes with an increasing number of data points to determine the elastic region and Young's modulus for when the strain is greater than 0 within the tensile branch.

The initial cyclic yield stress of the thermally stable material, k , was found by determining the radius of the elastic region in the second tensile branch (the centre of the linear elastic region to the stress value that deviates 5MPa from the region as previously shown). The upper limit of k was the yield stress of the material and the lower limit was 50% of the initial estimate of k for the optimisation process.

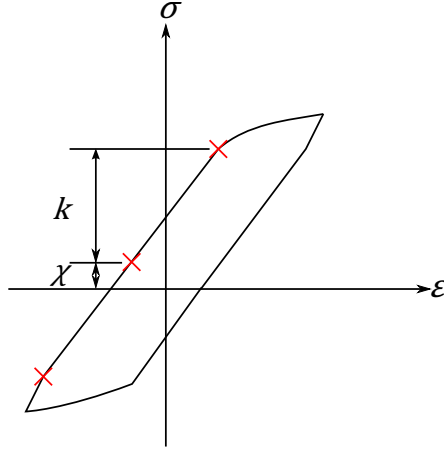


Figure 6.6: Determining initial cyclic yield stress of the thermally stable, k , from the second tensile branch.

6.3.2 Mechanical Softening Parameters

For samples 160°C-400h and 200°C-400h, it was assumed that the decrease in drag stress of the samples soaked for 400 hours was due to mechanical softening, R_m . The experimental R_m was estimated using Cottrell's stress partitioning method [105], where the yield surface radius, $\frac{\sigma_{el}}{2}$, was the sum of $R_m + k$ (equation 6.14).

$$\frac{\sigma_{el}}{2} = R_m + k \quad (6.14)$$

$$b_m = - \left(\ln \left(1 - \frac{R_m}{Q_m} \right) / p \right) \quad (6.15)$$

The term H_m was determined by finding the gradient secondary linear region of the drag stress as shown in Figure 6.7a. Once this was found, $H_m p$ was subtracted from the overall drag stress and the saturation value, Q_m , could be identified. Equation 6.9 can be rearranged (as shown in equation 6.15) to find b_m where the values for R_m and p were the position of a transitional point in the drag stress before saturation, demonstrated by the red circle in Figure 6.7b. The predicted curve was forced through that point. Figure 6.7c shows the predicted mechanical softening compared to the experimental values. The tertiary fatigue stage was excluded from this estimation since this current model does not cover such behaviour.

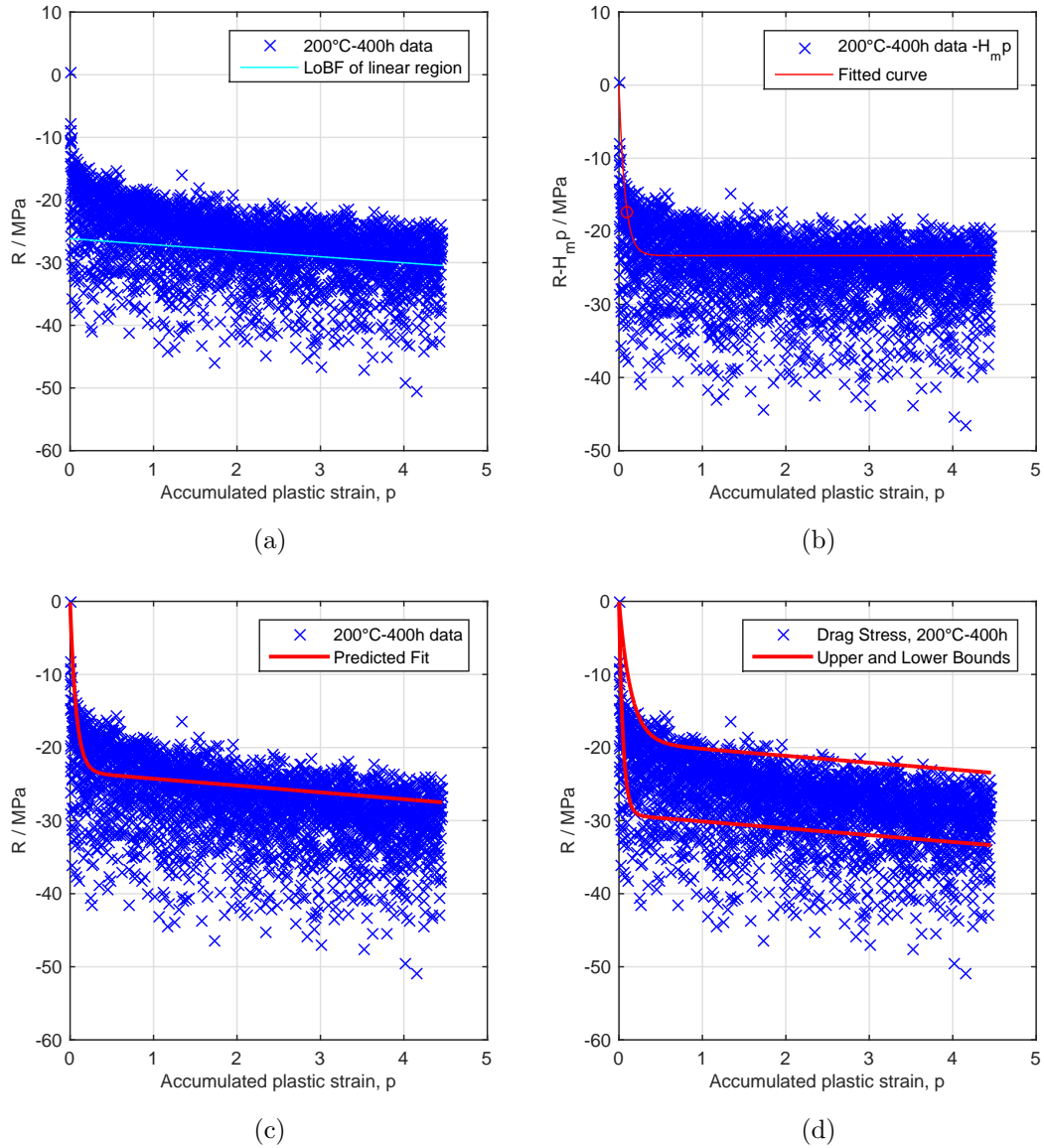


Figure 6.7: Drag stress data from sample 200°C-400h. An estimation of (a) H_m , (b) Q_m and b_m after $H_m p$ was subtracted for the drag stress, (c) the overall prediction of the drag stress versus accumulated plastic strain and (d) a representation of the bounds implemented in the optimisation process.

The bounds for Q_m were taken as the maximum and minimum drag stress values where the data scatter was most dense after $H_m p$ was subtracted. The bounds for b_m were chosen to ensure that the predicted curve remains on the outskirts of where the drag stress scatter was dense as shown in Figure 6.7d. The constant H_m remained the same during the optimisation to ensure that the rate of cyclic softening in the secondary softening region remained fix that follows the linear softening behaviour.

Figure 6.8 shows an example of how significant differences in the calculated yield surface occurred which accounts for the scatter in the experimental data shown above.

For some cases, a detectable deviation from the linear elastic region may not occur at the beginning of a tensile or compression branch. Therefore, σ_{el} can change significantly between cycles which directly affects the calculation for R_m .

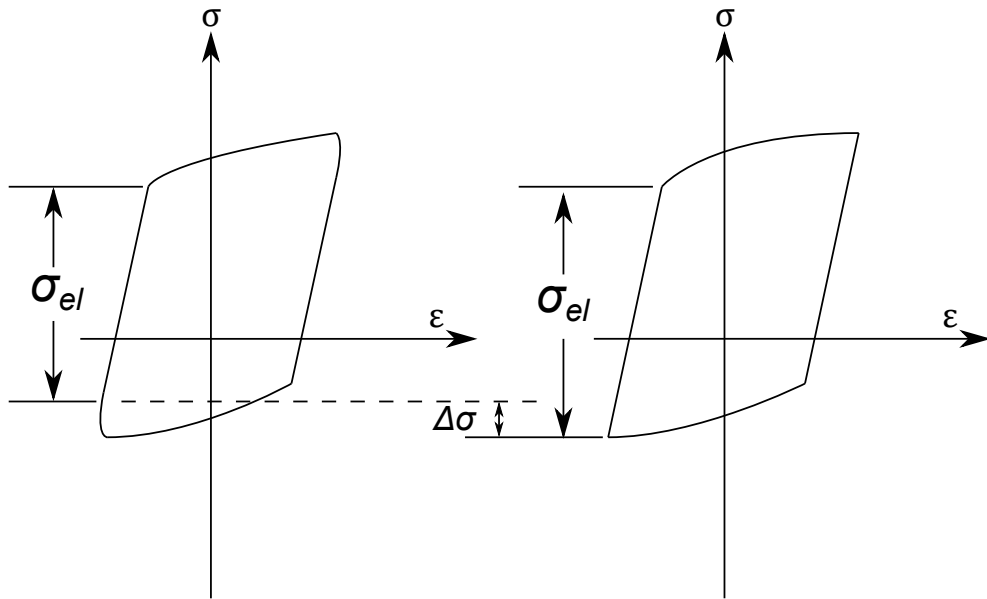


Figure 6.8: A schematic representation of how the variation experimental data can lead to significant scatter in the calculated yield surface, σ_{el} .

6.3.3 Kinematic Hardening Parameters

The monotonic loading region (first tensile branch) was used to determine the kinematic hardening parameters, assuming that all hardening was due to kinematic effects. It was also assumed that the back stress saturates to a maximum value by the end of this branch. Since there was scatter in the monotonic loading data for both 160°C-400h and 200°C-400h samples, polynomial equations were used to approximate the monotonic loading regions (see Figure 6.9).

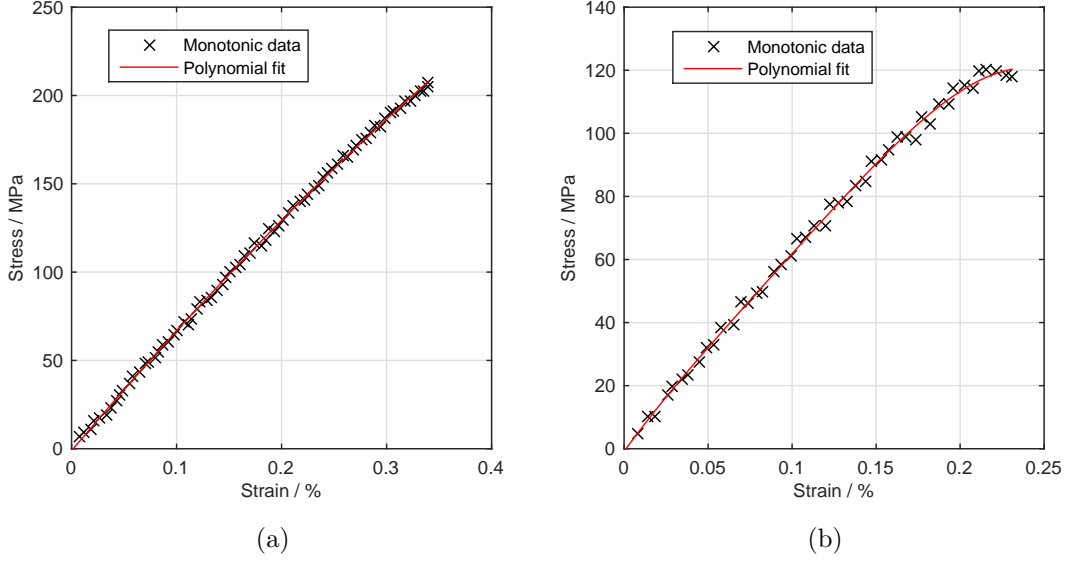


Figure 6.9: The monotonic loading regions of samples (a) 160°C-400h (b) 200°C-400h.

$$\chi_1 = \sigma - \sigma_y \quad (6.16)$$

$$\chi_2 = \sigma - \sigma_y - \chi_1 \quad (6.17)$$

$$C_i = - \left(\ln \left(1 - \frac{X_i}{a_i} \right) / p \right) \quad (6.18)$$

When the samples exceed their elastic limit, the back stresses χ_1 and χ_2 non-linear kinematic hardening takes place as shown in Figure 6.10. The point of the partition was chosen to be halfway in the plastic strain range. It was assumed that χ_2 had negligible influence in the χ_1 dominant region, allowing the back stress to be calculated using equation 6.16. As the plastic strain increases, χ_1 approaches saturation and χ_2 becomes more dominant. Therefore, χ_2 can be calculated using equation 6.17. The back stress was plotted against the plastic strain (see Figure 6.10) from which a_1 , C_1 , a_2 and C_2 was approximated. a_1 was the maximum stress in the χ_1 dominant region. C_1 was obtained in a similar way to b_m , where the chosen value for χ_1 and ε_p was taken at a transitional point on the χ_1 curve (as shown in Figure 6.11 by the red circle). The values for χ_1 and p were substituted into equation 2.15 and rearranged to form equation 6.18. For this case, the accumulated plastic strain, p , was equal to the plastic strain of the monotonic

curve. Once the parameters for χ_1 were found, the same process was repeated to find the parameters a_2 and C_2 by substituting χ_1 into equation 6.17 for every plastic strain value.

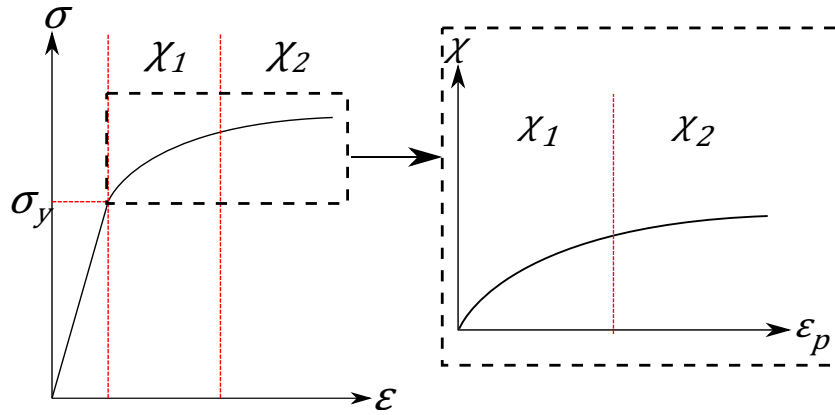


Figure 6.10: A schematic representation of how the monotonic curve was partitioned and the data used to determine the material constants for the back stresses χ_1 and χ_2 .

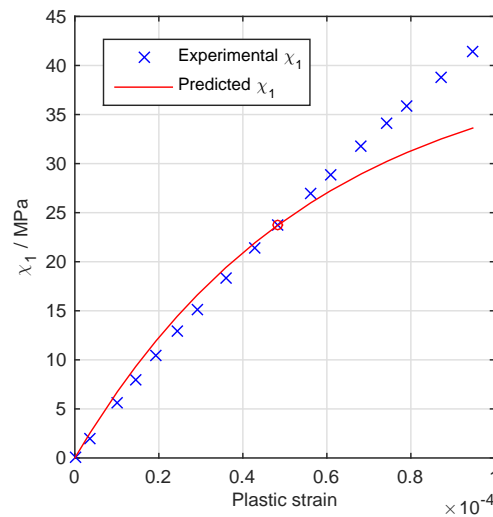


Figure 6.11: χ_1 vs ε_p for sample 160°C-400h. The red circle notates the point used to calculate C_1 .

The bounds for a_1 , C_1 , a_2 and C_2 were obtained by re-evaluating the associated parameters with the partition set at one quarter and three quarters of the plastic strain range as shown in Figure 6.12. This was to ensure that the search range for the appropriate materials constants was wide enough while remaining within bounds that make physical sense.

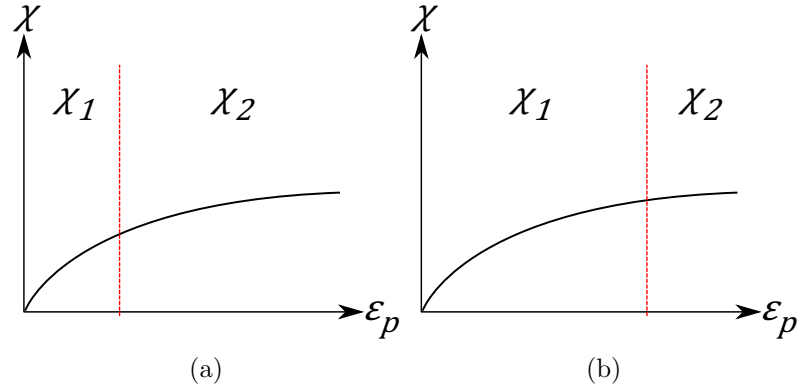


Figure 6.12: A representation of the method used to obtain the upper and lower back stress bounds by (a) setting the back stress partition set to one quarter of the plastic strain range and (b) setting the back stress partition to three quarters of the stress range.

6.3.4 Viscous Stress Parameters

The samples that were soaked for 400 hours at 160°C and 200°C were used to obtain the viscous parameters, Z and n . Taking the log of equation 2.20 gives equation 6.19. By plotting $\log(\dot{p})$ vs $\log(\sigma_v)$, n can be obtained from the gradient of the line of best fit and Z is the y-intercept. Therefore, all values of \dot{p} and σ_v during the stress relaxation of the samples are required. Due to the scatter in the data, the stress versus time was approximated using an exponential fit as shown in Figure 6.13b thereby avoiding positive viscous strain rates during periods of strain holds. Only the initial 150 seconds was considered since this was the most important time frame for which the stress relaxation behaviour would occur during the strain-controlled isothermal fatigue tests.

$$\log(\sigma_v) = \frac{1}{n} \log(\dot{p}) + \log(Z) \quad (6.19)$$

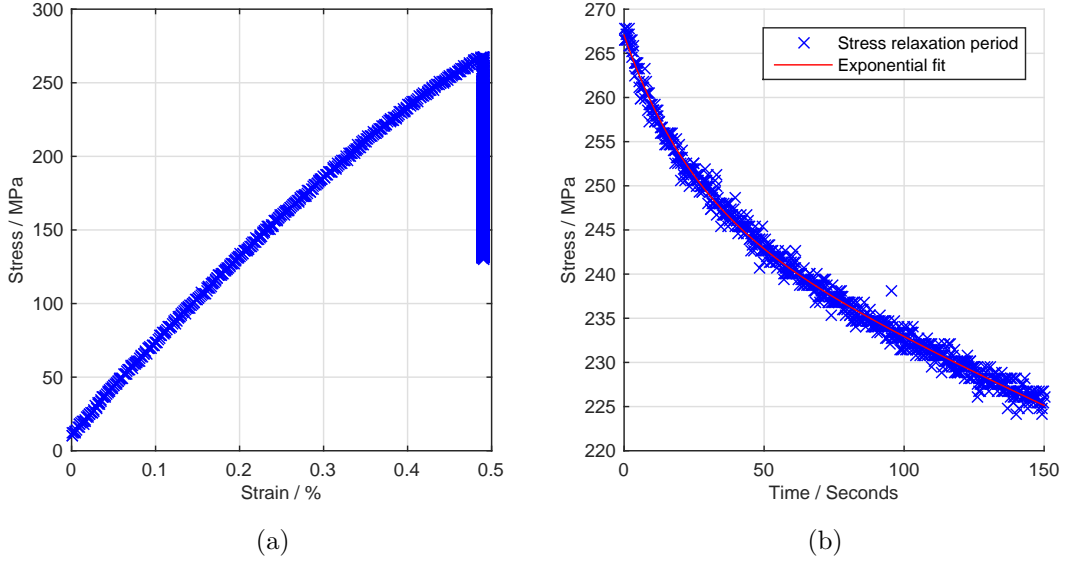


Figure 6.13: (a) Stress vs strain and (b) the initial 150 seconds of the dwell period.

$$\dot{\epsilon} = \dot{p} + \frac{\dot{\sigma}}{E} \quad (6.20)$$

$$\dot{\sigma} = \frac{\sigma_i - \sigma_{i-1}}{t_i - t_{i-1}} \quad (6.21)$$

The total strain rate can be described by equation 6.20, where $\dot{\epsilon} = 0$ during the stress relaxation period. Therefore $\dot{p} = -\frac{\dot{\sigma}}{E}$ and the stress rate, $\dot{\sigma}$, was calculated using a backwards difference method as shown in equation 6.21.

$$\sigma_v = \sigma - R - \chi_1 - \chi_2 - k \quad (6.22)$$

The viscous stress for every point can be calculated using equation 6.22. R , χ_1 and χ_2 were calculated using the material constants obtained previously for Q_m , b_m , H_m , a_1 , C_1 , a_2 and C_2 .

A plot of \dot{p} vs σ_v can be found in Figure 6.14 where the red line represents the line of best fit which was used to calculate Z and n .

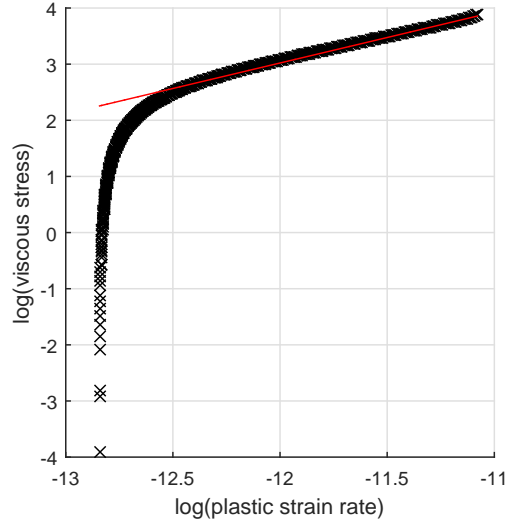


Figure 6.14: An example of a plot of $\log(\dot{p})$ versus $\log(\sigma_v)$ for a fully-aged sample at 200°C.

The upper and lower bounds for the viscous stress parameters were determined from the line of the best of different sections along the curve in Figure 6.14 before the knee of the curve. The highest and lowest values of Z and n were the bounds during the optimisation process.

6.3.5 Material Ageing Parameters

Once the material constants for the fully-aged samples were established, the ageing rate of the material was then estimated. The value of k is the initial cyclic yield stress of the material when it is fully aged, which would not be the same yield stress while the material is ageing. Therefore, to describe the material's yield strength as a function of time at temperature, it can be seen that a stress value, R_a , must be added to k that decays with time. Furthermore, R_a must decay to a value of 0 to accurately predict the stress data of the fully-aged samples, working with the assumption that after 400 hours the material no longer ages.

$$R_a = \frac{\sigma_{el}}{2} - k \quad (6.23)$$

To determine R_a , k was subtracted from the radius of the yield surface of each tensile branch, $\frac{\sigma_{el}}{2}$, (see equation 6.23), while noting the point in time of the cycle. By plotting R_a versus time in seconds in the curve fitting application in MATLAB, equation 6.10

was fitted using the least squares method to the data to approximate the constants Q_{a1} , Q_{a2} , b_{a1} and b_{a2} .

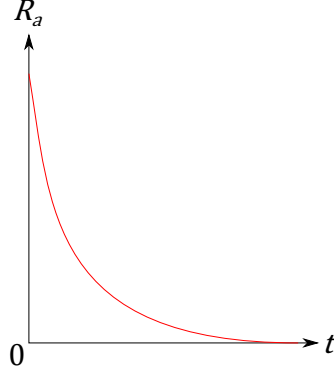


Figure 6.15: Approximation of the relationship between the change in R_a with time.

The upper and lower bounds for the material ageing parameters were $\pm 50\%$ of the estimated values of Q_{a1} , Q_{a2} , b_{a1} and b_{a2} to enable a search for the optimum values.

6.4 Objective Functions for the Optimisation Process

$$F = [F_1, F_2] \quad (6.24)$$

$$F_1(x) = \sum_i^{M_1} (\sigma(x)_i^{pre} - \sigma(x)_i^{exp})^2 \quad (6.25)$$

$$F_2(x) = \sum_i^{M_2} \left(\frac{\Delta\sigma(x)_i^{pre}}{2} - \frac{\Delta\sigma(x)_i^{exp}}{2} \right)^2 \quad (6.26)$$

$$x = [a_1, C_1, a_2, C_2, Z, n, Q_m, b_m, H_m, Q_{a1}, b_{a1}, Q_{a2}, b_{a2}, k, E] \quad (6.27)$$

$$LB \leq x \leq UB \quad (6.28)$$

$$w_j = \frac{\sum_1^N M_j}{M_j \max |A_i^{exp}|} \quad (6.29)$$

An optimisation process was required to determine a new set of constants that provided a better stress fit to the experimental data when using the Chaboche model. This process utilised an iterative non-linear least squares algorithm. F in equation 6.24 is an array that contains all objective functions used to define the fitting quality

of the predicted stress versus time. In this case, two objective functions were used to for general stress fitting (equation 6.25) and minimising the difference between predicted and experimental stress amplitude for each i th cycle (equation 6.26). σ^{pre} and σ^{exp} represent the predicted and experimental stresses respectively, where M_1 is the total number of data points considered for optimisation. $\frac{\Delta\sigma^{pre}}{2}$ and $\frac{\Delta\sigma^{exp}}{2}$ are the predicted and experimental stress amplitudes where M_2 is the total number of cycles considered for optimisation. x is the array containing all temperature and time dependent material constants (see equation 6.27), each with defined upper and lower boundaries, UB and LB respectively (see equation 6.28), to prevent a time consuming mathematical search for a local minimum. Furthermore, the bounds prevent the output of material constants that are not physically realistic but would otherwise be mathematically suitable i.e. minimise the objective function. A weighting value, w_j , was applied to the j th objective function as shown in equation 6.29 since objective function $F_1(x)$ contained an entry for every predicted stress value, whereas objective function $F_2(x)$ contained an entry for every stress amplitude per cycle. This was to ensure equal contribution of each objective during the optimisation process. N is the total number of objective functions M_j indicates the number of data points for the j th objective function, and $max|A_{ij}^{exp}|$ is the maximum experimental value associated with that objective function.

6.5 Numerical Methods and Implementation in MATLAB

$$y = [\varepsilon_p, p, \sigma, \chi_1, \chi_2] \quad (6.30)$$

The vector, y , in equation 6.30 contains a set of state variables required to calculate the predicted stress using the material constants stored in the array x .

$$\dot{\sigma} = E(\dot{\varepsilon} - \dot{\varepsilon}_p) \quad (6.31)$$

The ordinary differential equations (ODEs) 6.2 and 6.6 can be solved to obtain the state variables ε_p , p , χ_1 and χ_2 . The total stress rate can be found from the differential of equation 2.19 and $\dot{\varepsilon}_p$ is calculated from the flow rule equation (equation 2.7 in section

6.2).

$$y_{m+1} = y_m + \sum_{j=1}^6 \gamma_j k_j \quad (6.32)$$

The isotropic hardening or softening, R , was fully deterministic and was calculated after the ODEs were solved. The Dormand prince 4th/5th order Runge-Kutta method [203] (the Dormand-Prince pair) was chosen to solve the ODEs which estimated the state variables over the time span t_0 to t_f . This is represented in MATLAB as the in-built function “ODE45”. Equation 6.32 shows how the updated state variables, y_{m+1} , was calculated for the time step $m + 1$. The Runge-Kutta coefficients γ_j and k_j are the step size and calculated gradients, respectively, to find the solution in the step size.

The non-linear least squares function is another in-built function in MATLAB that uses the Levenberg-Marquardt algorithm [121, 122]. This was used to find the optimal set of material constants between predefined bounds that yielded the best fit to the experimental stress data. This algorithm is capable of finding a local minimum if the initial guess is close to the final solution. For each iteration, the vector containing material constants, x , is replaced by a new vector, $x + \Delta$ (where Δ is calculated in the algorithm), and the difference between predicted and experimental stress, defined by the objective functions in F , is calculated. If either the magnitude of Δ or the reduction in the sum of squares between numerical and experimental stress values (due to the latest iteration of $x + \Delta$) falls below the predefined limits, then the algorithm terminates and the latest set of parameters is considered to be the solution. A flowchart of the optimisation process is displayed in Figure 6.16.

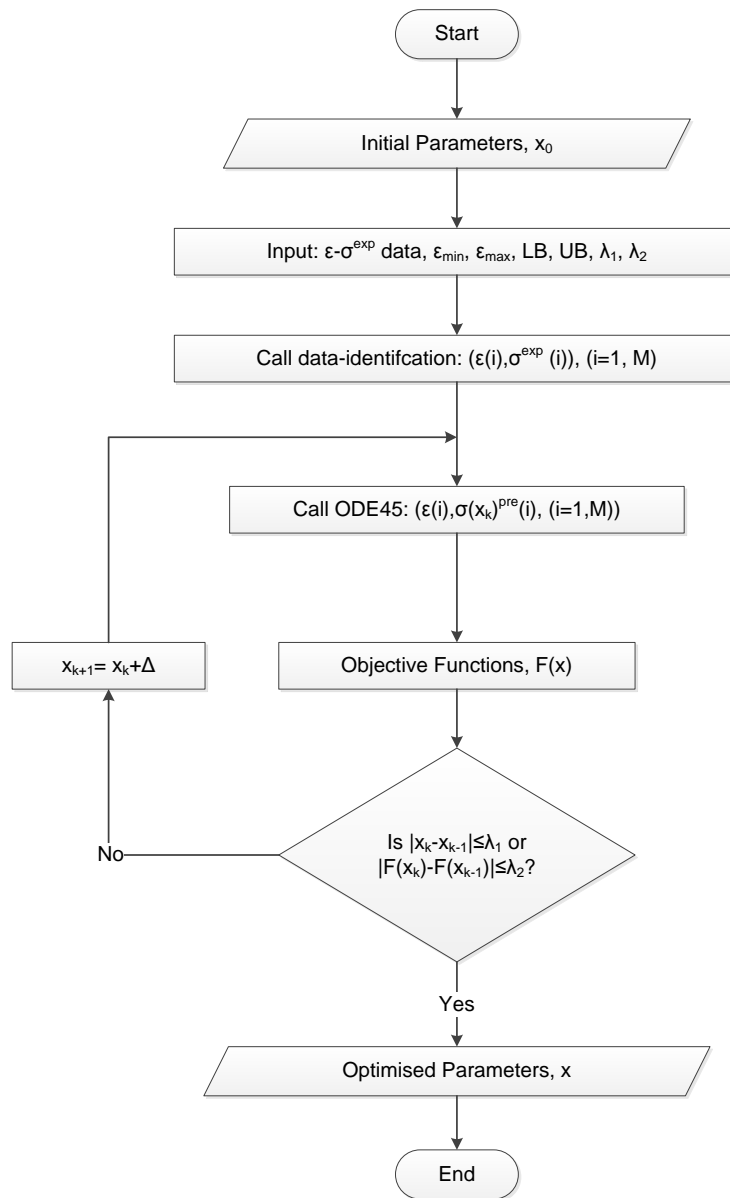


Figure 6.16: A flowchart of the optimisation process implemented in MATLAB.

6.6 Chaboche Model Predictions and Discussion

The experimental data shows that the novel variable waveform was able to decrease in strain amplitude as the material's yield stress decrease to induce plastic strain per cycle without exceeding the material's UTS. This allowed for enough data to be obtained for analysis and determination of initial material constants. For each cycle presented, the coefficient of determination for the optimised material constants, (r^2), error in the plastic strain range, $e_{\Delta\varepsilon_p}$, and the error in maximum stress, $e_{\sigma_{max}}$, between the experimental and the predicted results were calculated.

6.6.1 Stress Prediction of the "Fully-Aged" Samples

Figure 6.17a shows the experimental stress amplitude and the stress-strain loops for a few selected cycles and the predicted stress values using the initial and optimised materials constants for the samples 160°C-400h. The stress amplitude prediction at 160°C was within the scatter of the experimental data, but the rate of softening was not representative of the material behaviour. The gradient magnitude of the predicted linear softening region increases non-linearly, rather than remaining constant. Therefore, after 2000 cycles the predicted stress would begin to diverge from the experimental stress and decrease in accuracy. However, despite this issue the model accurately predicted the material response where the error in plastic strain range was below 14% and the error in the maximum stress was below 10%. Table 6.1 shows the time and temperature-dependent material constants before and after optimisation for sample 160°C-400h.

Figure 6.18 shows the experimental stress amplitude and the stress-strain loops for selected cycles, and the predicted stress values using the initial and optimised materials constants for the 200°C-400h sample. It can be seen that the errors are below 6% except for cycle 200 in Figure 6.18c, where both the error in plastic strain range and maximum stress are above 20%. Figure 6.18a shows that the predicted mechanical softening rate, before the linear softening region, was greater than expected and between cycles 150 and 300, the stress amplitude was less than the experimental values. This resulted in the predicted yield occurring at a lower stress value which led to an increase plasticity and a decrease in maximum stress.

Table 6.2 shows the initial and optimised constants sample 200°C-400h. The mechanical softening terms (Q_m and b_m) at 200°C reached the bounds set by for the

optimisation, in an attempt to decrease the saturation drag stress value and the rate at which this value was achieved. Therefore, an improvement in accuracy may be gained by widening the bounds of these two parameters to allow them to reach more appropriate values.

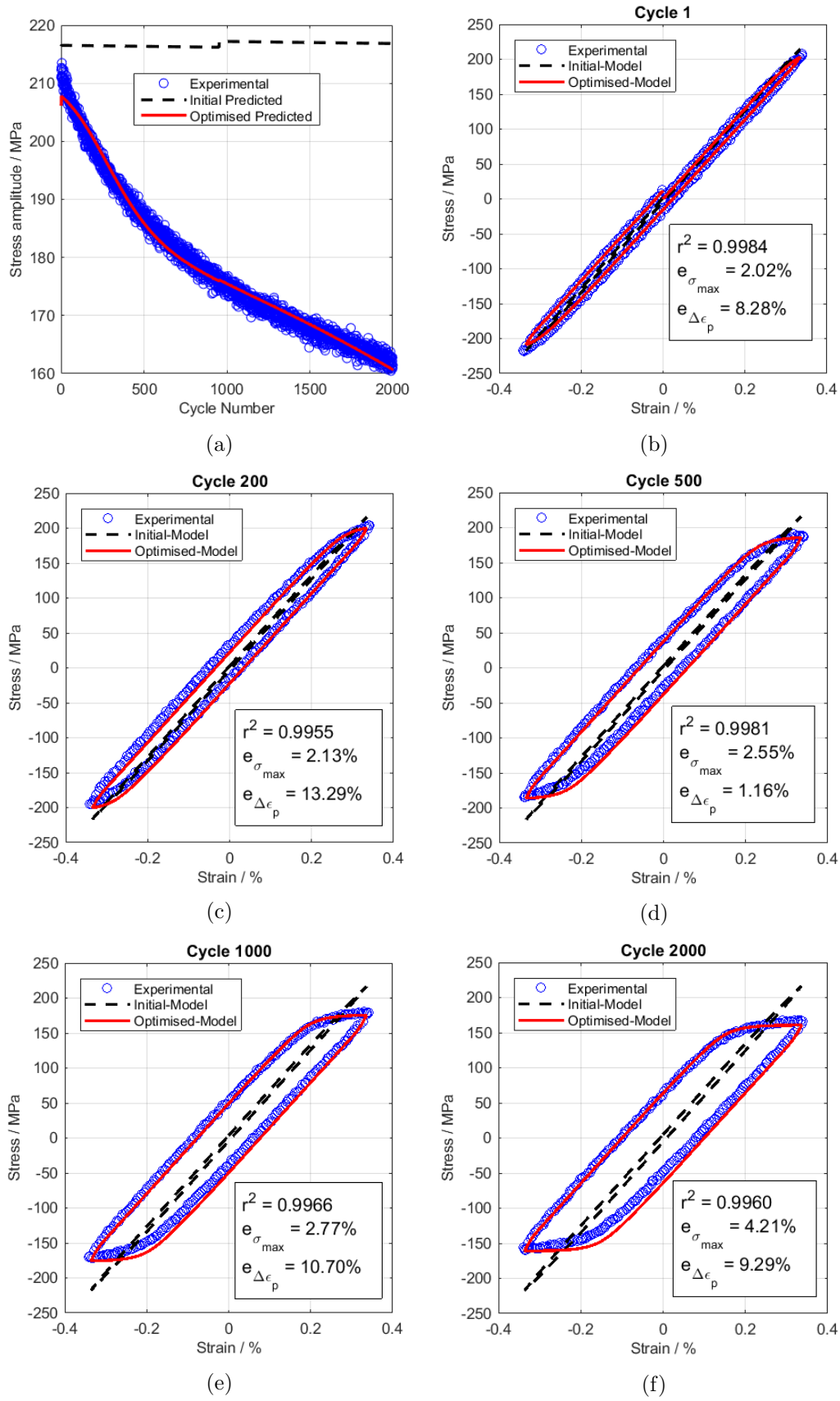


Figure 6.17: Predicted stress for sample 160°C-400h demonstrating (a) the cycle softening behaviour and (b)-(f) the hysteresis loops of selected cycles.

Table 6.1: A table of the initial and optimised material constants for the 160°C-400h, and the upper and lower bounds set for the optimisation process.

Constants	Initial	Optimised	LB	UB
a_1 (MPa)	13.3079	18.9977	5.0979	20.1241
C_1	52810	30539.2	30493	130370
a_2 (MPa)	14.332	22.1853	9.6494	22.1857
C_2	16541	19981.67	13627	20994
Z (MPa.s ^{1/n})	235660	91417.49	1776	2380500
n	1.4817	1.247	1.1776	2.9629
Q_m (MPa)	-37.0991	-32.3362	-44.3878	-28.78
b_m	1.9189	2.22542	1.4	2.4422
H_m (MPa)	-4.1922	-4.1922	-4.1922	-4.1922
Q_{a1} (MPa)	0	0	0	0
b_{a1}	0	0	0	0
Q_{a2} (MPa)	0	0	0	0
b_{a2}	0	0	0	0
k (MPa)	145	145.6117	110	197
E (MPa)	65000	64500.52	58000	67000

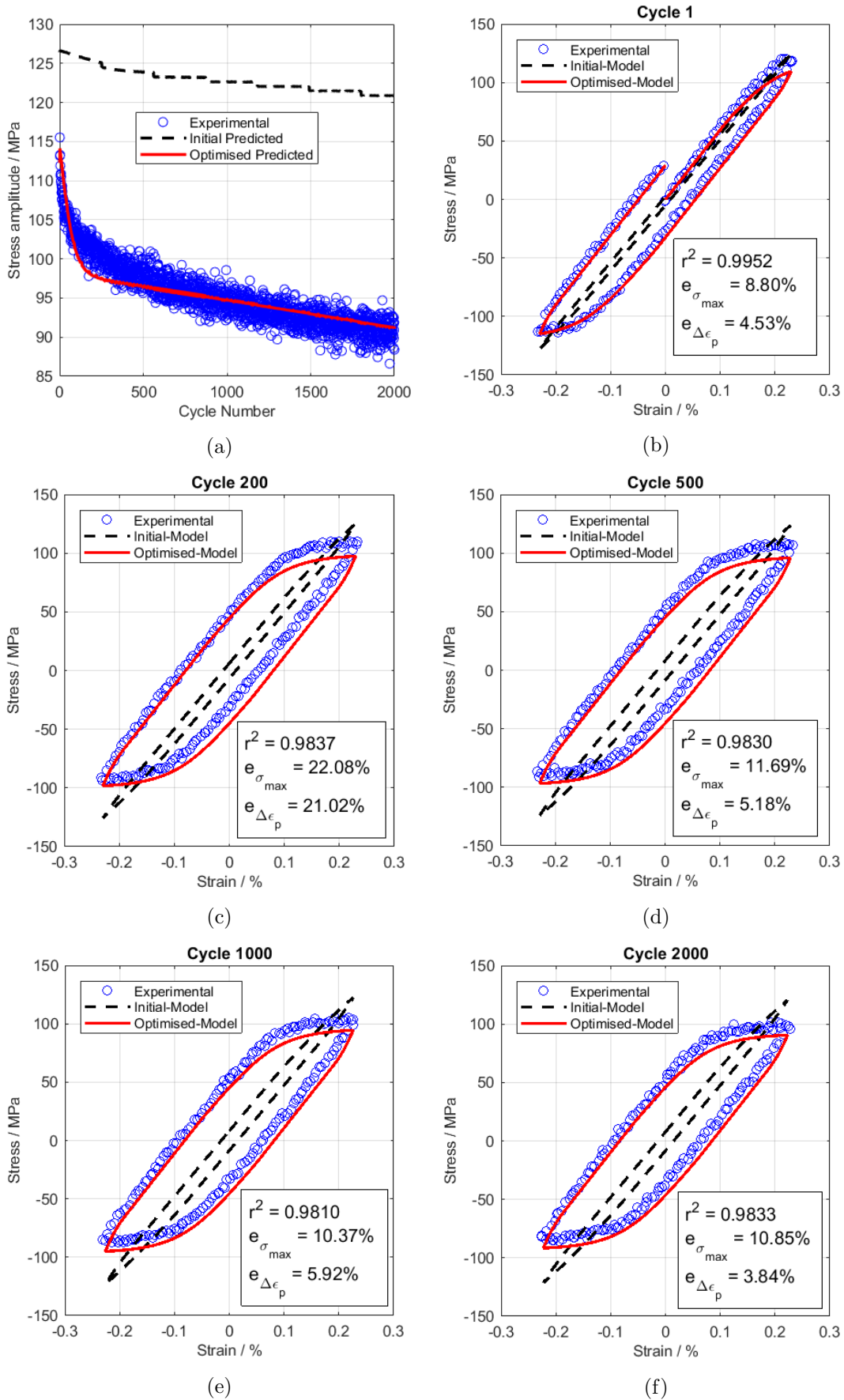


Figure 6.18: Predicted stress for sample 200°C-400h demonstrating (a) the cycle softening behaviour and (b)-(f) the hysteresis loops of selected cycles.

Table 6.2: A table of the initial and optimised material constants for the 200°C-400h, and the upper and lower bounds set for the optimisation process.

Constants	Initial	Optimised	LB	UB
a_1 (MPa)	14.71	18.1945	8.9680	18.4500
C_1	18514	16283	14156	33799
a_2 (MPa)	6.139	6.4333	2.8900	11.8100
C_2	5246.4	5689.7	4947.1	5689.9
Z (MPa.s ^{1/n})	543820	564700	2080.3	18918000
n	1.1692	1.0121	0.8658	1.214
Q_m (MPa)	-23.3236	-19.26	-29.18	-19.26
b_m	13.7896	6.8948	6.8948	20.6844
H_m (MPa)	-0.9368	-0.9368	-0.9368	-0.9368
Q_{a1} (MPa)	0	0	0	0
b_{a1}	0	0	0	0
Q_{a2} (MPa)	0	0	0	0
b_{a2}	0	0	0	0
k (MPa)	89	63.0408	44.5	99
E (MPa)	56000	59499	52000	59500

6.6.2 Stress Prediction of the As-Received Samples

Once the material constants for the “400h” samples were optimised the ageing parameters could be added to the model. During the optimisation of the ageing parameters the previously optimised parameters were kept constant.

Figure 6.19a shows that the initial predicted cyclic softening at 160°C was accurate but the transition into the secondary linear region occurred too early. Moreover, the predicted linear softening rate was greater than the experimental softening rate. This may be due to the inaccuracy of the predicted linear cyclic softening region (due to the mechanical softening parameters), which the optimisation of the material ageing parameters (described by two exponential terms) attempted to correct. Figures 6.19b to 6.19f demonstrate that the yield stress of the material was overestimated and the back stress saturated soon after yielding occurred. The error in maximum stress did not exceed 5.18% but the error in the plastic strain range can exceed 20%. Table 6.3 shows the initial and the final complete set of material constants for the Chaboche model of the 7175-T7351 aluminium alloy at 160°C.

Figure 6.20a shows the numerical prediction of the stress amplitude at 200°C was in general agreement with the experimental data. The predicted shapes of the hysteresis loops in Figure 6.20b to 6.20f show good accuracy where most of the errors in plastic strain range and maximum stress were below 10%. It can be seen that the hysteresis loops were slightly offset from the experiment loops, indicating that there may be some shortcomings in the back stress parameters.

These results highlighted a strong dependency of accurate mechanical softening parameters in order to obtain the material ageing parameters. Repeat tests may be useful to obtain averaged material constants (optimised simultaneously against all tests).

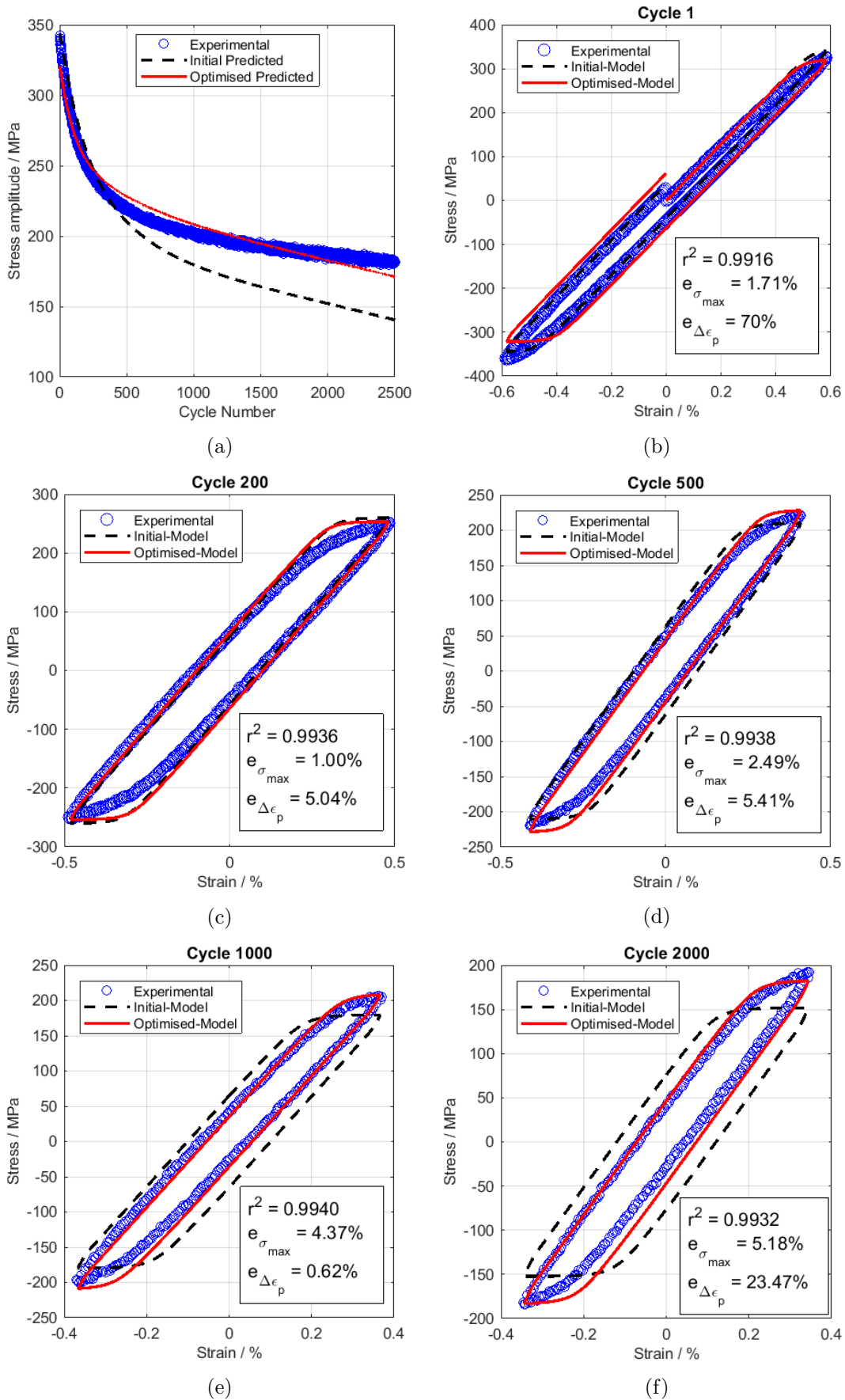


Figure 6.19: Predictions for sample 160°C-0h. (a) Cycle softening behaviour and (b)-(f) the hysteresis loops of selected cycles.

Table 6.3: A table of the initial and optimised set of material constants for the 160°C-0h, and the upper and lower bounds set for the optimisation process.

Constants	Initial	Optimised	LB	UB
a_1 (MPa)	18.9977	18.9977	18.9977	18.9977
C_1	30539.2	30539.2	30539.2	30539.2
a_2 (MPa)	22.1853	22.1853	22.1853	22.1853
C_2	19981.67	19981.67	19981.67	19981.67
Z (MPa.s ^{1/n})	91417.49	91417.49	91417.49	91417.49
n	1.247	1.247	1.247	1.247
Q_m (MPa)	-32.3362	-32.3362	-32.3362	-32.3362
b_m	2.22542	2.22542	2.22542	2.22542
H_m (MPa)	-4.1922	-4.1922	-4.1922	-4.1922
Q_{a1} (MPa)	128.300	73.9433	50	250
b_{a1}	-6.672E-06	-1.8216E-05	-6.672E-05	-6.672E-07
Q_{a2} (MPa)	0	30.7077	-30.4167	30.7083
b_{a2}	-6.672E-06	-2.0123E-05	-6.672E-05	-6.672E-07
k (MPa)	145.6117	145.6117	145.6117	145.6117
E (MPa)	64500.52	64500.52	64500.52	64500.52

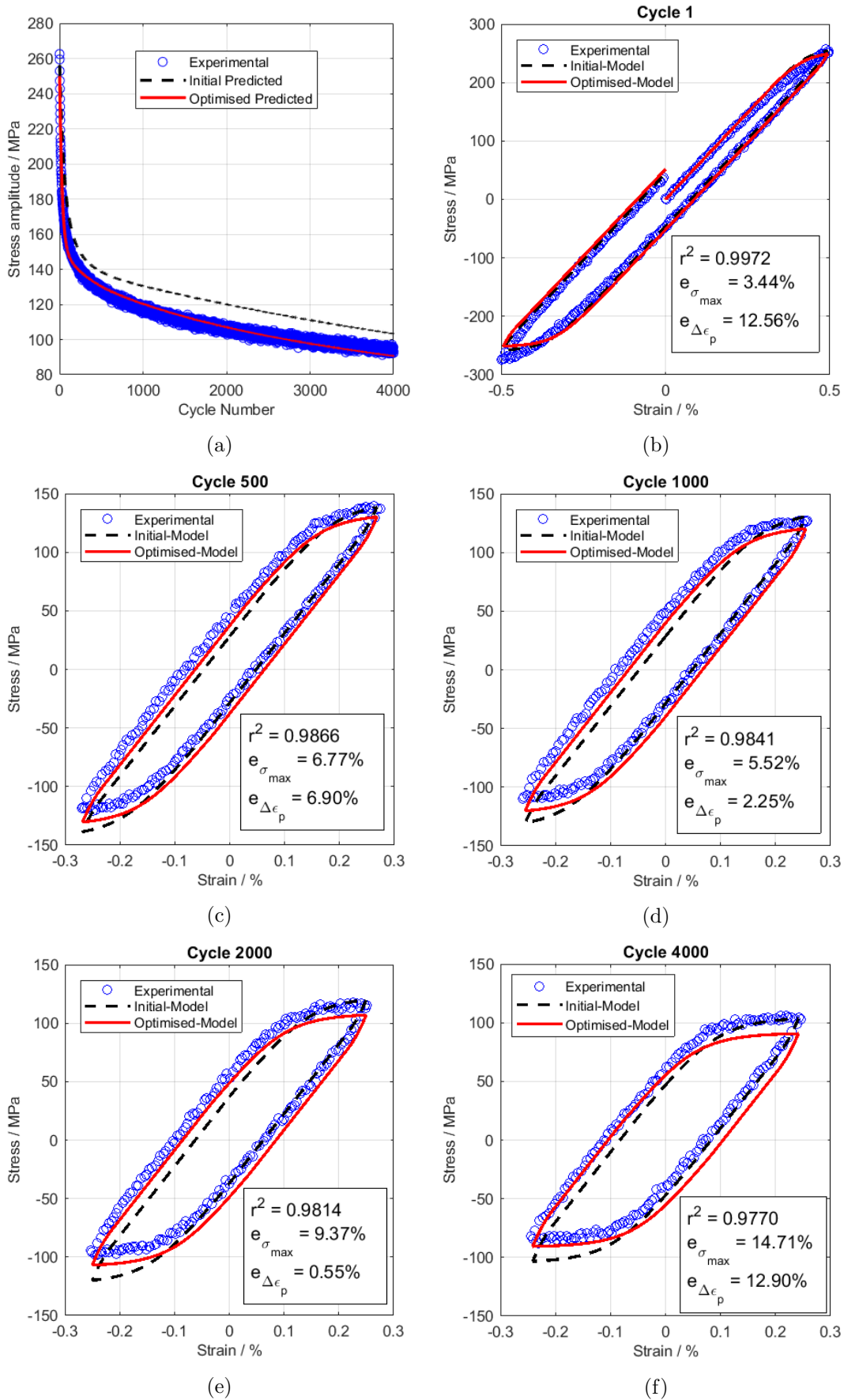


Figure 6.20: Predictions for sample 200°C-0h. (a) Cycle softening behaviour and (b)-(f) the hysteresis loops of selected cycles.

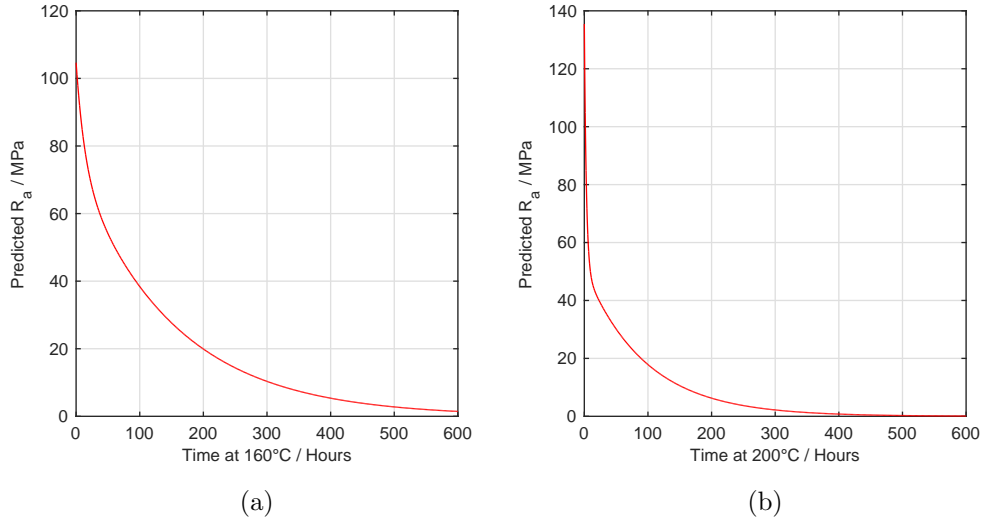


Figure 6.21: The change in R_a with time predicted by the optimised material ageing parameters at (a) 160°C and (b) 200°C.

As mentioned previously, the isotropic softening due to material ageing should asymptotically approach 0MPa, assuming the samples soaked for 400 hours were fully-aged. Figure 6.21 shows the change in R_a with time at 160°C and 200°C predicted by the optimised material ageing parameters. By 400 hours at 200°C, R_a decreased to 0.77MPa which was sufficient enough for the prediction of the fully aged material. However, up to the same time at 160°C, R_a was 5.37MPa, indicating that the predicted ageing rate was lower than expected. This be may caused by the inaccurate rate of mechanical softening obtained before the material ageing parameters were optimised.

Table 6.4 shows the initial and the final complete set of material constants for the Chaboche model of the 7175-T7351 aluminium alloy at 200°C.

Table 6.4: A table of the initial and optimised set material constants of the Chaboche model for the 7175-T7351 aluminium alloy at 200°C, and the upper and lower bounds set for the optimisation process.

Constants	Initial	Optimised/Final	LB	UB
a_1 (MPa)	18.1945	18.1945	18.1945	18.1945
C_1	16283	16283	16283	16283
a_2 (MPa)	6.4333	6.4333	6.4333	6.4333
C_2	5689.7	5689.7	5689.7	5689.7
Z (MPa.s ^{1/n})	564700	564700	564700	564700
n	1.0121	1.0121	1.0121	1.0121
Q_m (MPa)	-19.26	-19.26	-19.26	-19.26
b_m	6.8948	6.8948	6.8948	6.8948
H_m (MPa)	-0.9368	-0.9368	-0.9368	-0.9368
Q_{a1} (MPa)	86.91	84.5756	43.455	130.365
b_{a1}	-4.07E-05	-8.90E-05	-0.00041	-2.04E-05
Q_{a2} (MPa)	54.51	50.8856	27.255	81.765
b_{a2}	-1.59E-06	-2.91E-06	-1.59E-05	-7.93E-07
k (MPa)	63.0408	63.0408	63.0408	63.0408
E (MPa)	59499	59499	59499	59499

6.6.3 Complete Chaboche Model Validation - Stress Prediction of “Partially-Aged” and “Fully-Aged” Samples

The complete model was used to predict the test data of the “partially-aged” 160°C-100h and 200°C-75h samples, as well as the fully-aged data from section 6.6.1 to ensure that a similar stress-response was predicted compared to previously.

Figures 6.22 and 6.23 show the predicted stress of samples 160°C-100h and 160°C-400h. For both cases, the model over-estimated the stress amplitude by a maximum of 11% and 5% respectively. The prediction of the hysteresis loops in Figures 6.22b to 6.22f showed that the yielding occurred at a greater stress than expected which was most likely caused by the slow predicted ageing rate discussed previously. As a result, excluding the first cycle, the error in plastic strain range reached up to 45.4%.

Figure 6.24 shows that the material constants obtained for 200°C provided a good prediction for the material response of the 200°C-75h sample. Both the errors in plastic strain range and maximum stress were below 12%.

Figure 6.25 shows that when the material constants for 200°C were used to the predict the material response of the 200°C-400h sample, the results were still in good agreement. Both the errors in plastic strain range and maximum stress remained below 11%.

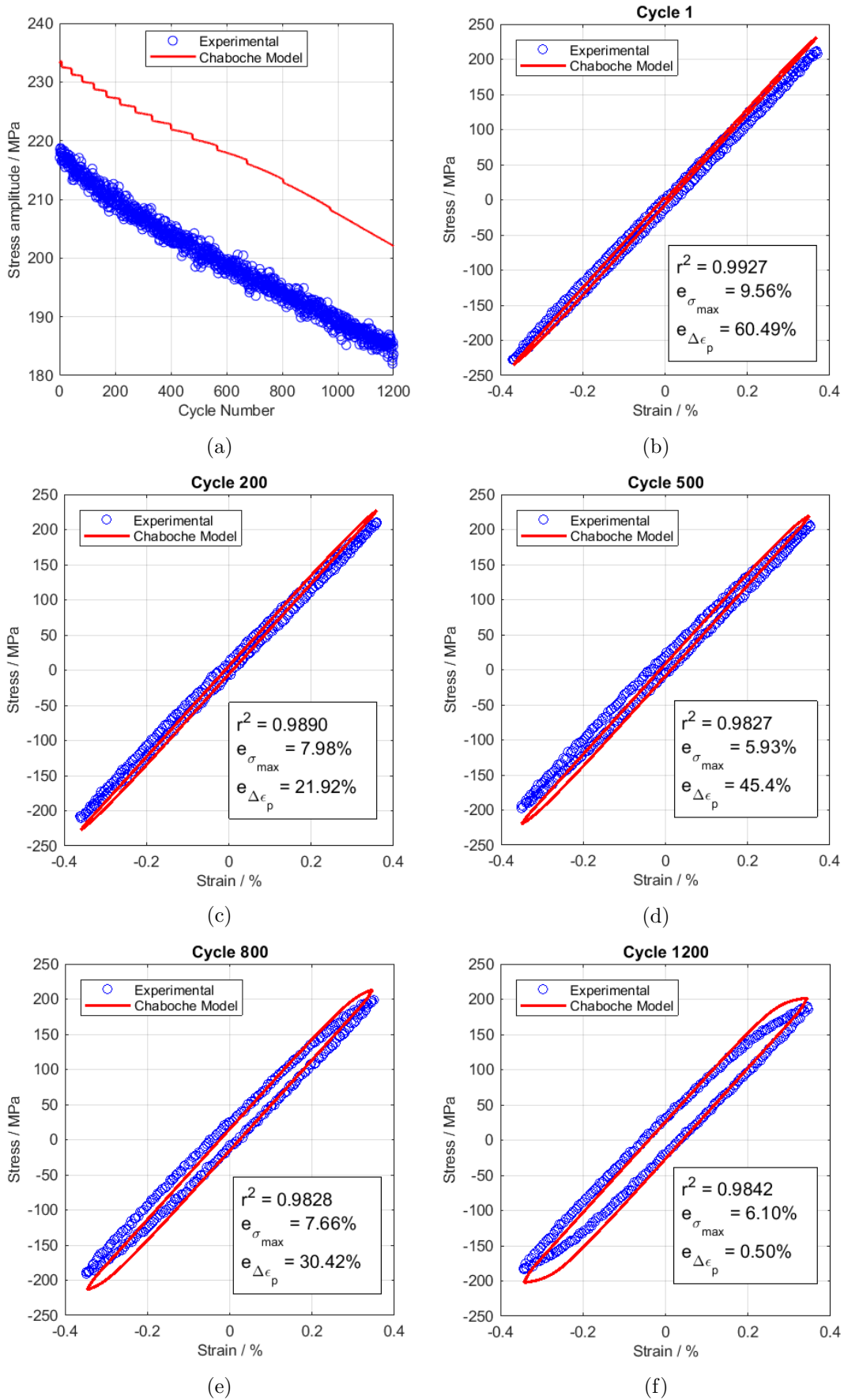


Figure 6.22: Predictions for the 160°C-100h sample using the complete set of material constants at 160°C. (a) Cycle softening behaviour and (b)-(f) the hysteresis loops of selected cycles.

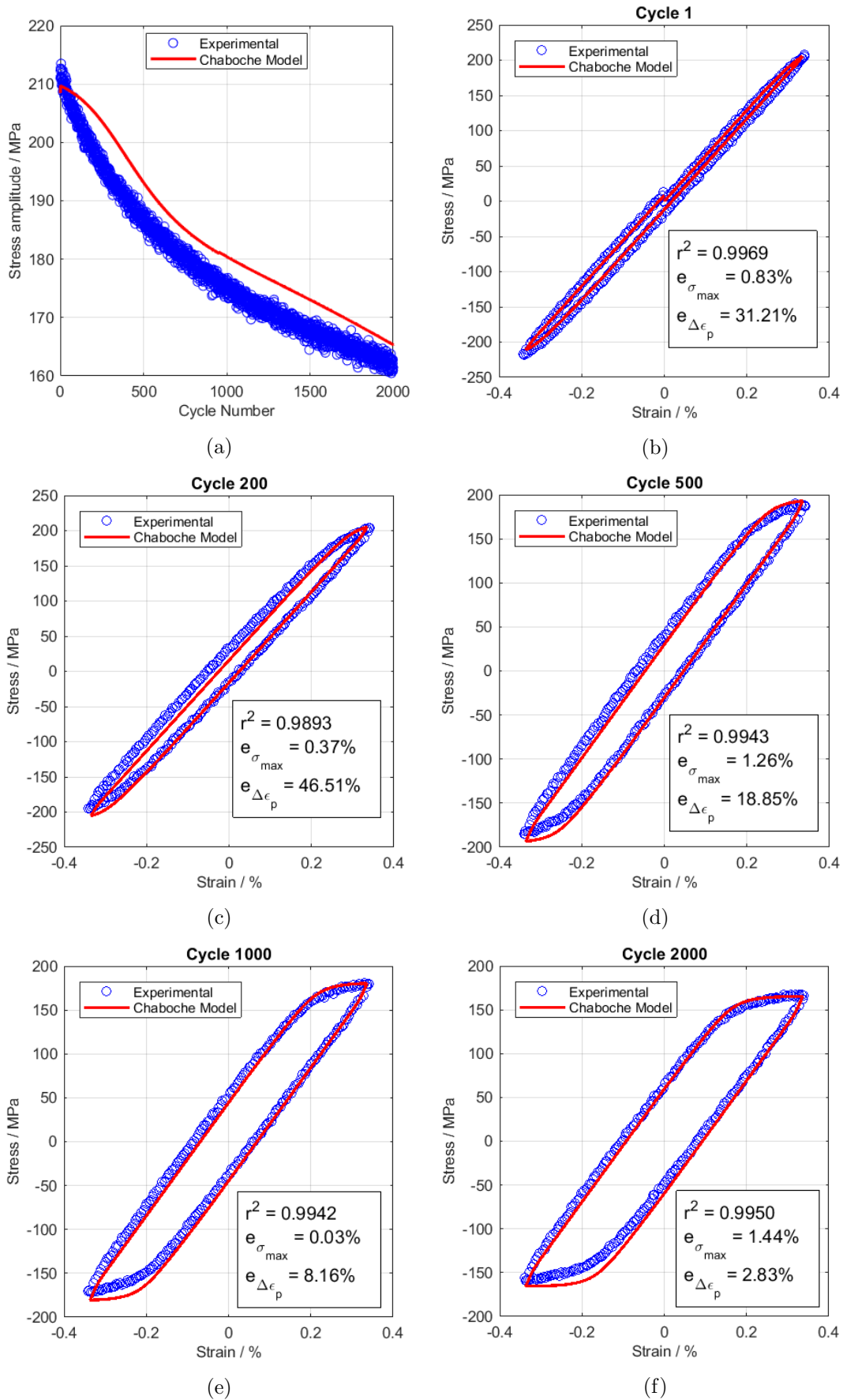


Figure 6.23: Prediction for the sample 160°C-400h using the complete set of material constants at 160°C. (a) Cycle softening behaviour and (b)-(f) the hysteresis loops of selected cycles.

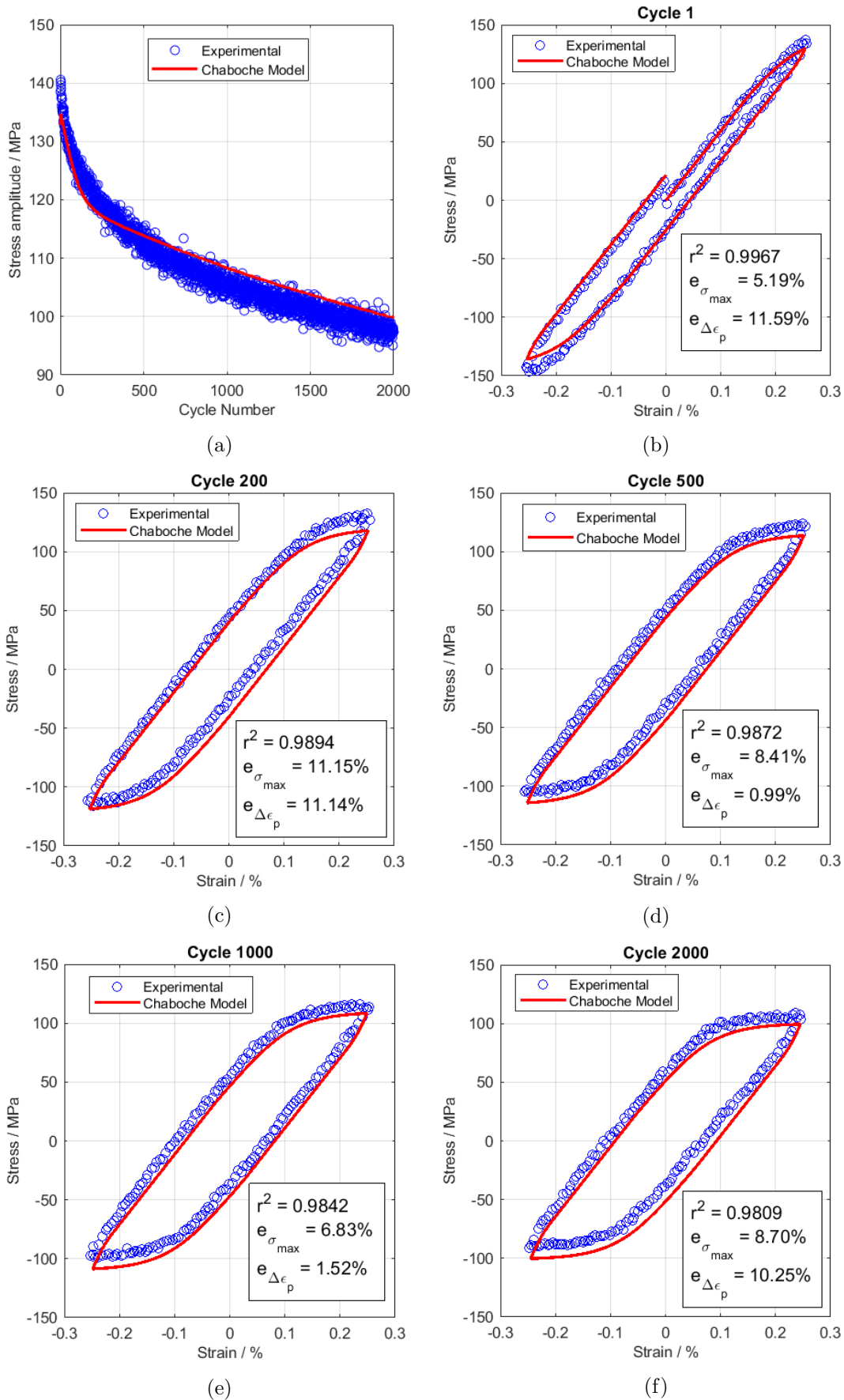


Figure 6.24: Prediction of the stress for the 200°C-75h sample using the complete set of material constants at 200°C. (a) Cycle softening behaviour and (b)-(f) the hysteresis loops of selected cycles.

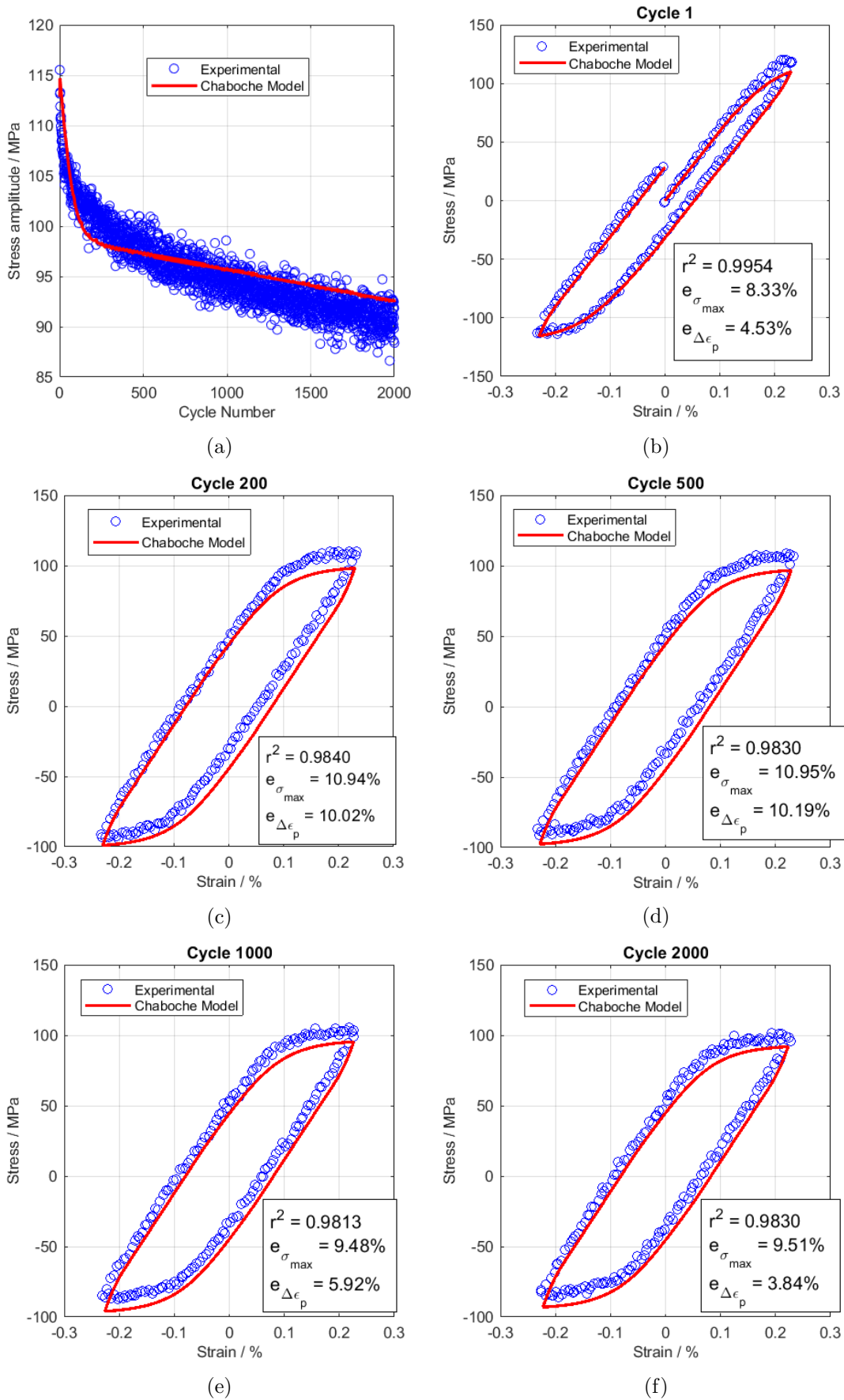


Figure 6.25: Prediction of stress for the 200°C-400h sample using the complete set of material constants at 200°C. (a) Cycle softening behaviour and (b)-(f) the hysteresis loops of selected cycles.

6.6.4 Prediction of Stress Relaxation Tests and Stress-Controlled Isothermal Fatigue Tests

A prediction of the cyclic stress relaxation data of a sample that was soaked for 75 hours at 200°C is shown in Figure 6.26. A good prediction of peak stress and the size of the hysteresis loops were obtained for each cycle presented which further validates the isotropic and kinematic parameters. However, a deficiency can be identified in the model's stress prediction from this type of load condition. In Figure 6.24b during the first dwell period (at 0.15%), a relaxation in the stress was observed which was not predicted at all by the Chaboche model. Furthermore, for all other dwell periods of each cycle, the power law only predicted stress relaxation above the material's yield surface (characteristic of viscoplastic behaviour), rather than continuing to relax as observed in the experimental results. This demonstrates that the material exhibits viscoelastic behaviour, where rate-dependent deformation continued to occur below the yield stress of the material under constant strain.

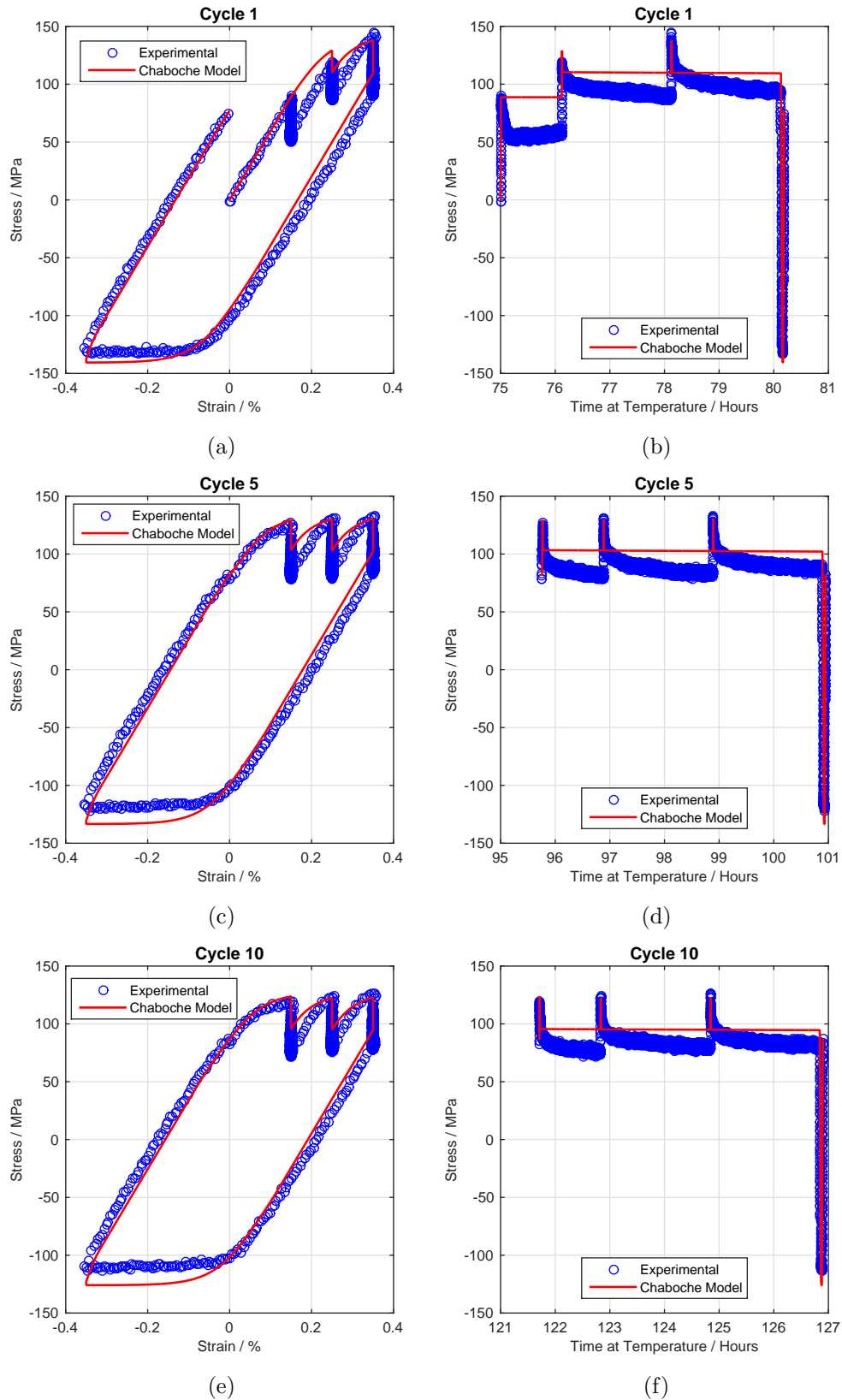


Figure 6.26: Stress relaxation prediction of a sample soaked (for 75 hours) and tested at 200°C, displaying (a) cycle 1, (b) cycle 5 and (c) cycle 10. For each cycle, the duration and strain of the dwell periods are as follows: 1 hour at 0.15%, 2 hours at 0.25% and 2 hours at 0.35%.

The total strain was comprised of elastic, plastic and viscoplastic strain, where the latter two are described by the variable, ε_p . In reality, an additional viscoelastic strain component should contribute to the total strain. The current Chaboche model uses a Norton's creep power law to describe the viscous stress behaviour which was dependent on the accumulated plastic strain rate. Evidently, this relationship was not sufficient to describe the long term stress relaxation in the viscoplastic regime. The hyperbolic sine law may be more suitable than Norton's creep power law to describe the stress relaxation behaviour since it accounts for the change in creep deformation mechanisms [204]. However, for the purpose of this work, this behaviour was not a concern during the strain-controlled fatigue tests since only short term results were considered.

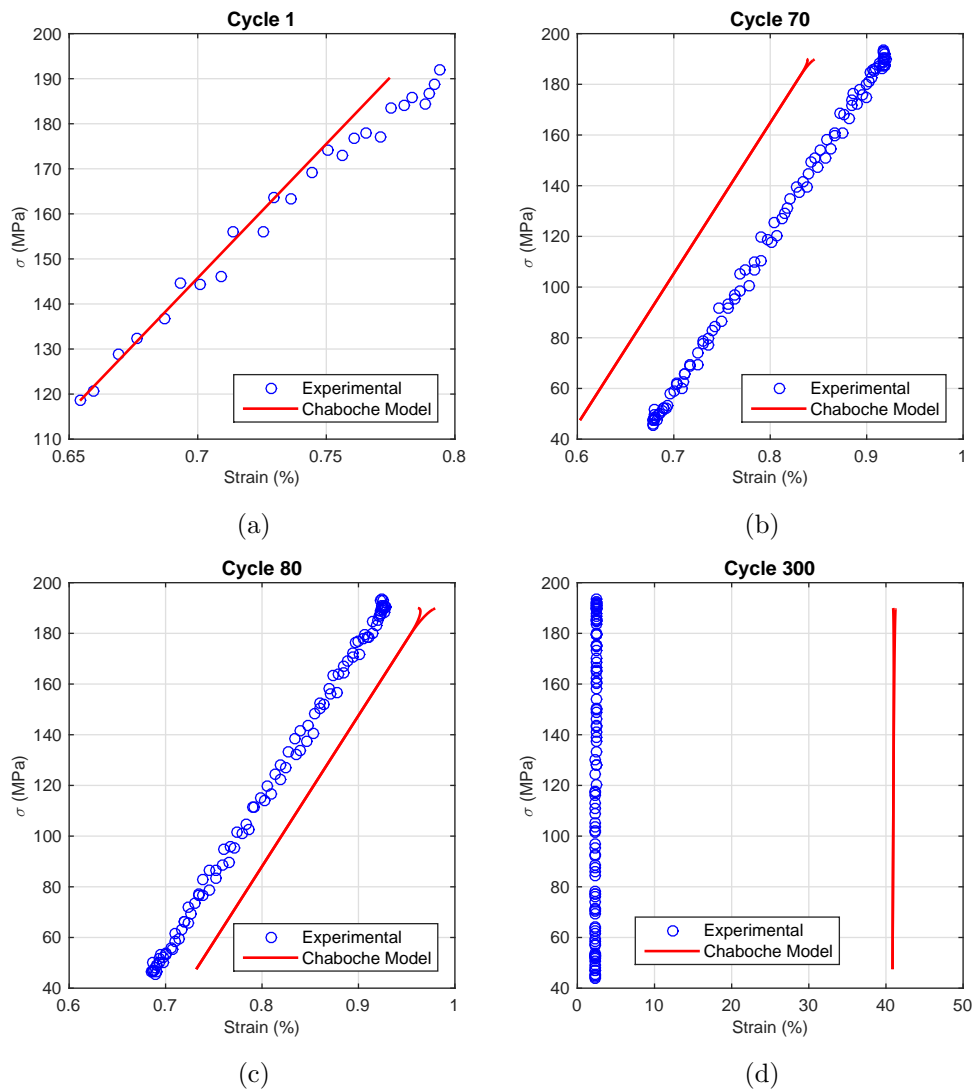


Figure 6.27: Prediction of stress-controlled isothermal fatigue data at 200°C ($\sigma_{max}=190\text{MPa}$ and $R_\sigma=0.25$) for (a) cycle 1, (b) cycle 70, (c) cycle 80 and (d) cycle 300.

Figure 6.27 shows the model's prediction of the stress-controlled fatigue test ($\sigma_{max}=190\text{MPa}$ and $R_{\sigma}=0.25$) of cycles 1, 70, 80 and 300. A complete cycle was represented as "peak-to-peak" stress. Initially the predicted strain ratcheting occurred at a slower rate than the experimental data but when the model began to predict yielding in the material, the model's ratcheting rate rapidly increased, facilitated by the plastic strain accumulation. As a result, large amounts of ratcheting strain was induced which was not representative of material behaviour.

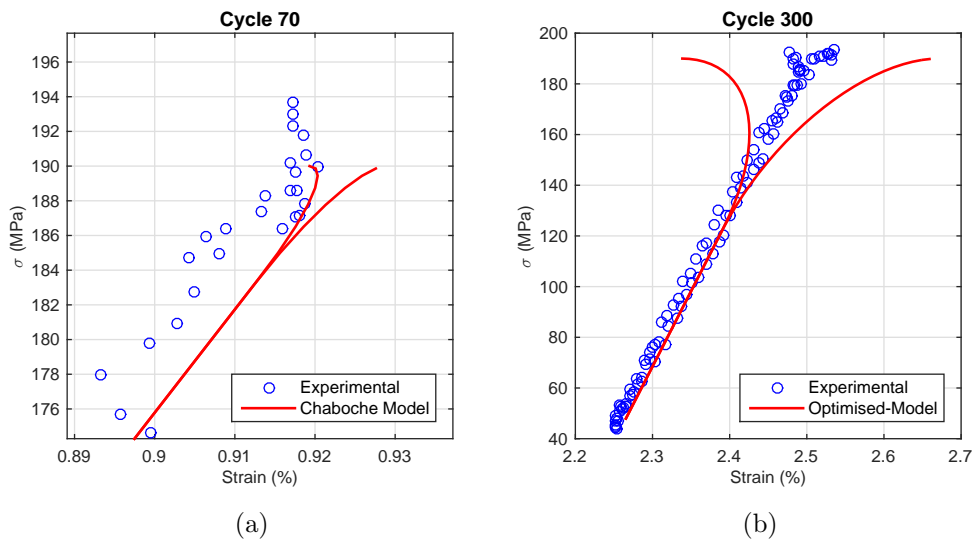


Figure 6.28: A comparison between predicted and experimental stress of (a) cycle 70 and (b) cycle 300.

Figure 6.28 shows the hysteresis of the predicted and experimental plastic strain of cycle 70 and 300. It can be seen that the predicted yield stress decreased at a greater rate compared to the experimental data. As stated previously, the sample was loaded elastically for the majority of the test. However, the material ageing parameters in the model were obtained from the strain-controlled fatigue tests where the material ageing was enhanced by the accumulated plastic strain. Therefore, the predicted ageing would have been overestimated and the material ageing parameters need to be adjusted to account for when the material is not plastically deformed.

It has been documented that the AF equations have a deficiency when predicting the ratcheting behaviour of stress-controlled fatigue with a non-zero mean stress. Researchers have modified the AF equation in an attempt to correct the hysteresis loops. The multiplicative kinematic hardening rule, for example, has been proposed to control the rate at which the saturation back stress is reached without changing the

saturation value [205]. The Ohno-Wang rule for non-linear kinematic hardening could also be used to improve the predict rate of ratcheting by introducing the critical state of dynamic recovery for each back stress component.

6.7 Conclusions

The objective of this chapter was to predict the 7175-T7351 stress response under strain-controlled isothermal fatigue conditions at 160°C and 200°C. It was assumed that the isotropic softening of the material could be decoupled into mechanical softening and material ageing (functions of accumulated plastic strain and time respectively).

The novel loading conditions successfully provided plenty of material data while avoiding fracture of the test samples. As a result, the hardening behaviour was able to be obtained. If a constant amplitude tests were implemented, the amount of plastic strain per cycle would have increased from when the tests had begun and would fail rapidly.

Overall, accurate model predictions were made of the fully-aged samples, 160°C-400h and 200°C-400h, assuming the cyclic softening was solely due to mechanical softening (material ageing parameters equal to 0). Errors in the plastic strain range and the maximum stress were mostly below 15%. The model was then used to predict the as-received material when the material ageing parameters were included. The results showed that there was strong dependency on establishing accurate material parameters before the material ageing parameters were introduced. For example, the predicted secondary mechanical softening region at 160°C was not representative of the material behaviour. The model provided an accurate prediction of the stress response of the material.

The optimisation process determined the final set of material constants that improved the fitting of the predicted stress to the experimental stress (as shown by the increased value of the coefficient of determination), using the initial estimated constants as a starting point. Furthermore, the utilisation of 2 objective functions proved sufficient to obtain the optimised material constants. As a result, accurate predictions in stress at 160°C and 200°C have been achieved.

Prediction of the “partially-aged” test data and the “fully-aged” test data at 160°C and 200°C were carried out to validate the model. At 160°C, the model provided a

reasonable prediction of the stress response but an over-estimation in the stress amplitude and the yield strength of the material was a result of the inaccurate rate of material ageing. The prediction of the “fully-aged” data with the completed model was not the same as prediction with the base model for the same reason stated. At 200°C, the model exhibited good predictive capabilities to a high degree of accuracy.

Deficiencies in the model arose when attempting to predict the experimental data of the cyclic stress relaxation and the stress-controlled isothermal fatigue tests. Norton’s creep power law could not predict the stress relaxation behaviour below the material’s yield surface. If creep deformation plays an important role in the design of the SAGB housing, then the governing law for viscous stress behaviour will need to account for dominant creep mechanisms that takes place at different stress regimes. The AF equation for kinematic hardening inaccurately predicted ratcheting rate for the experimental results for the stress-controlled fatigue tests. Modifications to the AF equation (such as multiplicative kinematic hardening rule or Ohno-Wang rule II) may be required to increase control over the ratcheting rate to improve the accuracy of the predicted material stress-strain state. Additionally, the predicted ageing rate was greater than the experimental data which led to large induced plastic strains and increased the ratcheting rate. Despite the deficiencies listed, the model provided a good starting point for the predict of uniaxial isothermal fatigue behaviour of the 7175 aluminium alloy. This model allows the prediction of the decrease in material strength when subjected to cyclic plasticity at the operating temperatures of the step-aside gearbox housing. The rapid ageing of this material suggests that monitoring the material’s strength is more imperative than predicting the fatigue failure of the material from a design perspective. Therefore, the housing life can be estimated if the 7175-T7351 alloy was chosen for this application. If an aluminium alloy with sufficient and sustained strength at operating temperatures is considered for this or similar applications, then the next step in the development of this model would be to predict fatigue life.

7 Discussion

The 7175-T7351 aluminium alloy is typically used for wing, fuselage and airframe applications due to its high strength, low density, and good corrosion resistance and fatigue strength. These desirable properties this alloy has been considered to replace the current materials used for the step-aside gearbox housing of the Trent 1000. However, the operating temperatures of the housing are higher compared to the temperature of wings and fuselage and therefore it was crucial to understand the material behaviour under such conditions to determine its suitability.

According to the received flight temperature profile of the gearbox housing, about 18 minutes (0.3 hours) is spent at maximum temperature (200°C), and about 9 hours at cruise where temperatures 160°C. The results from the tensile tests have shown that the alloy exhibited rapid material ageing behaviour when the subjected to these operating temperatures of the gearbox housing. When the test specimens were subjected to a temperature soak at 200°C (under zero applied load), the yield stress decreased from 230MPa (at 0 soak hours) to 165MPa after 2 hours. When the soak temperature was 160°C, the yield stress decreases from 300MPa (at 0 soak hours) to 220MPa after 100 hours and reached an asymptotic yield stress of 180MPa after 1000 hours. The maximum stress at climb and cruise are 190MPa and 150MPa respectively. It can be estimated that at in less than 6 flight cycles, the material's yield stress falls below the operating stress during. This suggests that the 7175-T7351 alloy is not suitable for the step-aside gearbox housing application.

The constitutive viscoplasticity Chaboche model, with the inclusion of material ageing parameters, was developed sequentially and has proven to be reasonably accurate in material response prediction under fully-reversed isothermal strain-controlled conditions at 160°C and 200°C. However, the errors that arose from the model were greater at 160°C and appeared to depend on the accuracy of the first optimisation step. The non-ageing parameters obtained for 160°C predicted the maximum stress and plastic strain range within 5% and 13% error respectively. On the other hand, the rate of cyclic softening was not representative of the experimental data and the predicted results would begin to diverge after 2000 cycles. Therefore, when obtaining the material ageing constants, the process attempts to compensate for the

inaccuracies of the mechanical softening parameters. This shortfall was less pronounced for the optimisation of the material constants at 200°C since the mechanical softening terms predicted a more representative cyclic softening rate before the material ageing parameters were found. This issue may be mitigated by expanding the limits on the material constant, H_m , which was fixed during optimisation process in an attempt to prevent divergence from the linear softening region. Although the model has four additional material constants, the sequential optimisation reduced the computational effort required to find all the optimal set material parameters at one time.

The model had a few short-comings when attempting to predict isothermal stress-controlled fatigue and stress relaxation behaviour. The rate of ratcheting was over predicted. As mentioned in section 6.6.4, the Ohno-Wang rule II [92] could be used to reduce the rate of ratcheting for greater predictive accuracy. A critical state is introduced for each recovery term which inhibits the amount of hardening. Smaller ratcheting strains can be predicted while maintaining the ability to predict non-linear kinematic hardening. Furthermore, the material ageing rate may need to be adjusted for load conditions below the material's yield stress. A comparison of the predicted and experimental hysteresis loops near the end of the tests showed that the amount of predicted plastic strain (demonstrated by the widening of the loops) was greater than the experimental data, suggesting that the predicted yielding of the material occurred sooner than expected (i.e. the material ageing rate was greater). An alternative function could be used to alternate from the relationship between the monotonic yield stress and time at temperature from the tensile tests before yielding occurs, to the predicted material ageing behaviour from the modified Chaboche model after plastic strain is induced.

The stress relaxation tests showed that the viscoelastic behaviour was not predicted by the power law over long strain hold durations. The use of the hyperbolic sine law instead of the power law could be used to predict viscoelastic behaviour since it accounts for the change in creep deformation mechanisms. Despite that, the model has potential for fatigue lifetime prediction for ageing materials and would be important for determining the suitability for applications. To extend the model for fatigue life prediction, a damage factor could be introduced, based on the decrease of Young's modulus. These extensions would be useful for when another candidate

aluminium alloy possesses sufficient thermal stability and material strength, and the most important design factor is fatigue life.

TEM and EDX analysis were conducted on samples that were soaked at 200°C for up to 400 hours to observe the microstructural evolution of the alloy. Unfortunately, the pattern interference from the matrix prevented clear diffraction patterns to be obtained from smaller particles within the grains. Therefore, element mapping via EDX was used to acquire the element composition of those particles. This revealed that the particles within the grains mainly consist of zinc-magnesium rich particles. They were assumed to be MgZn_2 precipitates based on particle identification analysis of larger particles that also had the same concentration of elements. Other key microstructural features such as dislocation density, grain size and degradation of grain boundaries were not accounted for which would have had an affect on the yield stress. TEM images of test samples at different stages of a tensile testing or fatigue could be examined to study how these features evolve and how they relate to the strength of the material, which in turn, could be incorporated into the model for direct physical links to the material.

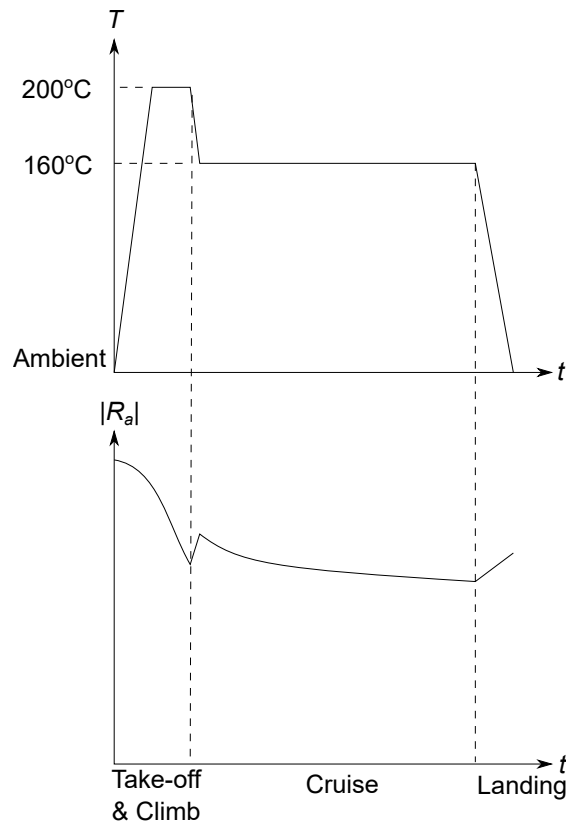


Figure 7.1: A simplified temperature profile of the step-aside gearbox housing during flight and the change in the material ageing term, $|R_a|$.

The following demonstrates how the constitutive model could be used to predict the component life for a single flight cycle. Figure 7.1 shows a simplified schematic of the temperature profile of the step-aside gearbox housing and how the magnitude of the material ageing term that affects the size of the yield surface, $|R_a|$ may change over a flight cycle for the 7175-T7351 alloy. It can be seen that during take-off the housing reaches peak temperature where the rate of material ageing is most rapid, therefore leading to the quickest reduction in material strength. Even though the take-off occurs for a short period of time, it would be important to account for the degradation of life for this alloy during this period since the maximum rate material ageing occurs. When the aircraft enters cruise, the load on the engines reduces and the temperature of the gearbox decreases. Some strength may be recovered as shown by the increase in $|R_a|$ when the operating temperature decreases (reduction of energy that aids dislocation motion). The majority of the flight cycle takes place at cruise conditions where the material ageing rate is lower than at take-off. By the end of the flight cycle, the component returns to ambient temperature and the material recovers some strength, due to the reduction of thermal energy, but not to its original strength since the microstructure has evolved.

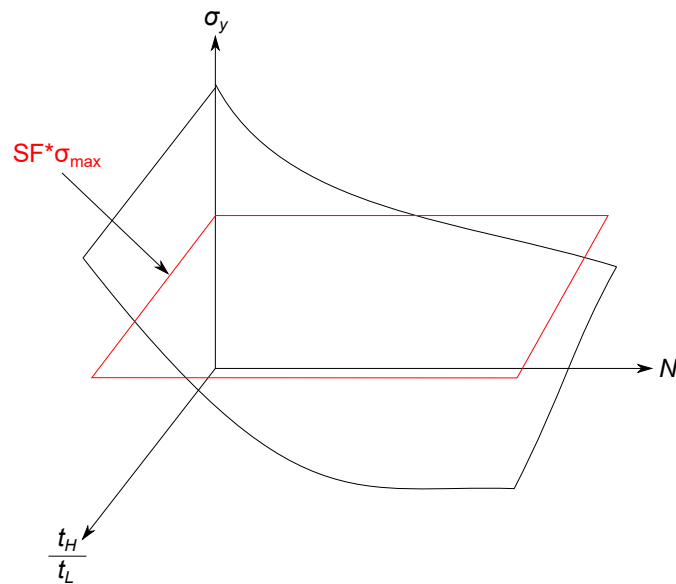


Figure 7.2: A schematic example of how the material yield stress, σ_y , changes with the number of flight cycles, N , and the ratio between the time spent at high temperature and low temperature per flight cycle, t_H/t_L . The red surface represents the required design component strength for safe operation.

Figure 7.2 shows how the suitability of a material could be assessed over a number of flight cycles. The schematic diagram shows how the yield strength of the material

(represented by the black surface) changes with the number of flight cycles, N , and the ratio between the time spent at high temperature (200°C), t_H , and low temperature (160°C), t_L , per cycle. Another surface, outlined in red, represents the stress which the material's yield strength must remain above in order for the component to be considered safe for use, where σ_{max} is the maximum operation stress and SF is a safety factor. Depending on the t_H/t_L ratio, the point at where the two surfaces intercept determines when the material is no longer suitable for use.

Constitutive models for other candidate aluminium alloys could be developed and evaluated to see which material possesses the greatest life. However, when aluminium alloys are compared against titanium alloys, it seems that the choice of material for the gearbox housing may be based on whether the cost of potentially replacing the gearbox housing multiple times would be less than the money saved by reduced fuel consumption. For example, titanium alloys are more than suitable for this application but the manufacturing cost is expensive. However, this material may not require maintenance due to its high tensile strength and fracture toughness and may not need to be replaced. If an aluminium alloy were to be used instead, the manufacturing costs may be lower but the strength over time may decrease and component will probably need to be routinely replaced. It must have sufficient strength at elevated temperatures that is thermally stable.

8 Conclusions

The motivation behind this work was to determine the suitability of the 7175-T7351 aluminium alloy for the step-aside gearbox applications in aero-engines to see whether it could lead to a weight reduction of the housing. The first objective was to characterise the alloy using a series of elevated temperature mechanical tests that are similar to the operating conditions of the housing. The second objective involved the creation of a viscoplastic model to predict the stress response of this alloy under strain-controlled IF conditions, which accounted for the evolution of its microstructure during time at temperature. The validity of this model would be a starting point for which the model could be “fine tuned” to increase the predictive accuracy of other material behaviour that may be exhibited under different load conditions. Furthermore, the basic method of obtaining material constants for this model could be used for other candidate materials so that their stress-response can be assessed for said application.

The temperature soak between 180°C to 230°C over 1000 hours showed that the greater the temperature, the greater the initial rate of decrease in hardness. After 1000 hours, the hardness significantly decreased by 48-60%. An asymptotic hardness value was reached depending on the soak temperature. The elevated tensile results showed that simply testing at 200°C reduced the yield stress of the material by 31% and soaking the material at that temperature for 20 hours before testing reduced the yield stress by 52% (below the maximum stress from the flight profile). Since the hardness of a material is related to the material’s yield stress, this revealed that the aluminium alloy aged rapidly at temperatures similar to the gearbox housing during operation. Therefore, such behaviour was important to characterise for the constitutive viscoplasticity model.

The material exhibited ratcheting behaviour in the positive strain direction under stress-controlled IF and TMF conditions (R-ratio=0.25). Furthermore, when the maximum temperature was 200°C for the IF and IP TMF tests, the material was elastically loaded for the majority of the test duration but would eventually accumulate plastic strain and increase the ratcheting rate. This would suggest that the applied stress exceeded the yield stress of the material after a certain period of time at temperature. Since the tests were not continued until sample failure, it was not possible to determine what the dominant mechanism would be. However, it would

seem that ratcheting is a significant component in the inelastic strain accumulation of the material.

Norton's creep law constants were obtained from the creep data for each temperature (160°C, 180°C and 200°C) and were used to predict the minimum creep rate for each creep conditions. The results showed that the numerical and experimental results were in good agreement. During cruise flight condition, the temperature of the step-aside gearbox housing can range between 160-190°C. The effect of prestrain on secondary creep behaviour remains unclear and further testing is necessary to understand the existing results.

The unified, viscoplastic Chaboche model accurately predicted the strain-controlled IF response, with the addition of the material ageing parameters, at 160°C and 200°C. It was clear from the prediction at 160°C that the accuracy of the complete model was highly dependent on the accuracy of the material constants obtained for mechanical softening, kinematic hardening and viscous stress behaviour, before the material ageing parameters were obtained. The prediction of the mechanical softening parameters at 200°C meant that most of the errors of the plastic strain range and maximum stress were below 15%. Nevertheless, the predicted stress response was in good agreement with the experimental stress data.

Deficiencies in the model were highlighted by the attempt to predict stress-controlled fatigue and stress relaxation data at 200°C. Currently, it is unable to accurately predict the ratcheting and viscoelasticity but this is outside the scope of this work and further discussed in next chapter. However, the model provides a good starting point in describing the behaviour of the 7175 alloy with the inclusion of material ageing effects as shown by the coefficient of determination calculated for the selected hysteresis loops. The prediction of the ageing behaviour at during time at operating temperatures could lead to a relatively simple lifetime model to rate the aluminium alloy. This would be based on the time at which the yield strength of the material falls below the operating stress multiplied by a safety factor.

Due to the rapid ageing of the 7175-T7351 aluminium alloy, the material is most likely not suitable for this application, especially if the component is overloaded due to unlikely circumstances (eg. the failure of one engine during take-off). A more thermally stable material in the component range should be used. However, it has been shown

that constitutive models for materials that exhibit material ageing are important for the life prediction of components subjected to elevated temperatures. Constitutive models for more suitable aluminium alloys can be evaluated based on the evolution of the alloys' yield strength per flight cycle.

9 Future Work

There were complications with complete strain measurement during the tensile tests since the strain measurement was dependent on the video gauge's ability to recognise the tracking areas on the highly ductile sample. This could be mitigated by the use of laser extensometry which does not require a pattern to track on the sample (if the window on the environmental chamber does not pose a problem). Alternatively, an investigation into whether the elevated temperature hardness measurements could be correlated to the elevated yield stress of the material. An estimation of yield stress may be sufficient enough to demonstrate the effect of temperature on elevated temperature tensile properties.

Referring to the scatter of the results from the repeated prestrained creep test with a creep stress of 190MPa, the reliability of the results was questionable without the support of repeats tests. Therefore, in future work, it would be recommended to carry out 3-5 repeat tests per combination of test parameters for improved validity of the results and perhaps then a trend could be established. Also, the Mayes 250 required the presence of the user to manually switch the machine from displacement control to load control when the prestrain level was reached. Another machine with automation may be more suitable for this type of testing.

The Chaboche model in Chapter 6 has shown good predictive capabilities of the stress response of the 7175-T7351 aluminium alloy under strain-controlled isothermal fatigue conditions. However, the rate of cyclic softening of the material could be improved by adjusting the mechanical softening terms Q_m and b_m by widening the bounds during optimisation. Additional isothermal fatigue test data at intermediate temperatures between 160°C and 200°C could be carried out to obtain the temperature dependent material constants. The model could then be generalised by interpolating the material constants for a specific temperature or for anisothermal conditions. Zhang et al [206] derived an elasto-plastic non-linear kinematic and isotropic model for two martensitic steels for anisothermal fatigue conditions.

The prediction of the stress-controlled test revealed that the inadequacy to represent the ratcheting behaviour when mean stress was a positive non-zero value. For future works to improve the model, a multiplicative kinematic hardening rule or the Ohno-

Wang rule II could be used [204]. It has been shown to give the model more control over the rate at which the saturation back stress is reached without change the saturation value.

Figure 6.1 shows that some samples exhibit rapid softening by the end of the fatigue tests which indicated the accumulation of damage towards fracture. A continuum damage model could be utilised to extend the model and determine the material behaviour during the tertiary stage. The damage parameters can be estimated by measuring the change in stiffness of the material with accumulated plastic strain using Cottrell's partitioning method. Fatigue life may also be possible to predict as well.

The comparison between numerical and experimental results of the stress relaxation tests shown in section 6.6.4 highlighted two deficiencies in the model: 1) it is currently unable to predict the viscoelastic behaviour of the material and 2) the Norton's power law was unsuitable to describe long term stress relaxation behaviour. However, the power law was able to predict short term viscous effects. The hyperbolic sine law could be used to amend both these issues since it has been used to predict a smooth transition between to types of creep mechanisms. Therefore, the hyperbolic sine function could replace Norton's power law for more accurate prediction of both long term and short term stress relaxation behaviour.

Other aluminium alloys that are specifically manufactured for elevated temperature applications and possess adequate strength could be considered as candidate materials. For example, aluminium alloys containing trialuminide intermetallic precipitates (Al_3X) or powder sintered aluminium alloys such as the Al-MS89, Al-SF25 or the Al-MD20 design for heat resistance could be investigated. The Chaboche model could be established for these materials to predict their stress response. If their strength retention at elevated temperatures is acceptable, then there are other abnormal flight conditions that can also be used to test the material's suitability such as windmilling (the airflow causing the turbofan of a non-operating engine to spin) and cool climbing (one engine shuts down during take-off and the remaining engine(s) are required to carry the full load).

Bibliography

- [1] Rodhe H. A comparison of the contribution of various gases to the greenhouse effect. *Science*. 1990;248(4960):1217–1219.
- [2] Ding L, Liu C, Chen K, Huang Y, Diao B. Atmospheric pollution reduction effect and regional predicament: An empirical analysis based on the Chinese provincial NO_x emissions. *Journal of Environmental Management*. 2017;196:178–187.
- [3] Rubbert PE. CFD and changing world 006Ff aircraft design. AIAA Wright Brothers Lecture. New York: AIAA Publications; 1994.
- [4] Atiik E, Meric C, Karlik B. Determination of yield strength of 2014 aluminium alloy under ageing conditions by means of artificial neural networks method. *Mathematical & Computational Applications*1. 1996;1(2):16–20.
- [5] Shriwas AK, Kale VC. Impact of aluminum alloys and microstructures on engineering properties - review. *IOSR Journal of Mechanical and Civil Engineering*. 2016;13(3):16–22.
- [6] Büyükdoan S, Gündüz S, Türkmen M. Influence of ageing treatment on microstructure, mechanical properties and adhesive wear behaviour of 6063 aluminium alloy. *Industrial Lubrication and Tribology*. 2014;66(4):520–524.
- [7] Gunderson AW. Elevated temperature mechanical properties of two cast aluminium alloys; 1969.
- [8] Eylon D, Fujishiro S, Postans PJ, Froes FH. High-temperature titanium alloys - a review. *Physical & Mechanical Metallurgy*. 1984;36(11):52–62.
- [9] Immarigeon JP, Holt RT, Koul AK, Zhoa L, Wallace W, Beddoes JC. Lightweight materials for aircraft applications. *Materials Characterization*. 1995;35(1):41–67.
- [10] Rolls-Royce. *The Jet Engine*. John Wiley & Sons; 2015.
- [11] The Rolls Royce Trent 1000, www.rolls-royce.com - Accessed: 30/06/2014;.
- [12] Chaboche JL. A review of some plasticity and viscoplasticity constitutive theories. *International Journal of Plasticity*. 2008;24(10):1642–1693.

- [13] Marquis D, Lemaitre J. Constitutive equations for the coupling between elasto-plasticity damage and aging. *Revue De Physique Appliquee*. 1988;23:615 – 624.
- [14] Cailletaud G, Depoid C, Massinon D, Nicouleau-Bourles E. Elastoviscoplasticity with ageing in aluminium alloys. *Continuum Thermomechanics*. 2000;p. 75–86.
- [15] ACARE. Strategic research & innovation agenda 2017 update. ACARE. 2017;.
- [16] Ommi F, Azimi M. Most effective combustion technologies for reducing NOx emissions in aero gas turbines. *International Journal of Multiphysics*. 2012;6(4):417–424.
- [17] Williams JC, Starke EA. Progress in structural materials for aerospace systems. *Acta Materialia*. 2003;51(19):5775–5799.
- [18] Roy MJ, Maijer DM, Dancoine L. Constitutive behavior of as-cast A356. *Materials Science and Engineering: A*. 2012;548:195–205.
- [19] Lin YC, Xia YC, Jiang YQ, Li LT. Precipitation in AlCuMg alloy during creep exposure. *Materials Science and Engineering: A*. 2012;556:796–800.
- [20] Securing the future of U.S air transportation: A system in peril (2003). Washington DC: The National Academies Press: Transportation Research Board and National Research Council; 2003.
- [21] Lee JJ. Historical and future trends in aircraft performance, cost, and emissions; 2000.
- [22] Meetham GW, de Voorde MHV, Voorde MH. *Materials for high temperature engineering applications*. Springer; 2000.
- [23] Tinoco EN. The changing role of computational fluid dynamics in aircraft development. *American Institute of Aeronautics and Astronautics*. 1998;(A98-323415):161–174.
- [24] Dursun T, Soutis C. Recent developments in advanced aircraft aluminium alloys. *Materials & Design*. 2014;56:862–871.

- [25] Kassapoglou C. Minimum cost and weight design of fuselage frames Part A : design constraints and manufacturing process characteristics. *Composites: Part A*. 1999;30:887–894.
- [26] Burt DN, Doyle MF. *American Keiretsu: A Strategic Weapon for Global Competiveness*. 1st ed. McGraw-Hill Companies; 1993.
- [27] Rambabu P, Eswara Prasad N, Kutumbarao VV, Wanhill RJH. *Aerospace materials and material technologies volume 1: aerospace materials*; 2017.
- [28] Design G. *CES EduPack 2009*; 2009.
- [29] Grandfield JF. *Ingot casting and casthouse metallurgy of aluminium and its alloys*. Woodhead Publishing Limited; 2011.
- [30] Otarawanna S, Dahle AK. *Casting of aluminium alloys*. Woodhead Publishing Limited; 2011.
- [31] Polmear I. *Light Alloys, Fourth Edition: from traditional alloys to nanocrystals*. Butterworth-Heinemann; 2005.
- [32] Meyes M, Chawla K. *Mechanical behaviour of materials*. Second ed. Cambridge University Press; 2009.
- [33] Taylor GI. No Title. *Proc Roy Soc London*. 1934;145A:362.
- [34] Orowan E. No Title. *Z Physik*. 1934;89:605.
- [35] Polanyi M. No Title. *Z Physik*. 1934;89:660.
- [36] Fleischer RL. Substitutional solution hardening. *Acta Metallurgica*. 1963;11(3):203–209.
- [37] Labusch R. Statistical, theory of solid solution. *Physica Status Solidi B*. 1970;41:659–669.
- [38] Linder J, Axelsson M, Nilsson H. The influence of porosity on the fatigue life for sand and permanent mould cast aluminium. *International Journal of Fatigue*. 2006;28(12):1752–1758.

- [39] Somoza a, Macchi CE, Lumley RN, Polmear IJ, Dupasquier A, Ferragut R. Role of vacancies during creep and secondary precipitation in an underaged Al-Cu-Mg-Ag alloy. *Physica Status Solidi (C)*. 2007;4(10):3473–3476.
- [40] Nový F, Janeček M, Král R. Microstructure changes in a 2618 aluminium alloy during ageing and creep. *Journal of Alloys and Compounds*. 2009;487(1-2):146–151.
- [41] Tiryakiolu M. On the relationship between Vickers hardness and yield stress in AlZnMgCu Alloys. *Materials Science and Engineering: A*. 2015;633:17–19.
- [42] Flemings MC, Kattamis TZ, Bardes BP. Dendrite arm spacing in aluminium alloys. *Transactions of the American Foundrymen's Society*. 1991;99:501 – 506.
- [43] Iben Houria M, Nadot Y, Fathallah R, Roy M, Maijer DM. Influence of casting defect and SDAS on the multiaxial fatigue behaviour of A356-T6 alloy including mean stress effect. *International Journal of Fatigue*. 2015;80:90–102.
- [44] Ceschini L, Morri A, Morri A, Gamberini A, Messieri S. Correlation between ultimate tensile strength and solidification microstructure for the sand cast A357 aluminium alloy. *Materials & Design*. 2009;30(10):4525–4531.
- [45] Ceschini L, Boromei I, Morri A, Seifeddine S, Svensson IL. Microstructure, tensile and fatigue properties of the Al10%Si2%Cu alloy with different Fe and Mn content cast under controlled conditions. *Journal of Materials Processing Technology*. 2009;209(15-16):5669–5679.
- [46] Di Sabatino M, Arnberg L. Castability of aluminium alloys. *Transactions of The Indian Institute of Metals*. 2009;62(4-5):321–325.
- [47] Linder J, Arvidsson A, Kron J. The influence of porosity on the fatigue strength of high-pressure die cast aluminium. *Fracture of Engineering Materials and Structures*. 2006;29(5):357–363.
- [48] Dabayeh AA, Xu RX, Du BP, Topper TH. Fatigue of cast aluminium alloys under constant and variable-amplitude loading. *International Journal of Fatigue*. 1996;18(2):95–104.

- [49] González R, Martínez DI, González JA, Talamantes J, Valtierra S, Colás R. Experimental investigation for fatigue strength of a cast aluminium alloy. *International Journal of Fatigue*. 2011;33(2):273–278.
- [50] Gao YX, Yi JZ, Lee PD, Lindley TC. The effect of porosity on the fatigue life of cast aluminium-silicon. 2004;p. 559–570.
- [51] Ammar HR, Samuel AM, Samuel FH. Porosity and the fatigue behavior of hypoeutectic and hypereutectic aluminum-silicon casting alloys. *International Journal of Fatigue*. 2008;30(6):1024–1035.
- [52] Wang T, Zhu T, Sun J, Wu R, Zhang M. Influence of rolling directions on microstructure, mechanical properties and anisotropy of Mg-5Li-1Al-0.5Y alloy. *Journal of Magnesium and Alloys*. 2015;3(4):345–351.
- [53] Wang B, Chen Xh, Pan Fs, Mao Jj, Fang Y. Effects of cold rolling and heat treatment on microstructure and mechanical properties of AA 5052 aluminum alloy. *Transactions of Nonferrous Metals Society of China*. 2015;25(8):2481–2489.
- [54] Rao ACU, Vasu V, Govindaraju M, Srinadh KVS. Influence of cold rolling and annealing on the tensile properties of aluminum 7075 alloy. *Procedia Materials Science*. 2014;5:86–95.
- [55] Polmear IJ. *Aluminium alloys A century of age hardening*. 2004;28:1–14.
- [56] Totten GE, MacKenzie S. *Handbook of aluminium: Vol. 1: physical metallurgy and processes*. Totten GE, MacKenzie S, editors. CRC Press, 2003; 2003.
- [57] Ilangovan S, Srikanthan R, Veda Vyass G. Effects of aging time on mechanical properties of sand cast Al-4.5Cu alloy. *International Journal of Research in Engineering and Technology*. 2014;3(5):57–61.
- [58] Nembach E. *Particle strengthening of metals and alloys*; 1997.
- [59] Siddiqui RA, Abdullah HA, Al-Belushi KR. Influence of aging parameters on the mechanical properties of 6063 aluminium alloy. *Journal of Materials Processing Technology*. 2000;102(1):234–240.

- [60] Kabir MS, Minhaj TI, Ashrafi EA, Islam M. The influence of ageing time and temperature on the structure and properties of heat treated A201 . 0 aluminum alloy. *International Journal of Recent Technology and Engineering*. 2014;3(3):78–83.
- [61] Dobrzański LA, Krawczyk G. Influence of the ageing on mechanical properties of the aluminium alloy AlSi9Mg. *International Scientific journal*. 2008;31(1):37–40.
- [62] Dwivedi DK, Mart E. Influence of solutionising and aging temperatures on microstructure and mechanical properties of cast Al Si Cu alloy. *Materials Science and Technology*. 2009;25(7):2–7.
- [63] Akhil KT, Arul S, Sellamuthu R. The effect of heat treatment and aging process on microstructure and mechanical properties of A356 aluminium alloy sections in casting. *Procedia Engineering*. 2014;97:1676–1682.
- [64] Chen Y, Weyland M, Hutchinson CR. The effect of interrupted aging on the yield strength and uniform elongation of precipitation-hardened Al alloys. *Acta Materialia*. 2013;61(15):5877–5894.
- [65] Lumley RN, Polmear IJ, Morton AJ. Temper developments using secondary ageing. *Materials Forum*. 2004;28:85–95.
- [66] Lumley RN, Polmear IJ, Morton aJ. Development of mechanical properties during secondary aging in aluminium alloys. *Materials Science and Technology*. 2005;21(9):1025–1032.
- [67] Hall EO. The deformation and ageing of mild steel: III discussion of results. *Proc Roy Soc (London)*. 1951;B64:474.
- [68] Petch NJ. The cleavage strength of polycrystals. *J Iron Steel Inst*. 1953;174:25.
- [69] Bobby Kannan M, Raja VS. Enhancing stress corrosion cracking resistance in AlZnMgCuZr alloy through inhibiting recrystallization. *Engineering Fracture Mechanics*. 2010;77(2):249–256.
- [70] Peng X, Guo Q, Liang X, Deng Y, Gu Y, Xu G, et al. Mechanical properties, corrosion behavior and microstructures of a non-isothermal ageing treated Al-Zn-Mg-Cu alloy. *Materials Science and Engineering: A*. 2017;688:146–154.

- [71] Ghiaasiaan R, Amirkhiz BS, Shankar S. Quantitative metallography of precipitating and secondary phases after strengthening treatment of net shaped casting of Al-Zn-Mg-Cu (7000) alloys. *Materials Science and Engineering A*. 2017;698:206–217.
- [72] Ranganatha R, Anil Kumar V, Nandi VS, Bhat RR, Muralidhara BK. Multi-stage heat treatment of aluminum alloy AA7049. *Transactions of Nonferrous Metals Society of China (English Edition)*. 2013;23(6):1570–1575.
- [73] Yang W, Ji S, Wang M, Li Z. Precipitation behaviour of AlZnMgCu alloy and diffraction analysis from η precipitates in four variants. *Journal of Alloys and Compounds*. 2014;610:623–629.
- [74] Wolverton C. Crystal structure and stability of complex precipitate phases in Al-Cu-Mg-(Si) and Al-Zn-Mg alloys. *Acta Materialia*. 2001;49(16):3129–3142.
- [75] Birbilis N, Cavanaugh MK, Buchheit RG. Electrochemical behavior and localized corrosion associated with Al₇Cu₂Fe particles in aluminum alloy 7075-T651. *Corrosion Science*. 2006;48(12):4202–4215.
- [76] Park JG, Lee DY, Choi J. Static creep behavior of Al-Zn-Mg-Cu and Al-Zn-Mg-Cu alloys. *Journal of Materials Science*. 1996;31:2719–2723.
- [77] Li X, J SM. The effect of compositional variations on the characteristics of coarse intermetallic particles in overaged 7xxx Al alloys. *Mater Sci Techn*. 2001;17:1324–28.
- [78] Starink MJ, Wang SC. A model for the yield strength of overaged AlZnMgCu alloys. *Acta Materialia*. 2003;51(17):5131–5150.
- [79] Tresca H. Memoire sur l'écoulement des corps solides. *Memoire Presentes par Divers Savants, Acad Sci Paris*. 1872;20:75–135.
- [80] Mises RV. *Mechanik der festen Körper im plastisch-deformablen Zustand*, Naehr. kgl. Ges. Wiss. Göttingen, Math Phys Klasse. 1913;p. 582–592.
- [81] Jones RM. *Deformation theory of plasticity*. Bull Ridge Publishing; 2009.

- [82] Chaboche JL, Rousselier G. On the plastic and viscoplastic constitutive equations - part 1: rules developed with internal variable concept. *Journal of Pressure Vessel Technology*. 1983;105(2):153 – 158.
- [83] Baushinger J. On the change of the positions of elastic limit of iron and steel under cyclic variation of stress. *Mitt Mech - Tech Lab, Munich*. 1886;13.
- [84] Chaboche JL, Rousselier G. On the plastic and viscoplastic constitutive equations - part 2: application of internal variable concepts to the 316 stainless steel. *Journal of Pressure Vessel Technology*. 1983;105(2):159 – 164.
- [85] Prager W. A new method of analyzing stresses and strains in work hardening. *Journal of Applied Mechanics*. 1956;23:493–496.
- [86] Ziegler H. A modification of prager's hardening rule. *Quarterly Applied Mathematics*. 1955;17:55–65.
- [87] Armstrong PJ, Frederick CO. A mathematical representation of the multiaxial baushinger effect. *Materials at High Temperatures*. 2007;24(1):1–26.
- [88] Chełmiński K, Neff P, Owczarek S. The Armstrong-Frederick cyclic hardening plasticity model with Cosserat effects. *Journal of Mathematical Analysis and Applications*. 2015;423(1):283–304.
- [89] Chaboche JL, Dang-Van K, Cordier G. Modelization of the strain memory effect on the cyclic hardening of 316 stainless steel. Berlin; 1979.
- [90] Chaboche JL, Rousselier G. On the plastic and viscoplastic constitutive equations, parts I and II. *Pressure Vessel Piping*. 1983;105:153–164.
- [91] Ohno N, Wang JD. Kinematic hardening rules with critical state of dynamic recovery, part I - formulation and basic features for ratchetting behaviour. II - application to experiments of ratchetting behaviour. *International Journal of Plas*. 1993;9(3):375–403.
- [92] Ohno N, Wang JD. Kinematic hardening rules with critical state of dynamic recovery, part II: application to experiments of ratchetting behaviour. *International Journal of Plasticity*. 1993;9(3):391–403.

- [93] Abdel-Karim M. An evaluation for several kinematic hardening rules on prediction of multiaxial stress-controlled ratchetting. *International Journal of Plasticity*. 2010;26(5):711–730.
- [94] Tong J, Zhan ZL, Vermeulen B. Modelling of cyclic plasticity and viscoplasticity of a nickel-based alloy using Chaboche constitutive equations. *International Journal of Fatigue*. 2004 aug;26(8):829–837.
- [95] Zhan ZL, Tong J. A study of cyclic plasticity and viscoplasticity in a new nickel-based superalloy using unified constitutive equations. Part II: Simulation of cyclic stress relaxation. *Mechanics of Materials*. 2007;39(1):73–80.
- [96] Zhan ZL, Tong J. A study of cyclic plasticity and viscoplasticity in a new nickel-based superalloy using unified constitutive equations. Part I: Evaluation and determination of material parameters. *Mechanics of Materials*. 2007;39(1):64–72.
- [97] Zhan Z, Fernando US, Tong J. Constitutive modelling of viscoplasticity in a nickel-based superalloy at high temperature. *International Journal of Fatigue*. 2008;30(7):1314–1323.
- [98] Hyde CJ, Sun W, Leen SB. Cyclic thermo-mechanical material modelling and testing of 316 stainless steel. *International Journal of Pressure Vessels and Piping*. 2010;87(6):365–372.
- [99] Hyde CJ, Sun W, Hyde TH, Saad AA. Thermo-mechanical fatigue testing and simulation using a viscoplasticity model for a P91 steel. *Computational Materials Science*. 2012;56:29–33.
- [100] Rouse JP, Hyde CJ, Sun W, Hyde TH. Effective determination of cyclic-viscoplasticity material properties using an optimisation procedure and experimental data exhibiting scatter. *Materials at High Temperatures*. 2013;30(2):117–128.
- [101] Rouse JP, Hyde CJ, Sun W, Hyde TH. Comparison of several optimisation strategies for the determination of material constants in the Chaboche visco-plasticity model. *Journal of Strain Analysis for Engineering Design*. 2013;48(6):347–363.

- [102] Rouse JP, Hyde CJ, Sun W, Hyde TH. Pragmatic optimisation methods for determining material constants of viscoplasticity model from isothermal experimental data. *Mater Sci Technol.* 2014;30(July):54–62.
- [103] Kyaw ST, Rouse JP, Lu J, Sun W. Determination of material parameters for a unified viscoplasticity-damage model for a P91 power plant steel. *International Journal of Mechanical Sciences.* 2016;115-116:168–179.
- [104] Lemaitre J, Desmorat R. *Engineering damage mechanics. Ductile, creep, fatigue and brittle failures.* Springer; 2005.
- [105] Cottrell AH. *Dislocations and plastic flow in crystals.* Oxford University Press. 1953;.
- [106] Mroz Z. An attempt to describe the behavior of metals under cyclic loads using a more general work hardening model. *Acta Mechanica.* 1969;7(2):199–212.
- [107] Jiang Y, Sehitoglu H. Comments on the Mroz multiple type plasticity models. 1996;33(7):1053–1068.
- [108] Sivakumar SM. *A non-proportional cyclic plasticity model for metals With ratchetting effects.* Louisiana State University and Agricultural & Mechanical College; 1993.
- [109] Mroz Z. On the description of anisotropic work-hardening. *J Mech Phys Mech.* 1967;15:163.
- [110] Dafalias YF, Popov EP. Plastic internal variables formalism of cyclic plasticity. *Journal of Applied Mechanics.* 1976;43:645–651.
- [111] Estrin Y, Mecking H. A unified phenomenological description of work hardening and creep based on one-parameter models. *Acta Metallurgica.* 1984;32(1):57–70.
- [112] Estrin Y. Dislocation theory based constitutive modelling: foundations and applications. *Journal of Materials Processing Technology.* 1998;80-81:33–39.
- [113] Cailletaud G. *A micromechanical approach to inelastic behaviour of metals.* *International Journal of Plasticity.* 1992;8(1):55–73.

- [114] Sauzay M, Brillet H, Monnet I, Mottot M, Barcelo F, Fournier B, et al. Cyclically induced softening due to low-angle boundary annihilation in a martensitic steel. *Materials Science and Engineering A*. 2005;400-401(1-2 SUPPL.):241–244.
- [115] Sauzay M, Fournier B, Mottot M, Pineau A, Monnet I. Cyclic softening of martensitic steels at high temperature-Experiments and physically based modelling. *Materials Science and Engineering A*. 2008;483-484(1-2 C):410–414.
- [116] Taylor GI. Plastic strain in metals. *Journal of the Institute of Metals*. 1938;62:307–324.
- [117] Barrett RA, O’Donoghue PE, Leen SB. A dislocation-based model for high temperature cyclic viscoplasticity of 9-12Cr steels. *Computational Materials Science*. 2014;92:286–297.
- [118] Barrett RA, O’Donoghue PE, Leen SB. A physically-based constitutive model for high temperature microstructural degradation under cyclic deformation. *International Journal of Fatigue*. 2017;100:388–406.
- [119] Atkinson KE. *An introduction to numerical analysis*; 2009.
- [120] Chaparro BM, Thuillier S, Menezes LF, Manach PY, Fernandes JV. Material parameters identification: Gradient-based, genetic and hybrid optimization algorithms. *Computational Materials Science*. 2008;44(2):339–346.
- [121] Levenberg K. A method for the solution of certain non-linear problems in least squares. *Quarterly of Applied Mathematics*. 1944;2:164–168.
- [122] Marquardt D. An algorithm for least squares estimation of nonlinear parameters. *SIAM Journal on Applied Mathematics*. 1963;11(2):431–441.
- [123] Hyde CJ. Thermo-mechanical fatigue and creep of high temperature materials, PhD Thesis. The University of Nottingham; 2010.
- [124] Guler O. *Foundations of optimisation*. 1st ed. New Yoek, U.S.A: Springer; 2010.
- [125] Guillaume P, Pintelon R. A Gauss-Newton like Optimisation Algorithm for ”Weighted” Nonlinear Least-Squares Problems. *IEEE Transactions on Signal Processing*. 1996;44:2222–2228.

- [126] Stephens RI, Fatemi A, Stephens RR, Fuchs HO. *Metal Fatigue in Engineering* (A Wiley-Interscience publication). John Wiley & Sons; 2000.
- [127] Albert WAJ. *Über Treibseile am Harz*. *Archiv für Mineralogie, Geognosie, Bergbau und Hüttenkunde*. 1837;10:215–234.
- [128] Rankine WJM. *On the causes of the unexpected breakage of the journals of railway axles, and on the means of preventing such accidents by observing the law of continuity in the construction*. In: *Institution of Civil Engineers, Minutes of Proceedings*; 1842. p. 105–108.
- [129] Wohler A. *Versuche zur Ermittlung der auf die Eisenbahnwagenachsen einwirkenden Kräfte und die Widerstandsfähigkeit der Wagen-Achsen*. *Zeitschrift für Bauwesen*. 1860;p. 583–616.
- [130] Basquin OH. *The exponential law of endurance tests*. *Proceedings, American Society for Testing and Materials, ASTEA*. 1910;10:625–630.
- [131] Coffin LF. *A study of the effects of cyclic thermal stresses on ductile metal*. *Trans ASME*. 1954;76:931–950.
- [132] Manson SS. *Behaviour of materials under conditions of thermal stress*. In: *NACA TN-2933, National Advisory Committee for Aeronautics*; 1954. .
- [133] Goodman J. *Mechanics applied to engineering*; 1899.
- [134] Gerber H. *Bestimmung der zulässigen Spannungen in Eisenkonstruktionen*. *Zeitschrift des Bayerischen Architekten und Ingenieur-Vereins*. 1874;6:101–110.
- [135] Soderberg CR. *Factor of safety and working stress*. *Transactions of the American Society of Mechanical Engineers*. 1939;52:13–28.
- [136] Paris PC, Gomez MP, Anderson WE. *A rational analytic theory of fatigue*. *The Trend in Engineering*. 1961;13:9 – 14.
- [137] Vratnica M, Cvijović Z, Degischer HP, Requena G, Rumlplmair G, Rakin M. *Crack growth resistance of overaged Al-Zn-Mg-Cu alloys*. *Materials Science Forum*. 2005;494:217–22.

- [138] Vratnica M, Cvijović Z, Gerić K, Burzić Z. The role of intermetallic phases in fatigue crack propagation behaviour of Al-Zn-Mg-Cu alloys. *Materials Science Forum*. 2007;555:553–558.
- [139] Alpay SP, Gurbuz R. The effect of coarse second phase particles on fatigue crack propagation of an Al-Zn-Mg-Cu alloy. *Metallurgical Transactions A*. 1994;30(11):1373 – 1376.
- [140] Jian Hg, Jiang F, Wen K, Jiang L, Huang Hf, Wei Ll. Fatigue fracture of high-strength Al-Zn-Mg-Cu alloy. *Transactions of Nonferrous Metals Society of China*. 2009;19(5):1031–1036.
- [141] Lindigkeit J, Gysler A, Lutjering G. The effect of microstructure on fatigue crack propagation behaviour of an Al-Zn-Mg-Cu alloy. *Metallurgical Transactions A*. 1981;12:1613 – 1619.
- [142] Desmukh MN, Pandey RK, Mukhopadhyay AK. Effect of aging treatments on the kinetics of fatigue crack growth in 7010 aluminum alloy. *Materials Science and Engineering: A*. 2006;435-436:318–326.
- [143] Thomas G, Bressers J, Raynor D. Low-cycle fatigue and life prediction methods. Brunetaud R, Coutsouradis D, Gibbons TB, Lindblom Y, Meadowcroft DB, Stickler R, editors. Dordrecht: Springer Netherlands; 1982.
- [144] Halford GR. Low-cycle thermal fatigue. 1986;.
- [145] Neu R, Sehitoglu H. Thermomechanical fatigue, oxidation, and creep: Part I: damage mechanisms. *Metallurgical Transactions A*. 1989;20A(9):1755 – 1767.
- [146] Neu RW, Sehitoglu H. Thermomechanical fatigue, oxidation, and creep: Part II: Life prediction. *Metallurgical Transactions A*. 1989;20A(9):1769–83.
- [147] Zhang JX, Harada H, Ro Y, Koizumi Y, Kobayashi T. Thermomechanical fatigue mechanism in a modern single crystal nickel base superalloy TMS-82. *Acta Materialia*. 2008;56(13):2975–2987.
- [148] Neu RW, Kupkovits RA, Smith DJ. Influence of minimum temperature on the thermomechanical fatigue of a directionally-solidified Ni-base superalloy. *Procedia Engineering*. 2010;2(1):687–696.

- [149] Amaro RL, Antolovich SD, Neu RW, Staroselsky A. On thermo-mechanical fatigue in single crystal Ni-base superalloys. *Procedia Engineering*. 2010;2:815–824.
- [150] Moverare JJ, Gustafsson D. Hold-time effect on the thermo-mechanical fatigue crack growth behaviour of Inconel 718. *Materials Science and Engineering: A*. 2011;528(29-30):8660–8670.
- [151] Jacobsson L, Persson C, Melin S. Thermo-mechanical fatigue crack propagation experiments in Inconel 718. *International Journal of Fatigue*. 2009;31(8-9):1318–1326.
- [152] Okazaki M, Sakaguchi M. Thermo-mechanical fatigue failure of a single crystal Ni-based superalloy. *International Journal of Fatigue*. 2008;30(2):318–323.
- [153] Saad AA, Hyde TH, Sun W, Hyde CJ, Tanner DWJ. Characterization of viscoplasticity behaviour of P91 and P92 power plant steels. *International Journal of Pressure Vessels and Piping*. 2013;111-112:246–252.
- [154] Nagesha A, Valsan M, Kannan R, Bhanu Sankara Rao K, Bauer V, Christ HJ, et al. Thermomechanical fatigue evaluation and life prediction of 316L(N) stainless steel. *International Journal of Fatigue*. 2009;31(4):636–643.
- [155] Fekete B, Kasl J, Jandova D, Jóni B, Misják F, Trampus P. Low cycle thermomechanical fatigue of reactor steels: microstructural and fractographic investigations. *Materials Science and Engineering: A*. 2015;640:357–374.
- [156] Nagesha A, Kannan R, Sastry GVS, Sandhya R, Singh V, Bhanu Sankara Rao K, et al. Isothermal and thermomechanical fatigue studies on a modified 9Cr-1Mo ferritic martensitic steel. *Materials Science and Engineering A*. 2012;554:95–104.
- [157] Bae KH, Kim HH, Lee SB. A simple life prediction method for 304L stainless steel structures under fatigue-dominated thermo-mechanical fatigue loadings. *Materials Science and Engineering: A*. 2011;529:370–377.
- [158] Bosefilho W, Defreitas E, Dasilva V, Milan M, Spinelli D. AlSi cast alloys under isothermal and thermomechanical fatigue conditions. *International Journal of Fatigue*. 2007;29(9-11):1846–1854.

- [159] Azadi M. Effects of strain rate and mean strain on cyclic behavior of aluminum alloys under isothermal and thermo-mechanical fatigue loadings. *International Journal of Fatigue*. 2013;47:148–153.
- [160] Merhy E, Rémy L, Maitournam H, Augustins L. Crack growth characterisation of A356-T7 aluminum alloy under thermo-mechanical fatigue loading. *Engineering Fracture Mechanics*. 2013;110:99–112.
- [161] Huter P, Oberfrank S, Grün F, Stauder B. Thermo-mechanical fatigue influence of copper and silicon on hypo-eutectic Al-Si-Cu and Al-Si-Mg cast alloys used in cylinder heads. *International Journal of Fatigue*. 2016;88:142–155.
- [162] Spigarelli S. *Creep of aluminium and aluminium alloys*; 1999.
- [163] Kassner ME, Perez-Prado MT. *Fundamentals of creep in metals and alloys*. Elsevier; 2004.
- [164] Ashby MF. A first report on deformation maps. *Acta Metallurgica*. 1972;20(7):887 – 897.
- [165] Coble RL. A model for boundary diffusion controlled creep in polycrystalline materials. *Journal of Applied Physics*. 1963;34(6):1679.
- [166] Herring C. Diffusional viscosity of a polycrystalline solid. *Journal of Applied Physics*. 1950;21(5):437.
- [167] Bressers J. *Creep and fatigue in high temperature alloys*. Applied Science Publishers; 1981.
- [168] Norton FH. *The creep of steel at high temperatures*. McGraw-Hill; 1929.
- [169] Kachanov LM. On creep rupture time. *Proc Acad Sci USSR Div Eng Sci*. 1958;8:26–31.
- [170] Robotnov YN. *Creep problems in structural members*. North-Holland Amsterdam; 1969.
- [171] Hyde TH, Xia L, Becker AA. Prediction of creep failure in aeroengine materials under multi-axial stress states. *International Journal of Mechanical Sciences*. 1996;38(4):385–403.

- [172] Hyde TH, Sun W, Williams JA. Prediction of creep failure life of internally pressurised thick walled CrMoV pipes. *International Journal of Pressure Vessels and Piping*. 1999;76:925–933.
- [173] Liu Y, Murakami S. Damage localization of conventional creep damage models and proposition of a new model for creep damage analysis. *Journal, JSME international*. 1998;41:57–65.
- [174] Sdobyrev VP. A long-time strength criterion for heat-resisting alloys under multiaxial states of stress. *Izvestia Akademii Nauk SSSR, Otdelenie Tekhnicheskikh nauk*. 1959;6:93–99.
- [175] Tai K, Endo T. Effect of pre-creep on the succeeding creep behaviour of a 2.25Cr-1Mo steel. *Scripta Metallurgica et Materialia*. 1993;29:643 – 646.
- [176] Cortellino F, Rouse JP, Cacciapuoti B, Sun W, Hyde TH. Experimental and numerical analysis of initial plasticity in P91 steel small punch creep samples. *Experimental Mechanics*. 2017;.
- [177] Ludtka GM, Laughlin DE. The influence of microstructure and strength on the fracture mode and toughness of 7XXX series aluminum alloys. *Metallurgical Transactions A*. 1982;13:411.
- [178] Embury JD, Wilcox BA, Clawer AH. The influence of microstructure on high-temperature creep and tensile deformation of Al-Zn-Mg-Cu alloys. *Journal of the Institute of Metals*. 1972;100:153–162.
- [179] Howard P, Lorimer GW, Pilkington R. Influence of microstructure upon the creep properties of an aluminium alloy. In: *Strength of Metals and Alloys: 7th International Conference*; 1985. p. 809–814.
- [180] Wilshire B, Willis M, Procedures IIE. Mechanisms of strain accumulation and damage development during creep of prestrained 316 stainless steels. *Metallurgical and Materials Transactions A*. 2004;35:563–571.
- [181] Ohashi Y, Kawai M, Momose T. Effects of prior plasticity on subsequent creep of type 316 stainless steel at elevated temperature. *Journal of Engineering Materials and Technology ASME*. 1986;108:68–74.

- [182] Kikuchi S, Ilschner B. Effects of a small prestrain at high temperatures on the creep behaviour of AISI 304 stainless steel. *Scripta Metallurgica*. 1986;20:159–162.
- [183] Kowalewski ZL. Effect of plastic prestrain magnitude on uniaxial tension creep of copper at elevated temperatures. *Journal of Theoretical and Applied Mechanics*. 1995;33(3):507–517.
- [184] Zhang YH, Knowles DM. Prestraining effect on creep behaviour of nickel base C263 superalloy. *Materials Science and Technology*. 2002;18(8):917–923.
- [185] Djakovic A, Dyson BF, Mclean M. Damage identification in creep of aluminium alloy 2650-T8. *Metalurgija*. 2005;11(3):243–250.
- [186] Motra HB, Hildebrand J, Dimmig-Osburg A. Assessment of strain measurement techniques to characterise mechanical properties of structural steel. *Engineering Science and Technology, an International Journal*. 2014;17(4):260–269.
- [187] Becker B, Dripke M. Choosing the right extensometer for every materials testing application. *Advanced Materials & Processes*. 2011;169:17–21.
- [188] ASM International. *Tensile testing*. 2nd ed. Davis JR, editor; 2004.
- [189] Morris AS, Langari R. Temperature measurement. In: *Measurement and Instrumentation*; 2016. p. 407–461.
- [190] Vernon-Parry KD. Scanning electron microscopy: an introduction. *III-Vs Review*. 2000;13(4):40–44.
- [191] Goldstein J. *Scanning electron microscopy and X-ray microanalysis*. Springer; 2012.
- [192] Heath J. *Energy dispersive spectroscopy*. 2nd ed. John Wiley & Sons; 2015.
- [193] Bean JJ, Saito M, Fukami S, Sato H, Ikeda S, Ohno H, et al. Atomic structure and electronic properties of MgO grain boundaries in tunnelling magnetoresistive devices. *Scientific Reports*. 2017;7(45594):1–9.
- [194] Baram M, Kaplan WD. Quantitative HRTEM analysis of FIB prepared specimens. *Journal of Microscopy*. 2008;232(3):395–405.

- [195] Williams DB, Barry Carter C. Transmission electron microscopy: A textbook for material science. Plenum Press, NY; 1996.
- [196] Lin Kl. Phase Identification Using Series of Selected Area Diffraction Patterns and Energy Dispersive Spectrometry within TEM. *Microscopy Research*. 2014;2:57–66.
- [197] Jauncey GEM. The scattering of X-rays and Bragg's law. *Proceedings of the National Academy of Sciences*. 1924;10:57–60.
- [198] Dingley D. Progressive steps in the development of electron backscatter diffraction and orientation imaging microscopy. *Journal of Microscopy*. 2004;213(3):214–224.
- [199] Geels K, Fowler DB, Kopp WU, Ruckert M. Metallographic and materialographic specimen preparation, light microscopy, image analysis, and hardness testing. ASTM International; 2007.
- [200] ICDD. PDF-2 2015 (Database), edited by Dr. Soorya Kabekkodu, International Centre for Diffraction Data, Newtown Square, PA, USA; 2015.
- [201] Schindelin J, Arganda-Carreras I, Frise E. Fiji: an open-source platform for biological-image analysis. *Nature methods*. 2012;9(7):676–682.
- [202] Freedman D, Diaconis P. On the histogram as a density estimator: L2 Theory. *Probability Theory and Related Fields*. 1981;57(4):453–476.
- [203] Fehlberg E. Low-order classical Runge-Kutta formulas with step size control and their application to some heat transfer problems. NASA Technical Report 315; 1969.
- [204] Barrett RA, O'Donoghue PE, Leen SB. An improved unified viscoplastic constitutive model for strain-rate sensitivity in high temperature fatigue. *International Journal of Fatigue*. 2013;48:192–204.
- [205] Dafalias YF, Kourousis KI, Saridis GJ. Multiplicative AF kinematic hardening in plasticity. *International Journal of Solids and Structures*. 2008;45(10):2861–2880.
- [206] Zhang Z, Delagnes D, Bernhart G. Anisothermal cyclic plasticity modelling of martensitic steels. *International Journal of Fatigue*. 2002;24(6):635–648.

Appendix

9.1 Detailed Schematics of Sample Location from Plate

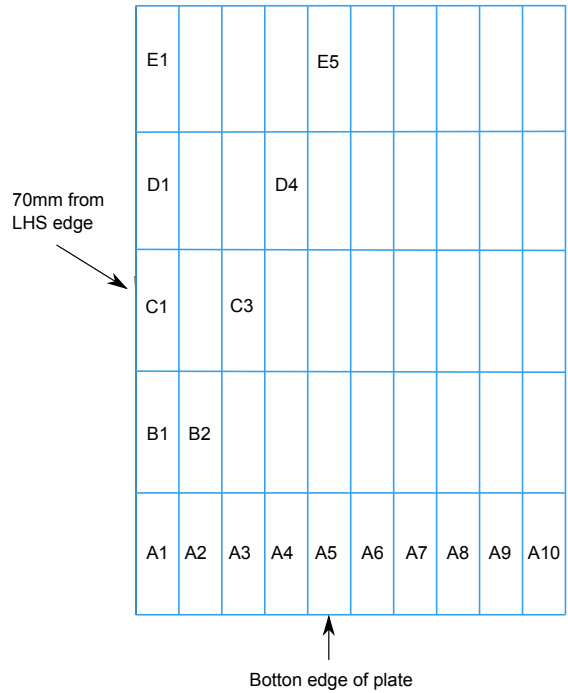


Figure 9.1: A schematic demonstrating the coordinate system used to assign fatigue sample ID

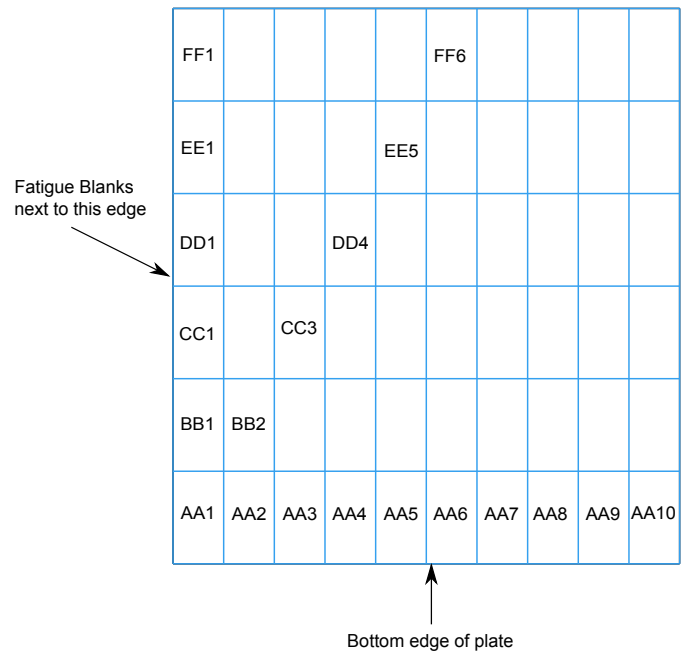


Figure 9.2: A schematic demonstrating the coordinate system used to assign creep sample ID

Adjustments Made to Stress Relaxation Tests

Intermittent regular dips in stress measurement were encountered which did not represent material behaviour. To investigate this problem, a thermocouple was placed close to the extensometer to observe the effect of ambient temperature on strain readings as shown in Fig. 3.24 while the extensometer was in contact with the sample. Fig. 9.3 shows that the strain fluctuated with the ambient temperature which consequently impacted the stress level. As the strain reading in the extensometer decreased, the machine compensated for this and increased the applied load to maintain the specified strain.

During the time of the experiment, a change in season was in effect, leading to a decreased difference between ambient and outdoor temperature. This meant that there was a lack of response from the air conditioning (AC) unit when there was a significant drop in temperature around the extensometer. Fig. 9.3 shows the sensitivity of the strain gauge in the extensometer to the ambient temperature and that heating from the AC was in regular bursts. The unit was switched to “winter mode” which kept the room temperature at 22-23°C. This greatly improved the stability in strain reading as shown in Fig. 9.4a. Insulation was attached around the extensometer as shown in Fig. 9.5 to see whether strain readings would differ but Fig. 9.4 shows the strain measurement stability was similar to when the extensometer was not insulated.

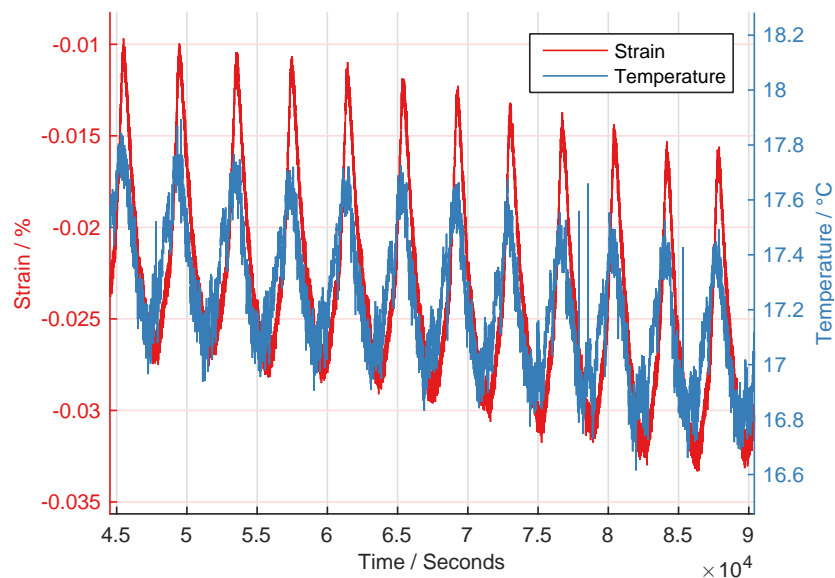
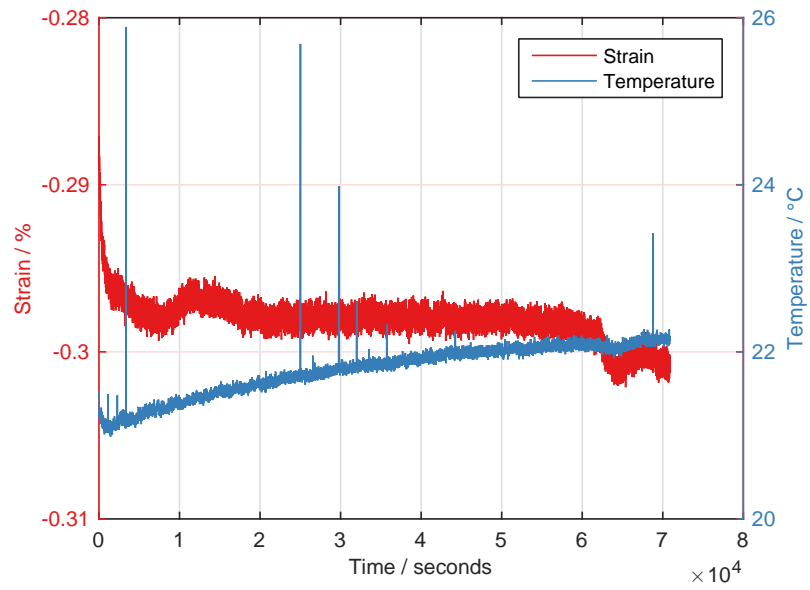
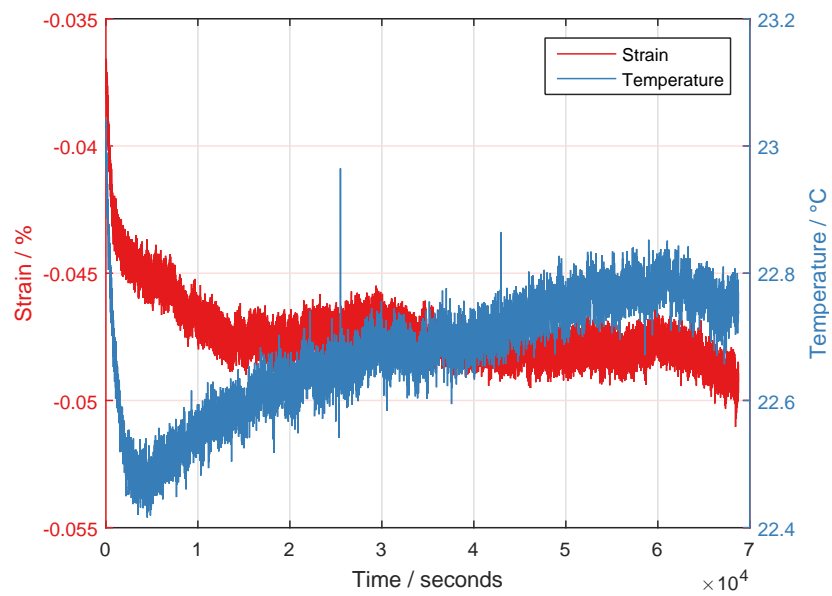


Figure 9.3: The sample strain and ambient temperature versus time before the room temperature setting was changed.



(a)



(b)

Figure 9.4: The sample strain and ambient temperature versus time after the room temperature was changed (a) with no insulation and (b) with insulation.

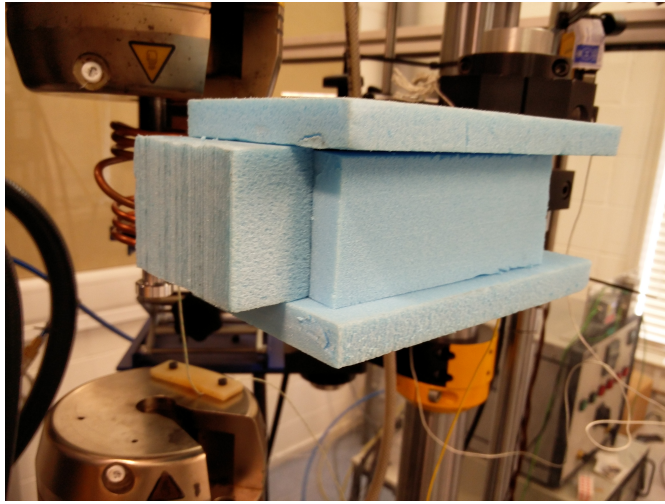


Figure 9.5: Insulated extensometer for the stress relaxation tests.